

STEPS TOWARD A THROUGH  
PROCESS MICROSTRUCTURAL  
MODEL FOR THE PRODUCTION OF  
ALUMINIUM SHEET

A THESIS SUBMITTED TO THE UNIVERSITY OF MANCHESTER  
FOR THE DEGREE OF DOCTOR OF PHILOSOPHY  
IN THE FACULTY OF ENGINEERING AND PHYSICAL SCIENCES

2016

**Liam Paul Dwyer**  
School of Materials



# Contents

<b>Abstract</b>	<b>18</b>
<b>Declaration</b>	<b>21</b>
<b>Copyright Statement</b>	<b>23</b>
<b>Acknowledgements</b>	<b>25</b>
<b>1 Introduction</b>	<b>27</b>
<b>2 Literature Review</b>	<b>29</b>
2.1 Introduction . . . . .	29
2.2 Aluminium Processing and Recycling . . . . .	30
2.2.1 Primary Production and Aluminium Recycling . . . . .	30
2.2.2 Commercial Sheet Process Route . . . . .	31
2.3 3XXX Series Aluminium . . . . .	34
2.3.1 Constituent Particles . . . . .	34
2.3.2 Dispersoids . . . . .	37
2.3.3 Nucleation vs Coarsening . . . . .	38
2.3.4 Quantifying Second Phase Particles . . . . .	38
2.4 Plastic Deformation in Aluminium . . . . .	46
2.4.1 Fundamentals of Slip . . . . .	46
2.4.2 Deformation within a Single Phase System . . . . .	49
2.4.3 Deformation in Multi-Phase Materials . . . . .	52
2.5 Restoration Processes . . . . .	63
2.5.1 Recovery . . . . .	63
2.5.2 Recrystallization . . . . .	64

2.5.3	Particle Effects on Restoration . . . . .	65
2.5.4	Solute Drag . . . . .	65
2.5.5	Particle Stimulated Nucleation . . . . .	66
2.6	Modelling Deformation around Particles . . . . .	69
2.6.1	Crystallographic Deformation Modelling . . . . .	69
2.6.2	Modelling Deformation in Two Phase Materials . . . . .	72
2.7	Rationale of the Study . . . . .	77
<b>3</b>	<b>Experimental Methods</b>	<b>79</b>
3.1	Material Studied . . . . .	79
3.2	Thermomechanical Processing . . . . .	80
3.2.1	Homogenisation . . . . .	80
3.2.2	Rolling . . . . .	80
3.2.3	Plane Strain Compression . . . . .	80
3.3	Sample Preparation . . . . .	83
3.3.1	Sample Cutting . . . . .	83
3.3.2	Polishing . . . . .	83
3.3.3	Gold Remodelling . . . . .	83
3.4	Scanning Electron Microscopy . . . . .	85
3.4.1	Secondary Electrons . . . . .	85
3.4.2	BackScatter SEM . . . . .	85
3.4.3	Serial Block Face SEM . . . . .	86
3.4.4	Visualisation and Quantification of 3D Data . . . . .	88
3.5	Strain Mapping (Digital Image Correlation) . . . . .	92
3.6	Crystal Plasticity Modelling . . . . .	94
<b>4</b>	<b>Results</b>	<b>97</b>
4.1	Particle ‘Closeness’ . . . . .	97
4.1.1	Measuring Distributions of Particles . . . . .	97
4.1.2	Dangalchev Closeness Centrality . . . . .	98
4.1.3	Neighbour Weighted Closeness . . . . .	101
4.2	Characterisation of Particles . . . . .	107
4.2.1	2D Analysis . . . . .	107

4.2.2	3D Analysis - Constituents . . . . .	114
4.2.3	3D Analysis - Dispersoids . . . . .	148
4.2.4	Combining the 3D Data . . . . .	156
4.3	Deformation Around Particles . . . . .	160
4.3.1	Strain Mapping Around Particles . . . . .	160
4.3.2	Crystal Plasticity FEM . . . . .	168
4.3.3	CPFEM - One Particle . . . . .	172
4.3.4	CPFEM - Two Particles . . . . .	181
4.3.5	Comparing the CPFEM Results . . . . .	189
4.4	Summary of Results . . . . .	192
<b>5</b>	<b>Discussion</b>	<b>193</b>
5.1	Novel 3D Studies using the 3View . . . . .	193
5.1.1	Constituent Population Measurements . . . . .	196
5.1.2	Dispersoid Population Measurements . . . . .	197
5.2	Deformation around Particles . . . . .	199
5.2.1	Strain Maps of Model Alloy . . . . .	199
5.2.2	Slip Bands Within CPFEM Simulations . . . . .	200
5.2.3	Linking the CPFEM to PSN . . . . .	201
5.2.4	Extending the Slip Shadowing Model . . . . .	203
5.3	Steps Toward a Through Process Model . . . . .	207
5.3.1	Parameters from the Serial Sectioning Analysis . . . . .	207
5.3.2	Parameters from the Deformation Analysis . . . . .	208
<b>6</b>	<b>Conclusions</b>	<b>209</b>
<b>7</b>	<b>Suggested Future Work</b>	<b>211</b>
<b>A</b>	<b>Appendix</b>	<b>227</b>
A.1	Modified Preprogram Subroutine . . . . .	227
A.2	Saltykov Method: Supplementary Plots . . . . .	237
A.3	Radon Transform MATLAB Code . . . . .	239
A.4	Radon Transforms - Input Strain Maps . . . . .	241
A.5	CPFEM: Supplementary Strain Plots . . . . .	242



# List of Tables

2.1	Solidification Reactions in 3003 Alloy Containing 1.19% Mn, 0.55% Fe and 0.18% Si taken from [Bäckerud et al., 1986] in [Eskin, 2008] . . . . .	34
2.2	The Minkowski Functionals [Hadwiger, 1957] . . . . .	39
3.1	Composition (wt%) of model alloy and commercial AA3003 . . . . .	79
3.2	Rolling Parameters for Deformation Studies . . . . .	81
3.3	Zeiss Evo50 BS-SEM Scanning Parameters . . . . .	85
3.4	Sirion BS-SEM Scanning Parameters . . . . .	86
3.5	3View Scanning Parameters . . . . .	86
3.6	CPFEM Material Parameters . . . . .	96
4.1	Closeness Contribution Table . . . . .	98
4.2	Neighbour Weighted Closeness Contribution Table . . . . .	102
4.3	Comparison of Neighbour Weighted and Non Weighted Closeness Contributions . . . . .	103
4.4	Summary of Closeness Measures . . . . .	106
4.5	Samples studied using SBF-SEM . . . . .	114
4.6	Characterisation of Example Particle Shown in 4.13 . . . . .	116
4.7	Parameters from As Cast Closeness Distributions . . . . .	124
4.8	Parameters from Homogenised Closeness Distributions . . . . .	129
4.9	Parameters from Rolled Closeness Distributions . . . . .	131
4.10	Number of Constituent Particles above the Threshold Size . . . . .	134
4.11	Weibull Coefficients and Fit Data for Constituent Size Distributions . . . . .	136
4.12	Weibull Coefficients and Fit Data for Sphericity Distributions . . . . .	139
4.13	Parameters from Homogenised Closeness Distributions . . . . .	141
4.14	Number of Dispersoids above the Threshold Size . . . . .	154

4.15 Weibull Coeffs and Fit Data for Fitting Curves for Dispersoid Data . .	156
4.16 Combined Volume Fractions of Second Phase Particles . . . . .	157
4.17 Comparison of CPFEM Results . . . . .	189

# List of Figures

2.1	Aluminium Processing Flow Chart . . . . .	30
2.2	Aluminium Sheet Process Stream . . . . .	32
2.3	Intermetallic particle wetting within a similar AA3XXX model alloy . .	35
2.4	Constituents in ingot-sourced 0.33-mm cold-rolled AA3004 sheet, three- dimensional optical microscopy . . . . .	36
2.5	Illustration of the contribution of different size particles to 2D data . .	40
2.6	2D SEM (a) showing what appears to be a single particle with full 3D visualisation (b) of the same particle (blue) showing a complex network structure . . . . .	41
2.7	Example stress-strain curve of an aluminium alloy produced from a compression test . . . . .	47
2.8	Resolving shear stress on a slip system from initial force . . . . .	48
2.9	The features of crystal deformation shown at increasing scale . . . . .	50
2.10	Microshear bands intersecting aligned cell bands in deformed aluminium [Hurley and Humphreys, 2003]. . . . .	51
2.11	Strain rate dependency on dislocation accumulation at particles . . . .	52
2.12	Formation of Orowan Loops . . . . .	53
2.13	The effect of particle deformation on slip homogeneity . . . . .	54
2.14	Relative misorientation at a 3 $\mu\text{m}$ particle in deformed Aluminium . . .	56
2.15	TEM images showing the deformation zones around two similar parti- cles within two crystals with the same orientation . . . . .	57
2.16	The maximum angle of lattice rotation at second phase particles in aluminium as a function of strain and particle size . . . . .	58
2.17	The Slip Shadowing Model . . . . .	58

2.18	Digital Image Correlation around a constituent particle in Al-Si alloy [Ko, 2014] . . . . .	60
2.19	Effect of Particle Size on Slip Band Evolution[Ko, 2014] . . . . .	61
2.20	Stages of Recovery . . . . .	63
2.21	Predicted Grain Size for a PSN efficient material . . . . .	68
2.22	CPFEM Simulations around a Particle . . . . .	73
2.23	Experimental and modelled deformation zones using 3D EBSD and CPFEM from [Humphreys et al., 2012] . . . . .	75
2.24	Simulation results of pseudo-2D and full 3D models. (a) Pseudo-2D strain, (b) 3D strain, (c) pseudo-2D rotation, (d) 3D rotation [Ko, 2014].	76
2.25	Strain and rotation plots comparing 3D and pseudo-2D CPFEM simu- lations [Ko, 2014]. . . . .	76
3.1	Temperature Profile of Homogenisation Treatment . . . . .	80
3.2	Channel die for plane strain compression experiments . . . . .	82
3.3	Gold Remodelling experimental set up . . . . .	84
3.4	An example of a the randomised speckled pattern of a remodelled region	84
3.5	Schematic diagram of the 3View system . . . . .	86
3.6	Schematic diagram of the 3View cutting and visualisation process . . .	87
3.7	Incomplete cuts make up 5% of the image stack but the missing data can be estimated . . . . .	88
3.8	Example of how images within the stack are processed . . . . .	89
3.9	Casino plot showing surface radius of backscattered electrons . . . . .	90
3.10	Casino plot showing penetration depth of backscattered electrons . . .	91
3.11	An example of subregion discretisation and the resulting displacement vector. . . . .	92
3.12	A schematic of the conversion from experimental particle to CPFEM input. . . . .	95
4.1	Contribution to closeness of $x_0$ from particles $x_1$ and $x_2$ decreases with distance $d$ . . . . .	98
4.2	Closeness profile of volume containing a random distribution of particles as a function of number fraction . . . . .	99

4.3	Incorporation of particle measurements can act to reduce the interparticle distances used in closeness measurements and therefore increase the closeness measure . . . . .	101
4.4	Contribution to closeness of $x_0$ from particle $x_1$ falls when the size of $x_1$ is considered. This is termed ‘weighted closeness’. . . . .	102
4.5	The effect neighbour weighting on the closeness profile of volume containing a random distribution of particles . . . . .	104
4.6	(a) Random distribution of particles in 2D [to scale], (b) closeness values calculated using only distance measures, (c) weighted closeness measures calculated using distance and particle size. The connections plotted illustrate closeness of $> 0.1$ with arrows indicating contributions from particle $i$ to $j$ . . . . .	105
4.7	BS-SEM images of the as cast and homogenised microstructures of the low manganese alloy PGL . . . . .	108
4.8	BS-SEM images of the as cast and homogenised microstructures of the medium manganese alloy PGM . . . . .	109
4.9	BS-SEM images of the as cast and homogenised microstructures of the high manganese alloy PGN . . . . .	110
4.10	Images taken at high magnification show the presence of dispersoids in homogenised PGM and PGN . . . . .	111
4.11	BS-SEM images of the microstructure of PGN after deformation . . . .	112
4.12	Raw images obtained using the 3View system for the respective samples of PGN (each image represents an area of $(51.2 \mu\text{m})^2$ ). . . . .	115
4.13	Example of visualised particle (taken from ‘as cast’ data set) and the calculated bounding box . . . . .	116
4.14	Visualised constituents within the as cast alloy . . . . .	117
4.15	Plot showing the number fraction (red) and volume fraction (bar) of particles with a given equivalent diameter in the as cast sample. . . . .	118
4.16	Zingg plot of particles found within the as cast visualisation . . . . .	119

4.17	(a) Scatter plot showing the general relationship between the sphericity of the particles within the as cast volume and their size. (b) Plot showing the number fraction (red) and the volume fraction (bar) of particles grouped according to their sphericity . . . . .	120
4.18	Scatter plots generated illustrating the (a) raw, (b) distance corrected and (c) weighted closeness of constituents in the as cast alloy, with (d-f) their corresponding closeness distributions. Three data points are coloured independently for later comparison . . . . .	122
4.19	Visualised constituents within the homogenised alloy . . . . .	125
4.20	Plot showing the number fraction (red) and volume fraction (bar) of particles with a given equivalent diameter in the homogenised sample. . . . .	126
4.21	(a) Plot showing the general relationship between the sphericity of the particles within the homogenised volume and their size. (b) plot showing the number fraction (red) and the volume fraction (blue) of particles grouped according to their sphericity . . . . .	127
4.22	Scatter plots generated illustrating the (a) raw, (b) distance corrected and (c) weighted closeness of constituents in the homogenised aluminium alloy, with (d-f) their corresponding closeness distributions . . . . .	128
4.23	Visualised constituents within the hot rolled alloy . . . . .	130
4.24	Plot showing the number fraction (red) and volume fraction (bar) of particles with a given equivalent diameter in the rolled sample. . . . .	131
4.25	(a) Plot showing the general relationship between the sphericity of the particles within the rolled volume and their size. (b) plot showing the number fraction (red) and the volume fraction (blue) of particles grouped according to their sphericity . . . . .	132
4.26	Scatter plots generated illustrating the (a) raw, (b) distance corrected and (c) weighted closeness of constituents in the hot rolled aluminium alloy, with (d-f) their corresponding closeness distributions . . . . .	133
4.27	Plot showing the change in volume fraction contribution of each constituent size during processing. The dotted lines show the path of the fitted Weibull curves. . . . .	135

4.28	Measured and calculated volume fractions of each size range in (a) homogenised and (b) hot rolled material . . . . .	137
4.29	Plot showing the change in volume fraction contribution by particles of different complexity during processing. The dotted lines show the path of the fitted Weibull curves. . . . .	138
4.30	Measured and calculated volume fractions of each sphericity range in (a) homogenised and (b) hot rolled material . . . . .	139
4.31	Local curvature visualisations showing progressive rounding from (a) as cast, to (b) homogenised and (c) rolled material . . . . .	142
4.32	Comparison of weighted closeness scatter plots (a-c) and plots of the resulting closeness distributions (d-f) across the populations of constituent particles . . . . .	143
4.33	2D and Saltykov corrected equivalent diameters of constituents in rolled aluminium compared to 3D data grouped using 0.1 $\mu\text{m}$ intervals . . . .	145
4.34	Plot showing the difference between measured 2D particle size, and the calculated 3D particle size from this dataset and the true 3D particle dimensions . . . . .	147
4.35	Example of particle break-off within high resolution cutting . . . . .	149
4.36	Visualised dispersoids within the homogenised alloy . . . . .	149
4.37	Plot showing the number fraction (red) and volume fraction (bar) of dispersoids with a given equivalent diameter in the homogenised sample.	150
4.38	Plot showing the number fraction (red) and volume fraction (bar) of sphericity values of dispersoids within the homogenised sample. . . . .	151
4.39	Visualised dispersoids within the hot rolled alloy . . . . .	152
4.40	Plot showing the number fraction (red) and volume fraction (bar) of dispersoids with a given equivalent diameter in the rolled sample. . . . .	153
4.41	Plot showing the number fraction (red) and volume fraction (bar) of sphericity values of dispersoids within the rolled sample. . . . .	153
4.42	Plot showing how the volume fraction contribution of dispersoids changes due to deformation. The dotted lines show the path of the fitted Weibull curves. . . . .	155

4.43	Plot showing the change in sphericity of dispersoids size during processing. The dotted lines show the path of the fitted Weibull curves. . . . .	157
4.44	Plots showing the volume fraction of dispersoids (red) and constituents (blue) grouped by equivalent diameter. . . . .	159
4.45	Nanopatterned gold on sample surface after remodelling (100 × 100 pixels in image, 65 pixels/μm) . . . . .	161
4.46	Raw images and the resulting strain map produced using step-wise plane strain compression on gold patterned aluminium. X Axis = TD, Y Axis = ND . . . . .	162
4.47	Local shear strain profiles taken (a) perpendicular to and (b) parallel to the primary slip bands . . . . .	163
4.48	Alignment of slip bands at 4% and 8% reductions, produced using a Radon transform from the shear strain data . . . . .	165
4.49	Rotation map produced using DIC from images taken at reductions of 0%, 4% and 8%. The particles visible on the surface have been included as a green overlay. All rotations are in degrees. . . . .	166
4.50	Raw images and the resulting strain and rotation maps produced using step-wise plane strain compression on gold patterned aluminium containing a particle cluster. X Axis = TD, Y Axis = ND . . . . .	167
4.51	Magnified rotation map illustrating the complex rotations near to a particle cluster . . . . .	168
4.52	Alignment of slip bands at 4% and 8% reductions, produced using a Radon transform from the data in figure 4.50c . . . . .	169
4.53	Variation in how the orientations are ‘perturbed’ alters local strain, each image shows the result from the 80th iteration of the respective models. . . . .	170
4.54	The variation in strain in the CPFEM with increasing deformation with varying initial orientation perturbed values . . . . .	171
4.55	Changes in local rotation of the matrix with increasing particle size . . . . .	173

4.56	(a) Plot showing how the maximum local strain (as a multiple of the global strain) within the CPFEM changes with particle size. (b) Plot showing the largest measured rotations (scatter) and the average area of the highly rotated zones (bar) within the CPFEM with changing particle size . . . . .	174
4.57	(a) Plot illustrating how the maximum local strain within the CPFEM changes with increasing particle aspect ratio. (b) The average size of each heavily rotated plume (bar) and maximum rotation predicted with changing aspect ratio. . . . .	176
4.58	Comparison of the particle size and aspect ratio plots for (a) maximum local strain and (b) average size of each heavily rotated zone (bar) and maximum rotation. . . . .	177
4.59	Changing the orientation of the non deformable region . . . . .	178
4.60	(a) Plot showing how the maximum local strain within the CPFEM changes with particle orientation. (b) Plot showing the largest measured rotations (scatter) and the area of the highly rotated zones (bar) within the CPFEM with changing particle orientation with respect to the $x$ axis	180
4.61	Images depicting how changing the distance between two non deformable regions aligned at $45^\circ$ to the $x$ axis changes the resulting rotations within the matrix . . . . .	181
4.62	(a) Plot showing how the maximum local strain within the CPFEM changes with interparticle spacing. (b) Plot showing the largest measured rotations (scatter) and the area of the highly rotated zones (bar) within the CPFEM with changing interparticle spacing when particles are aligned at $45^\circ$ to the $x$ axis . . . . .	183
4.63	Images illustrating how changing the distance between two non deformable regions aligned along the $x$ axis changes the local rotations within the matrix . . . . .	184

4.64	(a) Plot showing how the maximum local strain within the CPFEM changes with interparticle spacing. (b) Plot showing the largest measured rotations (scatter) and the area of the highly rotated zones (bar) within the CPFEM with changing interparticle spacing when particles are aligned at 45° to the $x$ axis . . . . .	185
4.65	Plots illustrating how changing the alignment (angle relative to $x$ axis) of two non deformable regions whilst maintaining the same interparticle distance affects the rotations of the matrix . . . . .	187
4.66	(a) Plot showing how the maximum local strain within the CPFEM changes with particle alignment. (b) Plot showing the largest measured rotations (scatter) and the area of the highly rotated zones (bar) within the CPFEM with changing particle alignment . . . . .	188
5.1	Varying separation of particles within the CPFEM results in fundamentally different slip behaviour, as illustrated by extended slip-shadowing diagrams . . . . .	204
5.2	Slip shadowing configuration for closely spaced particles aligned with a principle slip system . . . . .	205
5.3	Extended slip-shadowing diagram illustrating how partial alignment of particles can lead to partial slip shadowing . . . . .	206
A.1	[Raw 2D and Saltykov corrected equivalent diameters of rolled aluminium grouped using 0.2 $\mu\text{m}$ intervals . . . . .	237
A.2	Raw 2D and Saltykov corrected cumulative equivalent diameters of rolled aluminium grouped using 0.2 $\mu\text{m}$ intervals . . . . .	237
A.3	Raw 2D and Saltykov corrected equivalent diameters of rolled aluminium grouped using 0.3 $\mu\text{m}$ intervals . . . . .	238
A.4	Raw 2D and Saltykov corrected cumulative equivalent diameters of rolled aluminium grouped using 0.3 $\mu\text{m}$ intervals . . . . .	238
A.5	DIC Strain maps for the single particle case illustrating the presence of artefacts which diminish upon subsequent compression. . . . .	241
A.6	Changing the particle size effects the local strain found within the matrix	242

A.7	Changing the orientation of the non deformable region alters the resulting local strains . . . . .	243
A.8	Images depicting how changing the distance between two non deformable regions aligned at 45° to the $x$ axis changes the resulting local strain within the matrix . . . . .	244
A.9	Images illustrating how changing the distance between two non deformable regions aligned along the $x$ axis changes the local strain within the matrix . . . . .	245
A.10	Plots illustrating how changing the alignment (angle relative to $x$ axis) of two non deformable regions whilst maintaining the same interparticle distance affects the local strain within the matrix . . . . .	246



# The University of Manchester

Liam Paul Dwyer

Doctor of Philosophy

**Steps Toward a Through Process Microstructural Model for the Production of Aluminium Sheet**

**February 28, 2016**

Aluminium sheet production is a multi-stage process in which altering processing conditions can drastically alter the size and type of second phase particles found in the final product. The properties of these second phase particles also affects deformation and annealing processes, meaning that any attempt to create a through process model would require the ability to predict both how the particles would develop in the material, and how these particles then affect the alloy moving forward.

This project first focuses on gaining insight into how the particles in a model aluminium alloy change during homogenisation heat treatment and hot rolling. This has been accomplished by utilising serial block face scanning electron microscopy (SBF-SEM), a technique which allows the capture of 3D data sets at sub micron resolutions. This has allowed the populations of primary (constituent) and secondary (dispersoid) particles to be analysed at different stages of sheet production, and thus allowing the effects of homogenisation and hot rolling on particle populations to be quantified.

To discover how the particles would go on to affect further processing, digital image correlation has been used to examine the localised strain in the alloy near to a selection of particle configurations. This highlighted the heterogeneity in slip behaviour within the alloy and illustrated that plumes of rotation develop near to non deformable regions.

Rotation plumes have previously been modelled using a crystal plasticity model, and so further work is also presented expanding upon this model to simulate a variety of particle configurations. This has shown that in the case of single particles, local deformation is dependent on both the aspect ratio of the particle and how it is aligned to the active slip system. With the incorporation of a second particle, the interparticle spacing must also be considered.

Word count 39800



# Declaration

No portion of the work referred to in the thesis has been submitted in support of an application for another degree or qualification of this or any other university or other institute of learning.



# Copyright Statement

- i.** The author of this thesis (including any appendices and/or schedules to this thesis) owns certain copyright or related rights in it (the “Copyright”) and s/he has given The University of Manchester certain rights to use such Copyright, including for administrative purposes.
- ii.** Copies of this thesis, either in full or in extracts and whether in hard or electronic copy, may be made **only** in accordance with the Copyright, Designs and Patents Act 1988 (as amended) and regulations issued under it or, where appropriate, in accordance with licensing agreements which the University has from time to time. This page must form part of any such copies made.
- iii.** The ownership of certain Copyright, patents, designs, trade marks and other intellectual property (the “Intellectual Property”) and any reproductions of copyright works in the thesis, for example graphs and tables (“Reproductions”), which may be described in this thesis, may not be owned by the author and may be owned by third parties. Such Intellectual Property and Reproductions cannot and must not be made available for use without the prior written permission of the owner(s) of the relevant Intellectual Property and/or Reproductions.
- iv.** Further information on the conditions under which disclosure, publication and commercialisation of this thesis, the Copyright and any Intellectual Property and/or Reproductions described in it may take place is available in the University IP Policy (see <http://documents.manchester.ac.uk/DocuInfo.aspx?DocID=487>), in any relevant Thesis restriction declarations deposited in the University Library, The University Library’s regulations (see <http://www.manchester.ac.uk/library/aboutus/regulations>) and in The University’s Policy on Presentation of Theses.



# Acknowledgements

First of all, I would like to thank my supervisor, Prof. Joe Robson, for his continued support and guidance throughout the last  $4\frac{1}{2}$  years. Thanks also go to Dr. Nicolas Kamp and the team at Novelis for their alloys, their continued insights and their financial support.

I would also like to thank Dr. Claire Hinchliffe, Prof. Bradley Wynne and all staff and researchers associated with the Advanced Metallic Systems CDT, as well as the EPSRC, without whom the funding for my project and CDT itself would not exist. A special thank you goes to all members of my cohort within the CDT, for the encouragement over the years, the numerous coffees (I feel it only fair to give Janette Harris a special mention here), the entertainment during countless hours on trains, and without whom this experience would have been much less rewarding.

To all members of LATEST2 at the University of Manchester, and especially the Light Alloys group, past and present, thank you all for your help and support over the years. Special thanks to Dr. Lawrence Ko for sharing his experience with the DIC technique, and Teruo Hashimoto for his expertise in using the 3View system.

To Chris Smith and Jefri Draup. America. What else is there to say? Thank you for the experience of a lifetime.

To Sophie Pettigrew and Alicia Kidd, I can't remember what life was like without you. Thank you for always knowing how to make me smile.

To all members of Virgin Active Didsbury and Manchester Aquatics Centre, and any other health clubs where I have been fortunate enough to work over the years, thank you for providing a completely different environment to academia and helping me to keep my head.

Finally, thank you to David Haw for amongst other things, convincing me to never give up, and thank you to my parents because I don't say that enough.



# Chapter 1

## Introduction

Aluminium is one of the most versatile base materials with current uses ranging from construction and aerospace, to food packaging and sporting goods. Production of primary aluminium has increased globally from a daily average of approximately 33 thousand metric tonnes in the early 1970s to an estimated 150 thousand metric tonnes as of January 2015 [World Aluminium, 2015].

As an **elemental material**, the basic properties of aluminium do not change with mechanical or physical processing. This means that aluminium is intrinsically sustainable: once produced, it can be **recycled repeatedly without any loss in quality** and reused in the manufacture of consumer and industrial products.

*Executive Summary, Aluminum: The Element of Sustainability [The Aluminum Association, 2011]*

The above statement is an example of the widely held belief of the reusability of aluminium. However, the aluminium used in everyday applications is not the pure elemental material, but contains a wide variety of alloying elements, thus forming alloys. These additions are vital in tailoring the metal, providing the improved strength, corrosion resistance or formability needed for the material to be viable. It is also these alloying additions which drastically reduce the ‘intrinsic sustainability’ of aluminium products.

Alloying elements can disperse within the metal, creating a single phase alloy, or combine to form particles within the aluminium matrix. The size and shape of these

particles is dependent on not only the composition of the alloy, but also the processing route taken to produce the alloy. For this reason, the production of aluminium sheet requires precise control of composition, temperature and strain rates.

In all alloys containing second phase particles, it is the particles which are vital in altering how the aluminium behaves during thermomechanical processing, thus providing the desirable qualities of the alloy (or undesirable properties in the case of unwanted alloying elements). It therefore follows that to understand how and why an alloy behaves in a particular way, microstructural analysis must be undertaken to allow insight into the fundamental properties of the material.

Part of this work focuses on a novel method of characterising the microstructure of aluminium alloys. This has been shown to provide insights into the three dimensional structure of the particles found within an aluminium alloy, demonstrating how the morphology of the particles and the particle distribution as a whole, changes as the material is processed from an as-cast billet to a hot rolled aluminium sheet.

During deformation processes, the aluminium matrix itself interacts with non-deformable particles which in turn affects the crystal structure and relative orientation of the matrix near to particles. This effect has been modelled and verified for single simple particles using crystal plasticity finite element modelling. Part of this work aims to expand this model to determine the effect that increasing the complexity of the particle has on the deformed region of the matrix.

# Chapter 2

## Literature Review

### 2.1 Introduction

Within this review, a brief outline of the production of rolled aluminium products is presented along with a summary of current aluminium recycling technology.

This survey then concentrates on microstructural theory of aluminium, focusing first on the different phases found within the 3XXX series alloy group and how they are characterised. The focus then shifts to the crystallographic aspects of deformation including dislocation theory and the influence of second phase particles on deformation processes, with a brief discussion of how this relates to the stages of processing. Modelling of crystallographic deformation is then briefly summarised before the restoration processes of recovery and recrystallization, in single and dual phase materials, are discussed.

## 2.2 Aluminium Processing and Recycling

### 2.2.1 Primary Production and Aluminium Recycling

Primary aluminium production is a multi-step process which requires mining of bauxite ore, chemical processing of this ore to produce alumina, and energy intensive electrolysis to obtain the aluminium metal. This process requires approximately 45 kWh to produce 1 kg of primary aluminium [Das and Yin, 2007]. As of 2007, primary aluminium production consumed 2% of the worldwide electricity supply and though over 40% of this energy was from renewable sources [International Aluminium Institute, 2015], almost half was coal-generated electricity. As the electrolytic step of aluminium production also produces 0.4 tonnes of CO<sub>2</sub> per tonne of primary material, it is clear that primary aluminium production plays a significant role in global greenhouse emissions. However, compared to primary aluminium production, the recycling process consumes 95% less energy which also equates to greatly reduced carbon emissions [Green and Skillingberg, 2006]. An overview of aluminium production is shown in figure 2.1 [Nakajima et al., 2010].

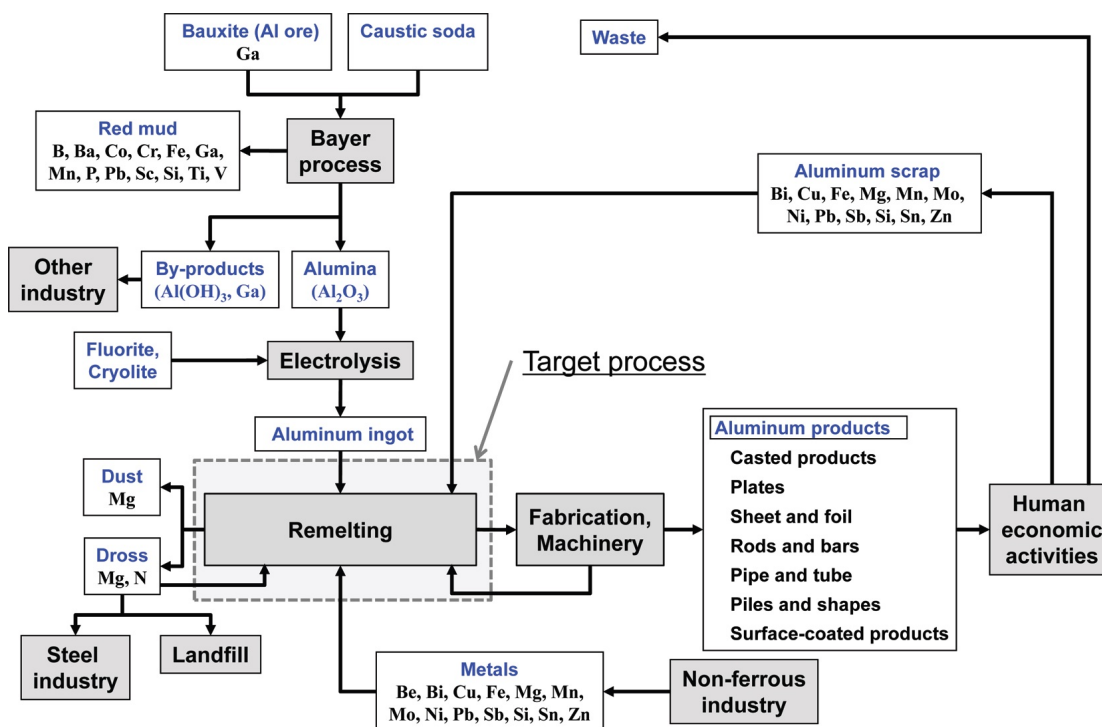


Figure 2.1: Flow chart of current aluminium production [Nakajima et al., 2010]

When recycling aluminium, scrap must be sorted by composition and processed

separately as some alloying elements can not be removed during the recycling process. Material is cleaned of any coatings or contaminants using high temperature treatments before remelting. Fluxes are added to the scrap to aid in the removal of magnesium and create an oxidation barrier on the surface of the melt [Utigard et al., 1998].

Some impurity elements found within recycled aluminium such as iron and silicon are not easy to remove from the melt, which limits the applications of the recycled material [Schmitz, 2006]. As the compositional tolerances of casting alloys are more forgiving in terms of impurity elements, as of 2010, most external scrap inside the European Union is utilised in the production of casting alloys [Kevorkijan, 2010]. For use in wrought aluminium alloy production, recycled material must be diluted with primary aluminium to reduce the concentration of impurity elements to within compositional limits. This issue ensures that primary aluminium production and the resulting energy costs and environmental consequences will remain necessary until either the current recycling technology improves, thus allowing economically viable methods of impurity removal, or new alloys with the desired properties are developed which are both tolerant to higher levels of impurity elements and accepted by industry as a viable alternative to currently produced materials.

Research in many institutions now focuses on uncovering methods to reduce the effects of impurity elements [Zhang et al., 2012] [Nakajima et al., 2010], therefore allowing greater use of recycled material and reduced dependence on virgin aluminium.

High purity (elemental) aluminium has a very low yield strength of 7-11 MPa [Polmear, 2006] whereas the incorporation of precise levels of alloying elements such as copper, magnesium, and zinc, amongst others, and careful processing can create aerospace grade alloy 7075 with an initial yield strength of 145 MPa. This is further strengthened to a yield strength of up to 476 MPa when the material is ‘peak aged’ [Alcoa, 2013]. This illustrates the importance of both the incorporation of tailored alloying elements, and the use of the most beneficial processing conditions when creating aluminium alloys.

### **2.2.2 Commercial Sheet Process Route**

A general overview of aluminium sheet production is shown in figure 2.2, although the exact temperature and thickness parameters will vary depending on the desired

product.

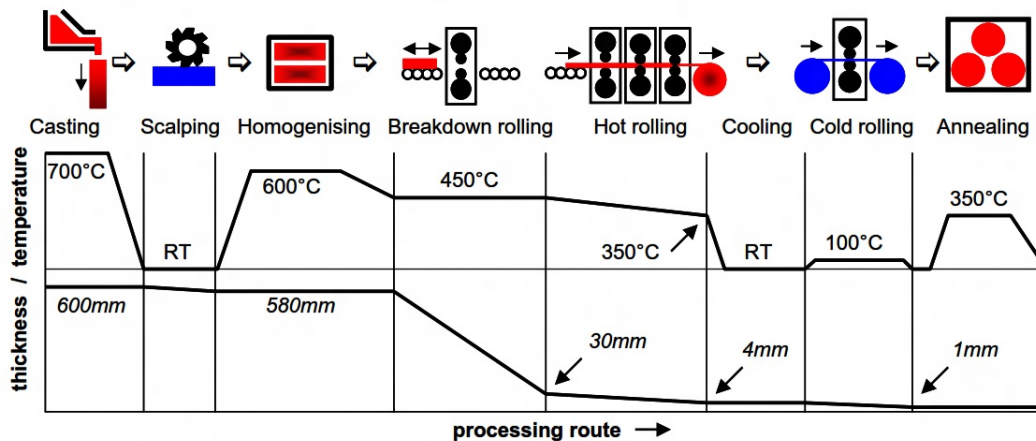


Figure 2.2: A generalised process stream used to produce aluminium sheet in industry [Anselmino, 2007]

## Direct Chill Casting

The first stage of sheet production involves the melting of pure aluminium, any added scrap and alloying elements (in the form of a master alloy) in a furnace [Polmear, 2006]. After the melt has settled, impurities are skimmed from the surface and inert gas is bubbled through the molten metal in an effort to remove dissolved gases. The use of a water cooled mould encourages solidification of the material, ensuring minimal segregation of alloying elements throughout the final billet. The cast billet consists of randomly oriented grains [Samajdar and Doherty, 1994].

In many aluminium alloys containing Si, Mn, Fe and Cu, rapid solidification results in the formation of a network of second phase particles throughout the cast microstructure, whilst the matrix itself remains supersaturated with some alloying elements [Li and Arnberg, 2003a].

Once cast, the billet is scalped (or trimmed) to remove any surface defects before further processing [Polmear, 2006].

## Homogenisation

Homogenisation heat treatments are designed with differing goals depending on the composition of the alloy and its intended use. Primarily, the goals of this initial heat treatment are to redistribute alloying elements, reducing any microsegregation

and supersaturation [Davies, 1993]. During heat treatment, the elevated temperatures result in an increase to the diffusion rate, which in turn allows any pockets of increased alloying element concentration to be re-dispersed. This allows the network of second phase particles, which formed during solidification, to break up (see section 2.3.1) while smaller second phase particles also nucleate (see section 2.3.2) [Polmear, 2006].

### **Rolling**

To produce aluminium sheet, ingot thickness is first reduced by breakdown rolling, which is a multipass procedure that occurs at high enough temperature to allow recrystallisation. The initially large grains of random orientation are first elongated in the rolling direction during deformation before they recrystallise [Blade, 1979]. This process also acts to break up any large second phase particles and disperse them throughout the material [Merchant et al., 1990].

Cold rolling describes further reductions in sheet/plate thickness which occur at temperatures below the recrystallisation threshold. During this stage the material can not recrystallise, resulting in strain hardened material [Doherty, 1974].

### **Annealing**

The final heat treatment when producing sheet can have many objectives depending on the alloy system. To increase formability of an alloy, a heat treatment may be designed to fully recrystallise the material (full anneal), whereas if alloy strength is more important, a partial anneal (during which the material recovers but recrystallisation does not take place) may be more suited [Chandler, 1996]. Recovery and recrystallisation are examined more closely in section 2.5.

## 2.3 3XXX Series Aluminium

The 3XXX series of aluminium alloys contain manganese as the main alloying element, with smaller additions of silicon, magnesium, iron, copper and zinc. Due to the relatively relaxed tolerances of iron and silicon in some 3XXX alloys (AA3004, AA3104, AA3015), the 3XXX series is considered to be recycle friendly. These alloys are some of the few wrought aluminium alloys that can be produced directly from recycled material [Das, 2006]. These general use alloys are relatively cheap (in comparison to aerospace grade 7XXX series) and have a wide variety of uses ranging from construction to food packaging.

### 2.3.1 Constituent Particles

In AA3003 and similar MnFeSi model alloys, intermetallic particles are known to form interdendritically by eutectic decomposition during casting [Li and Arnberg, 2003a, Bäckerud et al., 1986]. These species, which have been characterised as  $\text{Al}_6(\text{Fe,Mn})$  and  $\alpha\text{-Al-(Fe,Mn)-Si}$  (also defined as  $\text{Al}_{15}(\text{FeMn})_3\text{Si}_2$ ), are termed ‘constituents’ and exist as rods or networks which link together throughout the primary aluminium matrix.

Table 2.1: Solidification Reactions in 3003 Alloy Containing 1.19% Mn, 0.55% Fe and 0.18% Si taken from [Bäckerud et al., 1986] in [Eskin, 2008]

Reaction	Cooling Rate	
	0.5 K/s	17 K/s
$\text{L} \Rightarrow (\text{Al})$	655	655
$\text{L} \Rightarrow (\text{Al}) + \text{Al}_6(\text{FeMn})$	653	646-615
$\text{L} + \text{Al}_6(\text{FeMn}) \Rightarrow (\text{Al}) + \text{Al}_{15}(\text{FeMn})_3\text{Si}_2$ and/or $\text{L} + \Rightarrow (\text{Al}) + \text{Al}_{15}(\text{FeMn})_3\text{Si}_2$	641-634	589
Solidus	634	589

Table 2.1 shows the solidification reactions in commercial AA3003 [Bäckerud et al., 1986]. This shows that the solid aluminium phase will form first and that the solidification order seems independent of the cooling rate. Eutectic reactions follow with the production of the  $\text{Al}_6(\text{FeMn})$  species, with silicon containing  $\alpha$ -species the last to solidify. It was noted that the cooling rate affects the spacing between the constituent particles [Li and Arnberg, 2003a] as faster cooling results in a smaller interdendritic spacing.

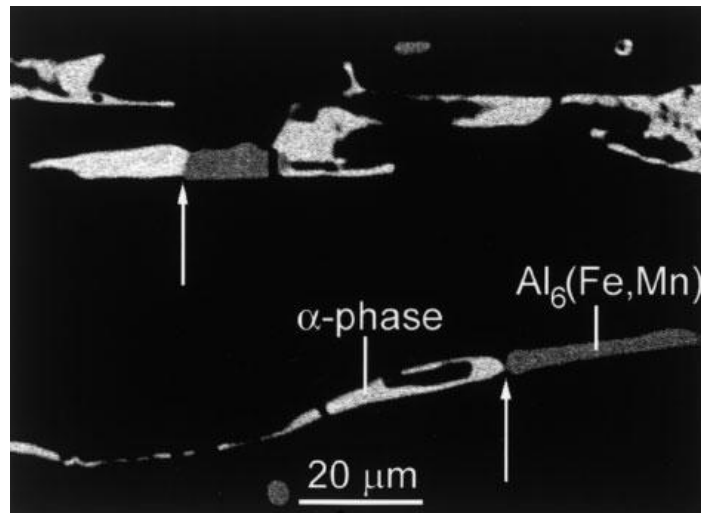


Figure 2.3: Intermetallic particle wetting within a similar AA3XXX model alloy [Alexander and Greer, 2005]

Heat treatments are known to break up the network of eutectic constituent particles. The two mechanisms for this are spheroidisation and particle break up due to thermal stress [Alexander and Greer, 2005]. If the alloy is heated quickly, the thermal expansion mismatch between the matrix and intermetallic particle leads to extensive fragmentation of particles. The resulting angular morphology of the particles suggests brittle fracture [Alexander and Greer, 2005]. However, the high rate of temperature change used to create this phenomenon ( $150 \text{ K s}^{-1}$ ) suggests that this is unlikely to be repeated at an industrial scale. The mechanism for spheroidisation is more closely linked to thermodynamics and is a diffusion controlled process where the surface area to volume ratio of the particle is minimised in order to reduce the interfacial energy, resulting in more rounded structures [Li and Arnberg, 2003a].

Alexander and Greer [Alexander and Greer, 2002, Alexander and Greer, 2004a, Alexander and Greer, 2004b] found that a phase transformation from  $\text{Al}_6(\text{FeMn})$  to “ $\alpha$ -phase” ( $\text{Al}_{15}(\text{FeMn})_3\text{Si}_2$ ) occurs during homogenisation heat treatments in 3XXX alloys. This is of great interest in the production of canning stock using AA3004 due to the increased galling resistance provided by the  $\alpha$  phase compared to the initial constituent phase. This conversion is reliant on the local availability of silicon in the aluminium matrix, and was found to occur frequently close to grain boundaries (offering evidence for enhanced diffusion of silicon though grain boundaries). Partial phase transformations have also been reported in these works. During lengthy heat

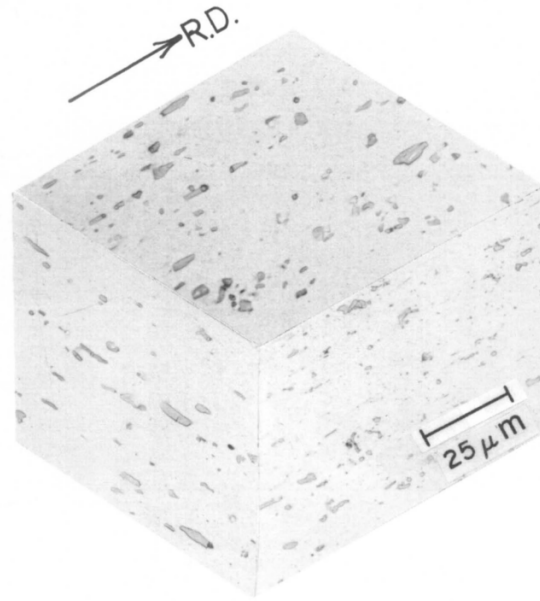


Figure 2.4: Constituents in ingot-sourced 0.33-mm cold-rolled AA3004 sheet, three-dimensional optical microscopy [Merchant et al., 1990]

treatments, duplex constituents that have undergone a partial transformation can separate into two regions. The boundary between the two intermetallic phases undergoes wetting by the aluminium matrix and spheroidisation of the two resulting particles follows, leading to separate intermetallic regions (as shown in figure 2.3).

Further coarsening of the constituents during homogenisation removes the smaller constituent particles in favour of increasing the size of the larger constituents and results in fewer particles per unit area overall. Again, the driving force for this is the minimisation of particle-matrix interfacial energy. This diffusion controlled process has been studied in depth using varying hold times and temperatures [Merchant et al., 1990]. Studies have also concluded that manganese atoms will substitute for iron atoms in the  $\alpha$ -Al(FeMn)Si phase [Li and Arnberg, 2003a].

Deformation processes such as rolling lead to further break up of this intermetallic network. Following deformation, constituent particles are found to align in the rolling direction, as shown in figure 2.4 [Merchant et al., 1990]. This also illustrates disparities across the sample, as regions of clustered particles and intermetallic free areas are clearly visible.

### 2.3.2 Dispersoids

During homogenisation heat treatment of alloys which are supersaturated with manganese, dispersoids form with widths ranging 0.05-0.5  $\mu\text{m}$  [Polmear, 2006]. The composition and crystal structures of these dispersoids are dependant on other alloying or impurity elements present and the homogenisation conditions. Dispersoid compositions reported include orthorhombic  $\text{Al}_6\text{Mn}$ , simple cubic  $\alpha\text{-Al}(\text{MnFe})\text{Si}$ , and metastable  $\text{Al}_{12}\text{Mn}$  [Lodgaard and Ryum, 2000, Jena et al., 1981]. Control of dispersoid distribution and size has been reported by Huang, using step homogenisation processes [Huang and Ou, 2009]. In this work, precipitation of dispersoids in single-step and multi step homogenisation processes was presented, illustrating the effects of the heating steps on the final dispersoid population. The aspect ratio of dispersoids (measured using Feret diameters) has been found to change during the homogenisation process. Particles are initially close to equiaxed when at 300°C, however the aspect ratio of these particles increases with increasing temperature. This peaks at 530°C, with further increases in temperature acting to reduce the aspect ratio [Li and Arnberg, 2003b]. Orientation relationships have also been established between crystal planes within dispersoids and the surrounding aluminium matrix [Li et al., 2012], which helps to explain the preferential growth of dispersoids along set crystallographic planes rather than uniform particle growth.

In simple binary alloys, high angle grain boundaries have been shown to act as initial nucleation sites for dispersoid particles, with boundaries of lower misorientation acting as secondary nucleation sites [Somerdar and Humphreys, 2003]. The addition of other alloying elements, however, provides many other possible nucleation sites including solute atom clusters and matrix-particle interfaces. As the formation of dispersoids reduces the amount of manganese in solid solution, resistivity measurements can be used as an indication of the dispersoid fraction and act as a useful tool when designing homogenisation heat treatments for new alloys [Li and Arnberg, 2003b]. Using this tool, increasing conductivity corresponds to a reduction of manganese in solid solution, and therefore an increase in dispersoid formation.

The nucleation of dispersoids can be tailored to occur during either homogenisation heat treatment, during deformation or within an annealing cycle depending on the conditions used [Lucke and Engler, 1990, Liu and Radhakrishnan, 2010]. Within the

process used to create rolled products from AA3003, these dispersoids form during homogenisation.

Recent work on the Al-Mn binary system has provided new insights into the coherence of dispersoid types and their effects on yield strength [Li et al., 2012].

### 2.3.3 Nucleation vs Coarsening

In 3XXX alloys, both nucleation of dispersoids and coarsening (of constituents and dispersoids), are competing mechanisms which involve the removal of manganese from the solid solution. As a result, it is imperative that hold times and temperatures of heat treatments are considered carefully to ensure the desired particle types are present within the final product [Huang and Ou, 2009].

An example of this competing nature is found in the existence of precipitate free zones (PFZ). These are regions surrounding constituents and near to grain boundaries in which dispersoid particles are generally not found. This absence is due to the low local availability of manganese within the matrix, due to segregation towards the constituent region. Studies have shown that the size of these zones can be modified by altering processing conditions such as isothermal soak time [Du et al., 2011].

### 2.3.4 Quantifying Second Phase Particles

Constituent and dispersoid particles are generally not simple spheroid regions of uniform size within the aluminium matrix. Each particle can be completely different in terms of size and shape, and the morphology can vary from one region to the next. It is therefore important that particles, which can be complex, are still easy to describe. The characterisation theory of Hadwiger [Hadwiger, 1957] states that all features of any complex geometry can be adequately described using a combination of four known parameters, listed in table 2.2, known as Minkowski Functionals.

These single values for each particle are combined across a sample to create 'densities' which are then used to describe the entire sample. An example would be the volume density which pertains to the total amount of the second phase within the sample, reflecting the composition of the material.

Table 2.2: The Minkowski Functionals [Hadwiger, 1957]

Symbol	unit	Description
V	m <sup>3</sup>	Volume of the particle
S	m <sup>2</sup>	Surface of the particle
M	m	The integral of mean curvature of the particle
K	-	The integral of the total curvature of the particle

### Particle Size and Shape

The length and width of particles in 2D images can be measured directly, however there are two different definitions of particle length. Length can be described as the longest edge of the minimum area bounding box which encompasses the particle. By instead taking the largest distance between two points on the particle, the maximal Feret diameter can instead be determined.

Aspect ratio values can be determined using either the bounding box measurements or a combination of the Feret maximum and minimal values.

### Processing Two Dimensional Data

The characterisation of the intermetallic particles within aluminium alloys has traditionally been performed using 2D methods such as optical microscopy and scanning electron microscopy (SEM) of polished specimens for the larger constituent particles, and transmission electron microscopy (TEM) for the sub-micron dispersoid particles. Within 3XXX series alloys, the cubic  $\alpha$  phase appears brighter than the orthorhombic  $\text{Al}_6(\text{Fe},\text{Mn})$  in backscattered SEM images due to differences in phase density, allowing the two phases to be easily identified.

As 2D images consist of cross sections of particles, corrections should be made to the particle population to ensure that the contributions of bisected large particles to the visible population of small particles are considered. This contribution is illustrated in figure 2.5. One stereological technique that incorporates this contribution is the Schwartz-Saltykov method [DeHoff and Rhines, 1968, Gokhale, 2004]. This method assumes that any imaged 2D surface consists of particles which have been bisected at a random distance from their centre, and uses a calculated table of probabilities to correct for this.

This method traditionally sets the largest particle within the area of study to be

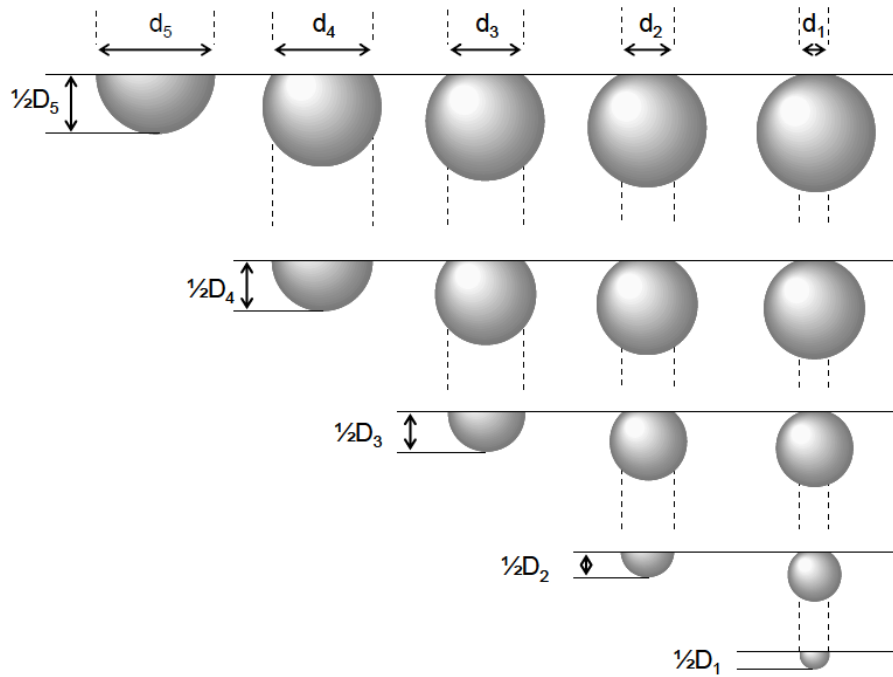


Figure 2.5: Illustration of the contribution of different size particles to 2D data [Anselmino, 2007]

the maximum particle size - which in itself is statistically unlikely when considering the overall area studied - and assumes that the particle population within the area studied is representative of the entire sample. As this method involves the assumption that all particles within a volume are spherical, this will not be a viable strategy in determining 3D particle measurements in materials with complex substructures, such as cast eutectic networks, but may be suitable for heavily processed constituent particles or dispersoid analysis.

The experimental error introduced as a result of the interaction volume of incident electrons when using SEMs must also be taken into account for all calculations of particle dimensions. This correction for the interaction volume has been included in an application of the Saltykov method in dispersoid data by Anselmino [Anselmino, 2007].

### Imaging in Three Dimensions

Though 2D methods give insight into particle shape, they provide limited indication of the true geometry of each particle, nor any detailed information pertaining to how particles are clustered or connected throughout the volume. A clear example of how

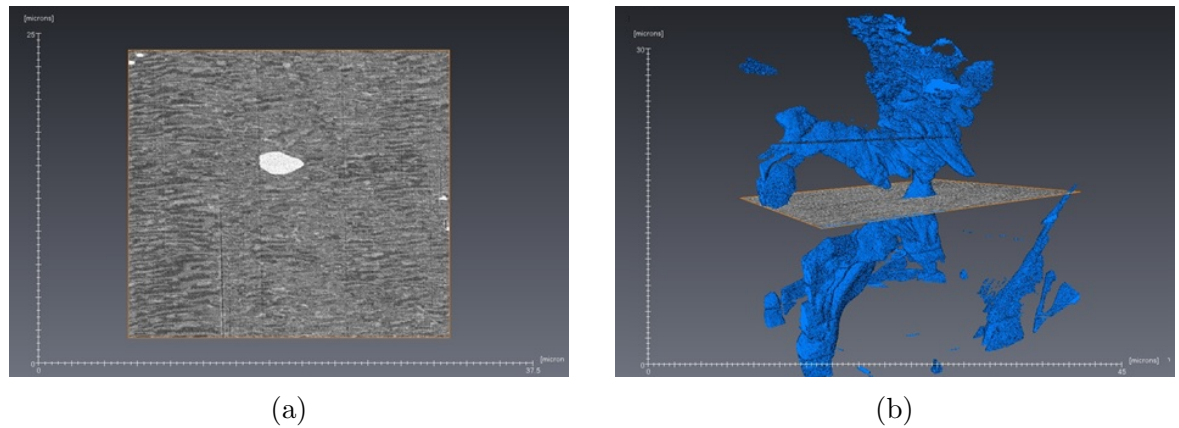


Figure 2.6: 2D SEM (a) showing what appears to be a single particle with full 3D visualisation (b) of the same particle (blue) showing a complex network structure

2D data can be misleading as shown in figure 2.6. Figure 2.6a shows an SEM image containing a single rounded particle, which may be considered to be a simple particle within the matrix. However, the true nature of the particle is shown in figure 2.6b, illustrating a complex geometry which would be completely overlooked using only 2D measurements.

This has been partially overcome by etching away the surface layer of matrix material to uncover more data of constituent particle shape, however, this pseudo-3D technique is restricted to showing only a limited number of particles that are still embedded within the remaining matrix after etching [Alexander and Greer, 2002].

Obtaining volumetric data is the only definitive method to determine information relating to particle connectivity, as well as spatial distributions and detailed feature geometry. One destructive technique used to obtain this data is termed serial sectioning, in which a sample is imaged and then processed to remove a thin layer of material and then re-imaged [Rhines et al., 1976]. However, previously reported serial sectioning methods are time consuming and the amount of material removed in each step can be difficult to determine. The removal of the surface layer has been performed by polishing away material using silica solution [Mangan et al., 1997, Kuijpers, 2002], milling using a focussed ion beam (FIB) [Velichko et al., 2007], or milling away thin layers of surface material (0.2 and 1-20  $\mu\text{m}$ ) using diamond tooling [Alkemper and Voorhees, 2001a].

With methods such as surface layer removal using silica solution, the depth of slice can not be guaranteed without precise calibration of polishing time and force, thus

micro-hardness indentation becomes necessary to confirm slice depth. This further increases the amount of time needed to acquire a series of images for 3D analysis.

Though FIB milling has shown to provide very quick data acquisition rates (approximately two minutes per slice) [Velichko et al., 2007], this rate can not be applied to all materials. In this example, the graphite particles characterised by FIB serial sectioning were first exposed from within an iron matrix using a deep etch. This greatly reduced the amount of time needed to ion mill the surface layer as only the exposed particles were milled with each processing step. Milling away a complete surface layer of material for serial sectioning purposes has been shown to take around 16 minutes using FIB [Zaefferer et al., 2008].

One of the first automated serial sectioning techniques was developed using a stage which travelled between a diamond milling tool and optical microscope [Alkemper and Voorhees, 2001b]. This technique offered images with a resolution of  $0.96\mu\text{m}$  in the imaging plane and slice depths as low as  $1\mu\text{m}$  between cuts, allowing networks of larger constituent particles to be visualised. This method greatly increased the rate of acquisition for 3D data sets, allowing up to 20 slices to be imaged per hour. However, this method also required correction for changes in temperature which can effect the alignment of the milling tool, and therefore affect the depth of the cut.

Non destructive 3D imaging using X-ray computed tomography (XCT) has recently been used to determine the size and shape of second phase particles within bulk metal matrices [Mackie, 2013, Parra-denis, 2007]. Reconstruction of the hundreds of X-ray projections that this technique creates, allows the density at each point within the specimen to be mapped in three dimensions to visualise the internal structure of a sample. This visualisation relies heavily on the presence of strong contrast between the matrix and the desired microstructural feature (second phase material, pores, etc) under x-ray illumination. The non-destructive nature of this technique could allow the study of a single specimen over time, therefore allowing true sample evolution to be monitored during processing. This technique can be performed either using lab x-ray sources or a synchrotron. The particles found within AA5182 have been studied at a range of deformation steps using a synchrotron source [Parra-denis, 2007], with a resolution of  $0.7\mu\text{m}$ . Within the alloys studied using XCT, a typical intermetallic particle measured over  $100\mu\text{m}$ , ensuring the resolution limit for this technique was

not a limiting factor in particle evolution studies. At the time of writing, lab sources, such as those used by Mackie [Mackie, 2013] are not yet powerful enough to resolve particles that are around 1  $\mu\text{m}$  in width whilst incorporating a large enough total volume to obtain a statistically significant number of particles.

### Measuring Particles in Three Dimensions

With the acquisition of 3D data that details particle morphology now possible, a new problem arises in determining how simple particle parameters are measured and presented. While volume measurements provide accurate information regarding how much mass a particle has, this does not explain how material is spatially oriented, and so information relating to the structure of the particle is lost.

In a similar vein to the 2D case, simple size measurements of length, width and thickness can be measured by calculating the dimensions of the smallest cuboid which would completely enclose the particle (i.e. bounding box). The 3D Feret diameter can also be determined which would again provide a different length measurement than the bounding box method, highlighting the importance of stating which measuring system is in use. However, these measurements do not provide any indication of complexity of a particle's structure.

If the surface area of a particle is known along with the volume, the sphericity ( $\Psi$ ) can be determined which offers a measure of how compact a particle is [Waddel, 1935]. Using this measure, which is defined in equation 2.1, the overall complexity of a 3D particle can be evaluated.

$$\Psi = \frac{\pi^{\frac{1}{3}}(6V_p)^{\frac{2}{3}}}{A_p} \quad (2.1)$$

where:

$A_p$  = Surface Area of the Particle

$V_p$  = Volume of the Particle

The sphericity of a particle can fall within the range of 0 to 1, with 1 corresponding to a perfect sphere.

One benefit of using this measure over other shape characteristics such as aspect ratio, lies with the parameters that this measure calls. Both volume and surface area

take into account all regions of all measured particles, whereas other widely utilised measures may only utilise information pertaining to the longest or shortest regions of a particle, but dismiss secondary areas or topological anomalies.

There are however potential problems with this measure, stemming from the overall ‘smoothness’ of the particle when determining the surface area. Any irregularities in the boundary of the particle would translate into a larger total surface area, which would in turn lead to the calculation of a reduced sphericity value. When dealing with particle distributions, this would result in a population deemed to be less spherical (or more complex) than may be the case.

### Particle Distributions

Characterisation of the spacial distribution of second phase particles within an alloy can be key in understanding its mechanical behaviour. For example, knowing that an alloy contains randomly aligned long and thin eutectic particles may help to explain crack propagation. By taking the barycentric coordinates of each particle in a volume, the distances between the centre points of all particles within a volume can be determined. It is this array of distances which can then be utilised to determine the nearest neighbour of any particle within the volume. Quantifying the spatial distribution of particles typically involves calculating the mean value of nearest neighbour distances for both an experimental dataset and a theoretical randomly distributed sample. The distribution is then defined as shown in equation 2.2.

$$Q = \frac{E_{\text{obs}}(\bar{\omega})}{E_{\text{pois}}(\bar{\omega})} \quad (2.2)$$

where:

$Q$  = Spacial distribution

$E_{\text{obs}}(\bar{\omega})$  = Observed mean of nearest neighbour distance

$E_{\text{pois}}(\bar{\omega})$  = Mean of nearest neighbour if random

Using this measure, the distribution of a sample is categorised as either random ( $Q = 1$ ), clustered ( $Q < 1$ ) or uniform ( $Q > 1$ ).

One drawback of this method is that only the closest particle is taken into account for each nearest neighbour calculation, meaning that any long range clustering within

the volume is ignored. This distribution has been altered to incorporate a radial density function [Çetin and Kalkanli, 2008], thus allowing local clustering to be measured within a sample.

## 2.4 Plastic Deformation in Aluminium

At the macro-scale, the deformation behaviour of aluminium can be described by a simple stress-strain curve, an example of which is shown in figure 2.7. This plot compares the true stress ( $\sigma$ ) and true strain ( $\varepsilon$ ) of a material and is created by measuring the changes in length of a test specimen as an external force is applied [Dieter, 2001].

This curve can be separated into the elastic and plastic regions. The elastic region of the curve describes the stresses which a material can withstand without a resulting permanent strain. The stress and observed strains are proportional in this region as:

$$\sigma = E\varepsilon \quad (2.3)$$

where:

$E$  = Modulus of Elasticity (Young's Modulus)

Applied stresses above the elastic limit (labelled  $X$  in figure 2.7) result in plastic (permanent) deformation. The crystallographic nature of this phenomena will be expanded upon in the following sections.

The region describing plastic deformation within stress-strain curves can be used to determine the strength co-efficient of a material ( $K$ ) and strain hardening exponent ( $n$ ), found in equation 2.4 [Kleemola and Nieminen, 1974].

$$\sigma = K\varepsilon^n \quad (2.4)$$

This fitting is accomplished by creating a log-log plot using the true stress and true strain values, where the slope of the plot becomes the strain hardening exponent, and y-intercept indicates the log of the strength coefficient. For the data in figure 2.7, the resulting values of  $K$  and  $n$  are 235.6 MPa and 0.27 respectively.

### 2.4.1 Fundamentals of Slip

At the micro-scale, deformation due to applied stress involves the movement of crystal planes relative to each other.

This involves the step-wise breaking and reforming of inter-atomic bonds along a slip plane, during which an extra half plane of atoms exists in one of the slipping crystals. This mechanism is what allows metals to flow and deform rather than shatter.

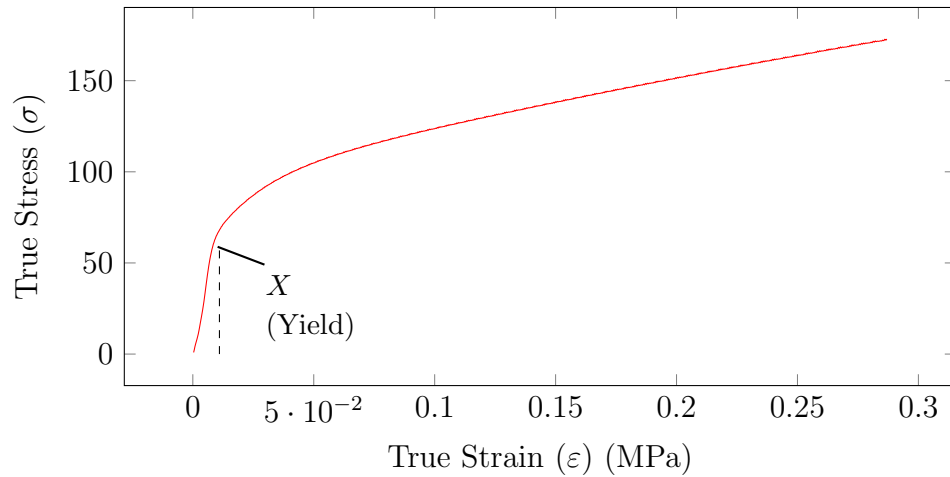


Figure 2.7: Example stress-strain curve of an aluminium alloy produced from a compression test

Around the extra half plane of atoms, a compressive force is created due to mismatch within the crystal structure, whilst a corresponding tensile force is created within the adjacent plane. This crystallographic mismatch is referred to as a dislocation.

The stress fields of multiple dislocations can interact, resulting in piling up of dislocations (which acts to constrain further dislocation movement, culminating in a work hardening effect), mutual annihilation of dislocations (removing the extra half plane of atoms), or repulsion (where the two dislocations move away from each other). The boundary dividing the slipped and unslipped region of the crystal is referred to as the dislocation line, and the magnitude and direction of slip is referred to as the Burgers vector ( $\mathbf{b}$ ). Depending on whether the burgers vector is parallel or perpendicular to the dislocation line, a dislocation may be defined as either ‘edge’ or ‘screw’ respectively.

It is possible for the lattice to shift exactly one atomic spacing, thus leaving the overall lattice unaltered. This is termed a ‘perfect’ dislocation. The energy of a dislocation is proportional to the square of the Burgers vector, thus perfect dislocations are rare as the formation of two partial dislocations would allow the defect to travel the same distance throughout the crystal but would require less energy. The region between two partial dislocations contains an interruption of the normal atomic ordering of the crystal. This is termed a ‘stacking fault’.

Aluminium is a face-centred cubic (fcc) material with 12 active slip systems. Slip occurs in the closed packed  $\{111\}$  planes and is observed in the  $\langle \bar{1}10 \rangle$  directions

[Polmear, 2006].

The movement of dislocations is a result of shear stresses, which are resolved from tensile/compressive forces as shown in figure 2.8.

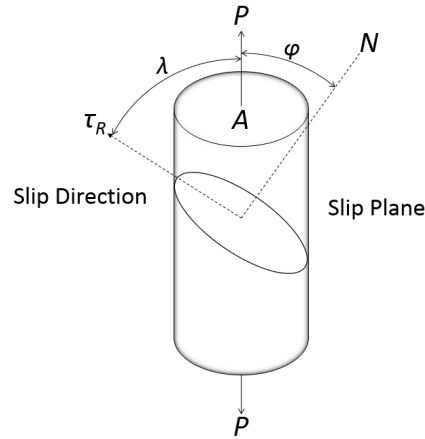


Figure 2.8: Resolving shear stress on a slip system from initial force [Dieter, 2001].

In this example, the tensile force  $P$  acts on the cross sectional area  $A$ . The slip direction lies at an angle  $\lambda$  from the tensile force, resulting in the resolved force of  $(P \cos \lambda)$  acting along the slip plane of area  $(A / \cos \phi)$ . The resolved shear stress ( $\tau_R$ ) is therefore:

$$\tau_R = (P \cos \lambda) / (A / \cos \phi) \quad (2.5)$$

$$\tau_R = (P/A) \cos \lambda \cos \phi \quad (2.6)$$

$$\tau_R = \sigma \cdot M \quad (2.7)$$

where:

$$M = \cos \lambda \cos \phi = \text{Schmid Factor}$$

Slip will not begin within a crystal until the shearing stress on the slip plane reaches a critical point, termed the critical resolved shear stress ( $\tau_{CRSS}$ ).

Deformation using a single slip system is not compatible with the structure of polycrystalline materials. Sachs' initial theory allowing multiple grains to deform by single slip quickly fails when the compatibility across multiple grains is studied, as overlaps and voids appear between grains. To allow for compatibility in this system, the Taylor Full Constraints model [Taylor, 1938] was put forward which suggests that

5 independent slip systems are activated in each grain, and that those which require the minimum energy to activate are selected when trying to model polycrystalline deformation. In the Taylor model, each grain is treated individually, allowing each grain to have differing stress states which when combined across the full system, will then satisfy the overall deformation conditions. Deformation modelling is discussed further in section 2.6.1.

As deformation occurs on the most favourable available slip system within a grain (i.e. the system that reaches  $\tau_{CRSS}$  first), this preferential deformation can result in a high proportion of grains having similar orientations. This is referred to as the deformation texture of the material and this further influences the macroscopic properties of the material, resulting in anisotropic behaviour.

### 2.4.2 Deformation within a Single Phase System

As deformation proceeds, most of the energy used to deform the material dissipates as heat with only a small percentage ( $\sim 1\%$ ) remaining stored within the material as dislocations [Humphreys and Hatherly, 2004]. As deformation proceeds, the dislocation density within a grain increases which in turn acts to hinder dislocation movement. This is termed work hardening [Mott, 1952].

#### Microstructural Features of Deformation

During initial deformation of aluminium, dislocations form randomly within the grain as dislocation tangles. As the density of dislocations increases, cellular structures begin to develop within the grain where the dislocations themselves rearrange to form the subgrain boundaries. Depending on whether these boundaries are diffuse (consisting of a broad tangle of dislocations) or sharp (a clear crystallographic boundary), these structures are termed cells or subgrains respectively [Exell and Warrington, 1972]. Larger grains can also subdivide as a result of increasing strain, thus forming regions which have very different orientations separated by deformation bands. The separate regions of the grain can then deform using different slip systems, resulting in dissimilar final orientations [Kreislner and Doherty, 1978]. These structures are shown schematically in figure 2.9. Shear bands show non-crystallographic shear in a metal and act across multiple grains.

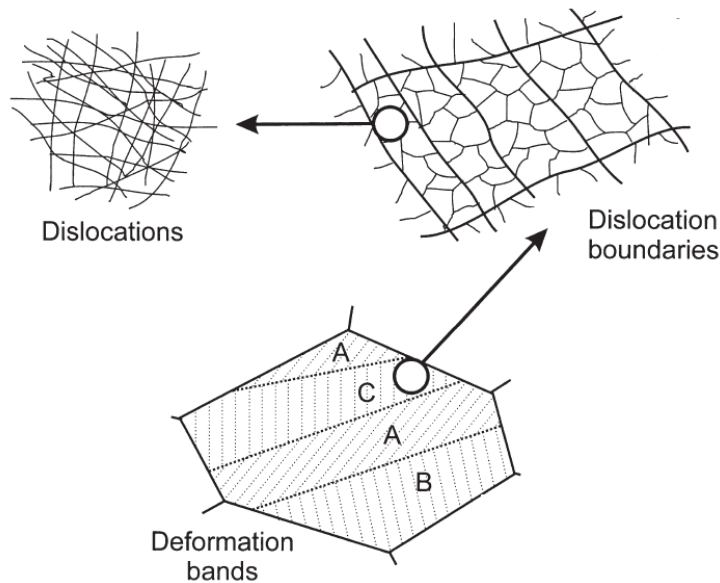
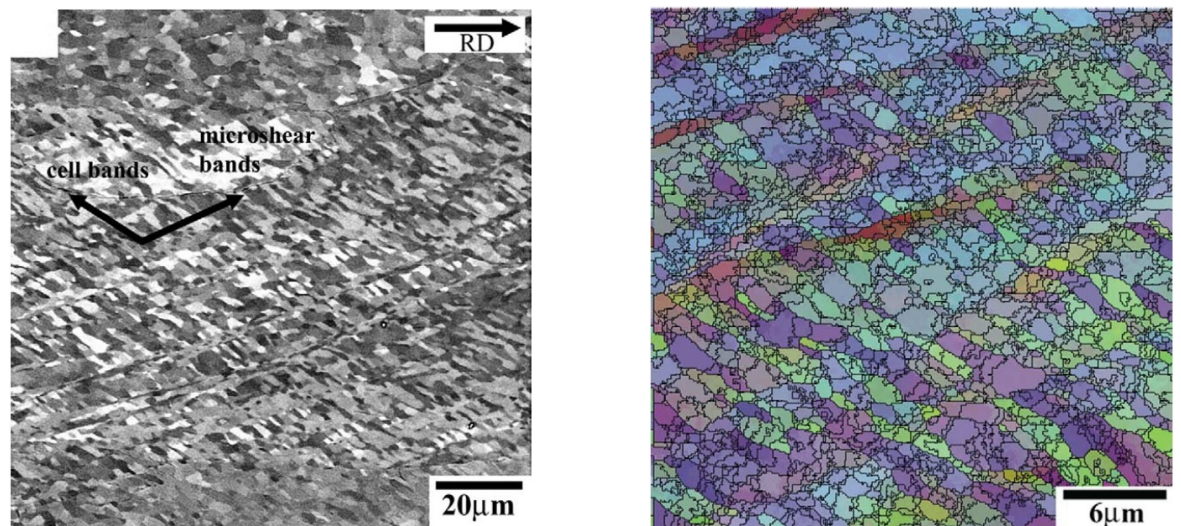


Figure 2.9: The features of crystal deformation shown at increasing scale, adapted from [Humphreys and Hatherly, 2004]

### Development of the Deformed Microstructure

At small strains ( $\epsilon < 0.3$ ), equiaxed cells of length  $0.5 - 1.0 \mu\text{m}$  develop with small misorientations in the order of  $1^\circ$ . The size and shape of these cells does not alter greatly during deformation and these cells are considered to be an equilibrium structure, resulting from the trapping and annihilation of dislocations [Liu et al., 1998]. Cell blocks are groups of cells which deform cooperatively [Bay et al., 1989], thus allowing each individual cell to deform using fewer than the five slip systems required by Taylor theory as described in section 2.4.1, leaving the overall strain to be accommodated by the block rather than the individual cell. In aluminium, cell blocks appear elongated (and are often referred to as cell bands) and align at an angle of  $25-40^\circ$  to the rolling plane [Hurley and Humphreys, 2003]. These cellular clusters are separated by dense dislocation walls (DDWs) which also referred to as microbands. The misorientation between DDWs is higher than those found between individual cells within a block/band, however, long range gradients are minimal as the misorientation across alternate cell bands tend to oscillate around a mean [Liu et al., 1998]. At low strains, these DDWs are considered to be transient features which are continually evolving during additional dislocation generation.

With increasing strain ( $0.3 < \epsilon < 1.0$ ) cell bands can be intersected by shear bands. This alters the shape of the already elongated cell bands to form S-bands, which are typically 1-2  $\mu\text{m}$  thick. Increasing strain leads to increases in the misorientation measured between the cell bands and newly developed S-bands, as shown in figure 2.10 [Hurley and Humphreys, 2003]. Figure 2.10a shows the typical substructure found within a grain, with the direction of alignment of cell bands and microshear bands shown. The cell bands in the sample are aligned at  $31^\circ$  to the rolling direction. By obtaining orientation information of this sample as shown in figure 2.10b, and including all  $0.5^\circ$  boundaries, it becomes clear that not only do the microshear bands form with similar orientations, but the cell structure is much finer within these structures compared to the rest of the sample.



(a) Backscattered image showing the typical substructure of a 50% cold rolled high purity Al alloy

(b) EBSD relative Euler orientation map of a 50% cold rolled high purity Al alloy

Figure 2.10: Microshear bands intersecting aligned cell bands in deformed aluminium [Hurley and Humphreys, 2003].

With continued deformation, ( $\epsilon < 1.0$ ), cell bands and S-bands become more closely aligned with the rolling plane. As strain increases, the DDWs themselves become persistent features within the microstructure, forming high angle grain boundaries [Hurley and Humphreys, 2003].

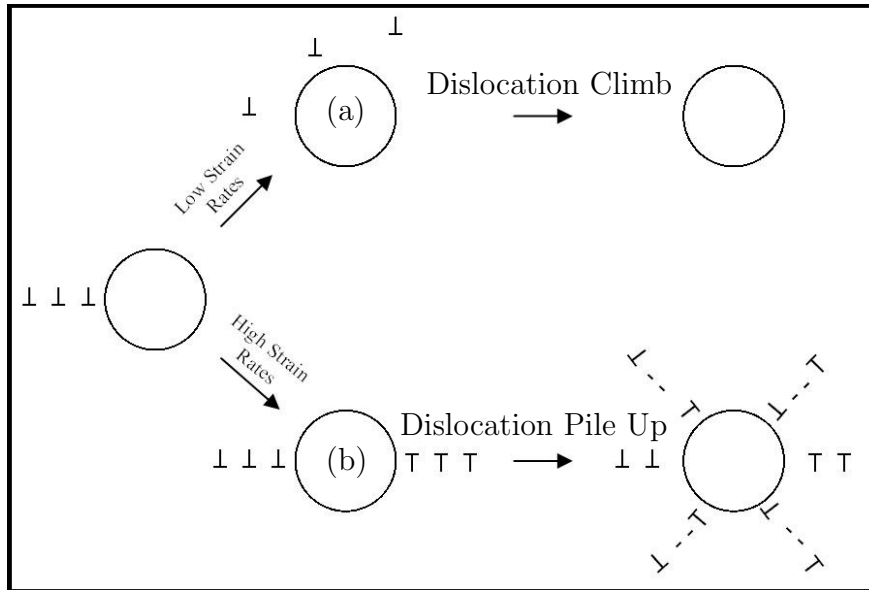


Figure 2.11: Dislocation pile up at particles is strain rate dependent. Dislocations are reaching (a) slowly enough for the dislocation to climb around the particle. Dislocations reach (b) much faster than the climb rate, resulting in dislocation pile up. [Humphreys, 1987].

### 2.4.3 Deformation in Multi-Phase Materials

Second phase particles within a matrix can drastically alter dislocation movement through a crystal.

In aluminium, which has a high stacking fault energy, dislocations can climb around second phase particles as shown in figure 2.11 but this is both temperature and particle size dependent [Lagneborg, 1973, Humphreys, 1987].

If the rate of dislocation climb is similar to the rate of dislocations reaching the particle (very low strain rate), two phase material will not show any dislocation accumulation. These low strain rates are generally linked to creep and are beyond the scope of this project. If the number of dislocations reaching the particle however is higher than the climb rate, dislocations can attempt to bow around the particle, creating Orowan loops. In this case, the force acting on each particle is:

$$F = \tau \mathbf{b} \lambda \quad (2.8)$$

where:

$\tau$  = Shear Stress

$\mathbf{b}$  = Burgers Vector

$\lambda$  = Interparticle Spacing

If the force ( $F$ ) produces a stress in the particle greater than the strength of the particle, it will deform. Otherwise, the dislocation forms an Orowan loop as shown in figure 2.12 [Ashby et al., 1969, Humphreys and Hatherly, 2004].

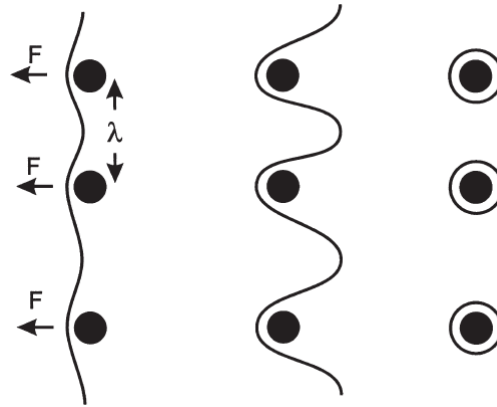


Figure 2.12: Formation of Orowan Loops [Humphreys and Hatherly, 2004]

### Deformable Particles

If a particle deforms with matrix as a result of dislocation movement, the effective slip plane through the particle becomes one Burgers length smaller with each passing dislocation. This is termed 'softening' of the slip plane, and allows each subsequent dislocation to move through the same slip plane with greater ease. In this mechanism, particle shearing results in concentrated slip along preferential slip planes, resulting in heterogeneous deformation as illustrated in figure 2.13 [Martin, 1980].

### Non-Deformable Particles

When a matrix is deformed while containing a non-deformable particle, strain incompatibility between the two phases arises. This can be accommodated by the formation of dislocations at the particle-matrix interface. The increased density of dislocations due to the presence of non-deformable particles hinders further dislocation movement on any given active slip system once slip has begun, creating a work hardening effect. This essentially ensures a increased homogeneity of macroscopic deformation

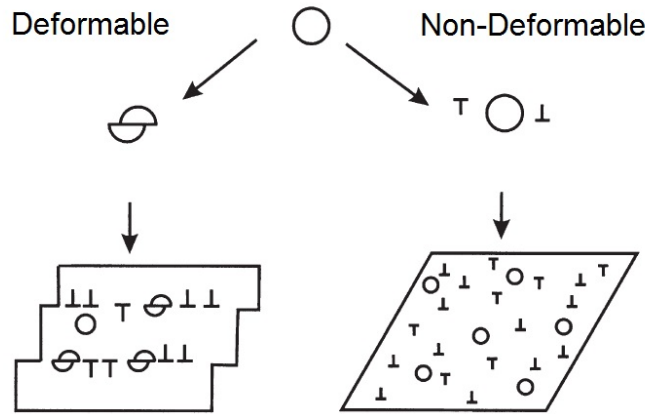


Figure 2.13: The effect of particle deformation on slip homogeneity [Humphreys and Hatherly, 2004]

than a deformable particle containing alloy as can be seen in figure 2.13 [Martin, 1980, Humphreys and Hatherly, 2004].

### Deformation Zones

As previously stated, Orowan loops are formed by the passage of dislocations around sufficiently strong particles. Continued deformation can result in multiple loops forming around a single particle, leading to very high local stresses, which are then relieved by the plastic flow of the matrix. These structures have been studied extensively using transmission electron microscopy (TEM) and have been used to determine how the lattice rotates with respect to the applied deformation [Humphreys, 1977, Engler et al., 1997, Humphreys, 1979].

Through these experiments, the regions of highest misorientation have been associated with areas closest to the non deforming particle, with this relative misorientation declining with distance from the particle as shown in figure 2.14. This behaviour was found to fit to the empirical equation:

$$\tan \alpha = \tan \alpha_{max} \exp\left(-\frac{Kx}{d}\right) \quad (2.9)$$

where

- $\alpha$  = Rotation  
 $\alpha_{max}$  = Maximum Rotation  
 $K$  = Constant (Determined to be  $\sim 1.8$ )  
 $x$  = Distance from Particle  
 $d$  = Particle Diameter

It was also confirmed through this work that a simple relationship could be used to estimate the mean misorientation at a particle larger than  $2.5 \mu\text{m}$  as a function of the shear strain.

$$\alpha_{mean} = \tan^{-1} \gamma \quad (2.10)$$

where:

$$\gamma = \text{Shear Strain}$$

The 1979 study also alludes to some effects of particle shape on deformation zone formation, noting that larger lattice rotations were found at the tips of elongated particles.

TEM images produced by Humphreys and Ardakani [Humphreys and Ardakani, 1994] (reproduced in figure 2.15) illustrate that though two particles are found to be approximately the same size and shape, and contained within identically oriented crystals, differences may still exist in the resulting deformation zone. This helps to illustrate that deformation zone morphology is dependent on not just the visible particle morphology and matrix orientation, but also external factors to local grain mobility (this may include the orientation and proximity of surrounding grains). It was also noted that in rolled polycrystals, deformation zones were elongated in the rolling direction, with equiaxed subgrains near to the particle-matrix interface having misorientations of  $40^\circ$  relative to the matrix.

The effect of particle size on the resulting deformation zone has been investigated as shown in figure 2.16 [Humphreys, 1979]. From this study, it is clear that the maximum lattice rotation within a deformation zone is directly correlated to the size of the second phase particle. This has been found to fit to the equation:

$$\alpha_{max} = K \cdot \tan^{-1} d \quad (2.11)$$

where:

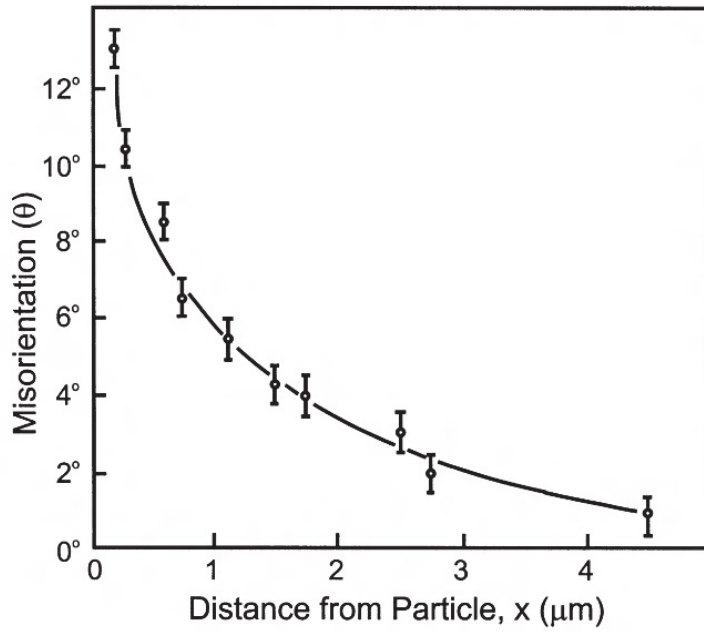


Figure 2.14: Relative misorientation at a  $3 \mu\text{m}$  particle in deformed Aluminium as a function of distance from the interface [Humphreys, 1979]

$K = \text{Constant}$  (determined to be  $\approx 40$  at a tensile strain of 0.5 in data from figure 2.16)

Some work on the effect of particle parameters on the resulting deformation zone, such the shape and size of particles has been reported in the literature [Humphreys, 1979, Liu et al., 2009, Ko, 2014], however these still require investigation. Gaps in the literature surrounding deformation zones include detailed studies which investigate any effects of particle orientation within a crystal, and the effect this may have on the resulting deformation zone. A second avenue of investigation may be determining how deformation proceeds around two closely spaced particles within a grain, and therefore whether there is a point at which two particles effectively act as one particle.

### Slip Shadowing

The size and shape of deformation zones were first described as a result of slip activity around a single non-deformable particle in the theory suggested by Humphreys and Ardakani [Humphreys and Ardakani, 1994]. This model incorporates a particle within a crystal of known orientation, and proceeds to categorise regions where slip would be effectively blocked by this non-deformable particle.

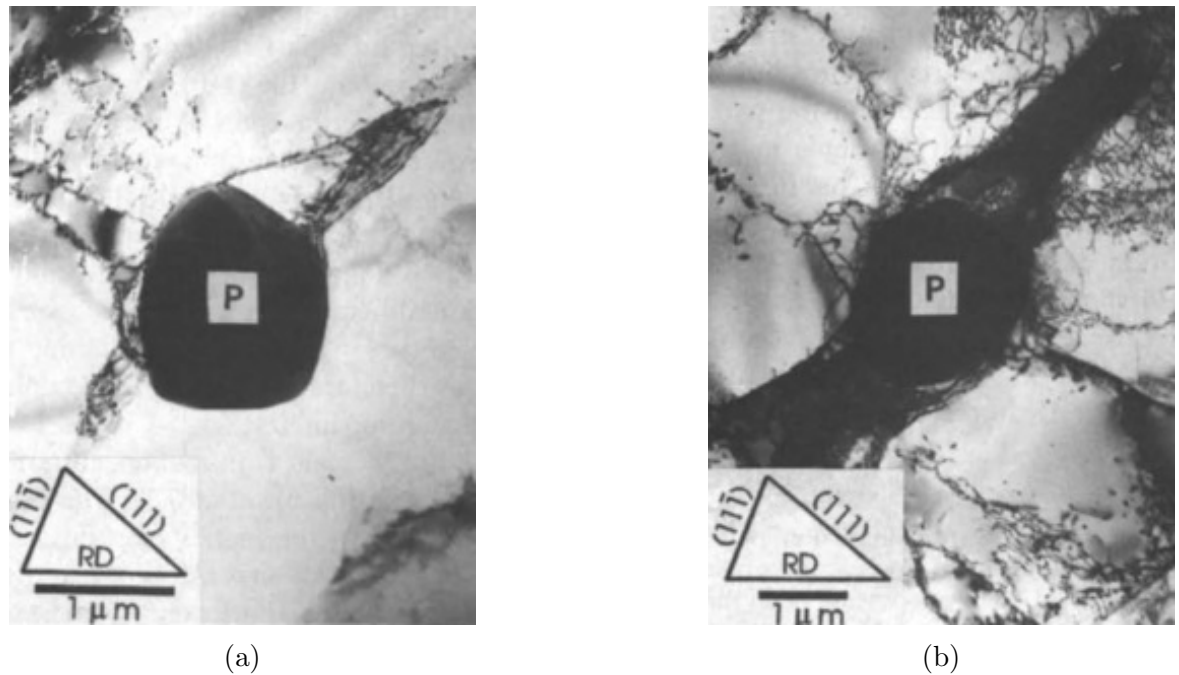


Figure 2.15: TEM images showing the deformation zones around two similar particles within two crystals with the same orientation

Within the slip shadowing model, as shown schematically in figure 2.17, by inhibiting different slip systems, changes to the deformation behaviour of the material are observed. If S1 slip is inhibited by the particle, region A would freely deform, while dislocations would build in region B. there would also be a dislocation gradient from regions B to C as the effect of the particle would dissipate with distance. The same pattern would also appear if S2 slip was blocked, though the locations of these regions would be translated.

By combining these two and blocking slip on both S1 and S2, as shown in (c), areas where one slip system is blocked remain, as regions D and E. These regions effectively overlap to form region F, in which two slip systems are blocked. This results in varying deformation of the matrix, and ensures different crystal rotations are observed in the vicinity of second phase particles.

Within this theory, the action of blocked slip leads to the formation of a strain gradient, beginning at zero and increasing with distance from the particle. This gradient can become complex when passing between regions where different numbers of slip systems become active.

Deformation in dispersoid containing material has also been investigated, but no clear deformation zones have yet been attributed to these particles, possibly due to

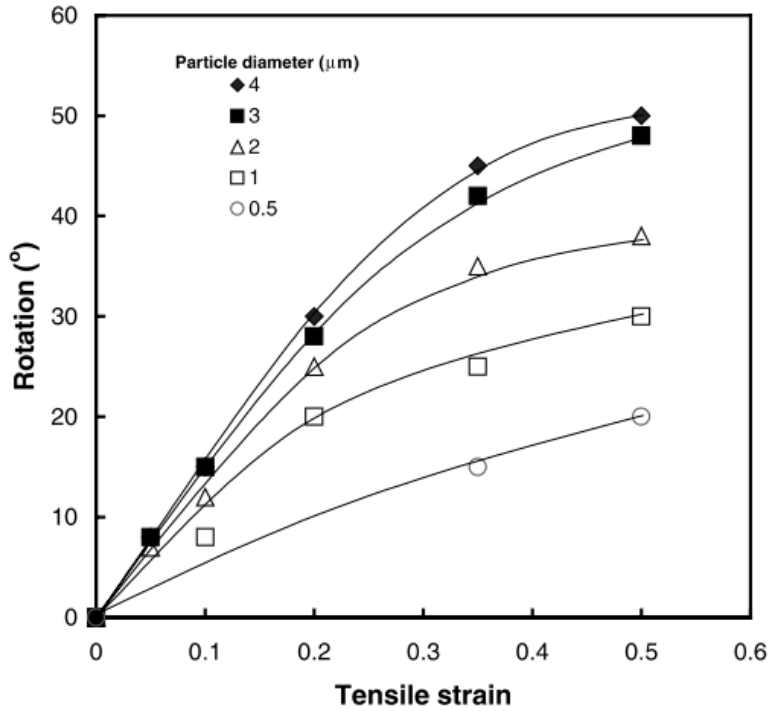


Figure 2.16: The maximum angle of lattice rotation at second phase particles in aluminium as a function of strain and particle size [Humphreys and Bate, 2003] (Data originally from [Humphreys, 1979])

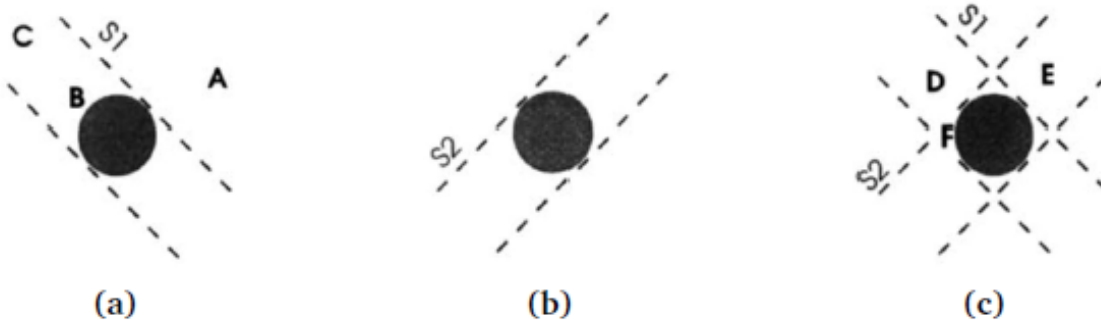


Figure 2.17: The slip shadowing model as proposed in [Humphreys and Ardakani, 1994]. (a) Slip on system S1 is restricted by the particle. (b) Slip on system S2 is restricted by the particle. (c) Slip is restricted on both systems S1 and S2.

their small size [Liu et al., 2009].

### Studying Deformation Zones

As presented earlier in figure 2.15, deformation structures are usually studied using TEM. More recent methods of studying deformation around particles include the use of high resolution electron backscattered diffraction (EBSD) maps and 2D Digital Image

Correlation (DIC) using gold patterning [Liu et al., 2009] [Di Gioacchino and Quinta da Fonseca, 2013]. These methods allow study of larger areas of deformation than is possible with TEM use alone.

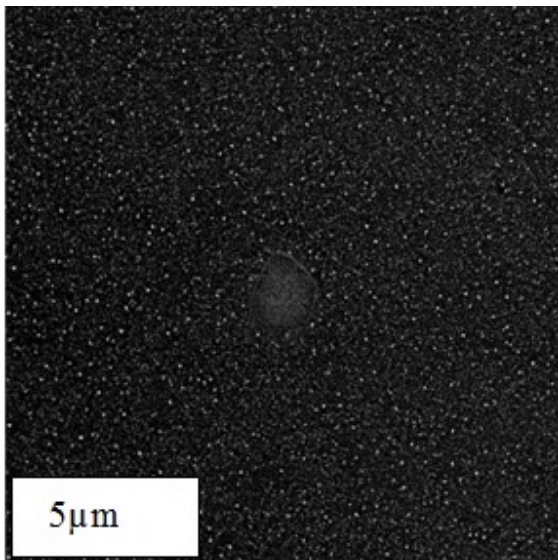
The use of digital image correlation (DIC), in which deformation is performed in small increments and the resulting microstructure is imaged directly, allows not only insight into the final deformed microstructure, but also the steps taken within the material to accommodate the compressive forces. Using this method, regions of a grain which are more readily deformable can be uncovered, and by pairing this with EBSD measurements, the DIC results can be linked to any underlying orientation differences. The use of this method in particle containing material can aid in showing how the matrix interacts with the particle, but also any secondary effects moving further into the matrix, such as rotation dead zones [Ko, 2014].

Figure 2.18a shows a backscattered SEM image of a sample to be analysed using strain mapping. The high contrast points on this sample are the gold particles which are used to track the deformation. Figure 2.18b contains the same region after a reduction of approximately 24%, containing slip bands throughout the surface. The ability to determine the lattice rotations around particles from this data, as shown in figure 2.18c, allows the experimental investigation into the evolution of rotated regions near to second phase particles [Ko, 2014].

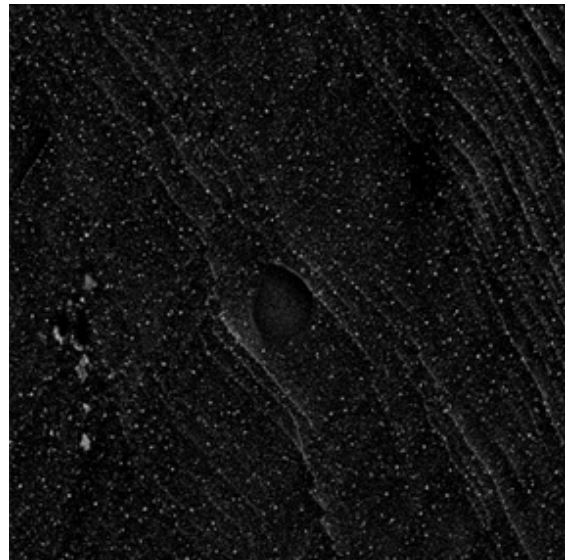
Figure 2.19 includes examples of the effects of particle size on the resulting slip lines resolved using the DIC method. In these plots, the axis represents the normalised strain. Figure 2.19a illustrates that the primary slip bands (which run from top left to bottom right of the image) are interrupted by a large particle. These primary slip bands can be halted (as shown in the bottom right corner of the image) or redirected to move around the particle (illustrated above and left from the particle). Secondary slip is also shown to run approximately perpendicularly to primary slip, and this is again interrupted by the large particle.

In the case of the medium sized particle (which measures approximately  $9\ \mu\text{m}$  across), the primary and secondary slip lines are again affected by the presence of a non deformable particle as the particle is larger than the slip line spacing.

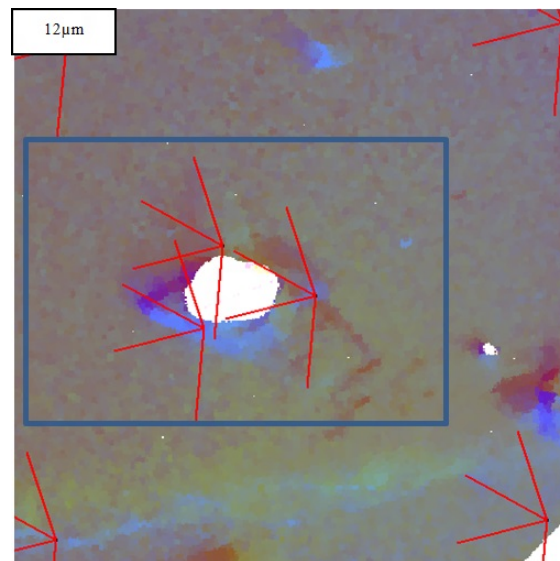
In the case of the small particle, which can fit between the slip lines, there is no evidence when examining the slip line evolution that small particles would lead to any



(a) Single particle within an aluminium matrix, with high contrast nano-patterned gold



(b) Single particle after deformation with shear bands clearly visible throughout the matrix



(c) Red and blue overlays are used to demonstrate positive and negative lattice rotations around the particle

Figure 2.18: Digital Image Correlation around a constituent particle in Al-Si alloy [Ko, 2014]

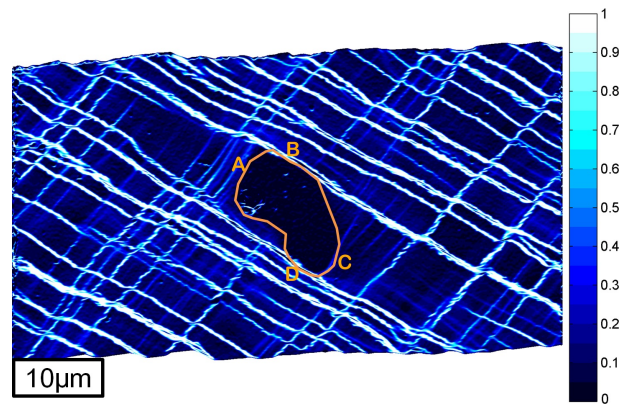
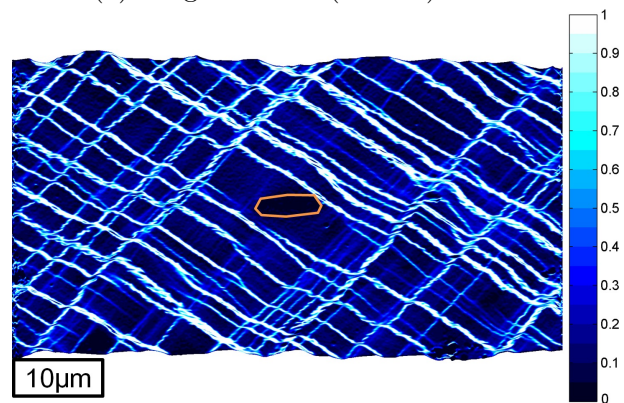
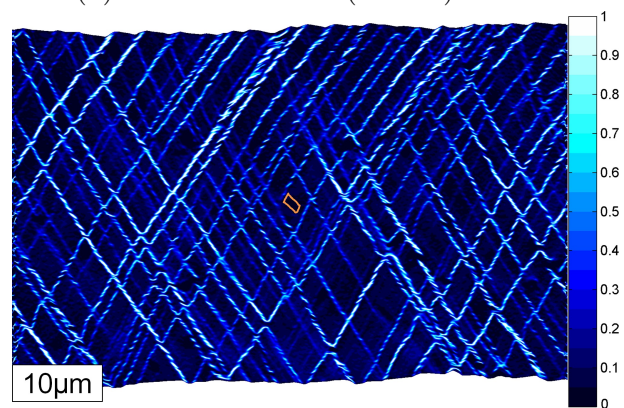
(a) Large Particle ( $\epsilon=0.31$ )(b) Medium Particle ( $\epsilon=0.33$ )(c) Small Particle ( $\epsilon=0.17$ )

Figure 2.19: Effect of Particle Size on Slip Band Evolution [Ko, 2014]

inhomogeneity in the local slip behaviour. It was through this work that links were forged between the particle size and slip line spacing. It was suggested that particles larger than the slip line spacing would result in larger interactions. Dispersoids were also found to reduce slip line spacing, suggesting that their presence would result in more homogeneous deformation [Ko, 2014].

## 2.5 Restoration Processes

The processes of recovery and recrystallization reduce the amount of stored energy within deformed material through two different mechanisms.

### 2.5.1 Recovery

Recovery refers to the rearrangement of dislocations within a material to lower its overall stored energy. This reduction is achieved by the mutual annihilation of dislocations and the rearrangement of any remaining dislocations to form ordered arrays [Perryman, 1954]. This recovery can occur at ambient temperatures [Kramer and Haehner, 1967] but dislocation movement is generally limited to glide and cross-slip under these conditions. If the material is heated, dislocation climb becomes increasingly favourable (climb is a diffusion controlled process and is a function of temperature), thus allowing greater levels of dislocation annihilation and faster rearrangement [Nix et al., 1985].

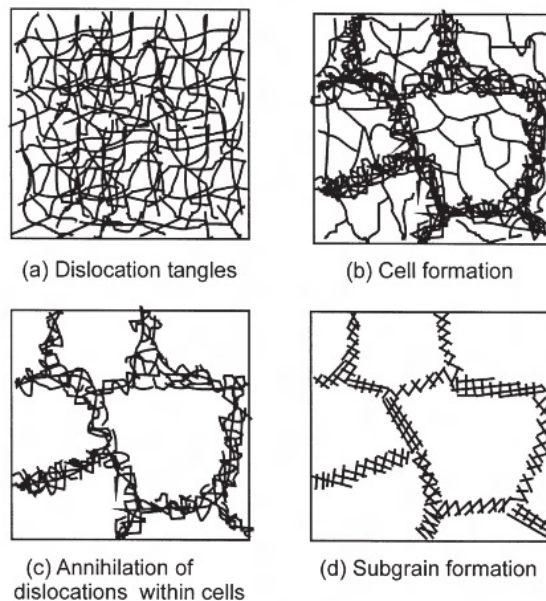


Figure 2.20: The stages of recovery within plastically deformed materials [Humphreys and Hatherly, 2004]

Figure 2.20 shows schematically the various stages of recovery following plastic deformation. Dislocation tangles (a) refer to the vast network of dislocations within the material following plastic deformation. Subsequent rearrangement of these dislocations allows regular cell structures to form within each grain, (b). The dislocation

density within the walls of each cell diminishes as recovery continues (c), until ideally, a final structure containing only the dislocations that are geometrically needed to maintain (ideally coherent) subgrain boundaries remain, (d). This is called polygonization [Cahn, 1950].

Further recovery takes place as subgrains grow, involving the migration of low angle grain boundaries. In single crystal specimens, the rate of subgrain growth has been linked to the misorientation between neighbouring subgrains, with a  $3^\circ$  increase in misorientation (from  $2.5^\circ$  to  $5.5^\circ$ ) resulting in a 50 fold increase in boundary mobility [Huang and Humphreys, 2000].

Recovery processes can take place during deformation, resulting in a dynamic equilibrium between dislocation creation and annihilation [Bullen and Hutchison, 1962]. This dynamic recovery limits the amount of work hardening that can be achieved and usually takes place in materials with a high stacking fault energy [Essmann and Mughrabi, 1979].

## 2.5.2 Recrystallization

If the recovery of a subgrain results in the formation of a high angle grain boundary, the subgrain will grow, consuming local regions containing dislocations to produce a new dislocation free grain with a lower overall free energy. This is termed recrystallization. The rate of grain growth in these cases is proportional to the amount of stored energy within the system and therefore proportional to the amount of deformation which the material has undergone [Anderson and Mehl, 1945, Huang and Humphreys, 1999]. Due to the requirement of a high angle grain boundary, many new grains nucleate around slip bands in single phase materials [Humphreys, 1997a]. Like recovery, recrystallization has also been found to take place dynamically in aluminium - although these findings are limited to high purity material [Ponge et al., 1997].

Just as the post deformation orientation spread is termed the ‘deformation texture’, the term for the spread of orientations after recrystallisation is referred to as the ‘recrystallisation texture’.

As recovery and recrystallization both aim to reduce the local stored energy within the material, these can be considered competing processes. There are conditions in which recrystallization can be offset, allowing the material to recover and by doing

so, reduce the ability of the material to recrystallize. This can be achieved by maintaining lower annealing temperatures and reducing the strain rate when processing [Humphreys and Hatherly, 2004].

### 2.5.3 Particle Effects on Restoration

In materials such as AA3003 and the high Mn model aluminium alloy used throughout this work, stable dispersoids can strongly influence the subgrain growth during recovery. These dispersoids act to pin subgrain boundaries, and can result in a particle-limited subgrain size [Jones and Hansen, 1981]. In this case, the subgrains grow until they reach a dispersoid particle which then pins the subgrain in place. The distribution of particles then becomes the limiting factor in subgrain growth. This pinning may also hinder the formation of a viable recrystallization nucleus, inhibiting recrystallization. By allowing nucleation of dispersoids during homogenisation, pinning effects during dynamic recovery processes are also possible [Ryum, 1969].

Larger second phase particles can also pin high angle grain boundaries in place, thus slowing grain boundary movement during recrystallisation and limiting recrystallised grain size. This is referred to as Zener pinning has been attributed to the reduction in surface energy as a grain boundary meets the small inclusions within the matrix [Smith, 1948]. The mechanism of Zener pinning is well understood and has been reviewed extensively by Nes et al. [Nes et al., 1985]. The extent of the pinning effect is dependant on many factors including the crystallographic coherence of the particle, as well as the size and morphology of the particle, and interparticle distance throughout the material [Mujahid and Martin, 1994, Li and Easterling, 1990, Nishizawa et al., 1997].

### 2.5.4 Solute Drag

The incorporation of solute atoms into the matrix has been found to greatly affect boundary mobility, with the nature of these effects being dependent on the individual solute-matrix system [Humphreys and Hatherly, 2004]. This is due to the formation of a solute atmosphere around the grain boundary which moves with the boundary, and can hinder its migration.

The addition of manganese solute atoms to an aluminium matrix greatly reduces grain and subgrain boundary mobilities as reported by Driver et al. [Driver et al., 2006]. It was also found that this experimental data complied with the well established Cahn, Lücke, Stüwe model (improved in [Lucke and Stuwe, 1971]).

### 2.5.5 Particle Stimulated Nucleation

As previously discussed, deformation in two phase material leads to the establishment of deformation zones around non deformable particles. These zones have higher dislocation densities, and therefore higher stored energy, than other areas of the matrix. It is this excess stored energy in the local matrix that acts as driving force for recrystallization. This is known as particle stimulated nucleation of recrystallization, or PSN [Humphreys, 1997b].

#### Nucleation of PSN

Just as in general recrystallization, for a subgrain to act as a viable nucleus, the relative misorientation must be large enough to allow a high angle grain boundary to form. The initial formation of the nucleus involves the growth of a subgrain along an orientation gradient, during which the crystal incorporates areas of progressively higher misorientation [Humphreys and Hatherly, 2004]. It has been noted that this subgrain does not necessarily form at the particle-matrix interface [Ørsund and Nes, 1988]. Subgrain growth along the orientation gradient continues until the critical misorientation of  $15^\circ$  is formed at the boundary. The time taken to reach this misorientation is inversely proportional to the magnitude of the orientation gradient [Huang and Humphreys, 2000].

Once the critical misorientation criteria is met, the growth rate of the subgrain is determined by two pressures: the driving pressure due to the high dislocation density (stored energy) in the neighbouring grain, and the retarding pressure due to the boundary curvature [Humphreys and Hatherly, 2004]. This relationship has been quantified to give the equation:

$$d_g \geq \frac{4\gamma_b}{\alpha\rho Gb^2} = \frac{4\gamma_b}{E_D} \quad (2.12)$$

where:

$$\alpha = 0.5$$

$$d_g = \text{Critical Subgrain Diameter}$$

$$\gamma_b = \text{Grain Boundary Energy}$$

$$\rho = \text{Dislocation Density}$$

$$G = \text{Shear Modulus}$$

$$E_D = \text{Matrix Stored Energy (Driving Force)}$$

The effects of any solute drag are not incorporated into this relationship. In cases where the critical particle size is not met, the growth of the new grain will be limited to the deformation zone around the particle [Humphreys and Hatherly, 2004].

### **Texture Effects of PSN**

The orientation of any new grains formed during PSN are determined by the orientation of the nucleus, which is in turn dependant on the initial orientation, deformation conditions and the dimensions of the particle local to the nucleus [Humphreys, 1977]. In single crystals containing sites viable for PSN, the overall texture is marginally reduced as all new grains are formed from within the deformation zone of similarly deformed material. This reduction however, is not a complete randomisation of the texture [Humphreys, 2000]. However, a weaker initial texture, such as those found in polycrystals may appear to become a random texture following PSN, due to the wider range of possible orientations of recrystallisation nuclei [Engler et al., 1997].

### **Efficiency of PSN**

Due to the growth of the nucleus consuming much of the deformation zone, it is expected that in most cases, each particle will result in the nucleation of one new grain, i.e. an efficiency of one (unity) [Humphreys and Hatherly, 2004]. By designing an alloy with a known volume fraction and particle size, and assuming that deformation is evenly applied to all points within the volume, it is theoretically possible to control the final grain size due to PSN, as shown in figure 2.21 [Humphreys, 1990].

It follows that PSN could allow grain size to be tailored as the number of nuclei, and therefore the number and size of grains could be modified. High efficiency has been found in materials with large non-deformable particles (5 to 10  $\mu\text{m}$ ), however this

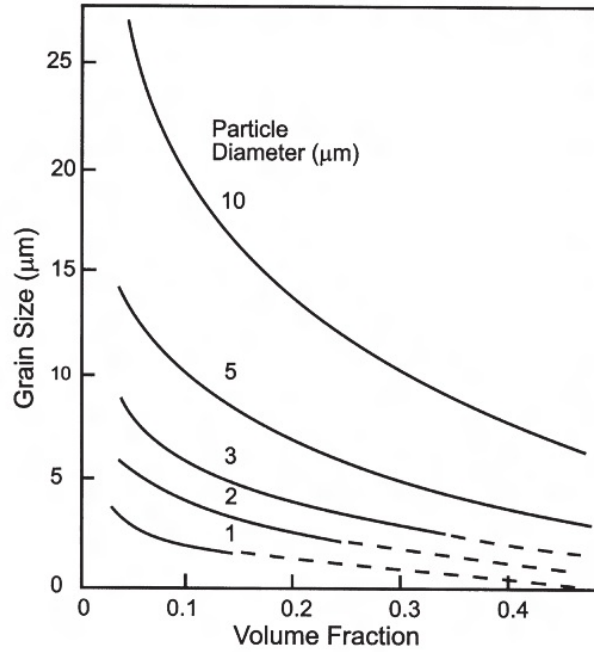


Figure 2.21: The effect of volume fraction and particle size on grain size assuming an efficient PSN process, with dashed lines showing conditions where Zener pinning may occur ([Humphreys, 1990] in [Humphreys and Hatherly, 2004]).

efficiency is greatly reduced in materials with smaller particles [Rios and Padilha, 2003]. This has been attributed to the nucleation of subgrains not taking place concurrently across the sample and the varying growth rates of each grain. This can allow a single nucleus to grow into the deformation zone of a second particle before a second PSN nucleus can form.

Little has been published explaining the low efficiency of PSN, indicating gaps in the current understanding of the process. To understand PSN more fully, and create a model for PSN which incorporates terms describing particle parameters, improved knowledge of the initial deformation zone formation around particles as described in section 2.4.3 is necessary.

## 2.6 Modelling Deformation around Particles

Various fields of engineering extensively use models to predict how an object will behave as a design tool before manufacturing takes place. This can allow theories to be tested quickly without the need for expensive manufacturing processes if enough related experimental data is already known and has been verified.

In metallurgy, models are used successfully to predict composition and macro scale behaviour of a metal, i.e. the elastic and plastic behaviour of a substance during deformation using commercially available software packages such as DEFORM [Scientific Forming Technologies Corporation, 2016].

However, to truly determine how a material will behave at a macroscopic level, the microscopic features of the material must be understood, and determining how something behaves at an atomic and crystallographic level poses many challenges that researchers worldwide are still trying to overcome.

### 2.6.1 Crystallographic Deformation Modelling

Crystal plasticity models use data pertaining to the mechanics of single crystals to predict how polycrystals will behave. These models have become more complex as more features of micron-scale plasticity become known. Modelling macro-scale deformation involves treating a volume of material as a homogeneous object. However, at the micro-scale, the ordered crystallographic structure of metals becomes apparent, as does the very different mechanical behaviour of the material.

#### The Sachs and Taylor Models

The earliest model that focussed on crystal plasticity was developed by Sachs [Sachs, 1928] (see section 2.4.1). The single slip system approach allows each grain to deform on the single slip system with the greatest resolved shear stress or Schmidt factor (see equation 2.7). In this model, the stress is assumed to be uniform in all grains and the resulting polycrystal yield stress is simply the average yield stress of all grains. In this model, each grain can deform independently of any neighbouring grains and so boundary compatibility is ignored. This model therefore breaks down at a fundamental level when modelling any form of polycrystal due to incompatibilities which develop

between neighbouring grain boundaries [Ashby, 1970].

The full-constraint Taylor model forces each grain to undergo the same change in overall shape, thus solving the problem of boundary conditions as the grain boundaries are essentially set, and utilises multiple slip systems within each grain to satisfy the individual strain conditions. As there are five independent strains within each grain according to Taylor theory, five independent slip systems are required for a grain to deform homogeneously. The slip systems chosen in this model are those which firstly those which meet the geometric conditions of the strain, and of these systems, the combination of five that has the lowest activation energy [Taylor, 1938].

The Taylor model succeeds in predicting how grains of cubic material would homogeneously deform, if interactions with neighbouring grains did not exist [Taylor, 1938]. This can be used as a tool to determine how a single crystal of a particular orientation may evolve when deformed along a specific axis. However in the case of polycrystalline deformation modelling, the Taylor model provides much stronger textures than those found experimentally due to the omission of constraints imposed by neighbouring grains. Though exaggerated, the results of Taylor models are still widely published as a comparative tool in texture model development [Bachu and Kalidindi, 1998].

The rigid constraints of the Taylor model have been modified to consider the deformation of non-equiaxed grains. In these ‘relaxed constraint’ models, fewer independent slip systems are activated than in the full constraint model, which is mathematically treated by allowing shear of the grain [Hirsch and Lucke, 1988]. These models are considered useful in predicting how flattened grains whose grain boundary is parallel to the rolling plane will behave under deformation, however the inability of this model to evaluate interactions between grains limits its accuracy [Hirsch and Lucke, 1988].

### **Multiple Grain Models**

In order to include the effects of local grains on deformation, the Lamel [Van Houtte et al., 1999] and Advanced Lamel (Alamel) [Van Houtte et al., 2005] models have been formulated to consider the interactions between two neighbouring grains. The Lamel model considers a stack of two grains of equal size and calculates how they would deform together. The model is constrained by fixing the grain boundary parallel to the

rolling direction, ensuring that the rolling plane remains undistorted and the rotation of the plane does not alter. Homogeneous strain is applied to the overall system, allowing the two grains to deform cooperatively, but utilising separate slip systems thus providing some insight into how neighbouring grains can impact deformation. This also allows cases of cooperative slip between two grains to be taken into account. This is applied to a polycrystal by first discretising a material data into several thousand orientations and randomly assigning the top and bottom grain orientations from the pool. The Alamel model expands the Lamel model, and has been shown to provide texture predictions comparable to those made using much more computationally intensive techniques [Van Houtte et al., 2005]. Upon its creation, it was hoped that the Alamel model could allow prediction of crystallographic texture for any deformation mode.

The grain interaction (GIA) model [Crumbach et al., 2006a, Crumbach et al., 2006b] allows simulation of eight grains within a cluster. This model is much more computationally intensive than the two grain variant, as it forces the cluster as a whole to comply with the Taylor conditions, while allowing the grains within the cluster to deform freely. Like the Lamel and relaxed constraints models, GIA is utilised to predict the effects of rolling.

So far, the methods described have succeeded in describing how a grain will deform under set conditions and with the incorporation of Lamel and GIA, short range interactions with neighbouring grains have been included.

### **Self Consistent Models**

By taking the average properties of a material, a homogeneous equivalent medium (HEM) can be developed. Single grains can then be modelled within this HEM to determine how a particular orientation would behave within the polycrystal. Using this method, all grains of the same orientation would deform in the same way. Interactions around the included grain can however be studied, and this model does allow any anisotropic behaviour to be investigated [Hill, 1965, Lebensohn and Tome, 1993].

## Crystal Plasticity Finite Element Modelling

In order to include long range interactions when modelling texture development, much more computationally intensive simulations are necessary, such as the incorporation of crystal plasticity into a finite element model. This full field approach allows interactions between all grains within the model to be considered [Liu and Radhakrishnan, 2010].

Using a crystal plasticity finite element model (CPFEM), specific orientations are applied to each element within a 2D or 3D mesh. The model then proceeds by imposing a displacement to the nodes which lie on the desired face of the mesh. The resulting displacements of each of the nodes within the mesh are then calculated using constitutive equations built in to the model. Several iterations may be required to reach an overall equilibrium across the mesh for each displacement step [Bate, 1999].

These simulations can be constructed to model the bulk behaviour of a metal under deformation (by setting each element as a different orientation), or conversely, sub-grain scale problems can be tackled (allocating orientations found within a single grain across multiple elements) [Humphreys and Bate, 2003]. Using this method, grain boundaries are not violated, as each point in the simulation deforms cooperatively with all points across the mesh. This however leads to much greater computational demand than other models [Duchêne and Habraken, 2007]. As well as strain and rotation around a particle [Humphreys et al., 2012], the CPFEM has previously been used for the modelling of intergranular stresses [Quinta da Fonseca and Bate, 2005], as well as the deformation of HCP materials [Honniball, 2014].

Of the models listed, which were all developed to aid in understanding texture development, only CPFEM allows direct simulation of a crystallographic region that takes into account long range compatibility across the simulation and maintains boundary compatibility during deformation. By definition, the study of how particle shape affects the local orientation requires this.

### 2.6.2 Modelling Deformation in Two Phase Materials

Initial attempts to quantify deformation around a non-deformable particle simplified the system by including a single spherical particle within a single crystal that was

confined to one slip system [Ashby, 1970]. Though this was modified to include more slip systems and applied to polycrystals, true predictions of lattice rotations around particles were not obtained until the incorporation of ‘slip shadowing’ by Humphreys and Ardakani [Humphreys and Ardakani, 1994].

### The Two Phase CPFEM

Crystal plasticity finite element models have been designed to model the deformation of matrix material around a non-deformable particle [Bate, 1999, Bate and Hutchinson, 1997, Humphreys and Bate, 2003]. In the current CPFEM framework, used in this work designed by Bate et al [Bate, 1999], boundary conditions are set, placing a single non deformable region inside a mesh. Separate input files containing crystallographic data for the elemental material are loaded into the preprogram along with deformation constraints. The CPFEM code then uses constitutive equations to determine the effect of the deformation constraints on each node in the mesh.

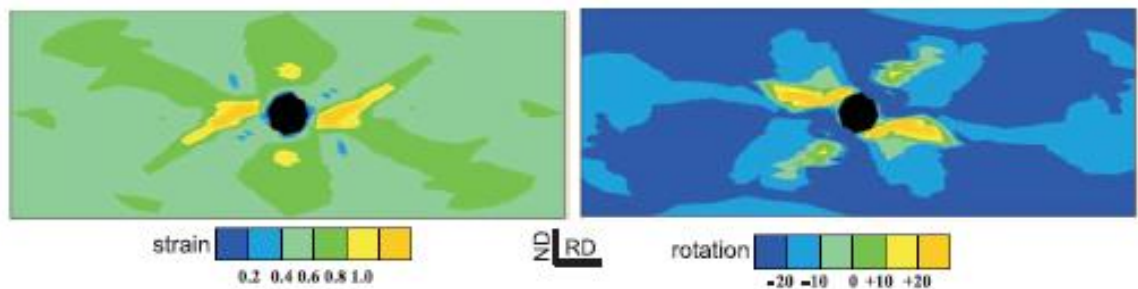


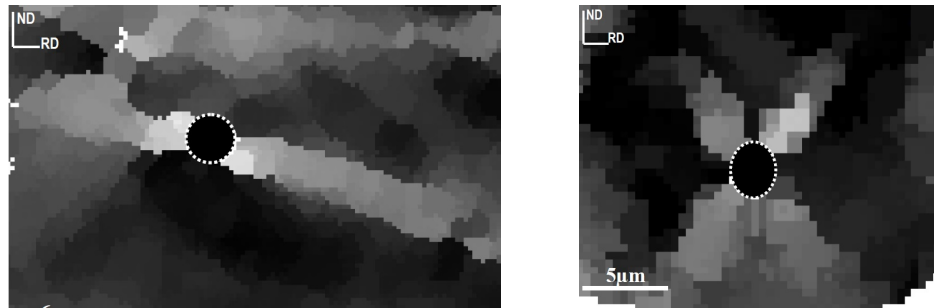
Figure 2.22: Simulations created using CPFEM showing strain and crystal rotation around a particle in material undergoing plane strain compression [Humphreys and Bate, 2003]

The deformation zone and the rotation of the lattice have been predicted for a circular particle as shown in figure 2.22 [Humphreys and Bate, 2003]. It is clear from these images that the main rotated regions in this model are above and below the particle relative to the slip plane which is in general agreement to the theory proposed by Humphreys [Humphreys, 1977]. The initial 2D model has since been expanded to incorporate a 3D mesh as detailed in [Humphreys et al., 2012], however, due to the computationally intensive nature of CPFEM, simulations have so far been limited to very simple particles using a limited number of elements, thus restricting the complexity of the problems that CPFEM can be used to solve. With time, improvements to

computing capabilities may allow increasingly complex CPFEM problems to be solved.

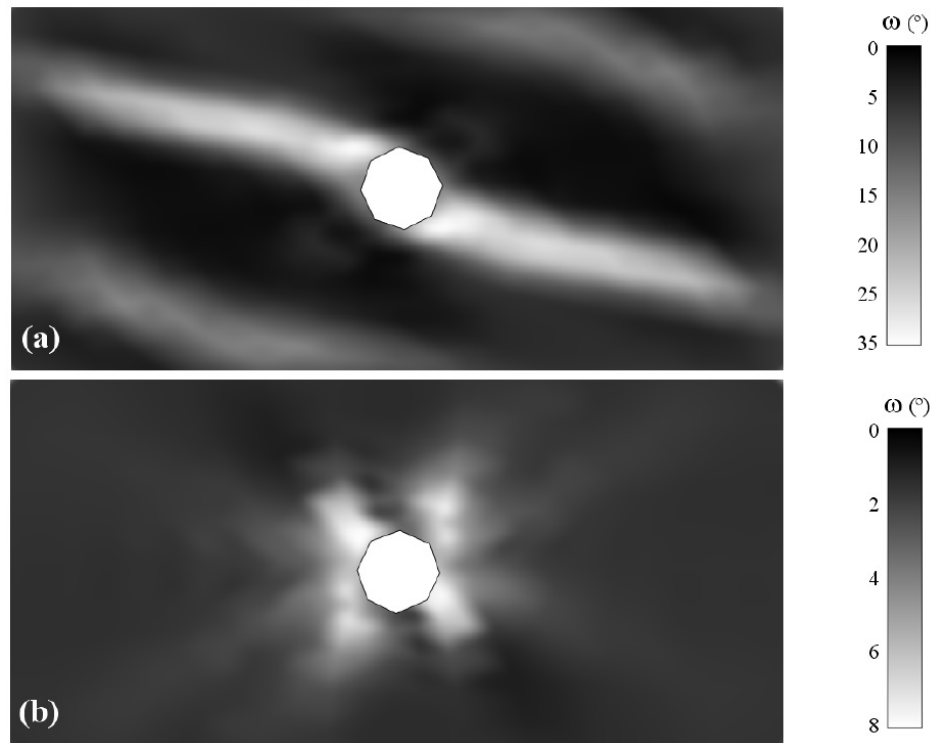
Humphreys and Bate have since published experimental validations of this model (as shown in figure 2.23) in which 3D EBSD measurements were obtained around approximately spherical particles, and similar shaped particles were incorporated into a model where the matrix was set to a closely matching starting orientation [Humphreys et al., 2012]. From this figure, it is clear that the shape of the resulting plumes are similar in both the experimental results and the model, however, the model acts to overestimate the extent of the rotations.

Detailed comparisons have been presented by Ko [Ko, 2014], which illustrate how results from the full 3D CPFEM ( $15 \times 15 \times 15$ ) compare to a pseudo-2D model ( $93 \times 70 \times 1$ ). An example for a cube grain is presented in figures 2.24 and 2.25. Figure 2.24 shows that the magnitude of the strains and rotations are similar in both the pseudo-2D and full 3D case, and the overall configuration of the plumes are the same. From the plots shown in figure 2.25, it can be seen that in a cube grain, the pseudo-2D case results in slightly lower strains and rotations compared to the full 3D simulation.



(a) Elongated deformation zones at a grain of orientation  $\phi_1, \Phi, \phi_2 = 83^\circ, 71^\circ, 41^\circ$

(b) Deformation zone at a particle in an S-oriented grain



(c) CPFEM predictions of the misorientation ( $\omega$ ) around a second phase region, giving (a) plumes (b) spatially limited symmetrical misorientation

Figure 2.23: Experimental and modelled deformation zones using 3D EBSD and CPFEM from [Humphreys et al., 2012]

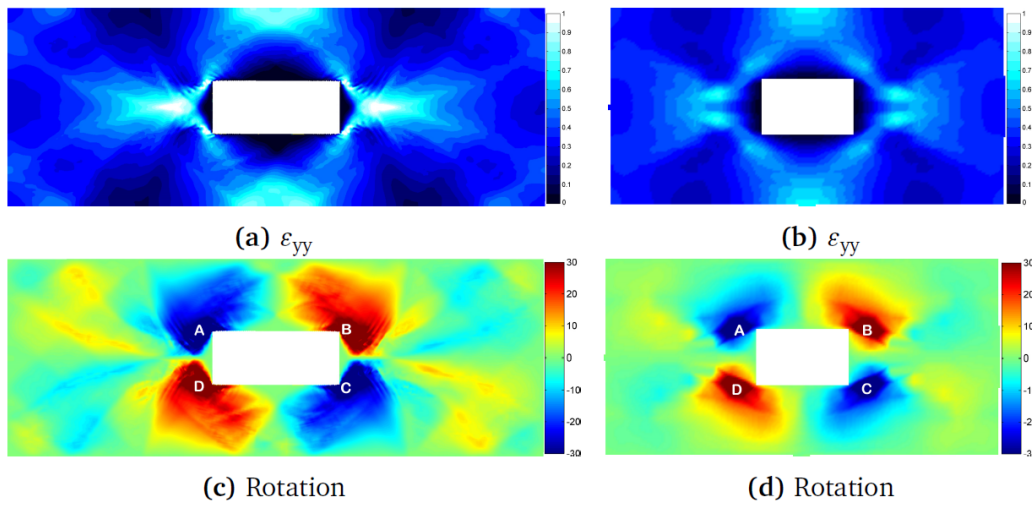


Figure 2.24: Simulation results of pseudo-2D and full 3D models. (a) Pseudo-2D strain, (b) 3D strain, (c) pseudo-2D rotation, (d) 3D rotation [Ko, 2014].

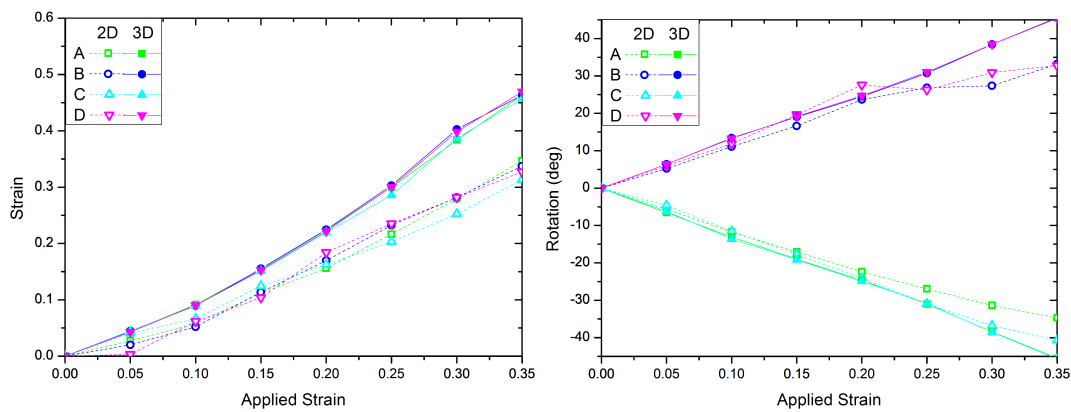


Figure 2.25: Strain and rotation plots comparing 3D and pseudo-2D CPFEM simulations [Ko, 2014].

## 2.7 Rationale of the Study

The creation of a through process microstructural model requires multiple cooperative modules which can interact. This would be used to determine how all aspects of the microstructure of an alloy would develop and the resulting material properties. Currently, many aspects of the the microstructural processes are understood at a fundamental level, however data which quantifies these processes has often not been obtained.

An example of this lies with the particles found within 3XXX aluminium alloys. These are well understood in terms of their composition and behaviour during processing (i.e. phase transformations and their effects on grain boundary mobility). However, a detailed investigation into the structure of the intermetallic network found in 3XXX alloys is yet to be completed. By undertaking volumetric studies of material from different stages of aluminium processing, an in depth analysis of how the constituent and dispersoid particle populations develop during processing has been generated in this study.

Much work has also been done to understand and model the deformation around non-deformable particles and the resulting restoration mechanisms. However, studies have so far not focused on the effects of particle shape and clustering on deformation, which as shown in the constituent particle study, is a necessary undertaking due to the complex array of particles found in 3XXX alloys. In this project, work was done using high resolution DIC in an attempt to show deformation zones around particle clusters. Model shapes and distributions were also used to provide new input parameters for CPFEM models to simulate, allowing effects on interparticle distance and orientation to be investigated.

By quantifying how particle populations change during processing, and determining how the local geometry and spacing of particles alter deformation zone morphology, the creation of a unifying model for aluminium sheet production will become closer.



# Chapter 3

## Experimental Methods

### 3.1 Material Studied

The material used throughout the bulk of this project is a direct chill (DC) cast test alloy created by Novelis Inc, designated 'PGN', the composition of which is shown in table 3.1. This alloy was created with two others ('PGL' and 'PGM'), each containing varying amounts of manganese, all of which were created as model alloys to aid in understanding aspects of the commercially available AA3003 alloy (the composition of which is also shown in table 3.1 for comparison).

Table 3.1: Composition (wt%) of model alloy and commercial AA3003

Alloy	Cu	Fe	Mn	Ni	Si	Zn	Al
PGL	0.001	0.356	0.051	0.001	0.150	0.002	Balance
PGM	0.001	0.384	0.289	0.001	0.150	0.002	Balance
PGN	0.003	0.366	1.041	0.002	0.157	0.002	Balance
AA3003	0.200	0.700	1.500	-	0.600	0.100	Balance

## 3.2 Thermomechanical Processing

### 3.2.1 Homogenisation

Samples of as-cast alloys were placed into a Eurotherm 3216CC furnace and exposed to the homogenisation conditions shown in figure 3.1. Each sample was water quenched to room temperature following heat treatment. These conditions were chosen as they promote the nucleation of dispersoids which are important in processing of AA3003 as detailed in section 2.3.2 [Hill, 2014].

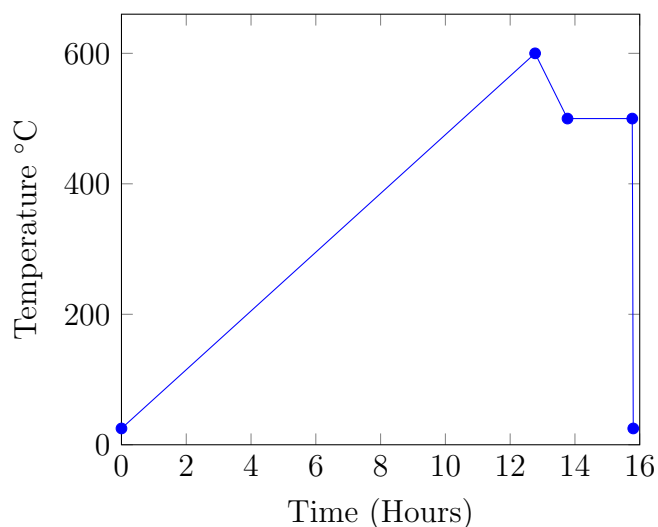


Figure 3.1: Temperature Profile of Homogenisation Treatment

### 3.2.2 Rolling

A simple rolling schedule was devised to create deformed material so that intermetallic particle evolution could be investigated.

As-cast material was cut to 166 x 41 x 24 mm blocks, homogenised and subsequently quenched. Before rolling, the material was reheated to 500°C. A Marshall-Richards Barcro rolling mill was used to roll the material to the rolling schedule shown in table 3.2. A furnace was used to reheat the sample between passes.

### 3.2.3 Plane Strain Compression

During rolling, the central region of the material is constrained and cannot freely deform. To understand how material moves within this central region, a channel die

Table 3.2: Rolling Parameters for Deformation Studies

Sample	Temperature (°C)	Step Reduction	Passes	Total Reduction
A	500	~ 10%	7	52%
B	500	~ 10%	16	81%

was utilised to compress the sample. As the region of interest in the case is not the face of the sample, but rather a cross sectional area, two cubes of material were placed side by side within the channel die. Using this method, the region of interest falls on the interface between the two samples as shown in figure 3.2.

Samples were first cut and polished to create cubes of length 7.5 mm. Samples (one of which was patterned using the gold remodelling technique explained in section 3.3.3) were then compressed in ~4% intervals using an Instron 5569 Mechanical Tester, whilst constrained within a channel die as shown in figure 3.2. A polytetrafluoroethylene (PTFE) film was placed between samples to aid in lubrication. Lubriplate L0034-086 was used to ensure that the die could move smoothly during the deformation. The sample height was measured after each loading step using a micrometer to ensure a 4% reduction had been achieved. At each interval, the sample was removed from the experimental set up, cleaned of any residual lubricant and imaged using an SEM. Due to problems with the characterisation of the gold pattern, this work includes up to 8% reductions only.

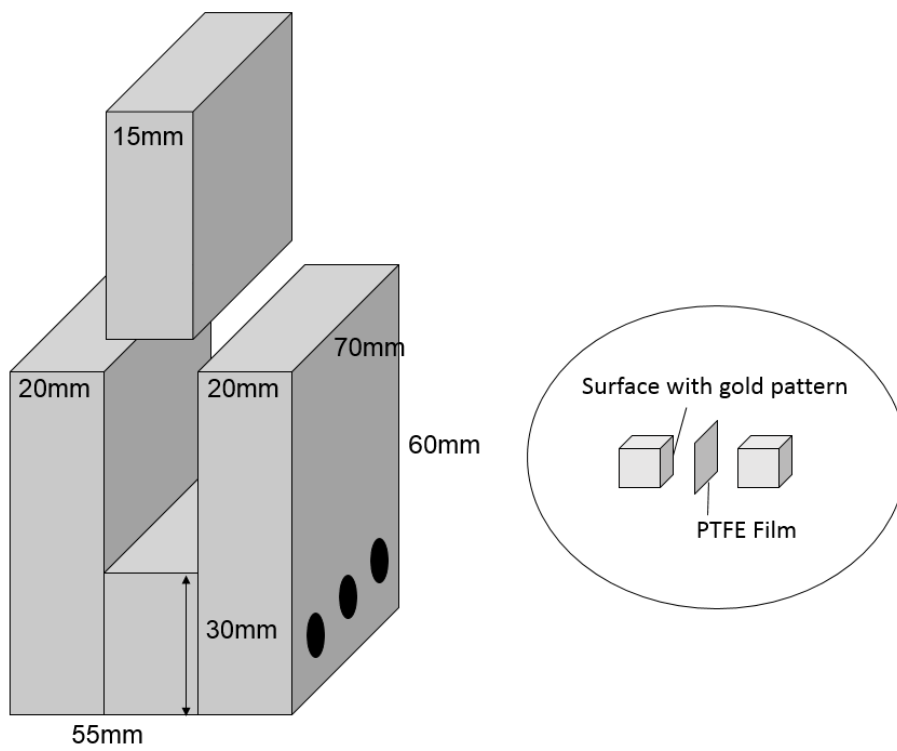


Figure 3.2: Channel die dimensions and orientation for plane strain compression experiments

## 3.3 Sample Preparation

### 3.3.1 Sample Cutting

All samples were cut using a Struers Discotom-6 with a lubricant cooled 20S25 250 mm cutting disc. For the more precise cutting needed for SBF-SEM and Plane Strain Compression experiments, a Struers Minitom was utilised.

### 3.3.2 Polishing

Samples were cold mounted in epoxy resin and prepared for microscopy using a Struers Tegraforce-5 and TegraPol-31. Successively finer SiC paper was used to grind samples, which were then polished using 6  $\mu\text{m}$  and 3  $\mu\text{m}$  diamond polishing wheels with a water based diamond polishing suspension. A 10% solution of OPS (colloidal silica) was used to complete the polishing process. Samples were cleaned after each stage of preparation using ethanol.

### 3.3.3 Gold Remodelling

To allow digital image correlation to be performed, a randomised gold pattern was produced on the surface of polished specimens. An Edwards S150B sputter coater was used add a 50 nm layer of gold to the surface of the sample as described in [Di Gioacchino and Quinta da Fonseca, 2013]. The sample was then exposed to water vapour at 200°C for 90 minutes using the experimental set up shown in figure 3.3, causing the gold to form a nanometre scale speckled pattern on the surface of the material as shown in figure 3.4.

During compression experiments, it became apparent that the gold pattern, while stable, is easily removed from the surface of the sample. This renders the sample unusable for analysis using digital image correlation (see section 3.5). Some post-patterning heat treatments consisting of isothermal holds at 250°C were performed in an effort to improve pattern adhesion.

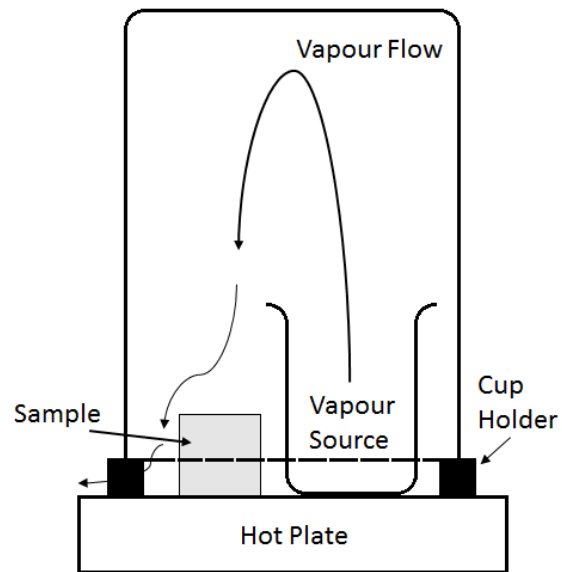


Figure 3.3: Experimental Set Up for Gold Remodelling

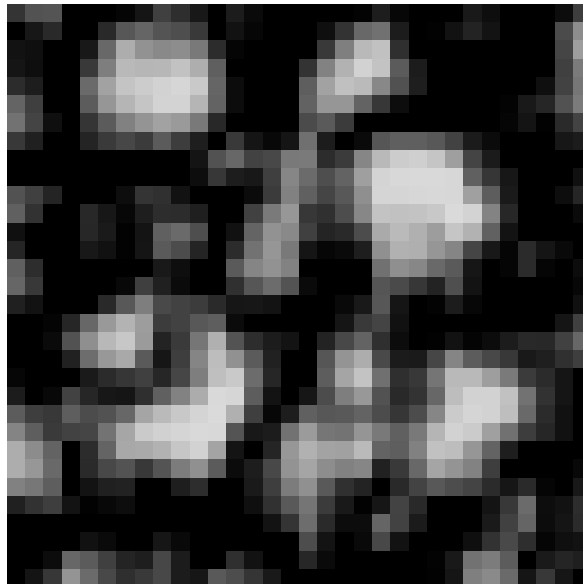


Figure 3.4: An example of a the randomised speckled pattern of a remodelled region (32 pixels ( $1.22 \mu\text{m}$ ) x 32 pixels ( $1.22 \mu\text{m}$ ))

## 3.4 Scanning Electron Microscopy

Scanning Electron Microscopy (SEM) involves measurement of the interaction between an electron beam and the sample surface. Multiple SEMs have been used as part of this project, fitted with varying detectors which provide different information about the sample studied.

### 3.4.1 Secondary Electrons

When incident electrons interact with the lower energy electron shells of near surface atoms, low energy secondary electrons (SE) are emitted. The quantity of electrons detected using an SE detector is affected by the local topology of the sample and as a result of this, high resolution topological data can be obtained [Goldstein et al., 2012].

### 3.4.2 BackScatter SEM

As incident electrons impact the positively charged atomic nuclei within the sample, their course is drastically altered and they are deflected back out of the sample. The number of backscattered electrons increases with the atomic number of the interacting nucleus, thus allowing images to be created which show contrast between regions of differing atomic number. These local compositional differences due to different phases within the material can therefore be easily visualised. Backscattered electrons can be reflected from within a given interaction volume, which varies depending on both the accelerating voltage of the SEM and the composition of the sample [Goldstein et al., 2012].

Single BS-SEM images were obtained to study the constituent and dispersoid morphology using a Zeiss EVO50 VP-SEM with the parameters shown in table 3.3.

Table 3.3: Zeiss Evo50 BS-SEM Scanning Parameters

Feature	Accelerating Voltage	Magnification	Working Distance	Image Size	Pixel Size
Constituent	20 kV	2000x	9.5 mm	1024 x 768	(143 nm) <sup>2</sup>
Dispersoid	20 kV	10,000x	9.5 mm	1024 x 768	(29 nm) <sup>2</sup>

High resolution BS-SEM images were obtained using a Sirion FEG-SEM with the parameters shown in table 3.4.

Table 3.4: Sirion BS-SEM Scanning Parameters

Feature	Accelerating Voltage	Magnification	Working Distance	Image Size	Pixel Size
Gold Pattern	22 kV	2000x	5 mm	3872 x 2904	(16 nm) <sup>2</sup>

### 3.4.3 Serial Block Face SEM

Samples were cut to approximately 2 mm x 5 mm x 10 mm before being placed into an Quanta FEG250 SEM fitted with the Gaton 3View system. The 3View system features an automated stage and ultramicrotome as shown in figure 3.5

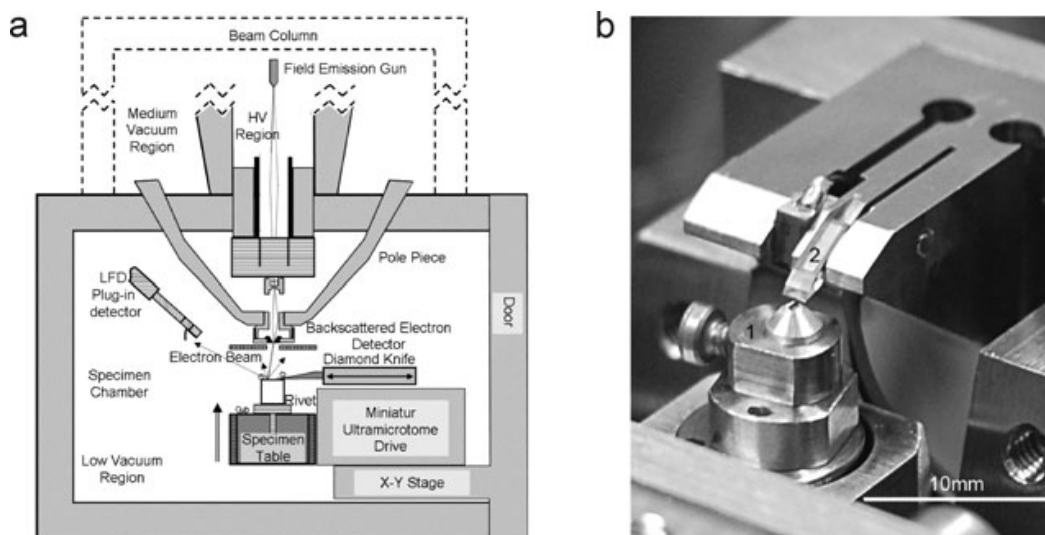


Figure 3.5: Illustration of the experimental set-up (a). Photograph (b) of the specimen holder (1) and the diamond knife (2) from [Zankel et al., 2009]

This device was set to record backscattered electron images using the parameters shown in table 3.5.

Table 3.5: 3View Scanning Parameters

Accelerating Voltage	Spot Size	Working Distance	Image Size	Pixel Size	Slice Depth
2.5 kV	3.5	3 mm	1024 x 1024	(49 nm) <sup>2</sup>	50 nm
2.5 kV	3.5	3 mm	1024 x 1024	(10 nm) <sup>2</sup>	15 nm

After an initial SEM image was captured, a sub-micron surface layer of the sample was removed using the automated in-situ ultramicrotome. The thickness of this cut was set depending on the size of the feature of interest within the sample (i.e. for larger constituent particle analysis, a 50 nm slice was removed, for smaller dispersoid particle analysis, a 15 nm slice was removed). The depth of 50 nm was chosen to ensure that a large enough volume could be studied over 1000 slices to obtain details of constituent morphology, while the 15 nm slice was chosen as this is the practical resolution limit when accounting for the interaction volume of the incident electron beam (see figure 3.10). To accomplish the cut, the stage holding the sample is elevated by the required distance before an ultramicrotome, set at the focal point of the backscatter detector cuts across the sample. After the surface layer is removed, the material is imaged again. This cutting and imaging is repeated as part of an automated process to create an array of images spanning the desired depth of the material as shown in figure 3.6.

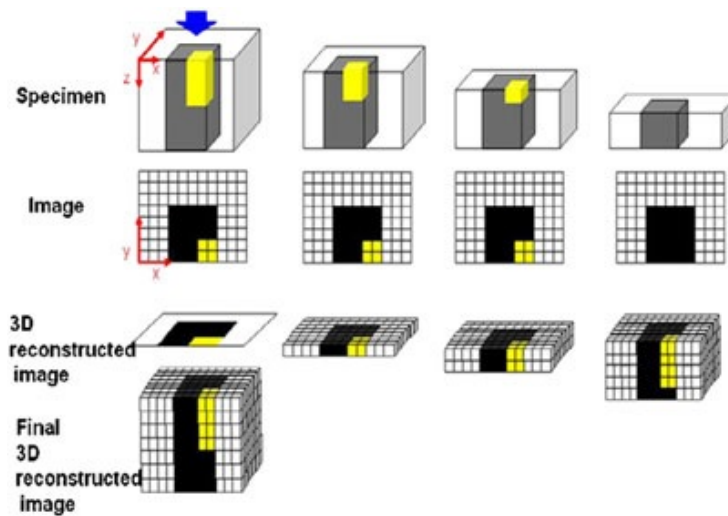
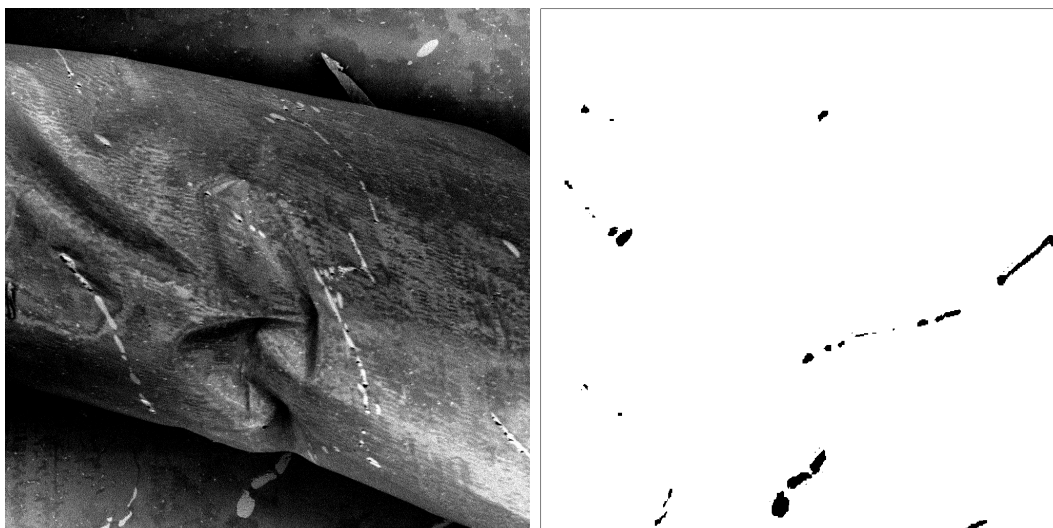


Figure 3.6: Schematic diagram of the 3View cutting and visualisation process from [Thompson et al., 2013]

During this process, a small percentage of cuts were incomplete leading to SEM images similar to that shown in figure 3.7. This has been attributed to debris remaining on the block surface [Zankel et al., 2009].

This method does result in the deformation of the surface layer of the viewed material, meaning that crystallographic data could not be obtained using this technique.



(a) The slice has rolled back across the sample, resulting in an unusable image (b) The slice was then interpolated using the labelled regions from surrounding slices

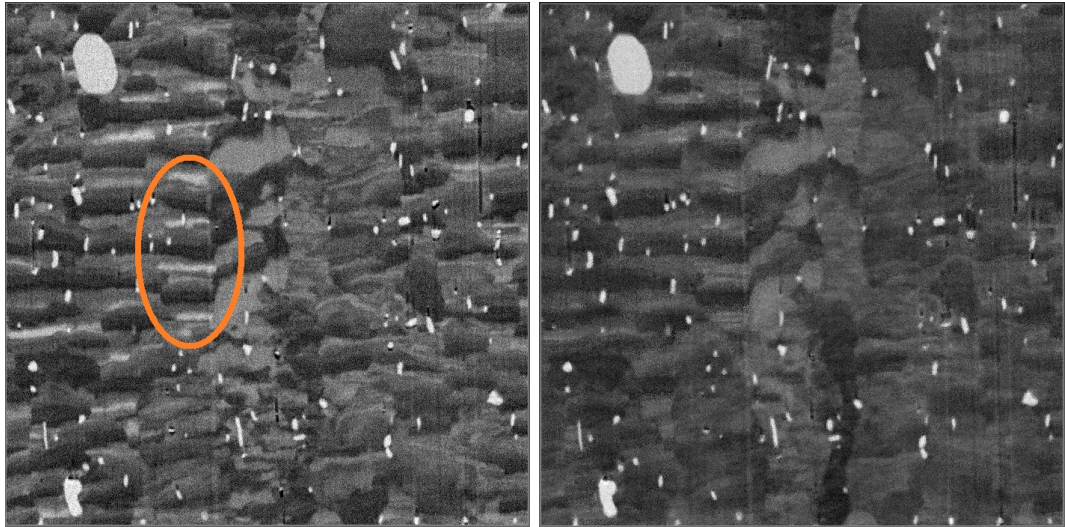
Figure 3.7: Incomplete cuts make up 5% of the image stack but the missing data can be estimated

### 3.4.4 Visualisation and Quantification of 3D Data

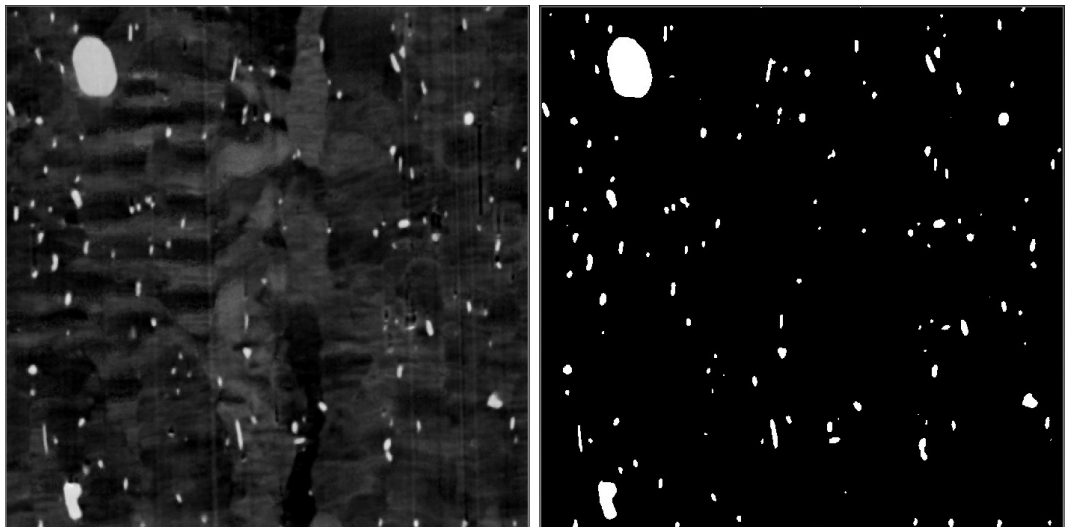
To analyse this data, the dataset of single SEM images was imported to the Avizo visualisation package as an image stack. However, before any meaningful data could be obtained, the image stack was aligned to ensure that any movement of the sample within the SEM was accounted for. This was done by taking an x-z cross section of each image stack and looking for inconsistencies in particle shape (e.g. jagged particles) which showed obvious signs of image stack displacement.

During visualisation, automated analysis of the SEM image stack could not be performed due to differences in contrast across the dataset. This was partially due to regions of incomplete cutting (as shown in figure 3.7), as well as the existence of pores within the material.

The procedure used to process the image stack is shown in figure 3.8. Raw images from this technique contain artefacts from the cutting process clearly visible in figure 3.8a. Within the oval, bands appear in the microstructure which have a similar contrast to the smaller second phase particles. Any attempt to threshold this data would result in either erroneous regions being included or conversely, the removal of all but the highest contrast particles in the volume. To aid in reducing the contrast of these artefacts, a 3D greyscale smoothing filter was applied to the image stack. The result is shown in



(a) Raw image (rolled PGN image stack) (b) Despeckling and greyscale averaging



(c) 3x3x3 median averaging

(d) Thresholding

Figure 3.8: Example of how images within the stack are processed

figure 3.8b as smoothing between the encompassing slices acts to reduce the severity of the deformation artefacts. Though this cleaned up image stack is improved, contrast must be increased further before particle analysis. For this,  $3 \times 3 \times 3$  voxel median averaging is used, which has the effect of further reducing artefacts within the matrix whilst smoothing bright areas (figure 3.8c). This can then be thresholded easily (figure 3.8d) and labelled before further analysis.

By performing a Monte Carlo simulation using Casino v2.48 with a composition similar to the PGN test alloy and an accelerating voltage of 2.5 kV, it was determined that for each pixel, the backscatter electrons originate from a volume that spreads 20 nm around the selected point (figure 3.9) and up to 50 nm in depth (figure 3.10). For this reason, the choice of thresholding value was adapted so that in the lower resolution scan where the interaction volume was of the order of the voxel (3D pixel) size, the thresholding took into account the very edge of the visualised particle, whereas on the higher resolution work, the thresholding value fell slightly within the particle outline in three dimensions to represent the comparatively larger interaction volume.

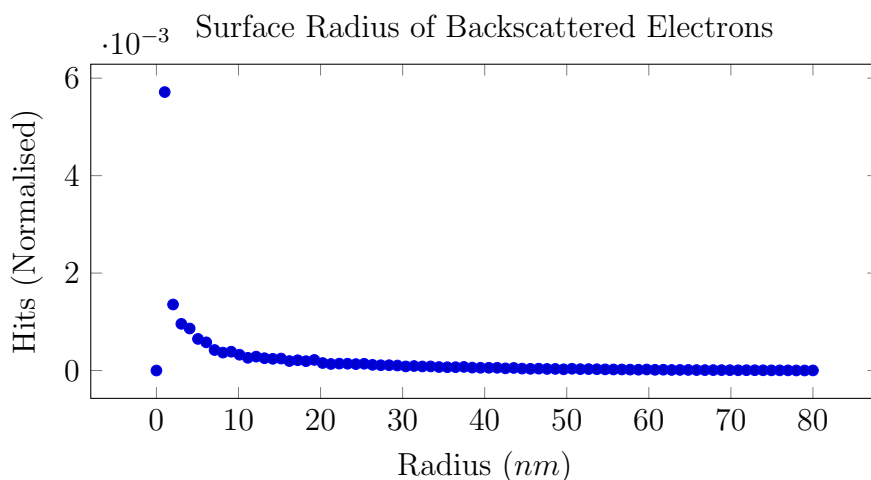


Figure 3.9: Casino plot showing surface radius of backscattered electrons

Overall, approximately 5% of SEM images produced in each 3View run could not be used due problems with incomplete cutting. To correct for this within the image stack, the data from the two adjacent slices to an incomplete cut were used to interpolate the missing data. An example of this is shown in figure 3.7, as particles shown towards the bottom centre of the interpolated data shown in figure 3.7b closely match the visible region of the incomplete cut shown in figure 3.7a. To correct for

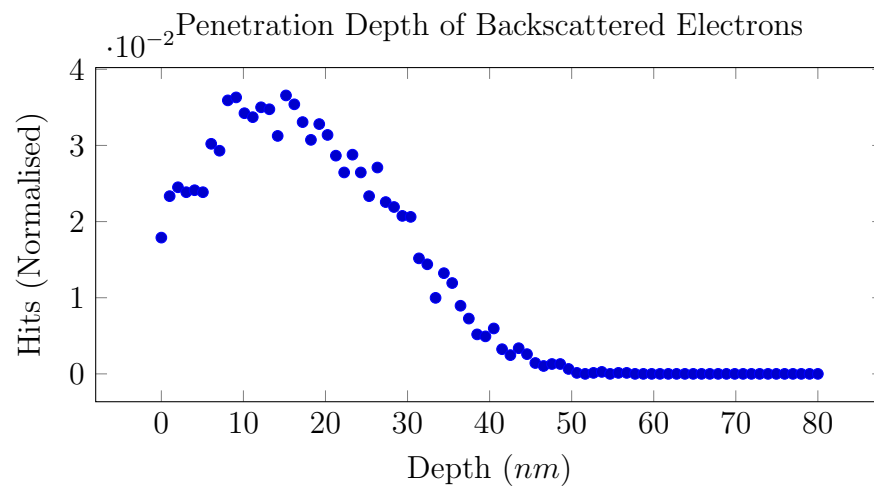


Figure 3.10: Casino plot showing penetration depth of backscattered electrons

the porosity of the material, porous regions were manually labelled as such, removing these regions from further analysis. This was to ensure any particles adjacent to the pore were not overestimated during the subsequent thresholding process.

### 3.5 Strain Mapping (Digital Image Correlation)

Strain maps were produced using a technique called “digital image correlation” or DIC using a series of images of a sample which had undergone successive deformation steps. Initially, the BS-SEM images produced, which contain the randomised gold pattern, are manually checked to ensure the central particle is aligned within the series of images. The DaVis software then runs an intensity correction algorithm on all input images to ensure the background levels are the same in all images. The software then discretises each image into subregions and attempts to match each subregion to that of the same region in the subsequent image, which is in this case, the more deformed sample, as illustrated in figure 3.11. Displacements are then calculated by comparing the images within the dataset using successively smaller window sizes (starting from  $512 \times 512$  and progressively shrinking to  $8 \times 8$  pixels) which allow a 50% overlap from one window to the next. The resulting displacements are then converted and plotted as strain maps.

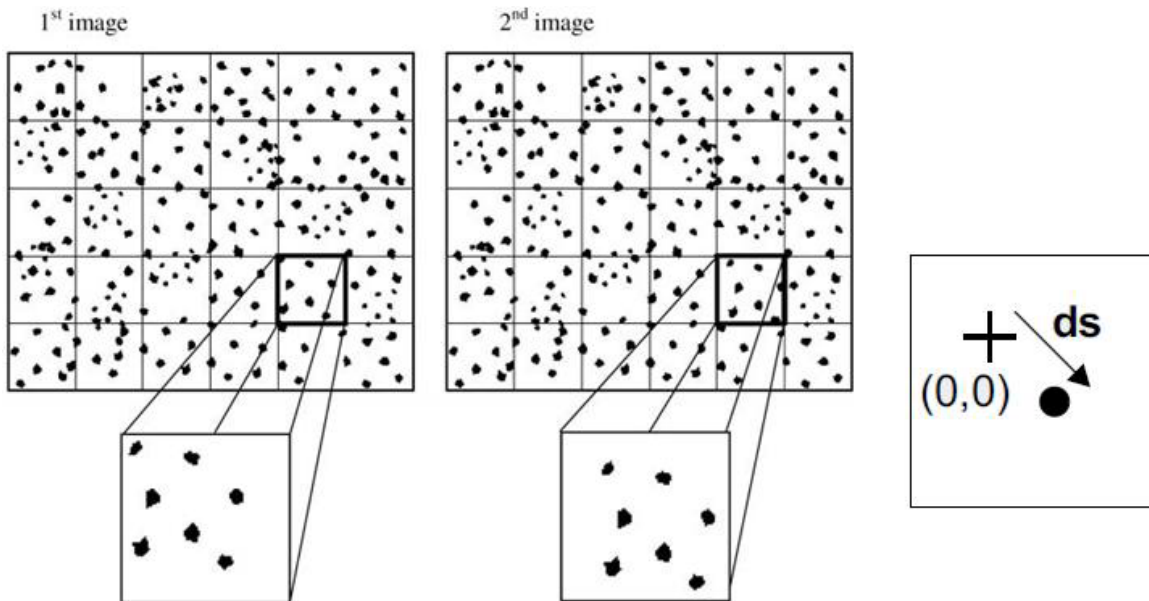


Figure 3.11: An example of subregion discretisation and the resulting displacement vector [Quinta Da Fonseca et al., 2005]

This has been shown to be a novel and reliable method for measuring strain around very large single second phase particles within a simple model aluminium alloy [Ko, 2014], however, it became apparent during this project that the gold pattern used for displacement mapping is very easily removed during the process of progressive sample

compression and image capture, which is likely to be a result of friction to the sample surface during plane strain compression. During the course of this project, numerous attempts resulted in unusable datasets due to pattern removal, while changes to the method in an effort to improve the adhesion of the gold pattern have not improved the durability of the gold pattern. An 8% reduction is the largest deformation which has resulted in usable images for strain mapping. The results of these compressions will be presented.

### 3.6 Crystal Plasticity Modelling

In order to model deformation around particles, crystal plasticity finite element modelling (CPFEM) has been employed. The model used was developed by Bate [Bate, 1999] to predict the formation of deformation bands and has more recently been used to simulate particle deformation zones (PDZ) [Humphreys et al., 2012] [Ko, 2014].

As part of this project, the preprogram for the established CPFEM (fs3pre) was studied and the region of code which designates the material properties for each element was modified. This was initially altered to include simple rectangles of a second phase to be incorporated at the centre of the mesh. Over time, further modification allowed a second input file to be called by the model which removed some restrictions to particle shape and location with the mesh. The edited subroutine is included in the appendix (A.1). The modifications to the code are the additions of “Operations 5-8”.

Due to the computationally intensive nature of the model, a pseudo-2D approach has been taken which allows more varied particle configurations to be investigated. Comparisons between full 3D and pseudo-2D configurations have been performed previously [Ko, 2014], which showed that the two approaches give similar results.

Using the altered preprogram, a mesh of 65 x 80 x 1 elements was created using 20 noded cubic elements, each with 8 integration points. Each simulation was designed to represent the internal structure within a single grain. For these simulations, all elements were programmed to have an initial orientation which fell within  $0.5^\circ$  of the target starting orientation. This is known as a ‘perturbed’ arrangement. This spread in orientation across the simulation allows internal stresses and strain gradients to develop, thus aiding to model the substructure of the grain. All results within this thesis were obtained using a ‘Cube’ oriented grain ( $\varphi_1 = 0^\circ$ ,  $\Phi = 0^\circ$ ,  $\varphi_2 = 0^\circ$ ).

Simple particle shapes such as approximations to rounded particles and diamonds were first simulated, allowing for differences in region size, clustering and region spacing to be investigated. Following this, more realistic particle shapes were used as inputs variables. A schematic of the conversion from experimental particle to CPFEM input is shown in figure 3.12. This process involved using a grid overlay over a single particle and manually determining which elements would correspond to a second phase particle. This was then converted to a 65 x 80 spreadsheet in which ‘1’ referred to matrix



crystal hardening curve using equation 3.1. The values used for the compliance tensor ( $S_{11}$ ,  $S_{12}$  and  $S_{44}$ ) were taken directly from [Xue et al., 2000].

Table 3.6: CPFEM Material Parameters

$\Theta_0$ (MPa)	$\Theta_{IV}$ (MPa)	$\alpha$	$\tau_s$
1525	10	12	70
$S_{11}$ (MPa $^{-1}$ )	$S_{12}$ (MPa $^{-1}$ )	$S_{44}$ (MPa $^{-1}$ )	
$1.59 \times 10^{-5}$	$-0.58 \times 10^{-5}$	$3.53 \times 10^{-5}$	

# Chapter 4

## Results

### 4.1 Particle ‘Closeness’

#### 4.1.1 Measuring Distributions of Particles

Particles within an alloy will be distributed throughout the material differently depending on alloy composition and the processing conditions.

To understand how second phase particles are distributed within an alloy, the population of particles within the volume must be studied as a whole.

If the barycentric coordinates of each particle within a volume are known, trigonometry can be used to create a distance map of the particles. This distance map can be used to determine the nearest neighbour of each particle within the volume, which allows one to determine the spatial distribution ( $Q$ ) of the particles within the volume. The main drawback with this measure, however, is that only the single nearest neighbour for each particle is taken into account, meaning any effects of clustering are lost when using this measure.

Another possible method is to set a limiting value, and determine the number of nearest neighbours which fall within this limit. By determining how many particles have a minimum number of neighbours within a set distance, a quantifiable measure of particle distribution can be obtained, though a problem arises in that there is no standard practice for this measure, resulting in difficulties when comparing datasets from different sources. For this reason, the following section will expand upon a measure used in graph theory and apply it to the characterisation of particle distribution.

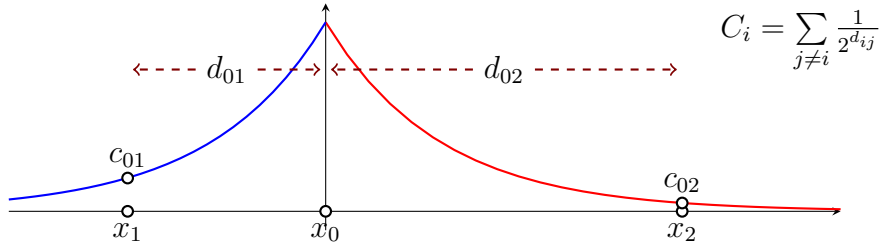


Figure 4.1: Contribution to closeness of  $x_0$  from particles  $x_1$  and  $x_2$  decreases with distance  $d$ .

### 4.1.2 Dangalchev Closeness Centrality

If all coordinates of particles within a volume are known, the dataset can be processed as a complete graph, where all points (particles) are linked. A measure termed ‘closeness centrality’ [Dangalchev, 2006] can then be determined for each particle.

$$C_i = \sum_{j \neq i} \frac{1}{2^{d_{ij}}} = \sum_{j \neq i} c_{ij} \quad (4.1)$$

where:

$C_i$  = Closeness of particle  $i$

$d_{ij}$  = Distance between particles  $i$  and  $j$

$c_{ij}$  = Contribution to  $C_i$  due to particle  $j$

Using this measure, the closeness value of each particle in the volume would be directly dependent on every other particle. However, the contribution of each separate particle to the overall closeness would be weakened with increasing distance. This is illustrated in figure 4.1 and quantitative examples of how this contribution deteriorates with distance is shown in table 4.1. This base equation has been expanded and modified as part of this thesis.

Table 4.1: Closeness Contribution Table

$d_{ij}$	—	1	2	3	4	5	10
$c_{ij}$	—	0.500	0.250	0.125	0.063	0.031	0.001

As shown in table 4.1, only structures that are within a few microns of the particle of interest will have a strong contribution to closeness. Using this method, each extra micron in distance between the barycentric coordinates will half the contribution to the closeness measure. The severity of this decline can be tailored by replacing the  $d_{ij}$

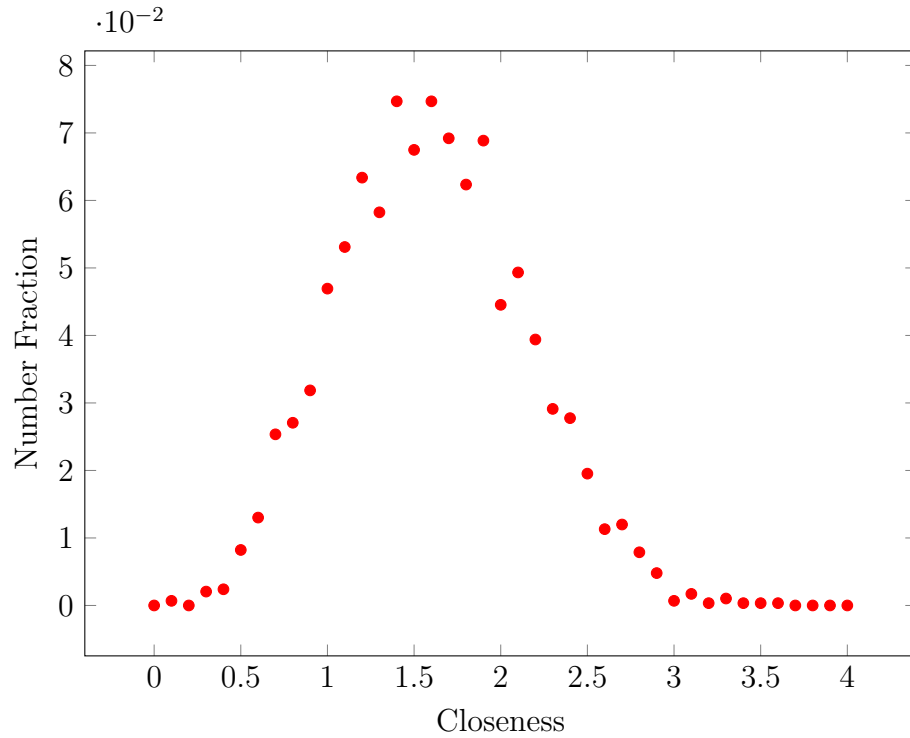


Figure 4.2: Closeness profile of volume containing a random distribution of particles as a function of number fraction

term with  $k_1 \cdot d_{ij}$ , where  $k_1$  is a scaling factor. By increasing the integer  $k_1$ , the effective reduction of  $c_{ij}$  with increasing  $d_{ij}$  can be adjusted. The closeness data produced using this method provides a new single measure for each particle which directly relates to how it is positioned with respect to neighbouring particles, but more importantly strongly describes the region closest to the particle. The distribution of closeness values calculated for a model sample<sup>1</sup> is shown in figure 4.2.

This profile could then be used to obtain the mean ( $\bar{C}_i$ ) and standard deviation of the closeness values within a particle population. By comparing this value for a population characterised though experimental means, with one calculated for a randomly populated sample containing the same number of particles within an equivalent volume, a ratio could be determined as shown in equation 4.2.

$$Q^{C_i} = \frac{\bar{C}_{i_{\text{obs}}}}{\bar{C}_{i_{\text{ran}}}} \quad (4.2)$$

where:

<sup>1</sup>A  $(50 \mu\text{m})^3$  volume was populated by 3000 particles which were assigned coordinates using a random number generator.

$Q^{C_i}$  = Closeness distribution

$\bar{C}_{i_{\text{obs}}}$  = Observed mean of closeness centrality

$\bar{C}_{i_{\text{ran}}}$  = Mean of closeness centrality if random

Using this measure,  $Q^{C_i} = 1$  would indicate randomly dispersed particles throughout the volume, with any increases in clustering within the sample acting to increase  $Q^{C_i}$ .

Distributions of closeness constructed from randomly populated volumes such as the plot shown in figure 4.2 will be used as a benchmark when analysing the distributions of real samples. Standard deviation measurements in calculated random and real samples may also be compared in a similar way to the mean as a way of characterising the range of closeness values within a sample. This ratio is useful in its ability to characterise uniformity within a sample, indicated in cases where:

$$\frac{SD_{\text{obs}}}{SD_{\text{ran}}} < 1 \quad (4.3)$$

where:

$SD_{(x)}$  = Standard deviation of the distribution of closeness values for dataset ( $x$ )

Due to the construction of this measure, large particles would tend to have a reduced closeness measure due to the calculation of distance between particles being taken as a function of the centre points of the particles, rather than the nearest edge of the particles. In the case of spherical particles, the equivalent radii can be taken from the interparticle distance measured using the barycentric coordinates as a correction for this distance measure. This is incorporated in equation 4.4, and illustrated in figure 4.3. However, when complex shapes are involved, the resulting calculation when two particles whose barycentric coordinates are close can result in a negative distance. Within this function, this would act to simply increase this overall closeness measure further. If surface to surface distances were known for the distribution of particles, this limitation would easily be overcome.

$$C'_i = \sum_{j \neq i} \frac{1}{2^{k_1 \cdot d'_{ij}}} \quad (4.4)$$

where:

$$d'_{ij} = d_{ij} - (r_i^{eq} + r_j^{eq}) \quad (4.5)$$

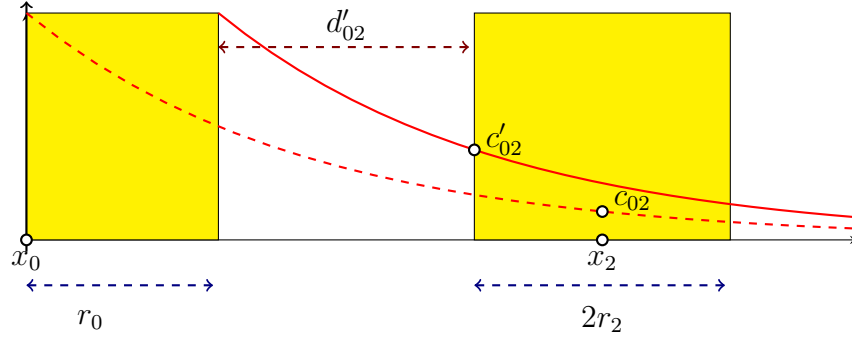


Figure 4.3: Incorporation of particle measurements can act to reduce the interparticle distances used in closeness measurements and therefore increase the closeness measure

The original closeness measure presented so far [Dangalchev, 2006] would aid in understanding particle distribution, however this function in its current iteration does not account for the size of each body which is neighbouring the particle in question. In samples which contain a bimodal particle distribution, the ability to differentiate between the different sizes of particles may be useful. An example of this may in determining regions within a material where the combined measures of size and interparticle distance are above a given threshold, which may have uses in characterising regions where the deformation structures around separate particles will interact.

A new definition of closeness which allows both decreased weighting with distance, and increased contribution for larger particles will now be outlined which may allow such characterisation.

### 4.1.3 Neighbour Weighted Closeness

By incorporating the corresponding radii of the neighbouring particles, as shown in equation 4.6, the closeness measure becomes much more size dependent. The new weighting of closeness centrality by local particle radii is shown in table 4.2.

$$C_i^{W'} = \sum_{j \neq i} \frac{r_j^{eq}}{2^{k_1 \cdot d'_{ij}}} = \sum_{j \neq i} c_{ij}^{W'} \quad (4.6)$$

where:

$C_i^{W'}$  = Neighbour Weighted Closeness

$r_j^{eq}$  = Equivalent radius of the neighbouring particle

$c_{ij}^{W'}$  = Contribution to  $C_i^{W'}$  due to particle j

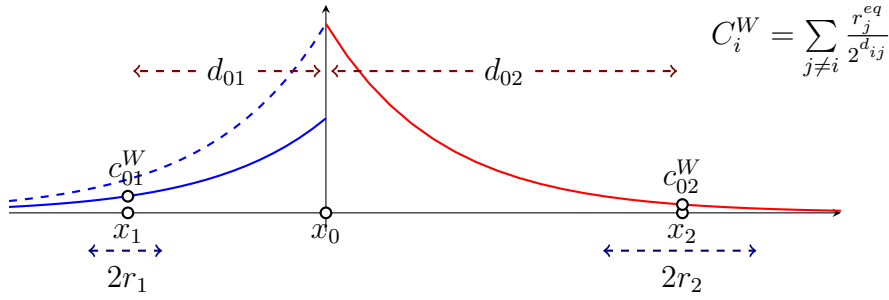


Figure 4.4: Contribution to closeness of  $x_0$  from particle  $x_1$  falls when the size of  $x_1$  is considered. This is termed ‘weighted closeness’.

The particle size weighting on the closeness measure is incorporated as a linear measure with respect to the equivalent radius. Using this method, contributions of two particles that are different sizes but are at equal distances from a particle of interest would be directly proportional.

Table 4.2: Neighbour Weighted Closeness Contribution Table

$C_i^{W,r}$	$d'_{ij}$						
	1	2	3	4	5	10	
0.25	0.125	0.063	0.031	0.016	0.008	0.0002	
0.5	0.25	0.125	0.063	0.031	0.016	0.0005	
1	0.5	0.25	0.125	0.0623	0.031	0.0010	
2	1	0.5	0.25	0.125	0.0623	0.0020	
3	1.5	0.75	0.375	0.188	0.094	0.0029	
4	2	1	0.5	0.25	0.125	0.0039	
5	2.5	1.25	0.625	0.313	0.156	0.0049	

A comparison of the weighted and non weighted closeness measures and the resulting differences in final closeness are presented in table 4.3. From this example, though the non-weighted closeness for the second and fifth neighbour are approximately equal, the inclusion of the neighbour weighting results in a marked difference in the contributions of each particle. A graphical representation of how the closeness changes with neighbouring particle size is shown in figure 4.4. In this figure, the earlier alterations from  $d_{ij}$  to  $d'_{ij}$  have been omitted for clarity, though these were included in full calculations.

By using this weighting method, it becomes clear that any closeness contributions from particles of less than  $2 \mu\text{m}$  in diameter will be reduced, while contributions will be exaggerated for larger particles. Again, a scaling parameter could be incorporated into this measure by replacing  $r_j^{eq}$  with  $k_2 \cdot r_j^{eq}$ , thus altering the turning point at which

Table 4.3: Comparison of Neighbour Weighted and Non Weighted Closeness Contributions

$d_{ij}$	$r_j^{eq}$	$c_{ij}$	$c_{ij}^W$
2.1	0.6	0.233	0.140
0.7	3.2	0.616	1.970
6.8	1.1	0.009	0.010
4.3	2.9	0.051	0.147
0.8	0.2	0.574	0.115
3	0.2	0.125	0.025
		$\sum c_{ij}$	1.608
		$\sum c_{ij}^W$	2.408

the particle size effect is increased.

The neighbour weighted closeness for each particle in the population used earlier was determined<sup>2</sup>, as shown in figure 4.5. In this figure, the newly weighted closeness profile has been reduced slightly, owing to the average particle radius of 0.8  $\mu\text{m}$ .

An example of a close network of particles and the calculated closeness and weighted closeness values for each particle within the network is shown in figure 4.6. In this figure, a simple distribution of particles found in a 2D plane is shown (4.6a). By taking the barymetric centres of each of these particles and calculating a distance map, the closeness value  $C'_{ij}$  was found for each particle as shown in 4.6b. The values given for closeness for each of these particles shows particle I as having the largest closeness value, owing to the close proximity of particle K and the nearby particle H. Note also that particle C has a low closeness using this measure. By weighting the closeness value as shown in figure 4.6, the largest closeness value of I is boosted further owing to the scale of particles K and H. However, the closeness of C has now doubled due to large contributions from particle B. Note also that the value of K drops with weighting due to the small size of its main contributor, particle I.

Just as with the non size weighted data, this weighted closeness distribution can be quantified by comparing measurements of a real particle population to that of a randomly placed calculated population. To ensure that these remain comparable, the

---

<sup>2</sup>A normal distribution of equivalent diameter measurements was constructed using values a random number generator calculated to create a normal distribution of vales. The normal distribution was calibrated to fit particle size data which was experimentally obtained and will be presented in section 4.2.2

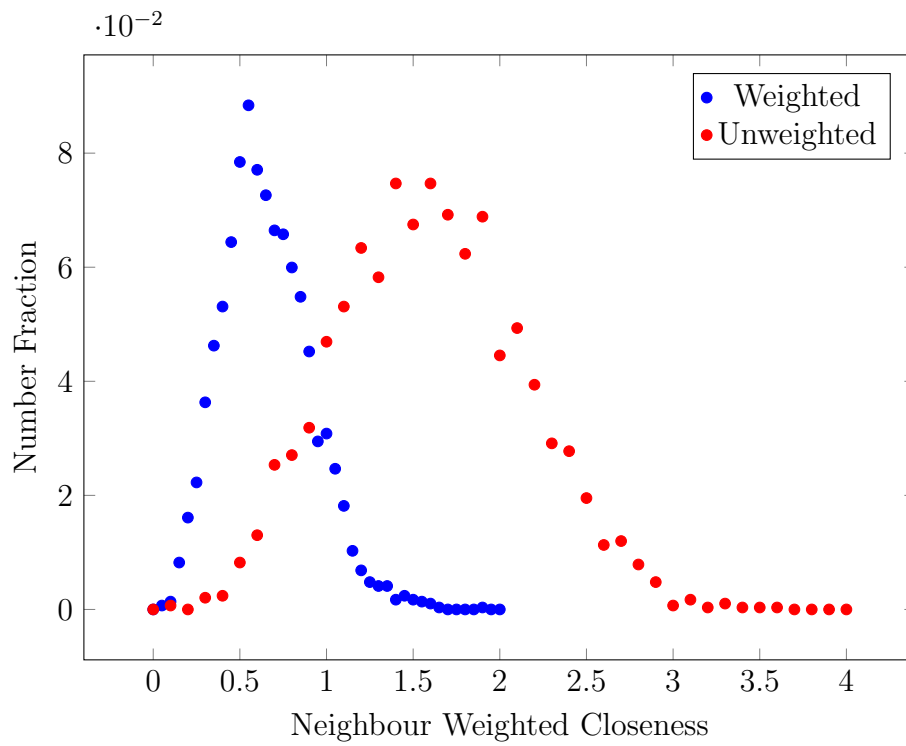


Figure 4.5: The effect neighbour weighting on the closeness profile of volume containing a random distribution of particles

same size weightings should be used, to ensure that the volume of particles included in the closeness calculations are the same.

A summary of these closeness measures and the population types which could be characterised using these measures are shown in table 4.4.

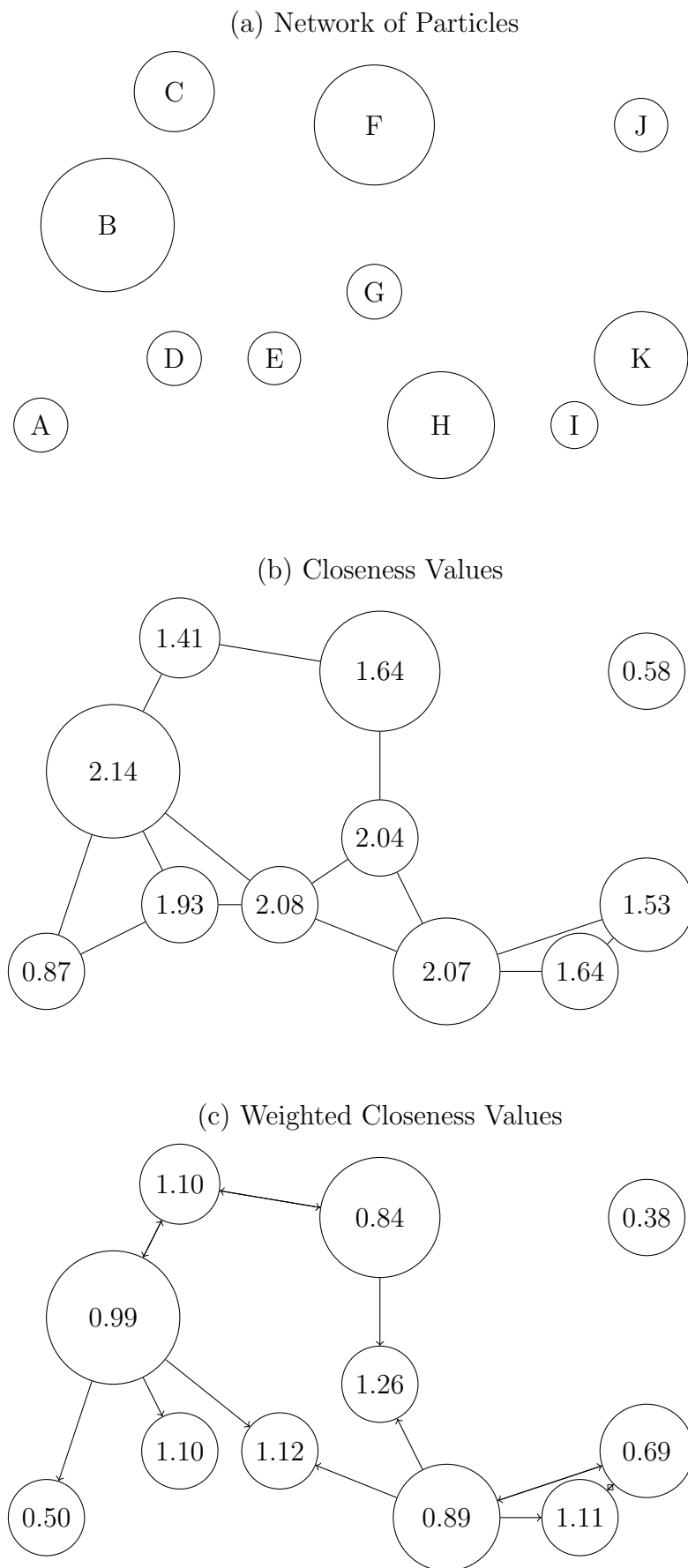


Figure 4.6: (a) Random distribution of particles in 2D [to scale], (b) closeness values calculated using only distance measures, (c) weighted closeness measures calculated using distance and particle size. The connections plotted illustrate closeness of  $> 0.1$  with arrows indicating contributions from particle  $i$  to  $j$

Table 4.4: Summary of Closeness Measures

Name	Measure From	Weighting	Appropriate Population Types	Example
Dangalchev	Midpoint	None	Particle size is approximately uniform and at least an order of magnitude smaller than interparticle distance	Sparse dispersoid population
Distance Corrected	Edge	None	Particle size is approximately uniform and similar order of magnitude to interparticle distance	Spheroidised constituent population
Neighbour Weighted	Edge	Neighbour Weighted	Particle size is varied	Bimodal population, eg Constituent and dispersoid containing alloy

## 4.2 Characterisation of Particles

This section focuses on characterisation of the size, shape and distribution of particles found at different stages of aluminium sheet production. Initially, results from traditional 2D microscopy are shown before datasets producing using an automated serial sectioning technique are presented. These 3D datasets, which show distributions of both constituent and dispersoid populations, are then analysed to produce plots detailing how equivalent diameter and sphericity of particles change during processing. Included in this analysis is the application of the ‘closeness’ measure developed in section 4.1. This 3D data is then used to evaluate the validity of the Schwartz-Saltykov method in predicting particle populations from 2D data.

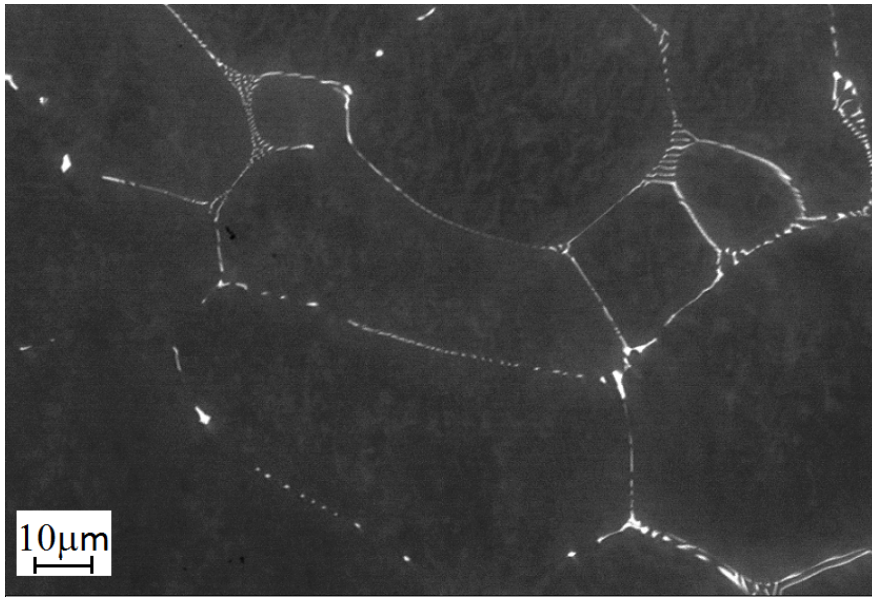
### 4.2.1 2D Analysis

Samples of each of the three alloys provided by Novelis were imaged using an SEM fitted with a backscattered electron detector to aid in understanding the morphology of particles found within the as cast microstructure of the alloys, as shown in figures 4.7a, 4.8a and 4.9a. Each of the microstructures were found to exhibit a typical dendritic structure with increasing amounts of second phase particles visible with increasing manganese concentration.

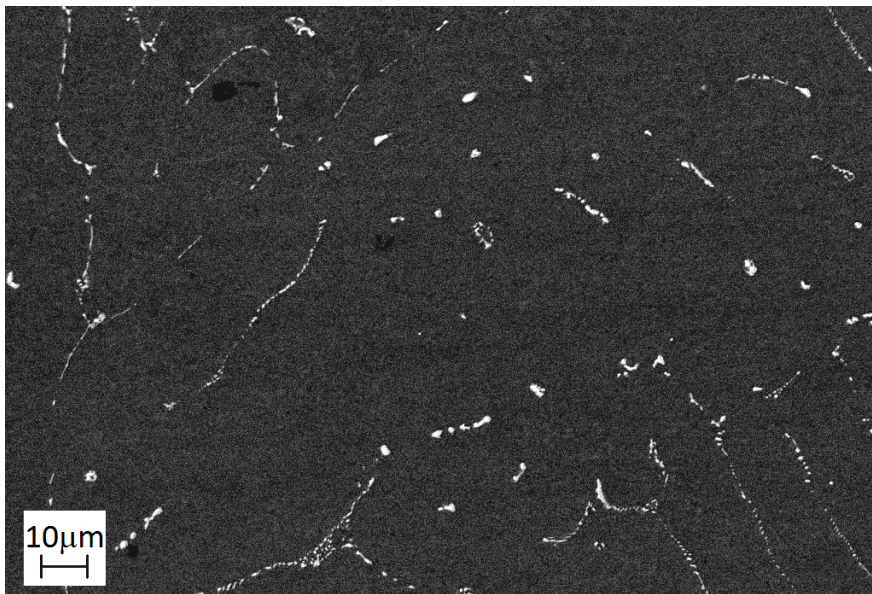
These alloys were then exposed to the homogenisation conditions described earlier in figure 3.1 and imaged to determine the homogenised microstructure. The homogenised microstructures of PGL, PGM and PGN are shown in figures 4.7b, 4.8b and 4.9b respectively.

Homogenisation of PGL showed a very clear change in the connectivity of the constituent particle population. The thin dendritic arms linking eutectic clusters shown in figure 4.7a become much less frequent within the microstructure after heat treatment, while the population of more rounded particles increases (figure 4.7b). Similar microstructural evolution is shown in the higher manganese alloys PGM and PGN (as shown in figures 4.8 and 4.9 respectively).

A combination of the increased manganese within PGM and PGN, and the two step heat treatment utilised, also results in the formation of smaller dispersoid particles as shown in figure 4.10. The dispersoids found in PGM (figure 4.10a) are relatively



(a) As cast

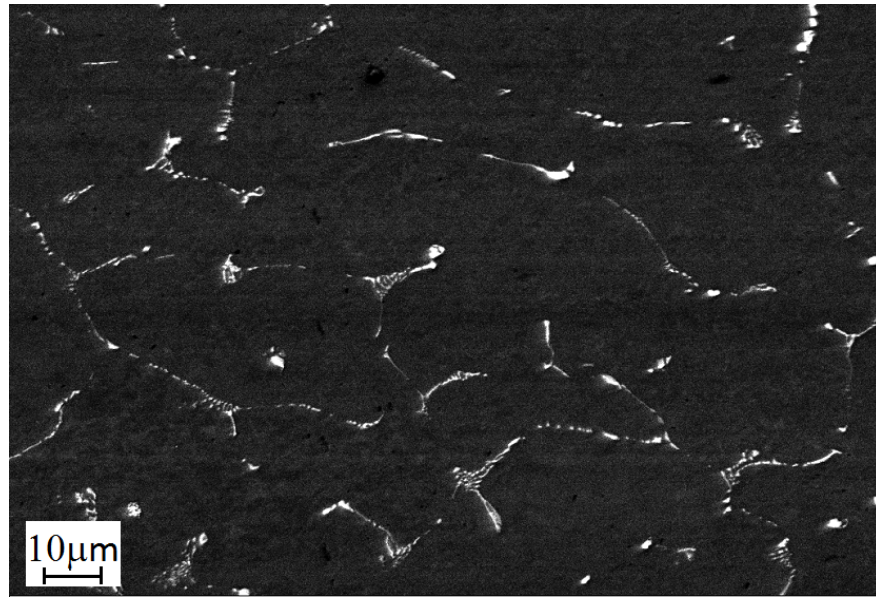


(b) Homogenised

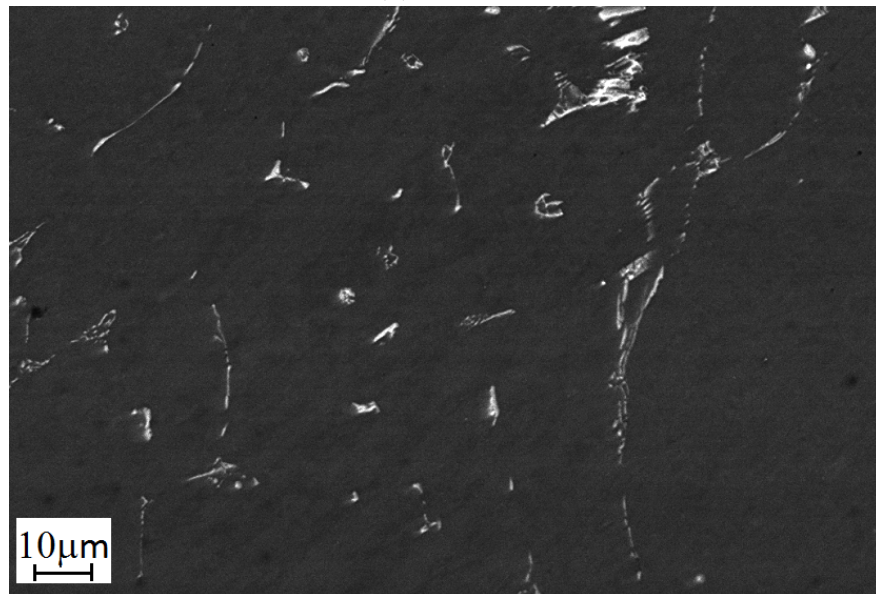
Figure 4.7: BS-SEM images of the as cast and homogenised microstructures of the low manganese alloy PGL

sparse in comparison to the high dispersoid density found in PGN (4.10b). When the difference in concentration of manganese found in each of the dispersoid producing alloys is considered, the difference in dispersoid density between these two alloys is unsurprising.

High resolution imaging shows that the population of dispersoids within the homogenised PGN is not uniform throughout the sample, but instead the particles are



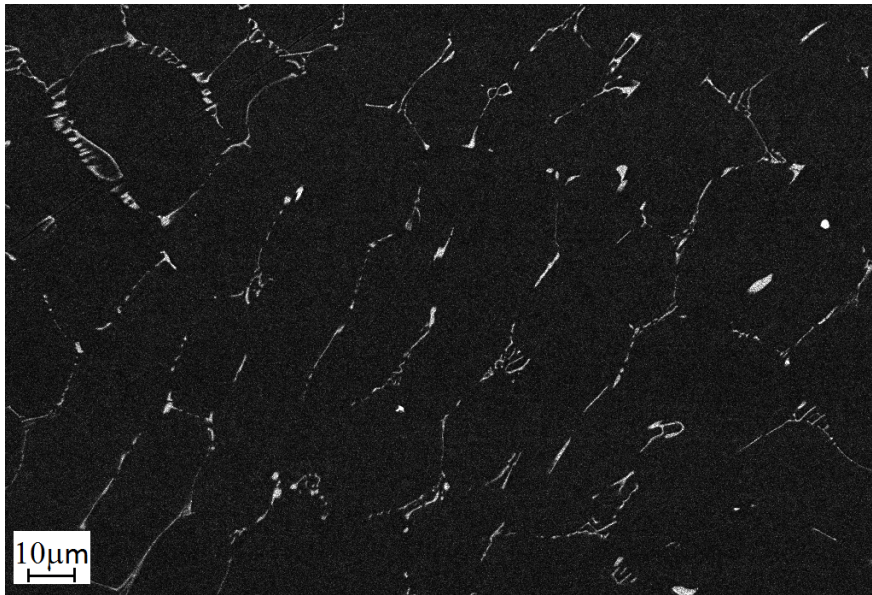
(a) As cast



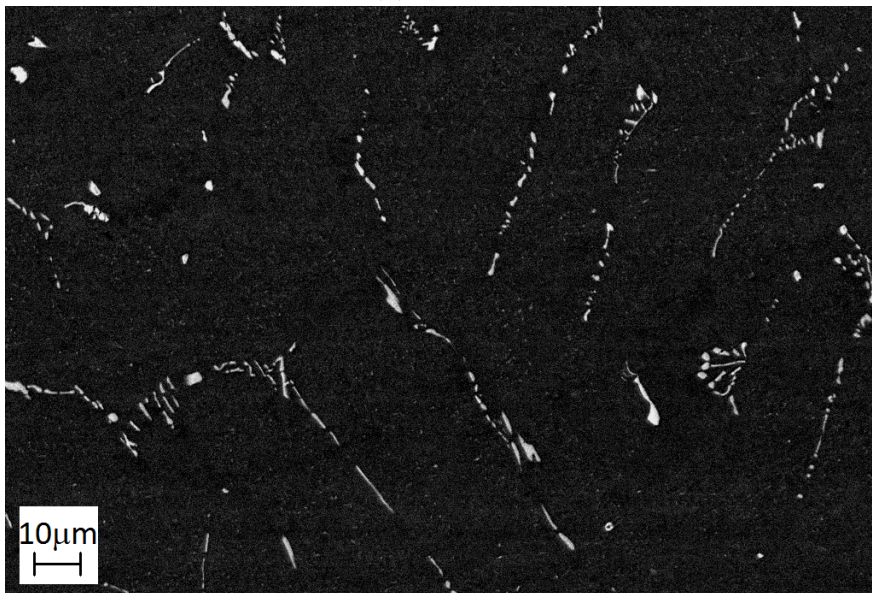
(b) Homogenised

Figure 4.8: BS-SEM images of the as cast and homogenised microstructures of the medium manganese alloy PGM

more densely clustered in regions away from constituent particles. Precipitate (dispersoid) free zones (PFZ) are also found around the constituent particles which can be seen in figure 4.10b. This feature is consistent with the competing processes of nucleation and coarsening described earlier in section 2.3.3. In this image, the size distribution of dispersoids also seems to change with distance from the constituent particle, with smaller dispersoids found bordering the PFZ, and larger dispersoids found further from constituents.



(a) As cast

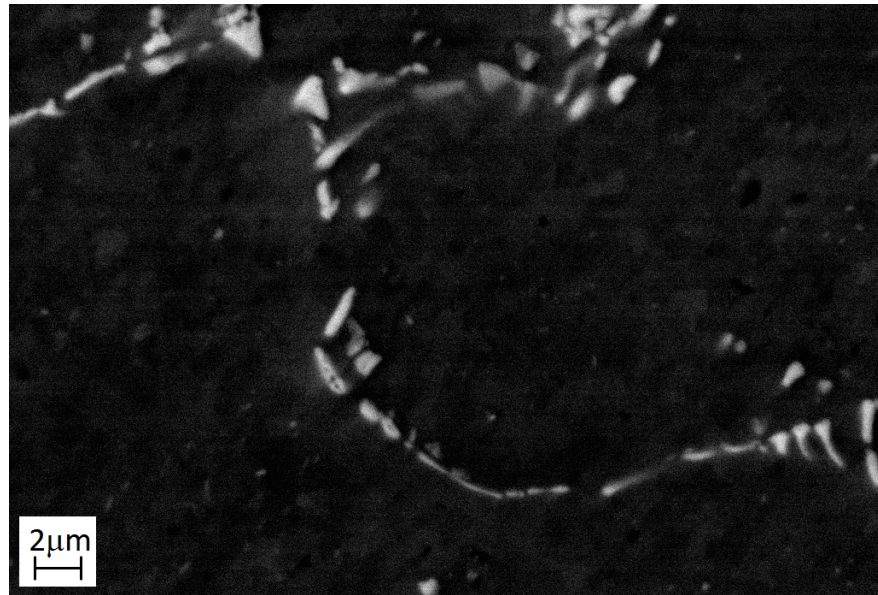


(b) Homogenised

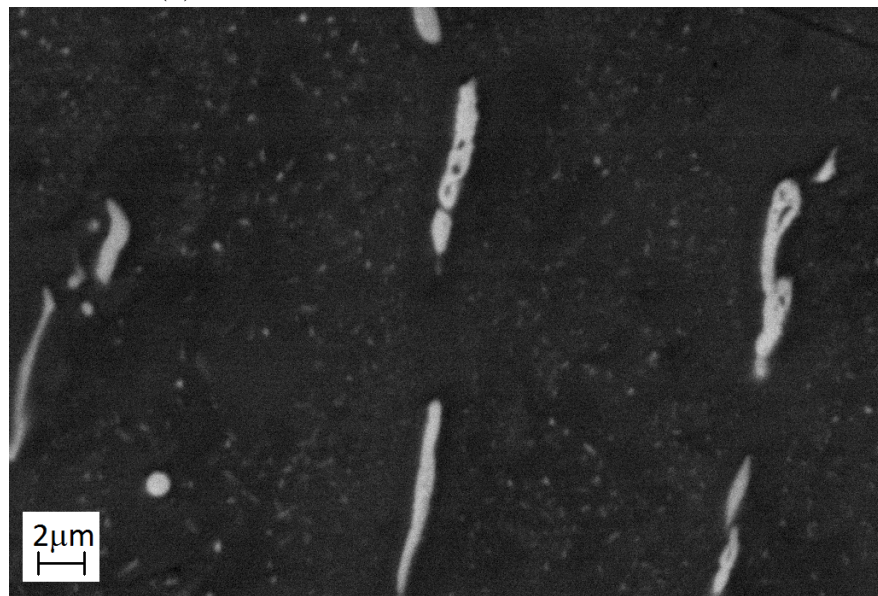
Figure 4.9: BS-SEM images of the as cast and homogenised microstructures of the high manganese alloy PGN

As the alloy with the higher manganese content, PGN, more closely matches the composition of alloys in use, such as AA3003, further microstructural studies were undertaken solely using the PGN alloy.

Homogenised PGN was deformed using the rolling schedule shown in table 3.2 to produce the microstructures found in figure 4.11 (images shown are of the transverse plane). At a reduction of 52% (figure 4.11a) the long thin particles found in heat treated material are no longer visible within the sample, suggesting that they have



(a) Dispersoids present in homogenised PGM

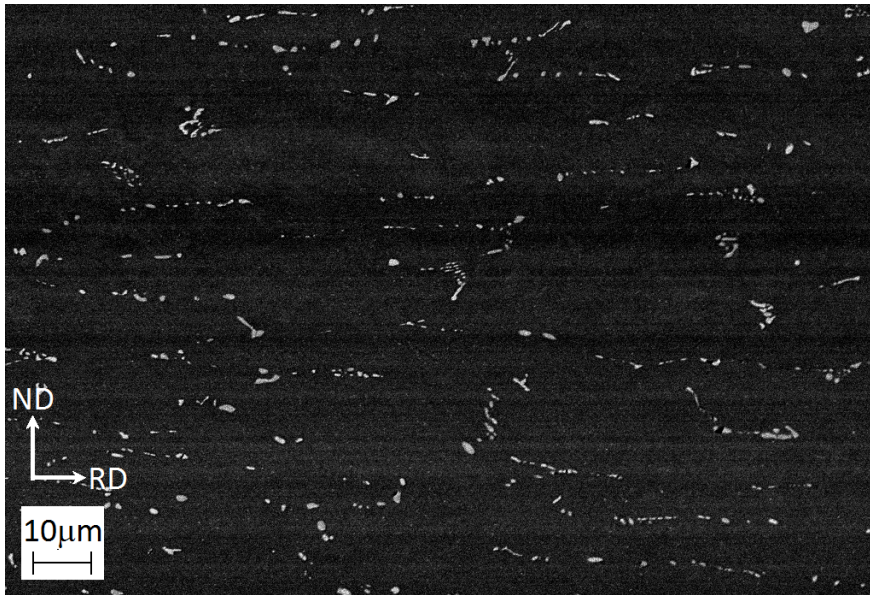


(b) Dispersoids present in homogenised PGN

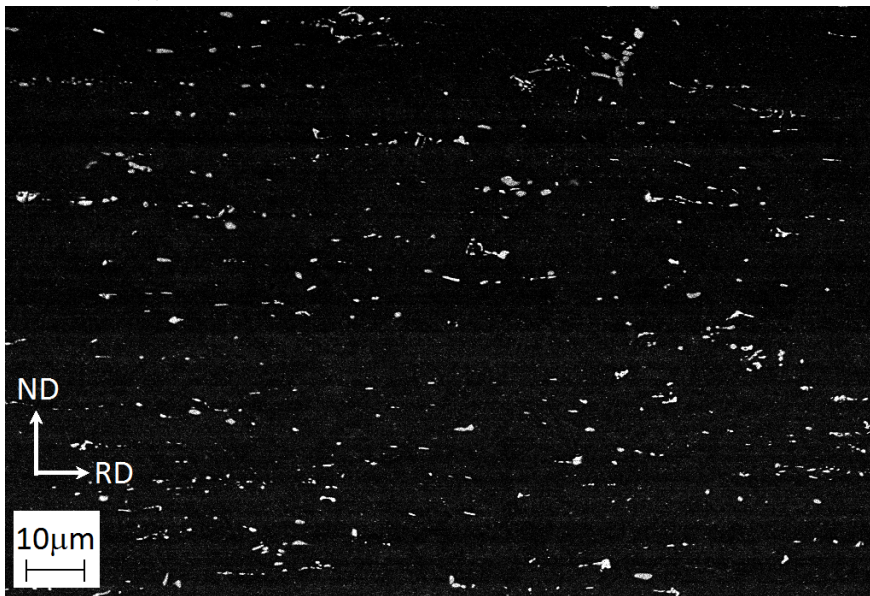
Figure 4.10: Images taken at high magnification show the presence of dispersoids in homogenised PGM and PGN

undergone break up during the deformation. The constituent particles visible seem to have a more rounded appearance and some clustering of particles exists, possibly as a remnant from the previously dendritic constituent distribution. There now also seems to be alignment of constituents in the rolling direction.

The microstructure obtained after further deformation to a reduction of 80% seems



(a) PGN alloy after 52% reduction by hot rolling



(b) PGN alloy after further cold rolling

Figure 4.11: BS-SEM images of the microstructure of PGN after deformation

to show an increased distribution of small equiaxed constituents throughout the matrix. This microstructure, shown in figure 4.11b, also exhibits clear alignment of constituents in the rolling direction, though clusters of particles are still very prominent throughout the sample.

The images presented so far are useful in obtaining qualitative information about the particles within the alloys at each of the described stages of processing (i.e. the presence of dispersoids after heat treatment, the break up of the constituents during deformation). However, the images were obtained using a relatively high accelerating

voltage (15 kV) which translates to a large interaction volume within the sample of up to a micron in depth, meaning that a correction must be undertaken to any results to account for this effect. This also means that any meaningful shape analysis of these particles can not be undertaken with any degree of certainty.

### 4.2.2 3D Analysis - Constituents

After initial runs to determine optimal slice depths and microscope parameters, serial block face scanning electron microscopy was performed on samples of as cast, homogenised and hot rolled (52% reduction) PGN, with the feature desired, slice depth and image resolution shown in table 4.5.

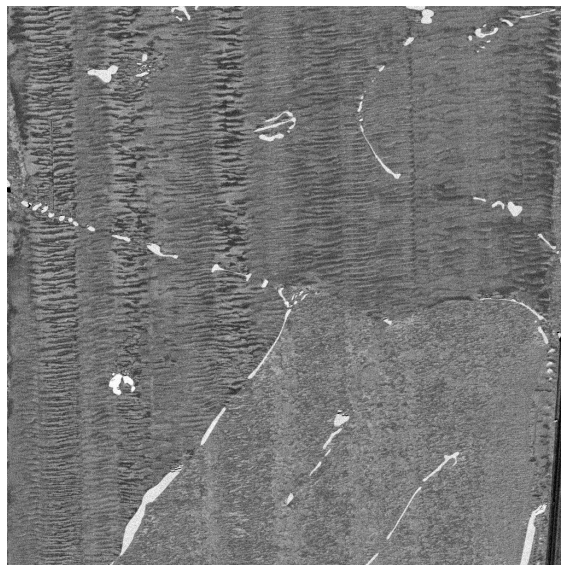
Table 4.5: Samples studied using SBF-SEM

Condition	Feature Studied	Number of Slices	Pixel Size	Slice Depth
As Cast	Constituents	1000	(49 nm) <sup>2</sup>	50 nm
Homogenised	Constituents	1000	(49 nm) <sup>2</sup>	50 nm
Homogenised	Dispersoids	500	(10 nm) <sup>2</sup>	15 nm
Rolled	Constituents	1000	(49 nm) <sup>2</sup>	50 nm
Rolled	Dispersoids	500	(10 nm) <sup>2</sup>	15 nm

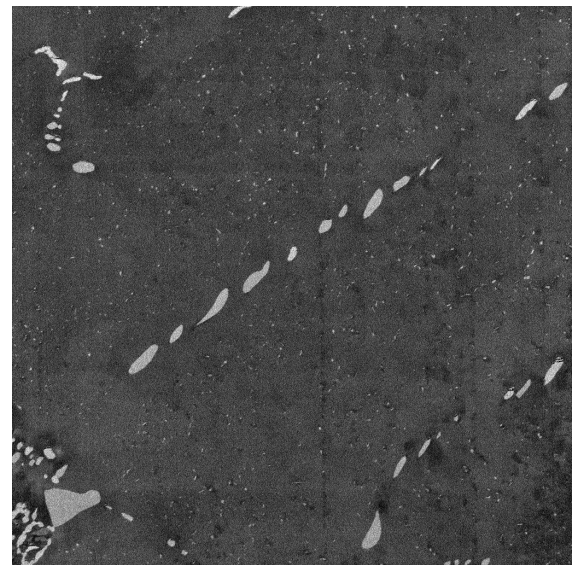
These parameters equate to a volume of  $50.176 \mu\text{m} \times 50.176 \mu\text{m} \times 50.000 \mu\text{m}$  for constituent analysis and  $10.24 \mu\text{m} \times 10.24 \mu\text{m} \times 5.00 \mu\text{m}$  for dispersoid analysis.

An example of the 2D slices produced using this technique are shown in figure 4.12. Surface deformation which stems from the sectioning of the sample is shown in figure 4.12a. In this image, the parallel banded regions, most clearly visible in the top left of the micrograph, demonstrate the impact that the cutting process has on the sample. It is of note that the region on the bottom right of the same image shows much less evidence of deformation. This may be due to each of these two regions having a different crystallographic orientation, resulting in contrasting behaviour during the slicing process. This phenomena is also visible to a lesser extent in the rolled image (figure 4.12c). Due to the destructive nature of this technique, it is impossible to go back and check the orientation of the grains to determine whether this is a crystallographic orientation dependent effect, however this may be something that could be investigated using a sample that has previously been characterised using EBSD.

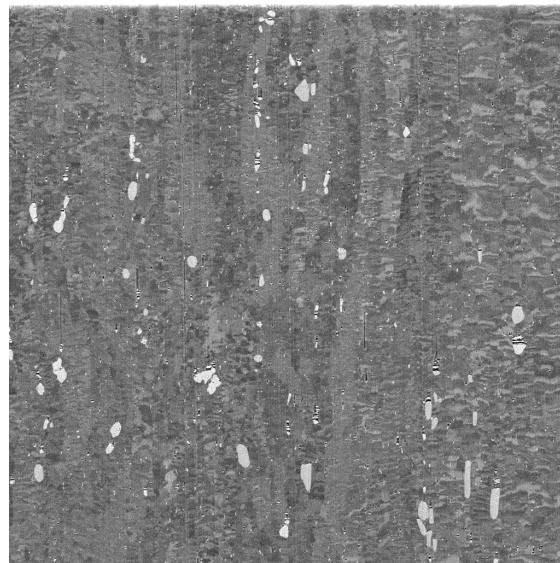
Though this surface deformation is not clear in the homogenised stack example shown in figure 4.12b, it does appear in other regions within the same image stack. This image provides a reference as to the minimal effect that the surface deformation was found to have on the resulting micrograph when using this serial sectioning method.



(a) As Cast



(b) Homogenised



(c) Rolled

Figure 4.12: Raw images obtained using the 3View system for the respective samples of PGN (each image represents an area of  $(51.2 \mu\text{m})^2$ ).

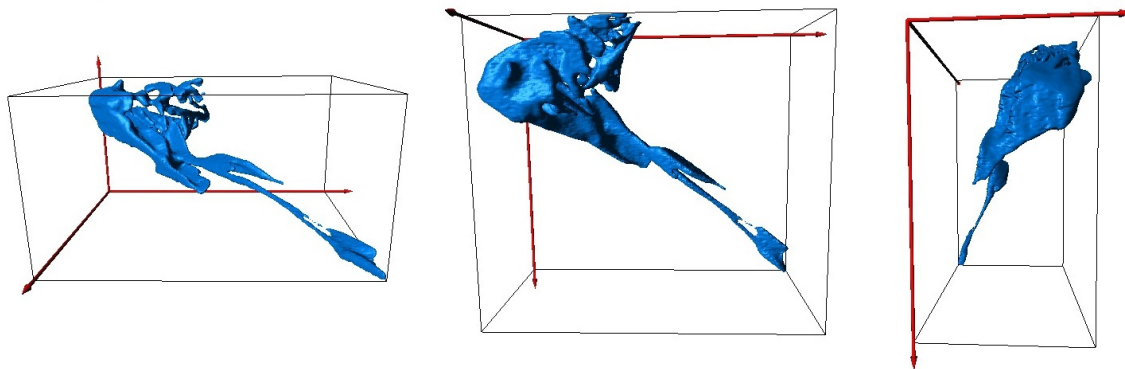


Figure 4.13: Example of visualised particle (taken from ‘as cast’ data set) and the calculated bounding box

Figure 4.13 shows the full 3D structure of one particle which has been investigated using the serial sectioning technique. The particle is shown within the smallest bounding box which would fully contain all of this particle, and would therefore be used for any bounding box dependent measurements. This helps to demonstrate the inaccuracies when using bounding box measurements to represent complex 3D shapes. A selection of the information which can be obtained for each particle within the 3D visualisation is shown in table 4.6.

Table 4.6: Characterisation of Example Particle Shown in 4.13

Measure	Value
Volume (V)	18.172 $\mu\text{m}^3$
Surface Area (S)	140.176 $\mu\text{m}^2$
Int Mean Curvature (M)	1.943 x 10 <sup>6</sup>
Int Total Curvature (K)	-282.743
Length (Longest)	17.045 $\mu\text{m}$
Equivalent Diameter	3.262 $\mu\text{m}$
BaryCenter X	23.535
BaryCenter Y	9.764
BaryCenter Z	3.229
Bounding Box X	13.279 $\mu\text{m}$
Bounding Box Y	6.811 $\mu\text{m}$
Bounding Box Z	12.000 $\mu\text{m}$

The barycentric coordinates within this table refer to the coordinate of the centre of the particle with respect to the entire 3D volume (this particle was taken from a larger volume), whereas all other measures are individual measures.

The 3D data for each of the conditions will be presented individually before comparisons are drawn in a later section.

### As Cast

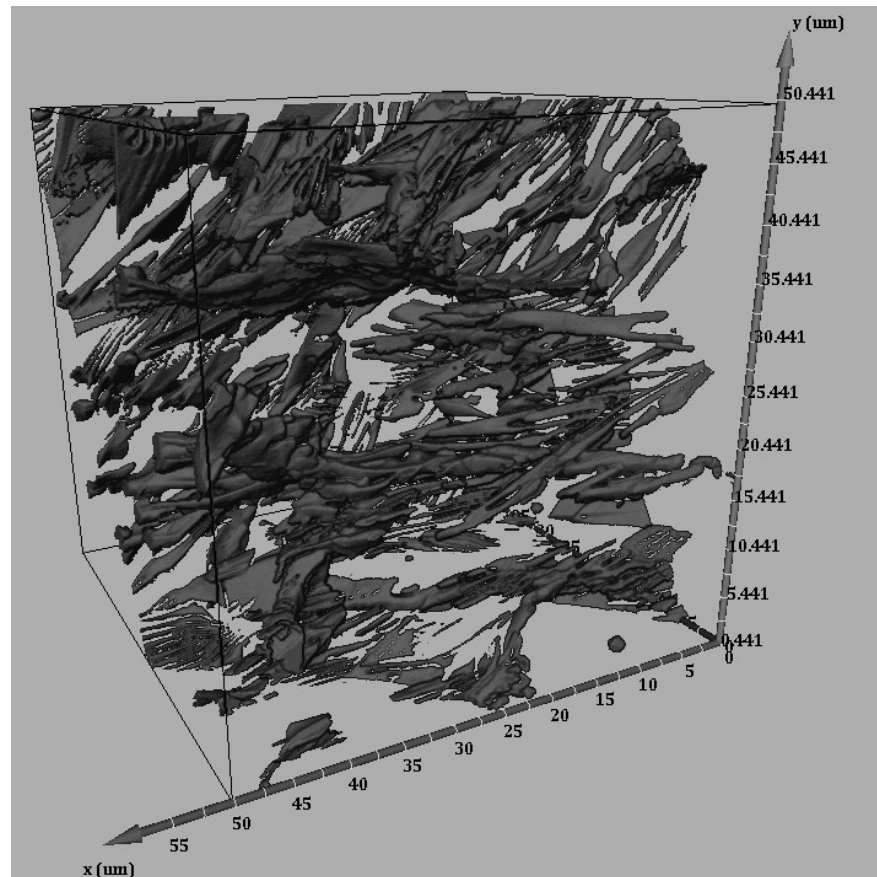


Figure 4.14: Visualised constituent network within the as cast aluminium alloy

The constituents present within the as cast volume are found mainly as a network of interconnected dendritic clusters as shown in figure 4.14. The large constituent clusters seem to have random orientation within the visualised sample, which is typical of eutectic solidification, while smaller rod like particles are found to align with larger particles found nearby. The minimum spacing between the closely spaced parallel constituents has been found to be around  $0.5 \mu\text{m}$  across this sample. Within the visualised region, 1032 separate particles have been characterised that are above a set threshold of an equivalent diameter of  $0.2 \mu\text{m}$ . These particles accounted for 2.4% of the total volume of the sample.

Volume measurements were taken from each of these particles and converted to equivalent diameter measurements as shown in figure 4.15. The number fraction of

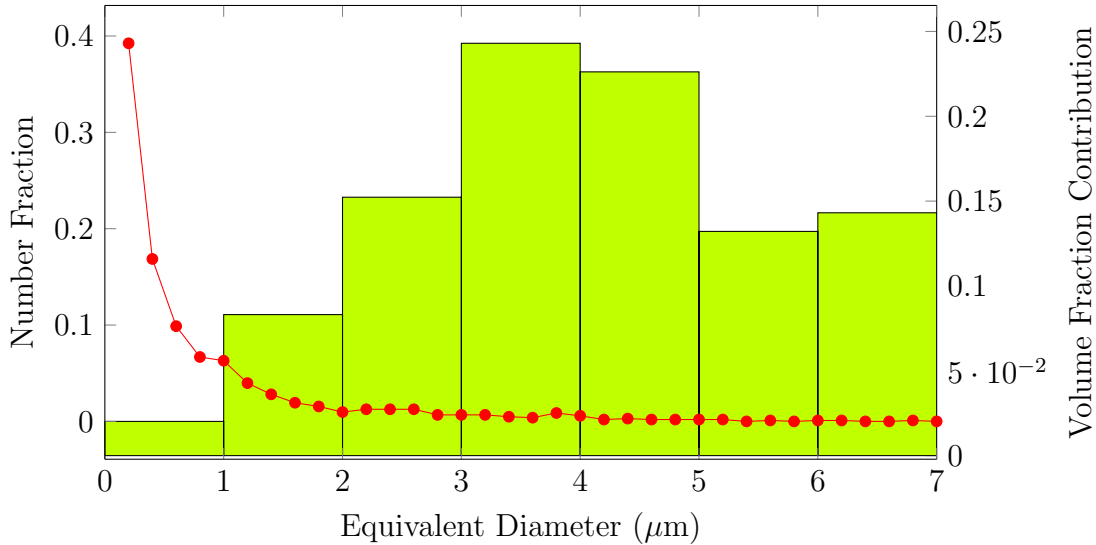


Figure 4.15: Plot showing the number fraction (red) and volume fraction (bar) of particles with a given equivalent diameter in the as cast sample.

constituents of a given equivalent diameter is shown as part of this plot, however, as the number of small particles within this sample dwarfs contribution of the larger particles, simply focussing on number does not give a precise representation of the microstructure. One way to improve upon this is to determine the contribution of each class of particle (grouped by size) to the overall volume fraction of constituent particles. In this sample, it becomes apparent that although over 70% of all particles have an equivalent diameter of less than 1  $\mu\text{m}$ , these particles do not in fact have a large influence when calculating the volume fraction, making up only 2% of the total constituent particle volume within the sample. Conversely, particles measuring between 3  $\mu\text{m}$  and 4  $\mu\text{m}$  make up 24% of the total constituent volume, but account for a mere 3% of particles by number.

Traditionally, particle morphology in three dimensions has been evaluated by first taking two ratios of particle dimensions (thickness/width and width/length, where length > width > thickness) and creating a scatter plot. Using the dimensions of the bounding box of each particle, these ratios have been calculated to produce the Zingg plot shown in figure 4.16. When producing this plot, the particles were grouped by volume (plotted as equivalent diameter) in an attempt to determine whether there was a correlation between particle size and location within the Zingg plot. As is clear from this plot, no such correlation was determined for this dataset.

By taking the ratios of particle dimensions, any information pertaining to how

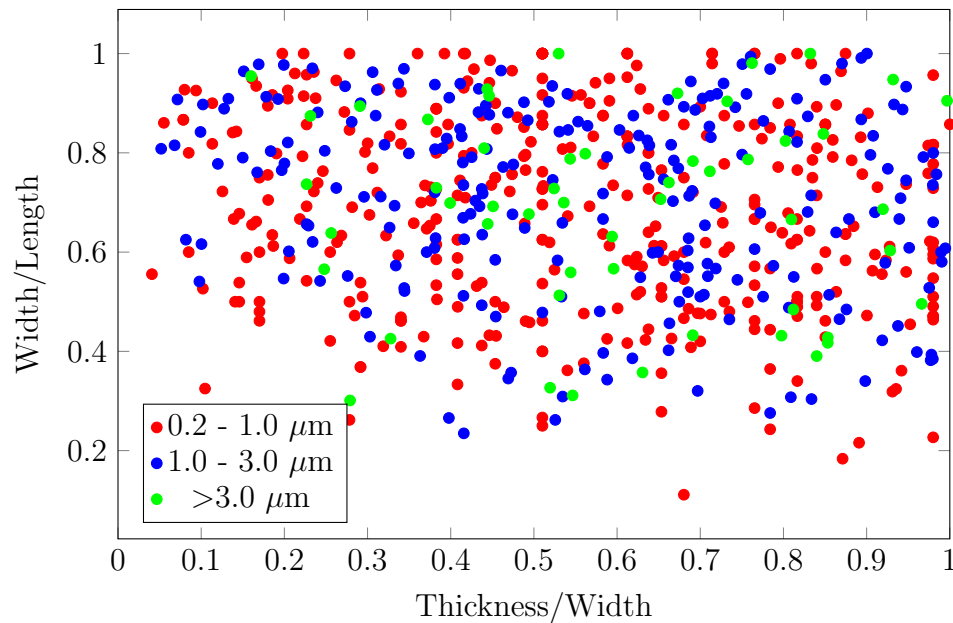


Figure 4.16: Zingg plot of particles found within the as cast visualisation

complex a particle is within the volume is lost. Though simple unconnected 'needle like' structures exist in isolation within the sample, the presence of larger interconnected regions of eutectic are greatly simplified when using this measure. Thus the use of Zingg plots may be unsuitable when analysing complex particle systems such as those found within an as cast microstructure.

As volume data can be used to give an equivalent diameter and the surface area of each particle is known, the sphericity ( $\Phi$ ) of a particle can be determined as shown in figure 4.17a. This allows comparisons of the link between particle size within the volume and its complexity.

The scatter plot shown in figure 4.17a indicates a general trend that as particle size increases, the overall structure of the particle becomes more complex (thus the sphericity decreases). Within this sample, high sphericity values ( $\Phi \geq 0.75$ ) are generally found in particles with an equivalent diameter of no more than  $1.5 \mu\text{m}$ , with only the smallest particles within the sample approaching a sphericity value of 1.

Figure 4.17b shows the number fraction and volume fraction contribution of the particles, grouped by the particle sphericity parameter. It is clear from this plot that although the number fraction of particles may be dominated by the more simple and spherical particles, it is the complex particles which have the larger influence on the volume fraction of constituents. As the small particles correspond to a comparatively

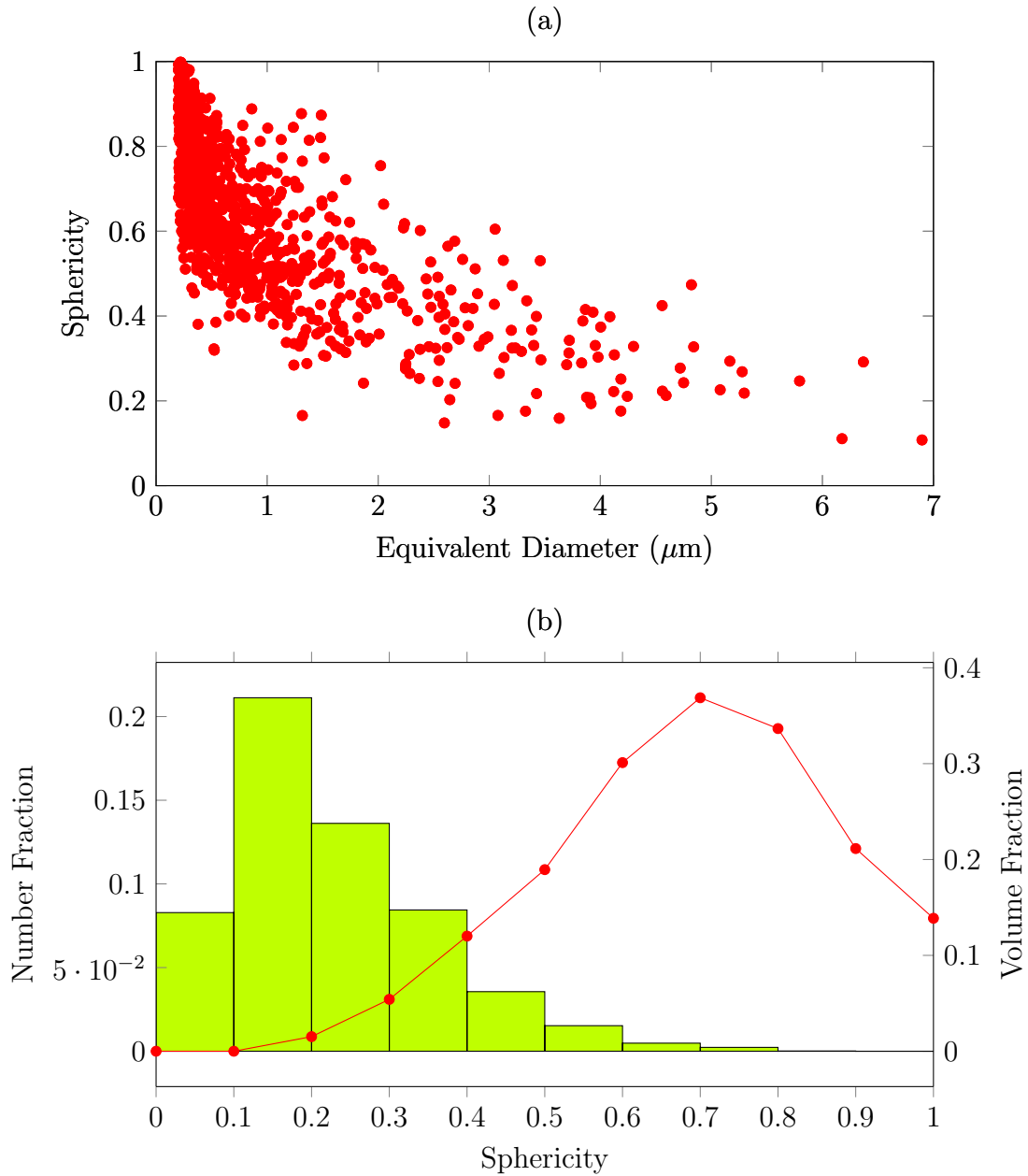


Figure 4.17: (a) Scatter plot showing the general relationship between the sphericity of the particles within the as cast volume and their size. (b) Plot showing the number fraction (red) and the volume fraction (bar) of particles grouped according to their sphericity

small number of voxels within the volume, it would not be possible for the particles to be classified as anything other than almost spherical due to the fact that they are simply not large enough to contain features that would greatly alter their surface area. It follows that the larger particles can be formed of more complex structures within the volume.

Parallels can be drawn here with particle size measurements, as again, the small number of large particles can also skew the sphericity profile of a sample when the volume fraction of constituents is used as a measure rather than the number fraction.

The barycentric coordinates of all particles and the measured distances between these barycentric points were measured to determine all interparticle distances within the volume. The closeness measures developed in section 4.1 such as  $C_i$  and  $C_i^W$  were found for this population and scatter plots were produced to demonstrate how each of the closeness measures described earlier apply to each constituent within the as cast sample. These are shown in figure 4.18. The scatter plots demonstrate that larger particles within the volume do not have the largest closeness values. This is most notable in 4.18a as only particles under  $3 \mu\text{m}$  have closeness values larger than 3. As there is a sharp decline of closeness with increasing distance, the correction for interparticle distance included in  $C_i'$  may provide a more adequate measure when calculating closeness in large particles. The new scatter plot when using this measure is shown in figure 4.18b. The incorporation of this corrected interparticle distance measure results in much higher values of closeness overall, whilst shifting the population so that the difference in closeness between larger and smaller particles is reduced. The added weighting introduced in 4.18c, which reduces any contribution to closeness from small particles while boosting contributions from larger particles reduces the closeness of the population as a whole. By incorporating these corrections for particle size, closeness values of particles with an equivalent diameter above  $3 \mu\text{m}$  are no longer dwarfed by those of small particles.

In real terms, the scatter plot in figure 4.18a simply illustrates that the centre points of the smaller particles are calculated to be generally closer to the centre points of their neighbouring particles than the larger constituents are. However, this is also expected to be true for any randomly constructed sample and does not provide a great deal of insight into the population as a whole. It is only by taking edge to

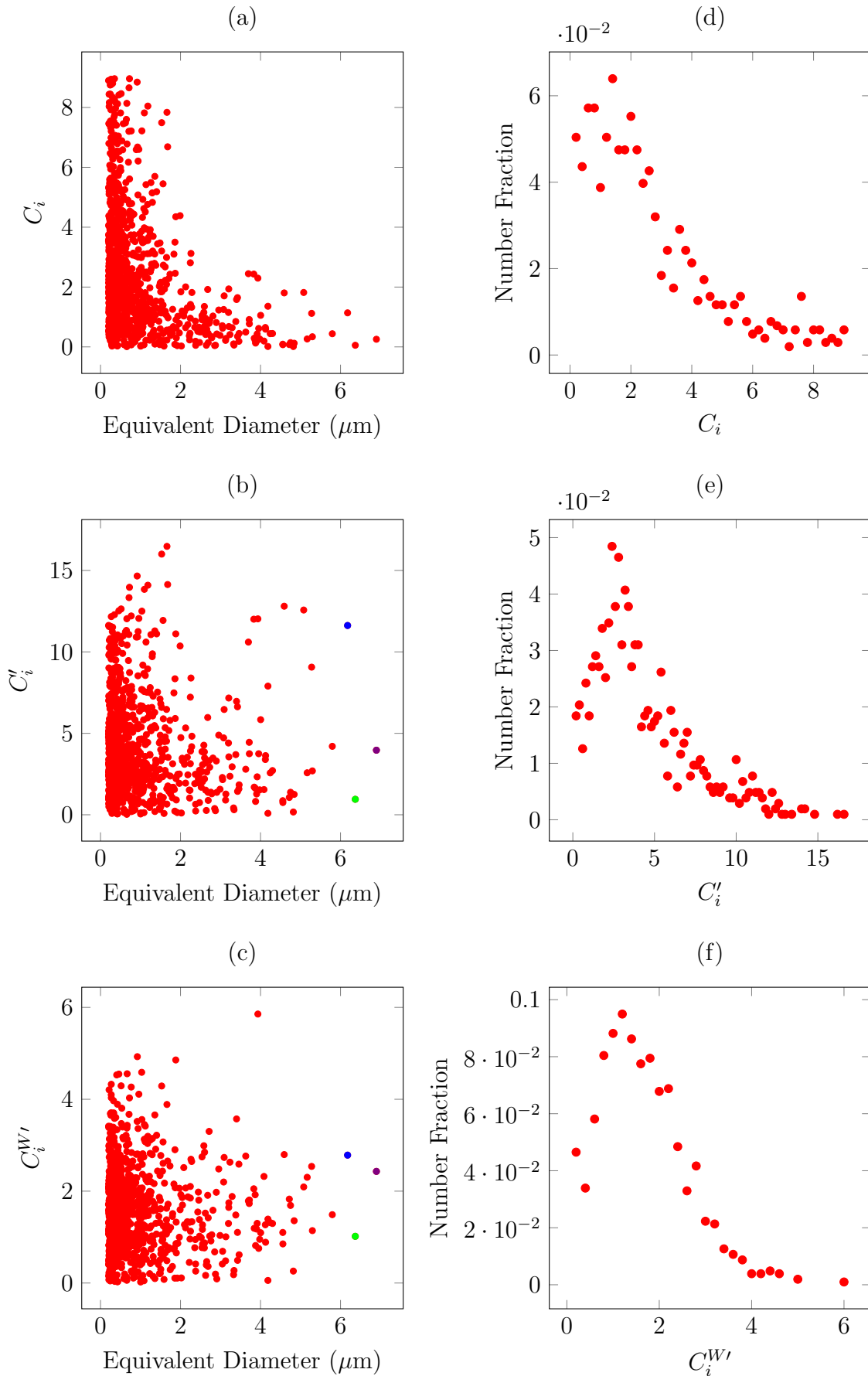


Figure 4.18: Scatter plots generated illustrating the (a) raw, (b) distance corrected and (c) weighted closeness of constituents in the as cast alloy, with (d-f) their corresponding closeness distributions. Three data points are coloured independently for later comparison

edge measurements, such as those incorporated into figure 4.18b (using the equivalent diameter estimate), that comparisons can start to be drawn between the closeness values of different particles sizes.

When removing the equivalent radii from  $d_{ij}$  to get a closer estimate to the true interparticle distance, discrepancies were noted where the function included a negative value of  $d'_{ij}$ . As this mathematical anomaly was expected due to the use of equivalent diameter measurements on non spherical particles, these occurrences were omitted from the final population of values. From the earlier sphericity measurements, it is clear that it is the particles with the most mass that tend to have the most complex morphologies within the volume. Because of this, there is an increasing amount of error associated with using  $d'_{ij}$  as the particles of interest become larger. For this reason, improvements in determining the interparticle distance using edge to edge measurements of the visualised particle surfaces would be the next logical step in improving the method of determining closeness. This inherent error will be reduced with an increasing population sphericity.

The weighting of the closeness with respect to the size of the neighbouring particle, as illustrated in figure 4.18c allows the direct visualisation of the extent of clustering within the volume. In this case, it can be seen that there are three particles within the volume of equivalent diameters greater than  $6 \mu\text{m}$ , and of these, two have similar weighted closeness values. These points have been coloured separately for clarity. By comparing the values of  $C'_i$  and  $C_i^{W'}$  for these larger particles, it becomes clear that the particle indicated by the blue mark on the scatter plot is adjacent to smaller particles than the green or purple constituents. The act of weighting the closeness function using the size of the neighbouring particles acts to provide a much smoother closeness profile, whilst also tightening the distribution of values as shown in figures 4.18d, 4.18e and 4.18f.

Mean and standard deviation measurements taken from the distributions of closeness from the as cast dataset and are shown alongside calculated measures for each of these values using a randomly computed dataset<sup>3</sup> in table 4.7.

These values show that the particles are not randomly distributed throughout the

---

<sup>3</sup>The calculated closeness values ( $C_i$ ) were obtained by populating a volume of  $50.176 \mu\text{m} \times 50.176 \mu\text{m} \times 50 \mu\text{m}$  with 1032 particles. The coordinates were determined using a random number generator. Experimentally obtained particle size measurements were applied to the randomly placed particles.

Table 4.7: Parameters from As Cast Closeness Distributions

Closeness Type	Measure	Observed	Calculated	Ratio (Q)
$C_i$	Mean	2.50	0.52	4.80
	Standard Deviation	2.03	0.26	7.79
$C'_i$	Mean	3.90	0.97	4.03
	Standard Deviation	2.82	0.54	5.18
$C_i^{W'}$	Mean	1.55	0.58	2.69
	Standard Deviation	0.92	0.46	1.98

sample, with  $Q$  values greater than 1 for all methods of calculating closeness. The standard deviation of the closeness of particles within characterised sample is much greater than that of a volume containing randomly distributed particles, confirming that the population of particles is also not ordered. The incorporation of a corrected interparticle distance reduces the ratio of mean values closeness measurements within the random population are more drastically altered than those in the measured sample. This shift also acts to reduce the differences in the spread of closeness values. The fully weighted approach acts to reduce both mean values while narrowing the distribution further, though differences between calculated and experimental closeness remain, indicating that clustering is present within the sample.

Overall, the volumetric study of particles within the as cast volume has shown a high proportion of small, simple particles which dominate number fraction measurements. Larger, more complex particles are small in number throughout the volume, but these interconnected regions of eutectic account for a high percentage of the total mass of second phase within the volume. By measuring closeness of these particles, it was determined that the particles are not randomly interspersed throughout the volume, but are instead clustered.

### Homogenised

The interconnectivity of constituent particles is greatly reduced after homogenisation as shown in the visualisation of the volume in figure 4.19. Here, rounding of the intermetallics (spheroidisation) is evident. The spacing between parallel constituents has also increased after heat treatment, and is now measured to be closer to  $0.8 \mu\text{m}$ . This has been attributed to the of partial dissolution of the eutectic particles. Within

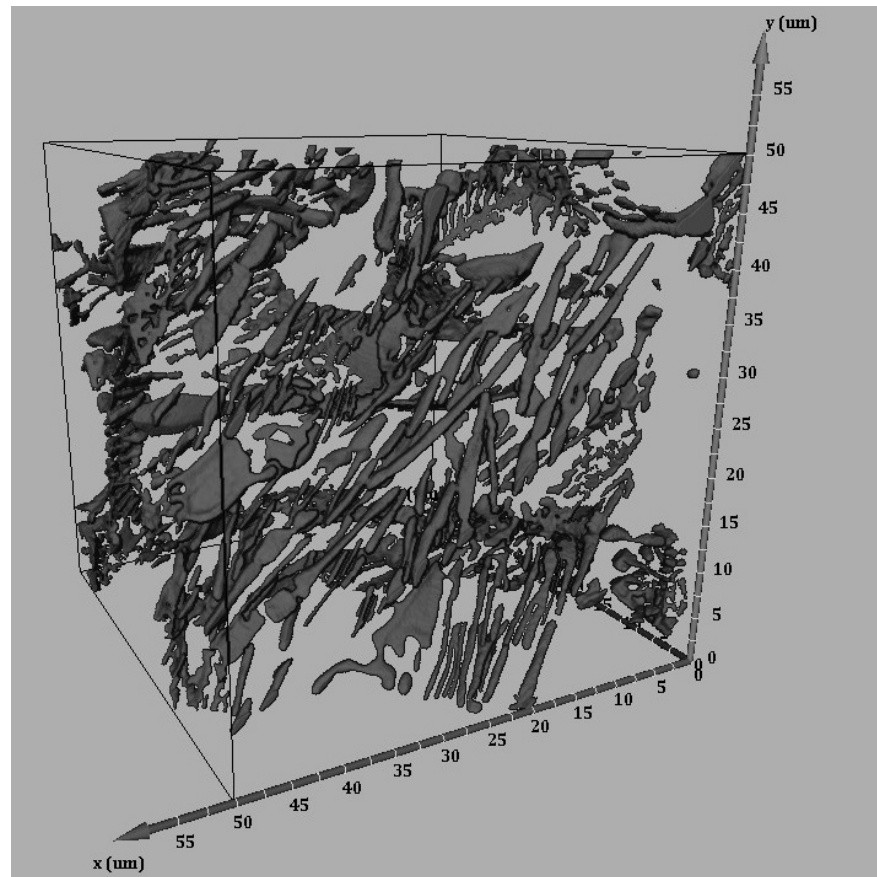


Figure 4.19: Visualised constituents within the homogenised aluminium alloy

the visualised homogenised sample, 1416 particles were found above the minimum threshold equivalent diameter value, accounting for 1.8% of the total volume of the sample. It is expected that this cut off also removes any newly nucleated dispersoids from analysis with the constituent particles. The distribution of particle volumes within the sample is shown in figure 4.20.

Within the homogenised sample, the majority of the second phase particle mass was found to be within a small number of particles with equivalent diameters of 2-4  $\mu\text{m}$ . Like the as cast volume, the majority of particles within the volume are found to be much smaller, with approximately 50% of all particles having an equivalent diameter between 0.2 and 0.5  $\mu\text{m}$ .

The sphericity of constituents within this sample and the resulting number and volume fraction profiles are shown in figures 4.21a and 4.21b. Again, the volumetric data shows that particle sphericity tends to decrease with equivalent diameter, while the number fraction is dominated by smaller, close to equiaxed particles.

A plot showing how closeness changes with increasing particle size is shown in figure

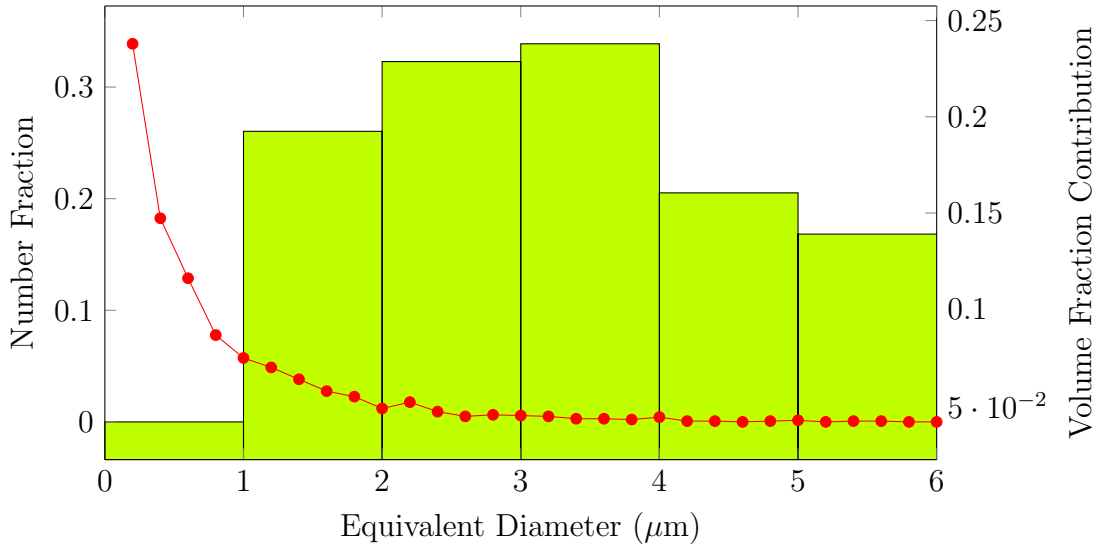


Figure 4.20: Plot showing the number fraction (red) and volume fraction (bar) of particles with a given equivalent diameter in the homogenised sample.

4.22a. The large closeness values attributed to small particles when only barycentric coordinates are used in the closeness calculation are still prominent in the homogenised sample. Overall, the resulting closeness values are much higher than those found within the as cast sample, suggesting the distribution of particles is more clustered. However, the increase in the number of particles within the volume compared to the as cast sample would immediately act to increase the number of terms within the sum used to produce the closeness value, leading to larger values of closeness without requiring any changes to particle distribution. The distribution associated with these closeness values is shown in 4.22d. In this case, the increase in closeness is found to be much greater from the expected increase due to a more densely populated region.

The correction for interparticle distance in figure 4.22b acts to amplify the closeness values of all particles within the volume. From the scatter plot, this is most noticeable when comparing the closeness values of the large particles. This correction also acts to increase the spread of closeness values as illustrated in figure 4.22e. This distribution is similar to that constructed from the as cast data, though the  $C'_i$  value for each individual particle is larger on average for the homogenised sample. The presence of very close particles may be due to the break up of one large particle during homogenisation which leads to two distinct intermetallics remaining in close proximity. Examples of this would create large contributions to the closeness measure of a particle.

Weighting due to neighbouring particle size, incorporated in figures 4.22c and 4.22f

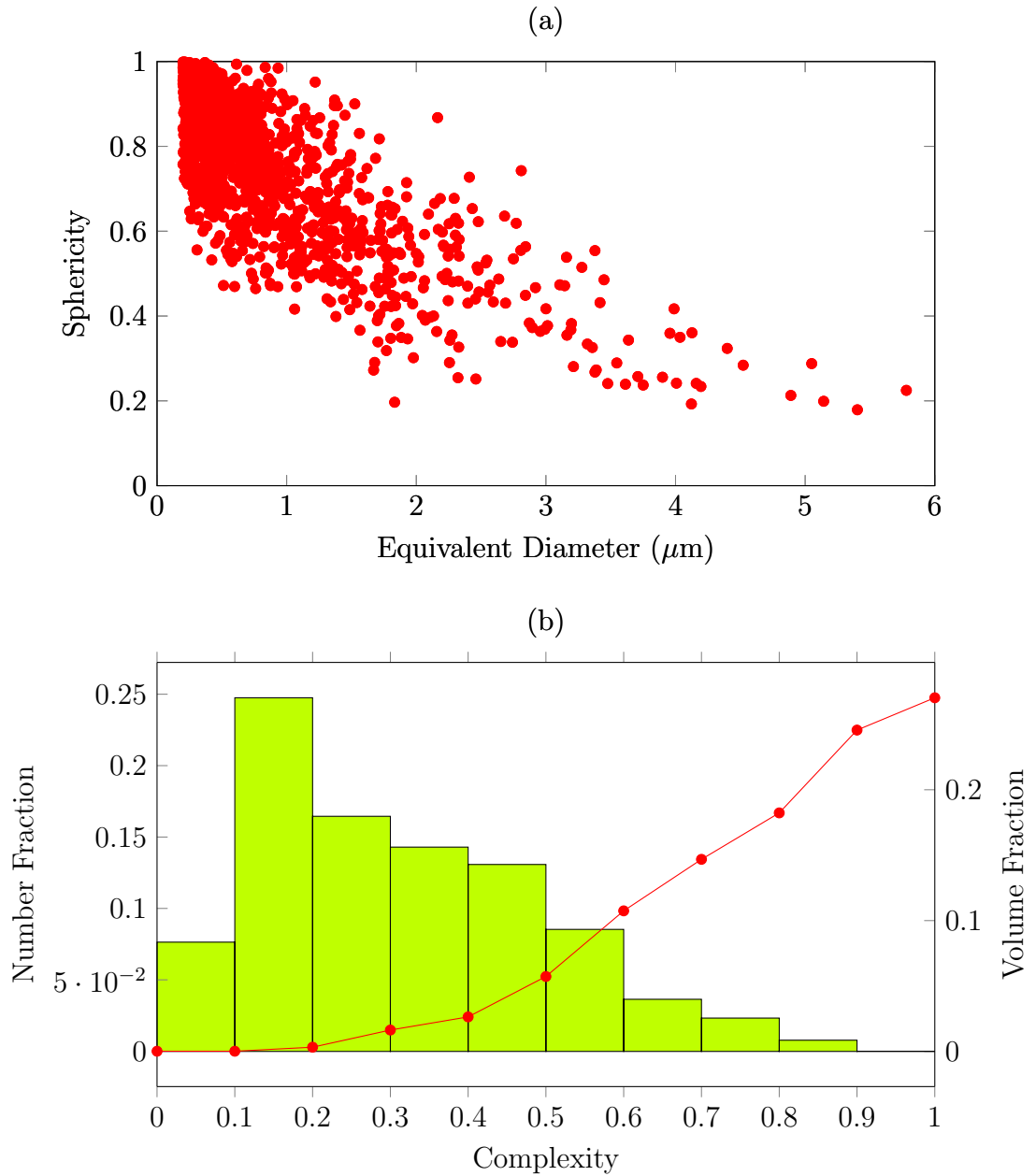


Figure 4.21: (a) Plot showing the general relationship between the sphericity of the particles within the homogenised volume and their size. (b) plot showing the number fraction (red) and the volume fraction (blue) of particles grouped according to their sphericity

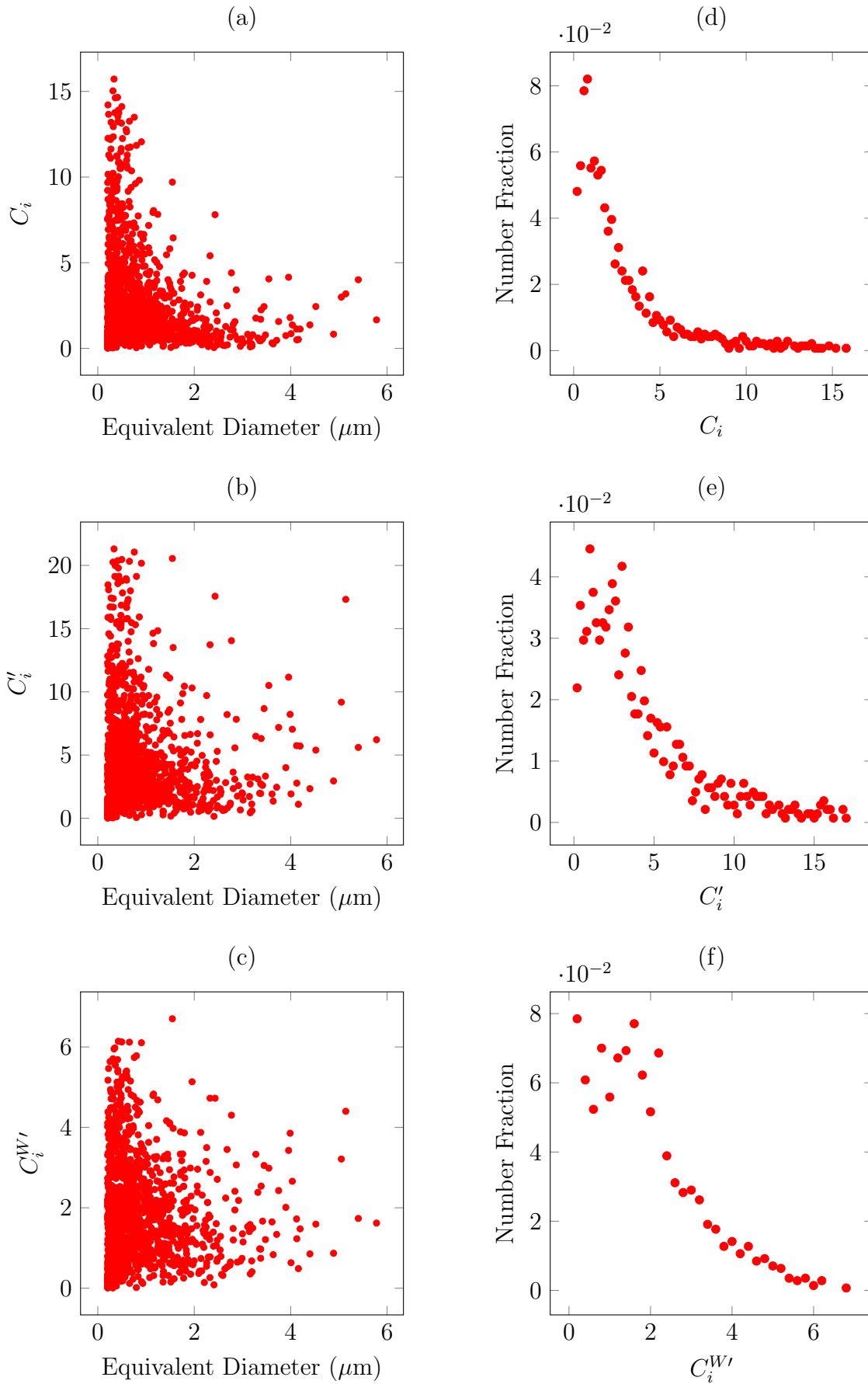


Figure 4.22: Scatter plots generated illustrating the (a) raw, (b) distance corrected and (c) weighted closeness of constituents in the homogenised aluminium alloy, with (d-f) their corresponding closeness distributions

acts to reduce the overall spread of closeness across the sample.

Table 4.8: Parameters from Homogenised Closeness Distributions

Closeness Type	Measure	Observed	Calculated	Ratio (Q)
$C_i$	Mean	2.64	0.72	3.65
	Standard Deviation	2.77	0.31	9.00
$C'_i$	Mean	4.27	1.29	3.32
	Standard Deviation	4.00	0.62	6.42
$C_i^{W'}$	Mean	1.75	0.66	2.65
	Standard Deviation	1.27	0.42	3.02

Numerical analysis of the closeness values of the homogenised sample is presented in table 4.8. From this table, all measures of closeness indicate that there is distinct clustering of particles within the volume. These values also confirm that there is a much wider distribution of closeness values within the homogenised dataset, much more than is calculated by randomly populating the same size volume with particles with the same distribution of particle sizes. The higher values of closeness obtained suggest very closely spaced particles within the microstructure.

Overall, the volumetric study of particles within the homogenised alloy volume has shown that although large particles are present within the microstructure, they are rounded and more spherical after heat treatment. A large population of small, simple particles remains in the matrix after heat treatment. The population shows strong signs of clustering when a distance map is constructed, and the closeness values obtained strongly suggest regions of very closely spaced particles within the volume, possibly an outcome of the break up of a larger particle during homogenisation.

### Hot Rolled

The particles found within the hot rolled sample are shown in figure 4.23. In this image, the rolling axis is oriented vertically (along the y axis), and it is clear that the alignment of particles suggested in 2D analysis (figure 4.11a) can be confirmed. The complex eutectic network found before deformation is no longer present, with much simpler constituent particles now found within the volume. This particle break up resulted in analysis of the volume returning 2693 individual particles above the threshold of  $0.2 \mu\text{m}$ , which accounted for 1.2 % of the total volume analysed.

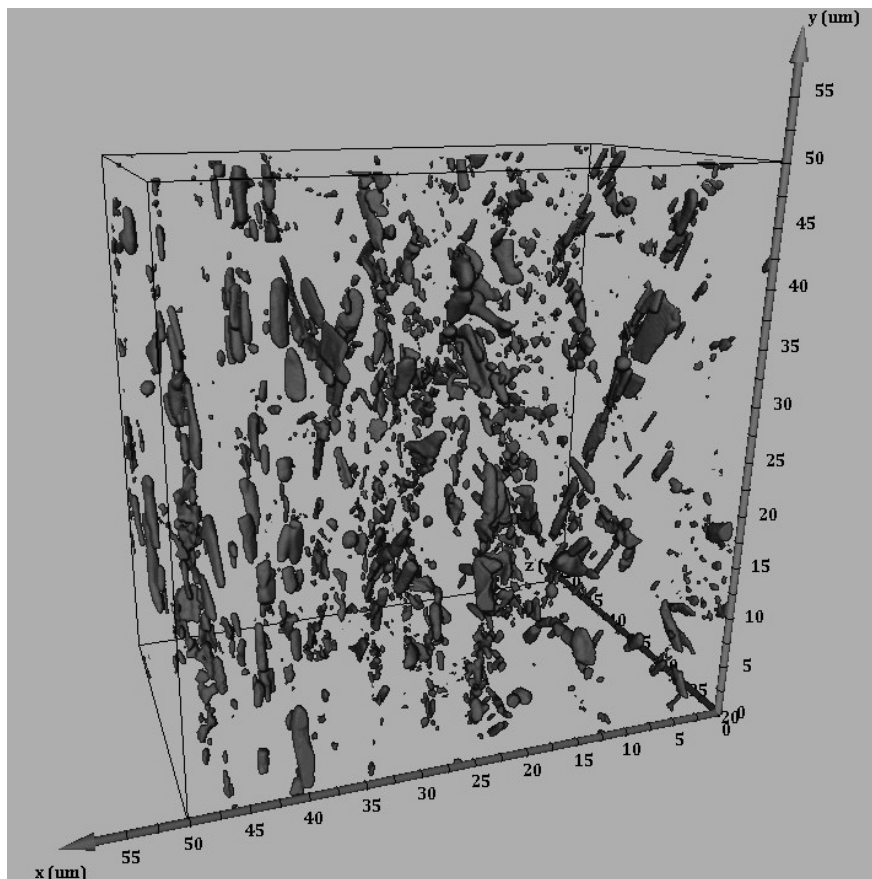


Figure 4.23: Visualised constituents within the hot rolled aluminium alloy ( $x = \text{ND}$ ,  $y = \text{RD}$ ,  $z = \text{TD}$ )

Well over 50% of the particles analysed within the rolled sample were found to have an equivalent diameter of less than  $0.5\mu\text{m}$ , with 78% of the particles classed as submicron in terms of equivalent diameter, as shown in figure 4.24. These  $0.2\text{-}1.0\mu\text{m}$  particles account for just under 14% of the total mass of measured particles within the volume, while only 4% of that mass existing in particles over  $3\mu\text{m}$ .

The sphericity measurements shown in figure 4.25a show a the link between a high sphericity value and small particle size, while the plot in figure 4.25b illustrates that the main mass of the particles is found within particles that have a sphericity value of between 0.4 and 0.7.

Closeness values are again presented for this particle population in figure 4.26. Again, the particles with highest closeness values are found to be amongst the smallest particles in the volume when only particle coordinates are used (4.26a). This trend is initially suppressed with the equivalent diameter correction, increasing all values of closeness, but more drastically affecting the result for larger particles (4.26b). The

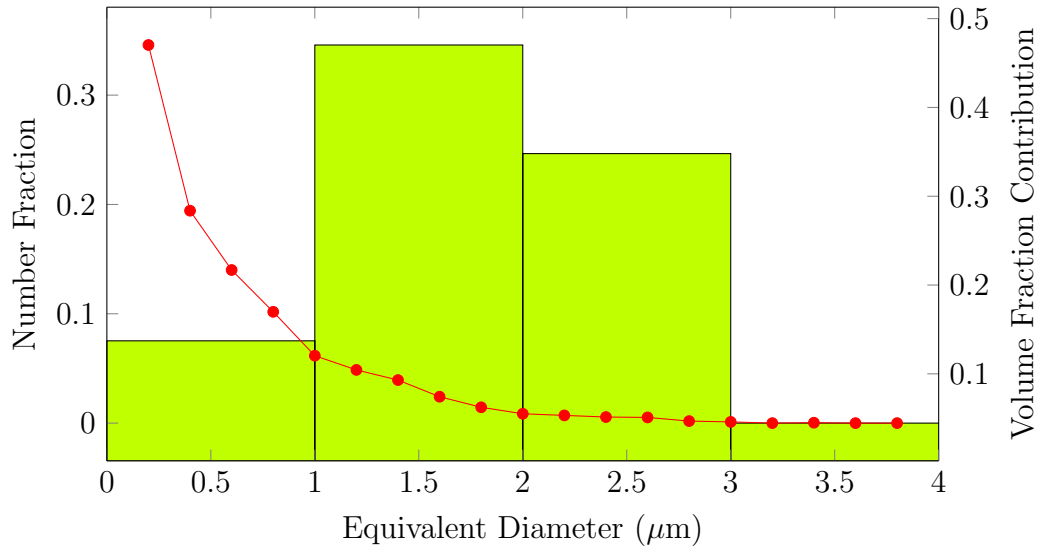


Figure 4.24: Plot showing the number fraction (red) and volume fraction (bar) of particles with a given equivalent diameter in the rolled sample.

trend is reversed when the size of contributing particles is considered, with the largest particles in the volume calculated to have the highest closeness measure (4.26c). The distributions plotted alongside these scatter graphs in figure 4.26d-f were used to obtain values in table 4.9.

Table 4.9: Parameters from Rolled Closeness Distributions

Closeness Type	Measure	Observed	Calculated	Ratio (Q)
$C_i$	Mean	2.45	1.41	1.74
	Standard Deviation	1.59	0.50	3.20
$C'_i$	Mean	3.90	2.31	1.68
	Standard Deviation	2.37	0.90	2.63
$C_i^{W'}$	Mean	1.42	0.93	1.53
	Standard Deviation	0.79	0.43	1.84

The average closeness value within the rolled sample is higher than that of a calculated random sample, suggesting that some clustering is present within the volume. One noteworthy point in this table is that the act of correcting the interparticle distance and weighting the calculation using neighbour size, does not greatly alter the value of  $Q$  obtained using the mean values. The difference in standard deviation values however is more prominent due to the two corrections acting to reduce the overall spread of closeness values.

The 3D study of constituents in the hot rolled sample has shown a population

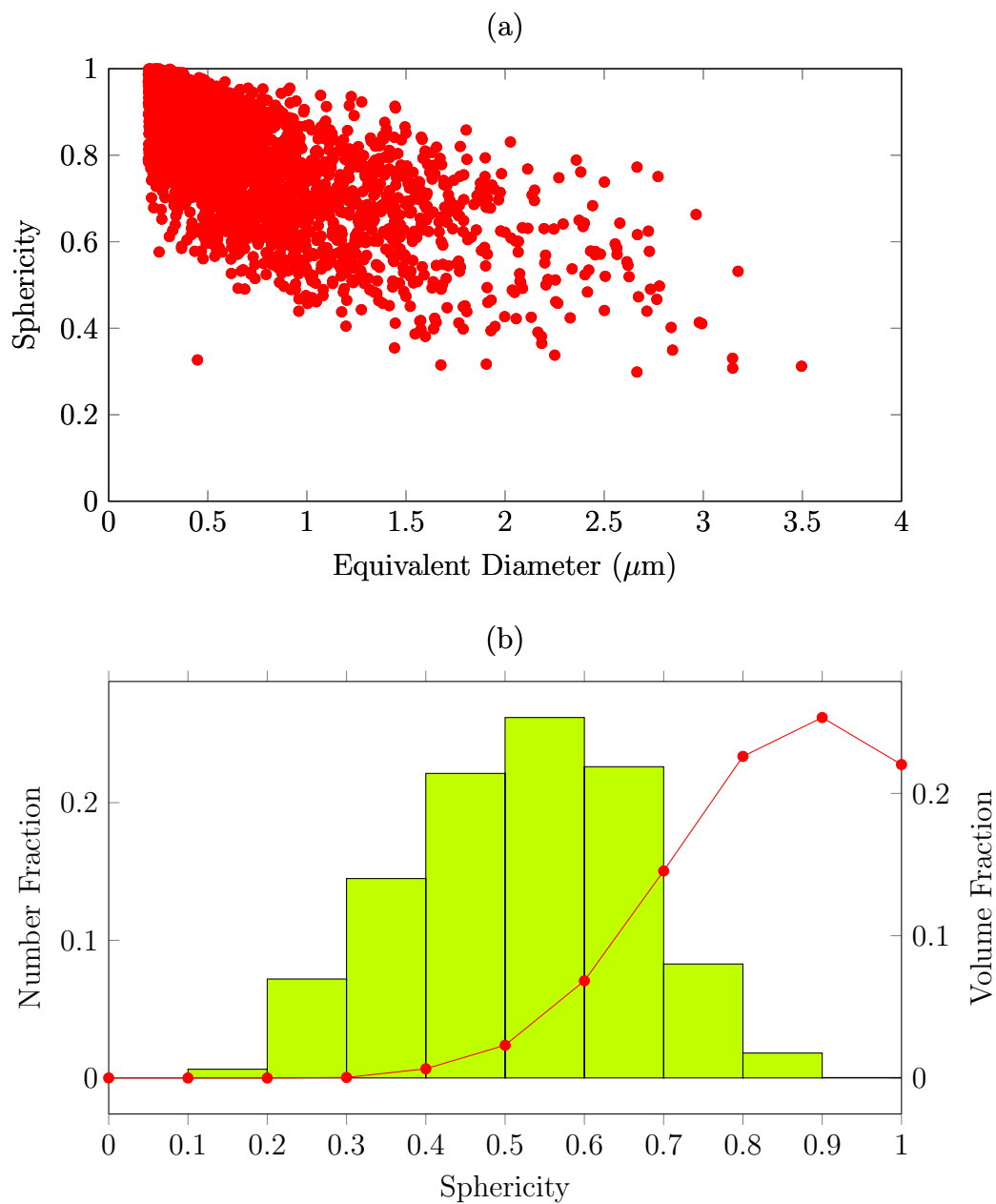


Figure 4.25: (a) Plot showing the general relationship between the sphericity of the particles within the rolled volume and their size. (b) plot showing the number fraction (red) and the volume fraction (blue) of particles grouped according to their sphericity

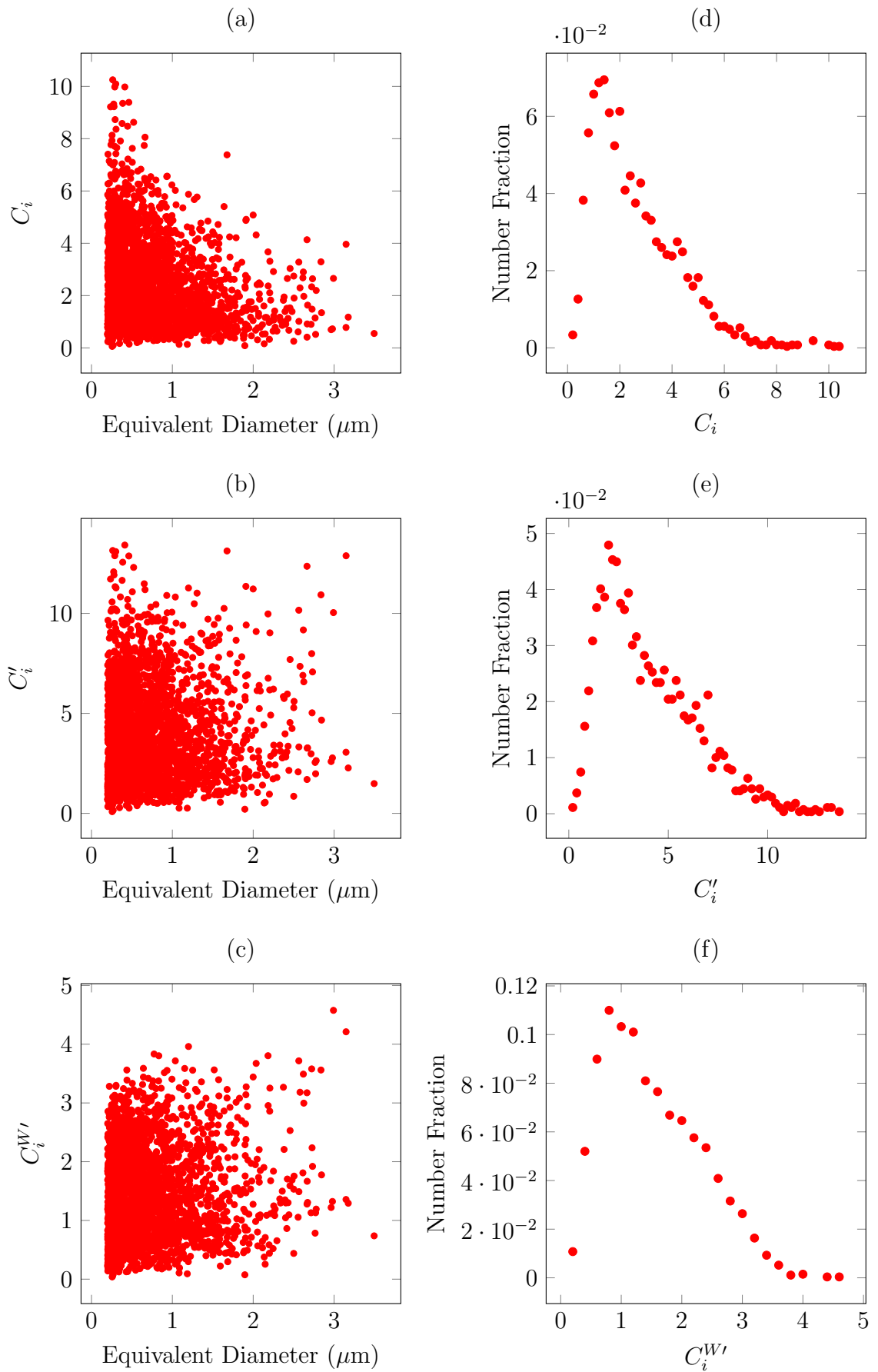


Figure 4.26: Scatter plots generated illustrating the (a) raw, (b) distance corrected and (c) weighted closeness of constituents in the hot rolled aluminium alloy, with (d-f) their corresponding closeness distributions

containing a large number of particles per unit volume that are generally simple, and seemingly well distributed throughout the matrix. Closeness measures have shown that these particles exhibit some degree of clustering.

### Comparing 3D Volumes

The measured volume fractions and number of separately identified particles are shown in table 4.10. From this table, it is clear that as processing advances, the number of particles above the threshold limit increases, while the total volume of constituents measured decreases overall.

Though the dissolution and break up of the eutectic phase is expected, the extent of the reduction in volume fraction of second phase in these samples is high. However, the measurements included at this scale do not incorporate any contribution that dispersoid particles may have to the volume fraction of second phase material. Measures of dispersoid volume fraction are included in the high resolution datasets in the following section.

Table 4.10: Number of Constituent Particles above the Threshold Size

Condition	Number of Constituents	Volume Fraction
As Cast	1032	0.02389
Homogenised	1416	0.01842
Rolled	2693	0.01157

Figure 4.27a illustrates how an increasing volume fraction of the second phase is due to smaller constituents as processing continues. The comparison of particle size measurements shows that the biggest change in size distributions occurs during the hot rolling of the aluminium sample, with a shift from 50% of the second phase contained within particles larger than  $3 \mu\text{m}$ , to less than 5% after deformation, with the biggest proportional increase in the population of particles with an equivalent diameter of between 1 and  $2 \mu\text{m}$ . The maximum particle size within the volume is categorised as having an equivalent diameter which is  $1 \mu\text{m}$  smaller after homogenisation, and a further  $2 \mu\text{m}$  smaller after deformation.

This volume fraction data for each of the constituent populations was fit to the general model Weibull curve (included as equation 4.7) and the parameters for the

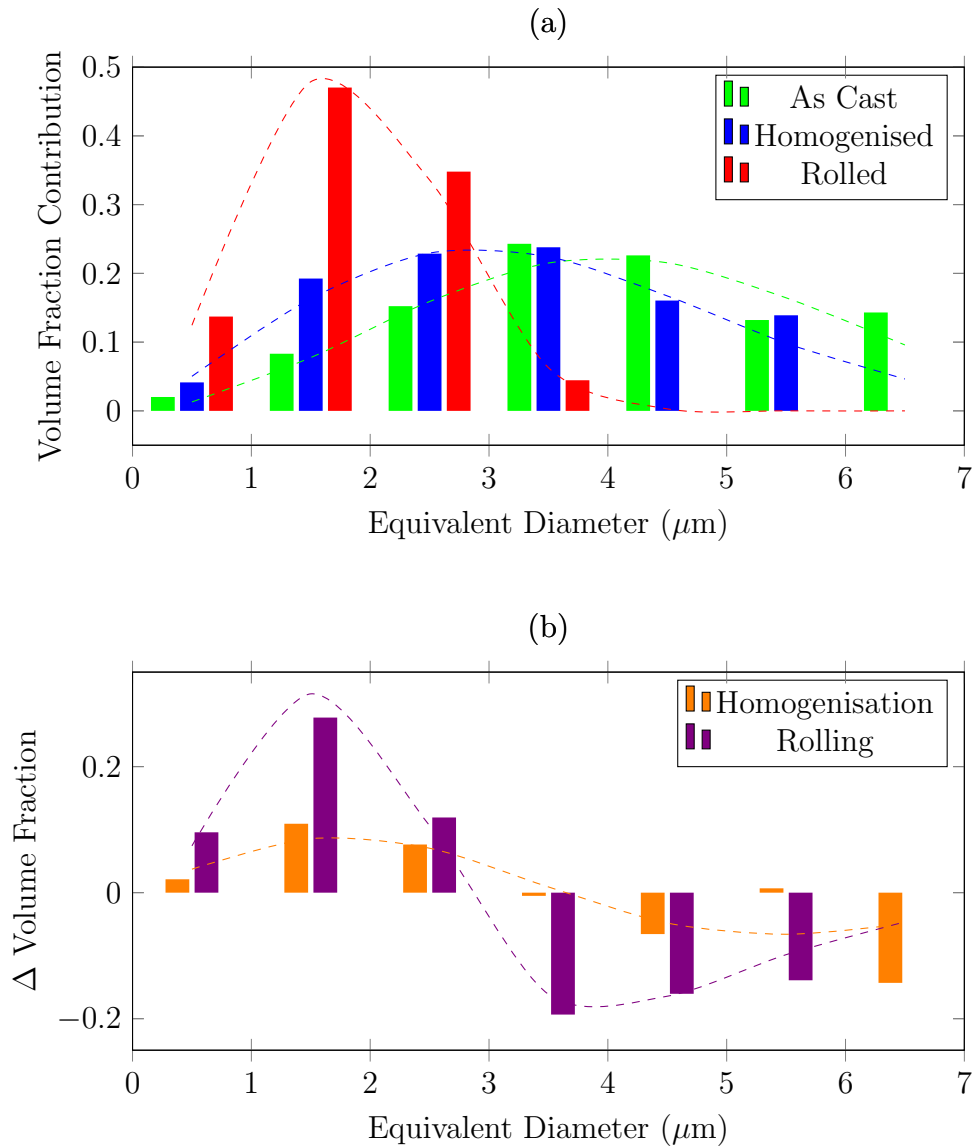


Figure 4.27: Plot showing the change in volume fraction contribution of each constituent size during processing. The dotted lines show the path of the fitted Weibull curves.

resulting curves are listed in table 4.11 along with the r-squared values. These curves are included in figure 4.27a.

$$VF_x = \lambda \cdot k \cdot x^{k-1} e^{-\lambda x^k} \quad (4.7)$$

where:

$VF_x$  = Volume Fraction of  $x$

$\lambda$  = Scale Parameter

$k$  = Shape Parameter

Table 4.11: Weibull Coefficients and Fit Data for Constituent Size Distributions

Sample	Scale Parameter ( $\lambda$ )	Shape Parameter ( $k$ )	r-squared
As Cast	0.0155	2.666	0.8797
Homogenised	0.0528	2.178	0.8920
Rolled	0.1483	2.589	0.9936

By taking the difference between the curves produced for the populations of the as cast and homogenised constituents, a new secondary curve was created which acts to model the difference in the population of constituent particles as a result of the homogenisation process. In general, these difference curves are created as:

$$\Delta VF = VF_{\text{final}} - VF_{\text{initial}} \quad (4.8)$$

where:

$\Delta VF$  = Change in Volume Fraction

$VF_{\text{final}}$  = Equation of Resulting Particle Distribution

$VF_{\text{initial}}$  = Equation of Initial Particle Distribution

This homogenisation curve has been included in figure 4.27b, alongside a similar curve produced to demonstrate the effect of rolling, and the calculated effects of the two processes taken directly from the experimental data. As the equations of these curves are relatively simple, they could be used to modify a known population of as cast constituents in a similar alloy to estimate the effects of homogenisation and rolling on the particle size distributions.

The homogenisation and rolling curves have been used to modify the constituent populations from the experimentally measured samples as shown in figure 4.28. The true values obtained for the homogenised sample are shown with the ‘homogenisation adjusted’ as cast population in figure 4.28a. This plot illustrates that the equations produced from the Weibull curves produce reasonable estimates for the volume fraction values for the particles ranging from 0.2 to 5  $\mu\text{m}$ , though deviations occur in the populations of larger particles. A similar process has been undertaken in figure 4.28b, which illustrates how the true rolling volume fraction distribution differs from those generated by modifying other populations. Again, it is the populations of the smaller particles which seems to be more accurate.

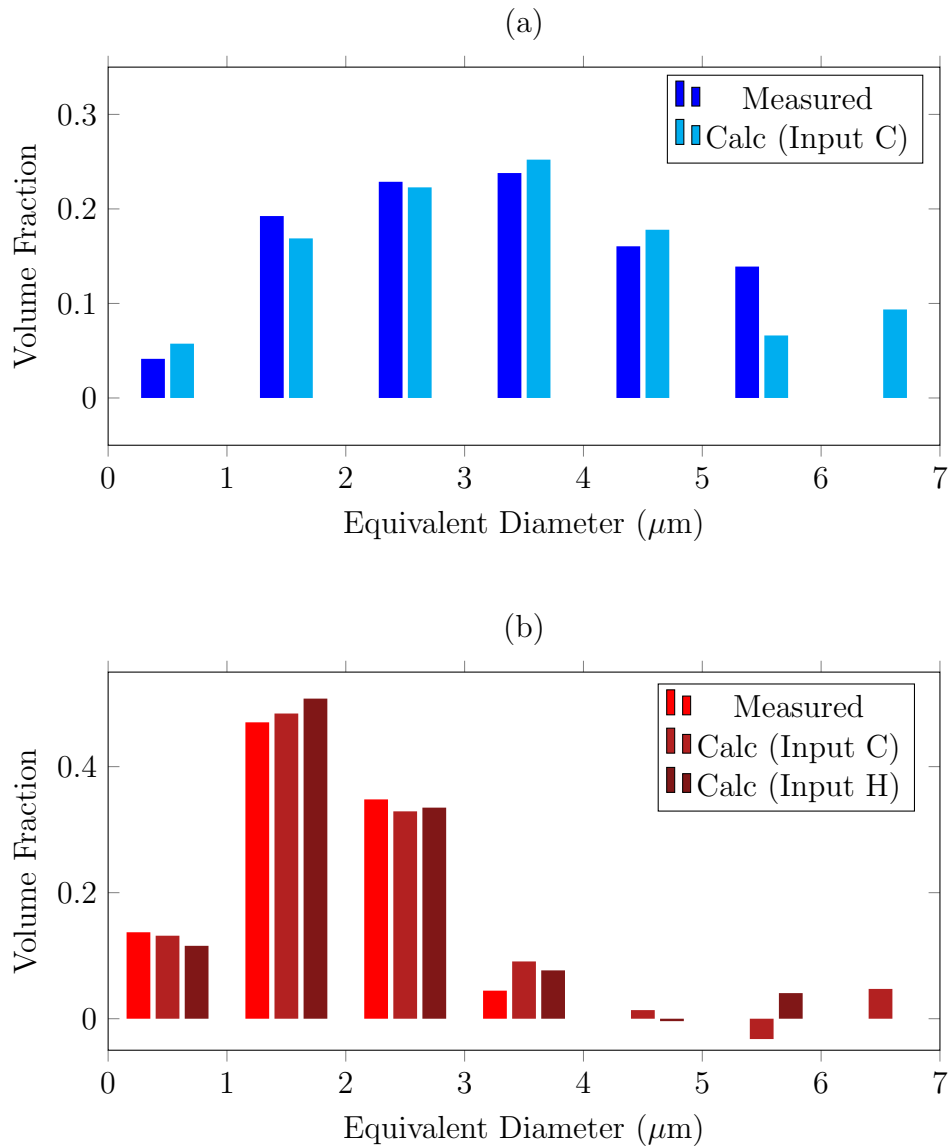


Figure 4.28: Measured and calculated volume fractions of each size range in (a) homogenised and (b) hot rolled material

Figure 4.29 shows how the sphericity of the constituents changes during processing. This illustrates that the sphericity of particles increases after homogenisation, but it is during rolling that biggest shift in the sphericity of the population occurs. To compare the shift in complexity between datasets, the sphericity range of 0.3-0.4 will be used to separate complex particles (defined as  $\Phi = 0-0.3$ ) from simple particles ( $\Phi > 0.4$ ). This point was chosen due to each particle population having a very similar volume fraction falling within the sphericity range of 0.3-0.4. From figure 4.29b, the volume fraction associated with complex particles is reduced by a combined value of 0.21 as a result of homogenisation. This equates to an overall shift of approximately 28% of the volume

fraction originally associated with complex particles. The hot rolling acts to further reduce the total volume of constituents classified as complex using this measure, with a total reduction in volume fraction of 0.45, equating to a 60% reduction from the rolling process itself, or an 88% reduction when combining the two processes.

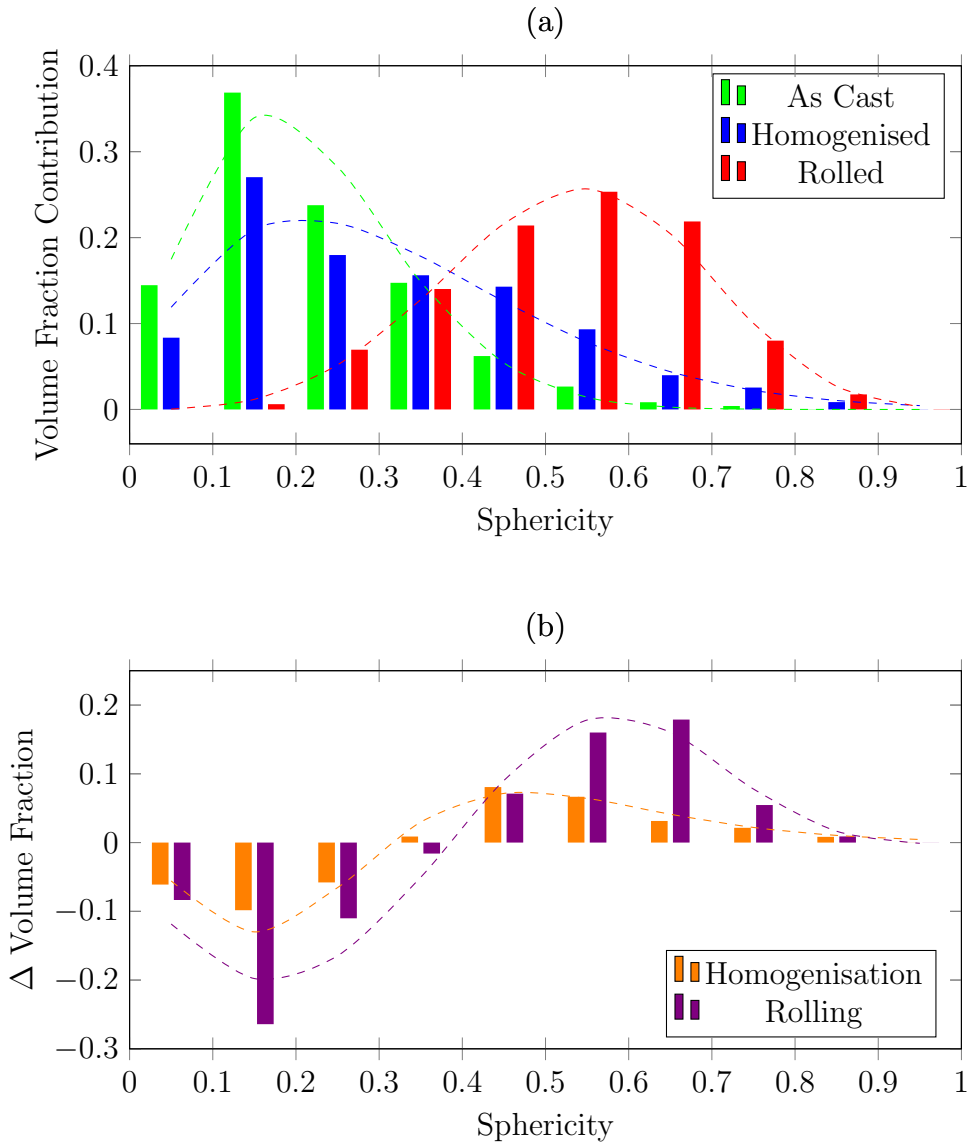


Figure 4.29: Plot showing the change in volume fraction contribution by particles of different complexity during processing. The dotted lines show the path of the fitted Weibull curves.

The dashed lines included within figure 4.29a illustrate the curves which fit each of the sphericity histograms, which were again produced by fitting to a model Weibull curve<sup>4</sup>. The coefficients for these curves are listed in table 4.12 along with the r-squared values indicating the accuracy of the fit.

<sup>4</sup>All sphericity curve fitting was performed by using a conversion of  $x = 10 \times \Phi$

Table 4.12: Weibull Coefficients and Fit Data for Sphericity Distributions

Sample	Scale Parameter ( $\lambda$ )	Shape Parameter ( $k$ )	r-squared
As Cast	0.1806	1.919	0.9714
Homogenised	0.1178	1.696	0.8922
Rolled	0.0009	3.96	0.9889

The differences between the calculated Weibull distributions were determined as shown by the dashed lines included in figure 4.29b. This difference plot was applied to the measured sphericity profiles to produce figure 4.30.

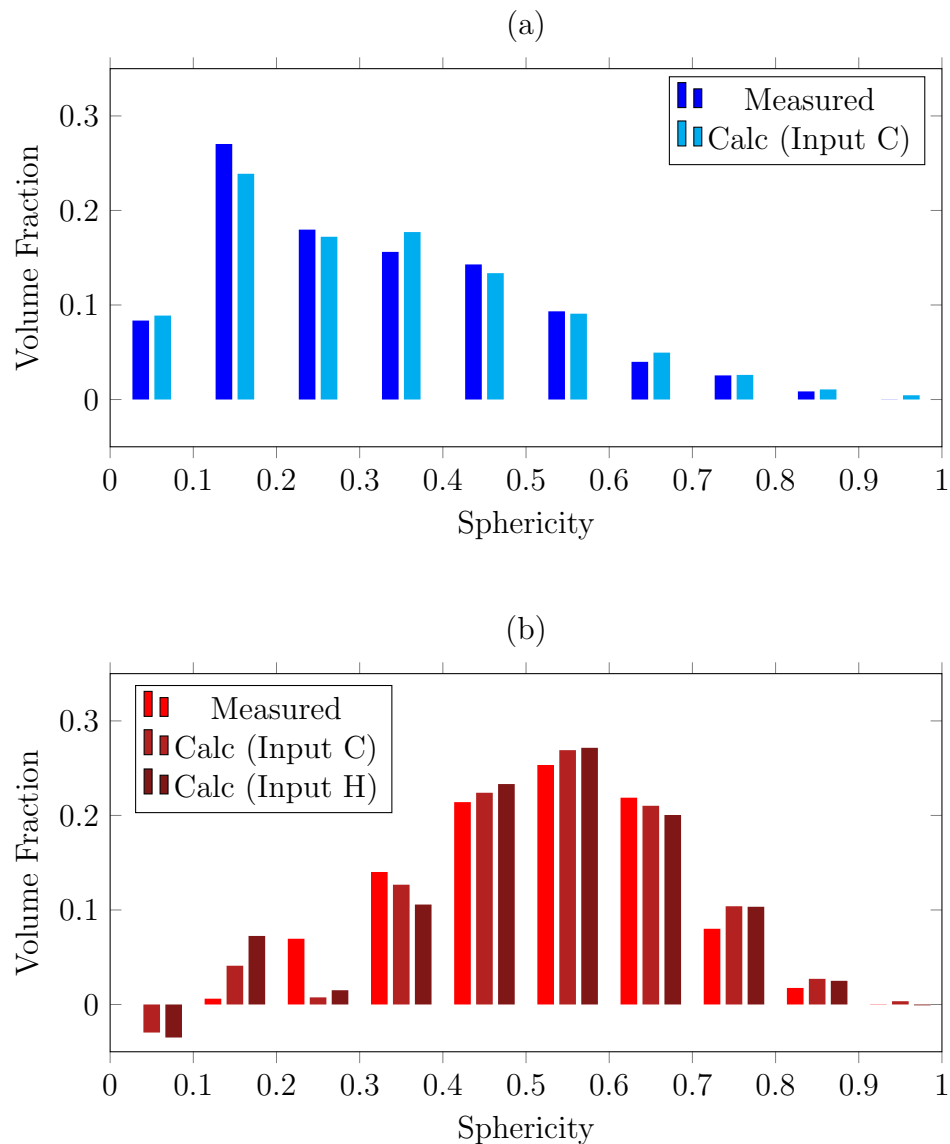


Figure 4.30: Measured and calculated volume fractions of each sphericity range in (a) homogenised and (b) hot rolled material

Figure 4.30 illustrates the fit between measured volume fraction of each sphericity

range and the fraction calculated from the initial as cast condition using the Weibull curves as a tool for estimating particle evolution. In figure 4.30a, the equation describing changes due to sphericity during homogenisation is shown to produce a distribution which closely matches the values determined for the measured homogenised volume.

Figure 4.30b shows the measured sphericity profile for the rolled sample along side two calculated distributions. In this case, the calculated values were determined using both the measured values from the homogenised dataset and the values calculated in 4.30a.

The localised sphericity can be determined for regions of each particle. This is termed curvature and has been visualised within the 3D microstructure as illustrated in the false colour visualisations shown in figure 4.31. Within these images, regions coloured in yellow illustrate a lower local curvature, whereas red and purple shading indicates progressively higher curvature. In this figure, long thin eutectic particles found within clusters in the as cast sample exhibit high curvature (purple). Homogenisation removes the majority of these high curvature regions, with spheroidisation acting to simplify any large structures. Smaller elongated structures with high curvature may have dissolved/broken up resulting in omission from analysis due to thresholding. Rolling results in slightly higher local curvature within the visualisations as the flat regions of larger particles are no longer present after particle break up.

The scatter plots of closeness values against equivalent diameter, and their resulting distribution plots for each of the conditions have been combined to produce figure 4.32. Figure 4.32(a-c) shows that overall, the particles with the largest closeness values are found in the homogenised material. As the closeness values determined for the homogenised dataset are larger than the other particle populations, conclusions can be drawn that either the spacing between particle centre points within the homogenised sample is much lower, or the number of neighbours contributing to the closeness measures of these particles is higher, suggesting increased clustering. Higher closeness values are also obtained for the larger ( $>3 \mu\text{m}$ ) constituents within the homogenised volume, compared to the measured values obtained from within the as cast dataset. Though there are fewer particles in this category within the rolled volume, the closeness value determined for these particles also peak at higher values than the as cast material.

The weighted closeness which incorporates the interparticle distance correction ( $C_i^{W'}$ ) for the three particle populations is shown in figure 4.32(a-c). As previously explained, though the act of correcting the interparticle distance would result in a much higher value of closeness, the weighting calculation makes this closeness value much more dependent on the size of neighbouring particles. In the case of the majority of high weighted closeness values within the homogenised sample, the particles though closely spaced, are also very small, and by comparing the weighted and non weighed values (as shown earlier in figure 4.22) it is also clear that majority of neighbours responsible for the high closeness of small particles are other similarly sized constituents. By taking the ratio of the peak values of closeness attributed to small particles in both the weighted and non weighted scatter plots, it becomes apparent that the neighbours in the as cast material responsible for closeness are generally larger than those in the homogenised material, which are in turn larger than constituents within the rolled sample.

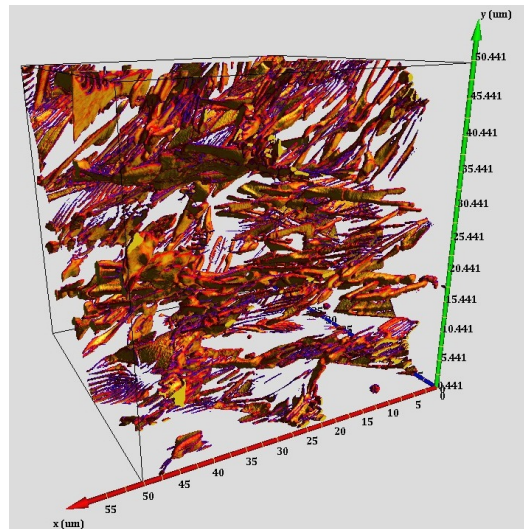
After weighting, the closeness of the larger particles in both as cast and homogenised volumes is increased. Again, it is the as cast particles which receive the greatest boost in comparison to their original closeness value, with the effect on large particles in both the homogenised and rolled samples much more difficult to determine from the scatter plots.

The mean values of  $C_i$  and  $C_i^{W'}$  have been listed along with the values of the 95th percentile of closeness measurements in table 4.13.

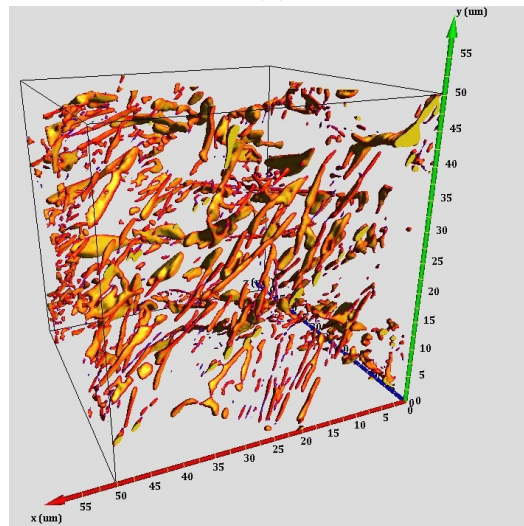
Table 4.13: Parameters from Homogenised Closeness Distributions

Measure	As Cast	Homogenised	Rolled
$C_i$ Mean	2.51	2.64	2.45
$C_i$ 95th Percentile	7.12	8.71	5.39
$C_i^{W'}$ Mean	1.55	1.75	1.42
$C_i^{W'}$ 95th Percentile	3.23	4.36	2.86

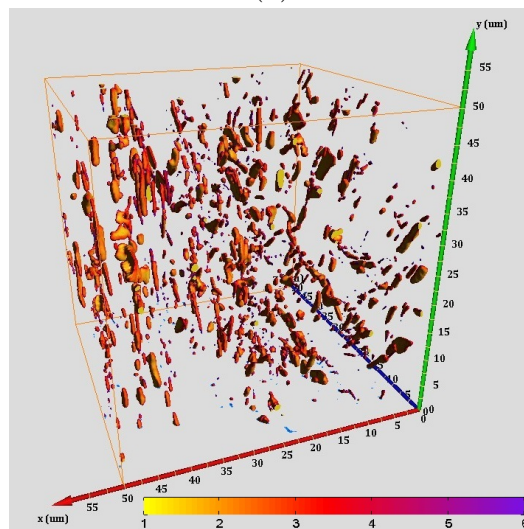
The mean values listed confirm that the particles within the homogenised sample exhibit the highest average closeness. The 95th percentile data shown within this table also confirms that overall, the individual particles with the highest values of closeness are found within the homogenised sample, whilst the particles with the lowest closeness value are within the rolled sample.



(a)



(b)



(c)

Figure 4.31: Local curvature visualisations showing progressive rounding from (a) as cast, to (b) homogenised and (c) rolled material

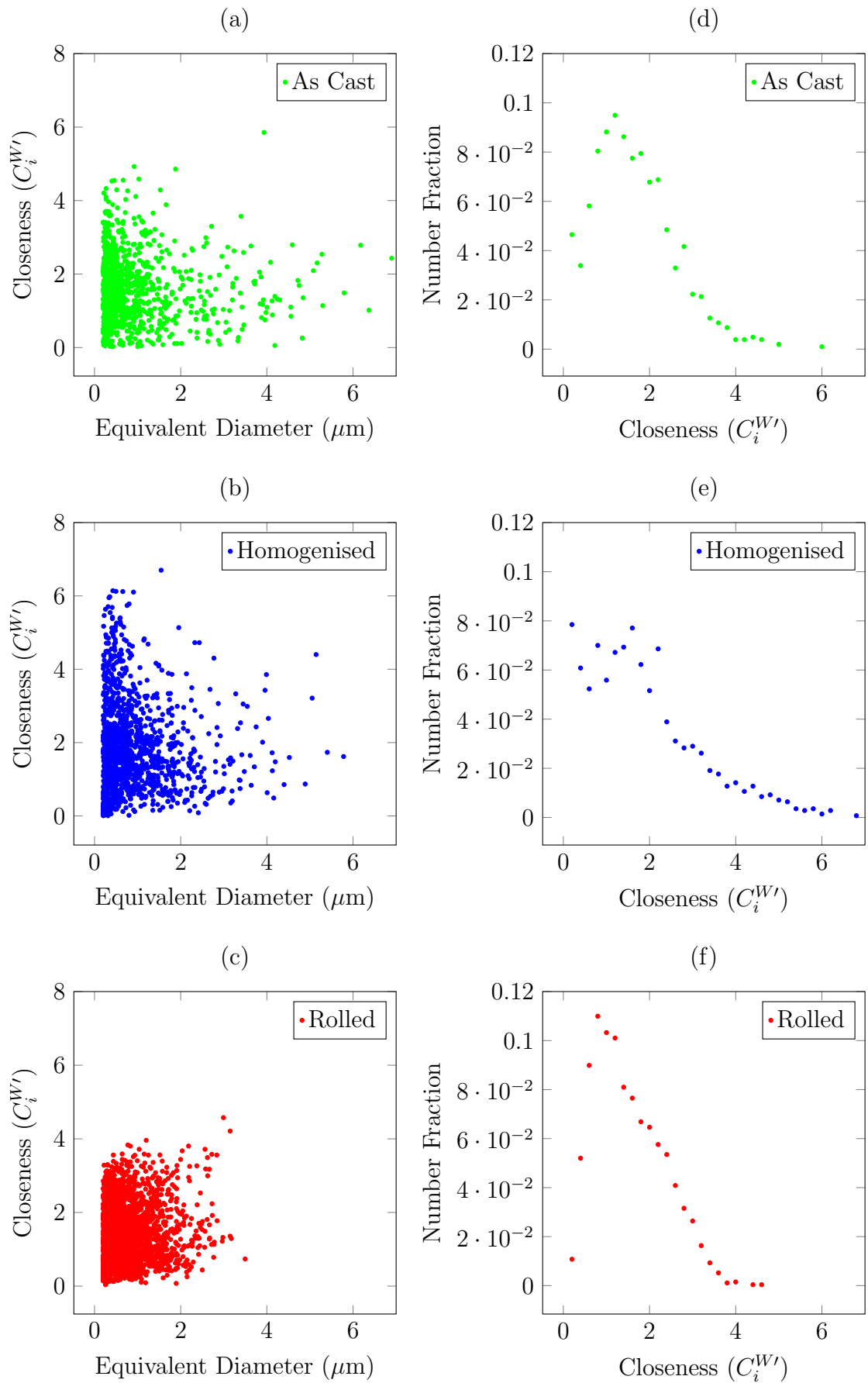


Figure 4.32: Comparison of weighted closeness scatter plots (a-c) and plots of the resulting closeness distributions (d-f) across the populations of constituent particles

### Comparing 2D and 3D Data

As the 3D dataset created using serial sectioning is a combination of closely spaced 2D slices, comparisons can be drawn between the 2D data and the interpolated 3D data. By selecting random 2D slices from the labelled 2D dataset of the rolled sample and using image analysis, the area measurements from 1071 regions of particles were obtained and used to determine equivalent diameter measurements. These diameters were used to create a histogram and the data is presented in figure 4.33.

By assuming that particles within this sample are spherical, these equivalent diameter measurements were processed using the Saltykov method described in section 2.3.4. The largest equivalent diameter within the measured 2D particles was found to be  $2.55 \mu\text{m}$  (classified as  $2.6 \mu\text{m}$  within the histogram). The result of this Saltykov method provides an estimate for the size of particles to be expected within a 3D volume, which is accomplished by determining the contribution of bisections of large particles to the populations of small particles. This corrected data is also presented in blue in figure 4.33. For comparison, the equivalent diameter measurements from the full 3D dataset are also presented in figure 4.33.

One main difference between the 2D and 3D equivalent diameter measurements for these populations occurs in the submicron range and can be attributed to the stark cut off in the 3D data with no particles having an equivalent diameter of less than  $0.2 \mu\text{m}$ . As the 2D slice measurements may contain regions of a particle that falls below this  $0.2 \mu\text{m}$  thresholding value, discrepancies between the 2D and 3D populations of these small particles are both expected and unavoidable unless further data manipulation (omission) is incorporated.

One other anomaly introduced with the Saltykov method occurs at the equivalent diameter grouping of  $2.5 \mu\text{m}$ . In the 2D data, no particles fall within this category and so when the Saltykov correction is applied, a negative value is determined for this grouping. This numerical flaw quickly resolves itself as the correction is applied to further groups of particles in the population, but the existence of a negative number fraction is notable. This negative value can also not be simply removed as this would alter the number of particles in the final Saltykov population.

The data from the visualised 3D dataset has been compared to that of the raw and Saltykov corrected 2D data as shown in figure 4.34. In this plot, the differences

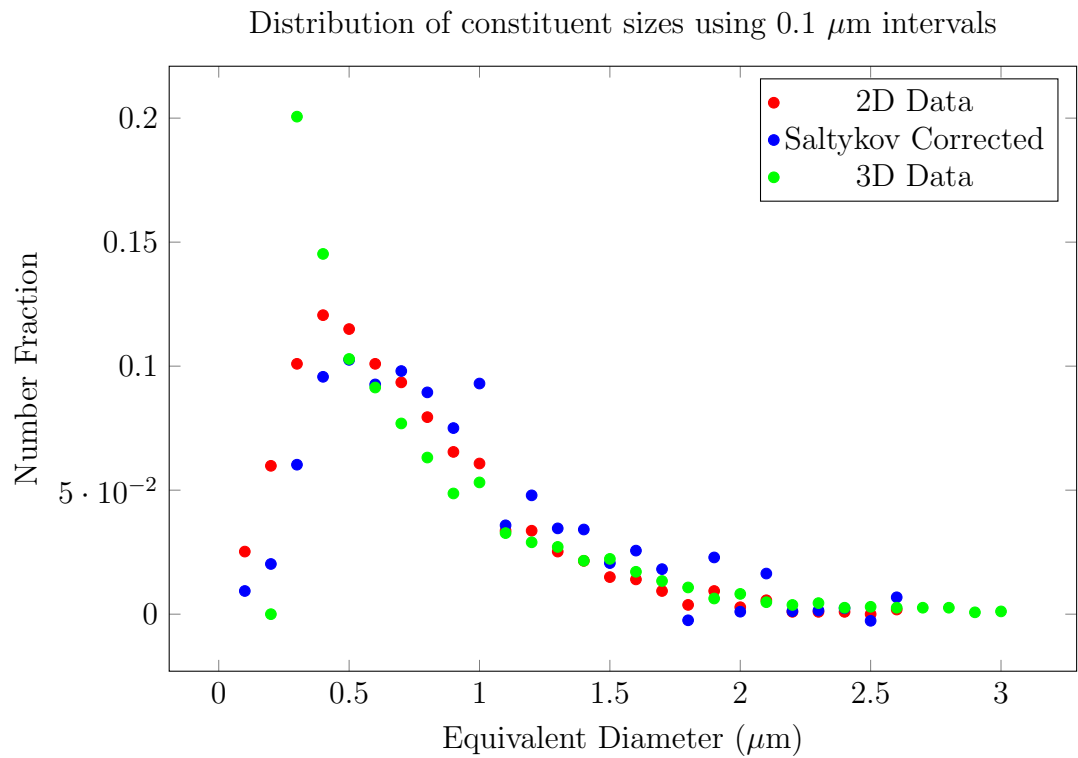
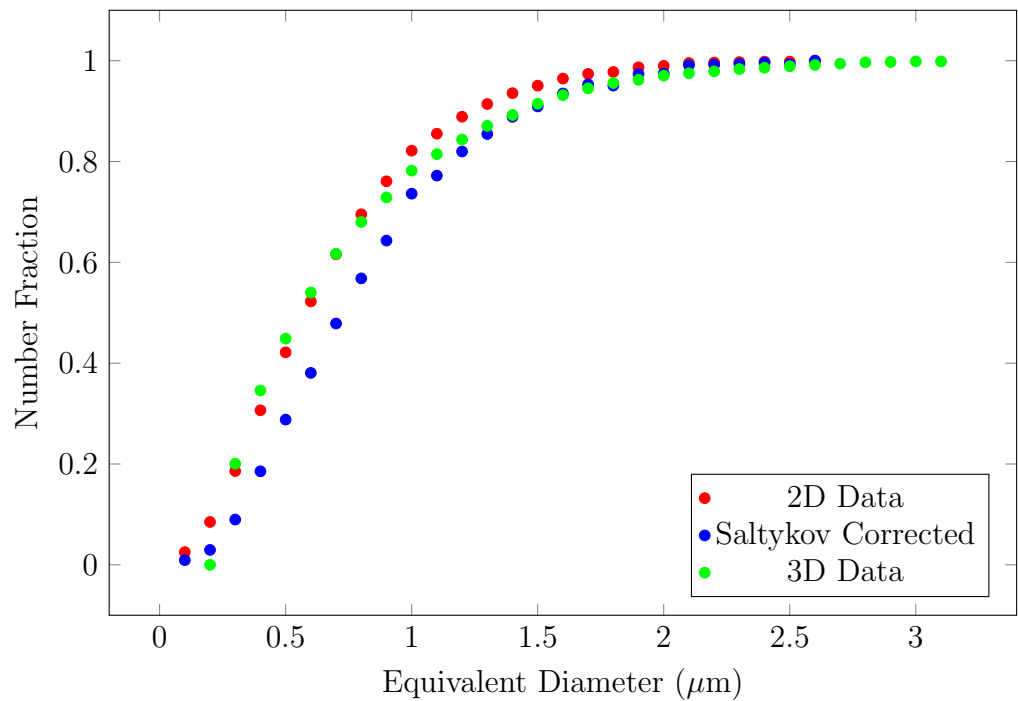
Cumulative fraction of constituent sizes from using  $0.1 \mu\text{m}$  intervals

Figure 4.33: 2D and Saltykov corrected equivalent diameters of constituents in rolled aluminium compared to 3D data grouped using  $0.1 \mu\text{m}$  intervals

between the number fractions of each particle grouping are presented. The plot in red shows the fluctuation between the raw 2D particle size fraction and the 3D measurements, whereas the blue plot shows deviations between the Saltykov corrected population and the visualised volume. In figure 4.34a, the disconnect between the 2D and 3D measurements is immediately noticeable when analysing the difference between the populations of submicron particles, though these differences tend to dissipate with increasing particle size. The Saltykov corrected particle size distribution for this sample also has the biggest variance from the 3D data when comparing the submicron particle population. However, the differences between Saltykov and 3D distributions are generally larger than those obtained when comparing the raw 2D and 3D measurements. This result is unexpected, as this implies that the application of the Saltykov method can push a measured 2D distribution further from the true 3D result. Though the differences between the Saltykov distribution and the 3D measurements are less prominent when comparing the number fractions of larger particles, discrepancies still exist at a greater scale than are observed in comparisons with the raw 2D measurements.

By taking the differences between the cumulative number fraction measurements, this divergence of particle size from the 3D distribution after application of the Saltykov method is more clearly visualised as shown in figure 4.34b.

This apparent decrease in the accuracy of the particle size distribution after the application of the Saltykov method may be due to a number of assumptions which are incorporated within this technique. Firstly, this method assumes that all particles within the volume are spherical, and this allows the measured particle population to be corrected by attributing part of each size classification to the bisection of larger particles. However, it is known from figure 4.25 that though some particles are close to spherical, the majority of constituents within the volume are not. As a result of this, bisections of long thin regions in the raw data may result in exaggerated numbers of particles with a given particle size. The assumption that all bisections are from varying distances from the centre of a sphere, would then result in a boost of a particular particle size within the Saltykov approximation, leading to a reduction in accuracy rather than an improvement. Further analysis has been performed by altering the step size used for the Saltykov analysis. This resulted in less turbulent plots, however

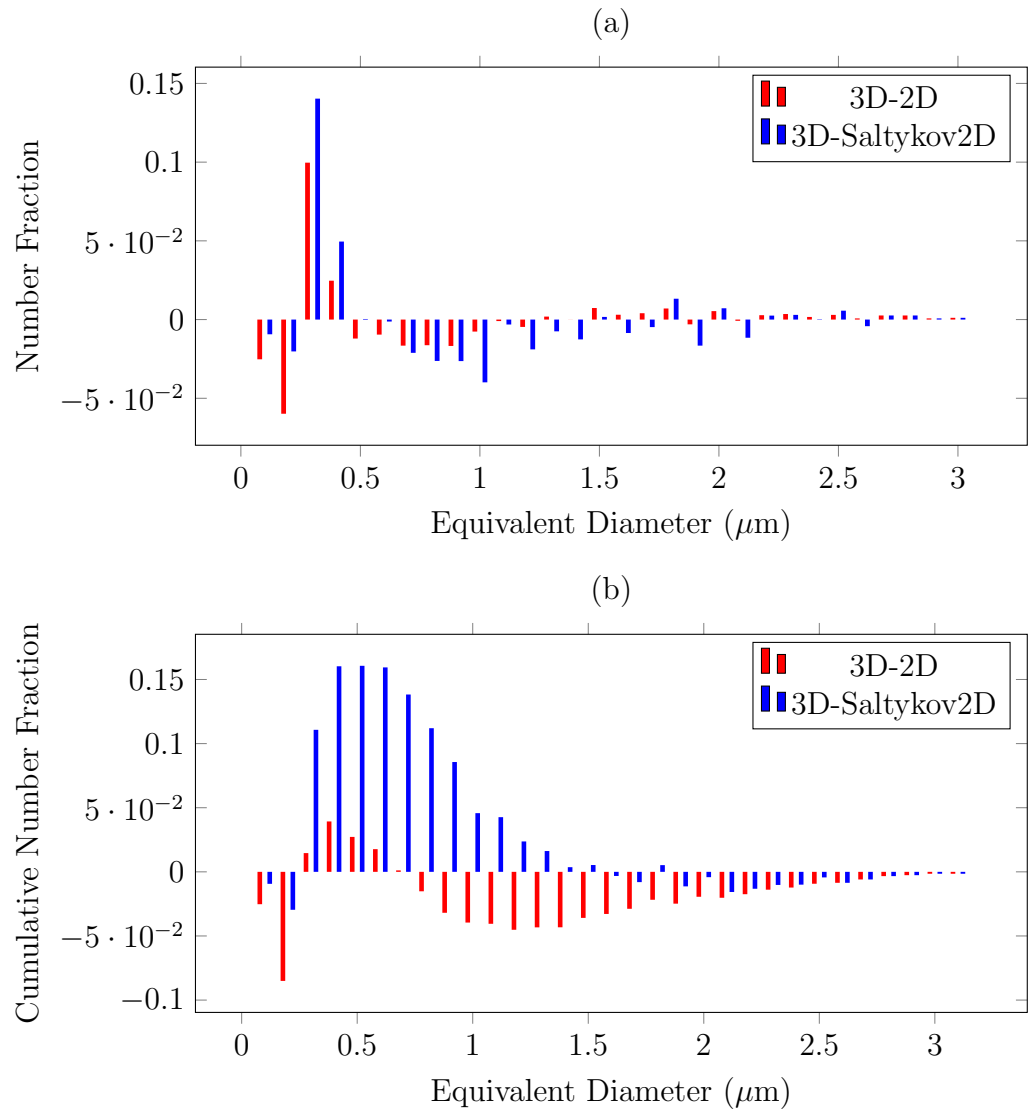


Figure 4.34: Plot showing the difference between measured 2D particle size, and the calculated 3D particle size from this dataset and the true 3D particle dimensions

the outcome in terms of Saltykov accuracy is unchanged. For completeness, these plots are included in the Appendix (section A.2).

### 4.2.3 3D Analysis - Dispersoids

By using higher magnification when imaging and reducing the slice depth to the operating minimum of 15nm, it is possible to obtain detail of the dispersoid particles which nucleate during thermomechanical processing. This results in a image stack containing data for a volume of  $10.24 \mu\text{m} \times 10.24 \mu\text{m} \times 5.00 \mu\text{m}$ .

However, care must be taken when working at higher resolutions due to different behaviour of the constituent particles when very thin slices are removed from the sample. During a cut, a section of an intermetallic particle may break away from the bulk, and become embedded in the matrix. This is shown in figure 4.35. Within this image, the orange highlighted area shows ‘break off’ from a constituent on a grain boundary, while the green area indicates the scratches that are produced as a result of the broken region being pushed along the surface by the ultramicrotome. Due to the directional nature of the cutting process, any re-embedded particle will be found above the original particle in the 2D image stack. These scratches can be useful in negating re-embedded particles from any measurement of dispersoids within the volume. When larger slices are removed (as when imaging the constituent network) fewer such instances of particle ‘break off’ were detected. If these splintered regions are not isolated from the rest of the particles when visualising the volume, a population of particle fragments would be found as a streak near larger particles, which may skew any distribution measures or PFZ analysis.

#### Homogenised

Figure 4.36 shows a visualised high resolution image stack. In this image, the darker regions correspond to constituent particles while the newly nucleated dispersoids are shown as lighter structures. This higher resolution allows much greater detail to be visualised with relation to the structure of constituent particles. In this image, variations in thickness along the length of the constituent can be seen.

This image stack contains 1667 individual particles which have an equivalent diameter of at least 60nm which have been labelled as dispersoid particles for quantitative analysis. This illustrates that this technique allows 3D data to be obtained for a statistically significant numbers of submicron particles. This number does not include particles which fall above a threshold size of 400 nm in length (classified as constituents),

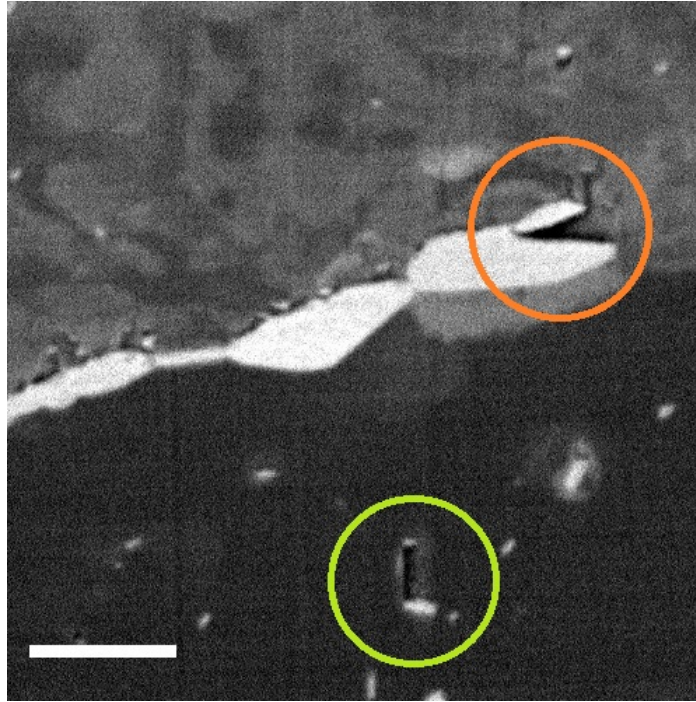


Figure 4.35: Example of particle break-off within high resolution cutting (Scale bar represents 1  $\mu\text{m}$ )

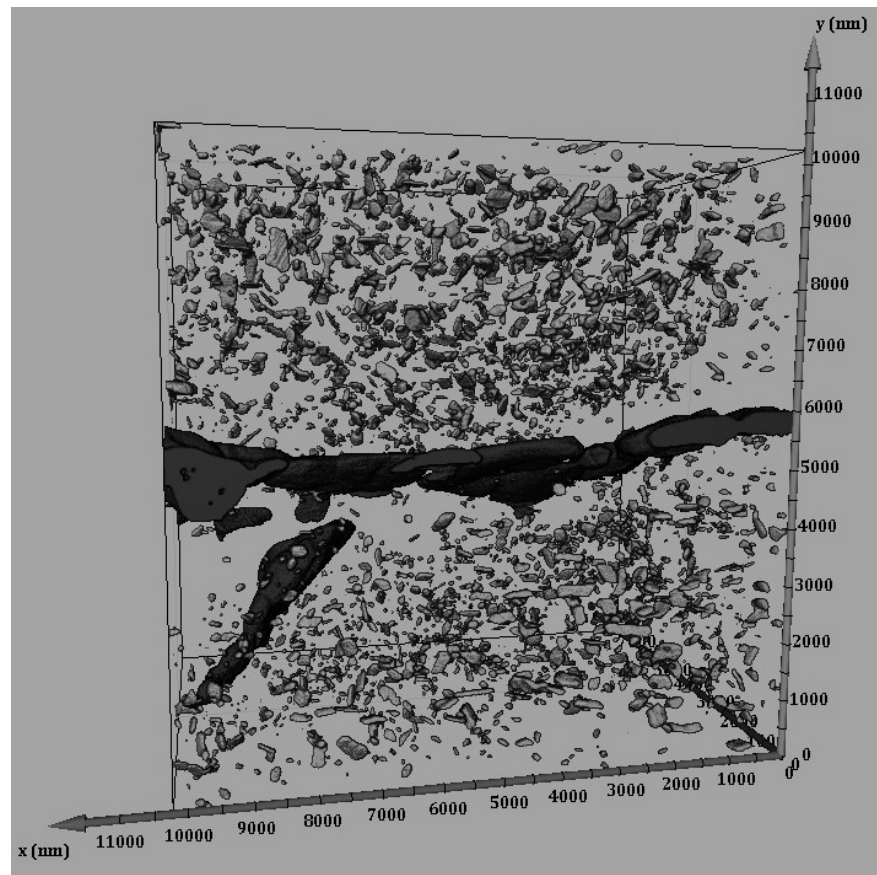


Figure 4.36: Visualised dispersoids within the homogenised alloy

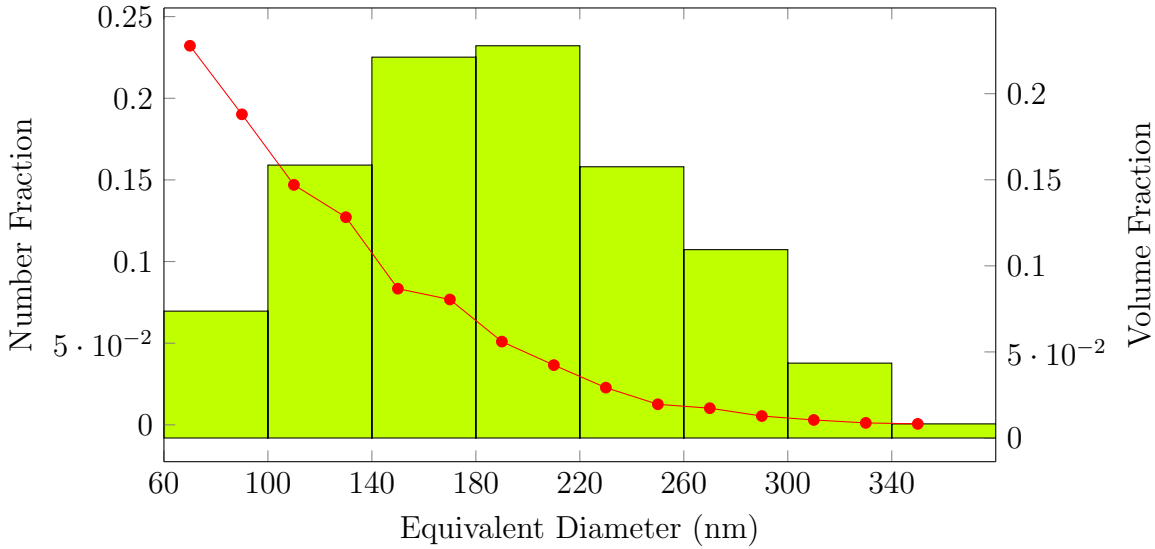


Figure 4.37: Plot showing the number fraction (red) and volume fraction (bar) of dispersoids with a given equivalent diameter in the homogenised sample.

nor any regions attributed to the fragmentation of particles during the cutting stage of 3D data capture. This image stack was obtained across a grain boundary, with the different orientations of the grains resulting in differences in the base grey-scale values at different regions within the image stack. A clear precipitate free zone is also visible, indicated by the lack of smaller particles in the vicinity of the boundary. The precipitate free region measures on average  $1.6 \mu\text{m}$  wide across the grain boundary, and also extends approximately  $0.8 \mu\text{m}$  from the edge of the constituent particles within the volume.

Figure 4.37 shows the number fraction and volume fraction measurements obtained for the dispersoids found within the homogenised sample. In this sample, over 70% of the measured dispersoids were found to have an equivalent diameter of less than 140 nm, though these particles were found to account for only 23% of the total mass of dispersoids within the volume. The majority of the dispersoid mass is attributed to particles which are between 140 nm and 260 nm, making up 61% of the dispersoid mass, and accounting for 28% of the dispersoids by number. The remaining 2% of particles are larger than 260 nm and contain 16% of the total mass attributed to dispersoids. This high percentage of small dispersoids within the homogenised sample mirrors the findings from the constituent particle study.

Figure 4.38 shows the result when the same sphericity measurement obtained for constituent particles was applied to the population of dispersoids. Previously, particles

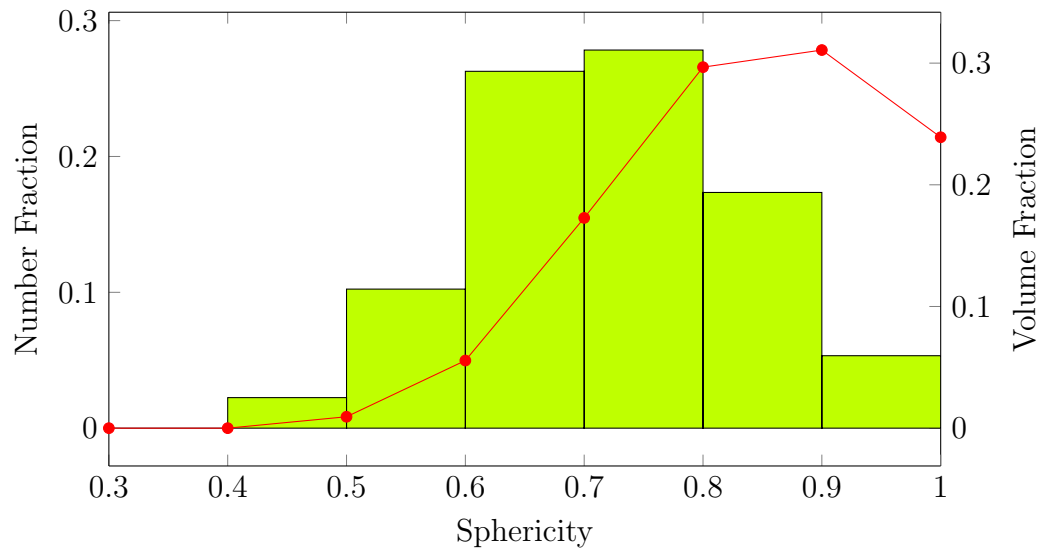


Figure 4.38: Plot showing the number fraction (red) and volume fraction (bar) of sphericity values of dispersoids within the homogenised sample.

were considered to be complex if they resulted in a sphericity value of less than 0.3, however, in this population of particles, no dispersoids fit this criteria. This fits with generally accepted theory that dispersoid particles are small, simple particles. The fact that the dispersoids are not spherical is also expected due to the non uniform growth of dispersoids outlined earlier (section 2.3.2). Here the majority of the dispersoid particles are shown to have a high sphericity value, though when the mass of these particles is considered, the volume weighted sphericity profile is shifted, illustrating that the bulk of mass of dispersoids are found within less spherical particles.

### Hot Rolled

Dispersoid data visualised from the 52% hot rolled PGN is shown in figure 4.39. The constituent particles, again visualised as dark regions within the figure, are more compact than those found in the homogenised condition which is expected when considering the findings from the lower resolution data. Precipitate free zones are visible as in the homogenised condition but are now much harder to distinguish with dispersoid particles found within  $0.2 \mu\text{m}$  of the constituent particles. This deformed sample was found to have 2799 particles between the cut off equivalent diameters of 60 nm and 400 nm.

The particle sizes have been collated to produce the distributions shown in figure 4.40. The highest contribution to the number fraction of dispersoids is due to the

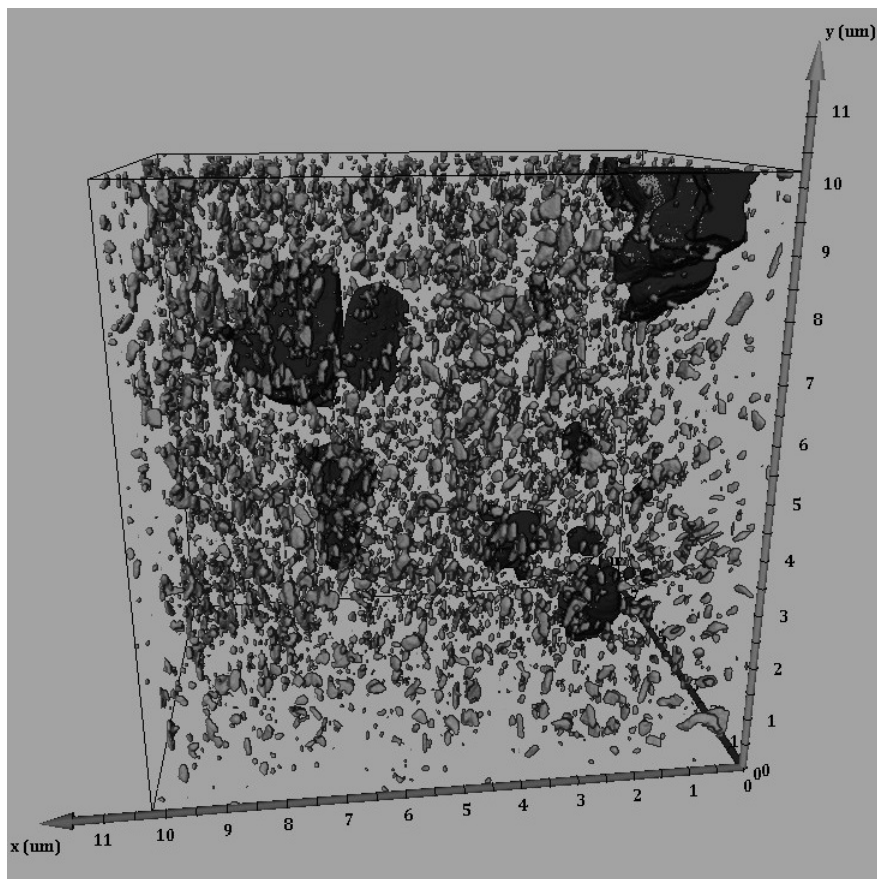


Figure 4.39: Visualised dispersoids within the hot rolled alloy ( $x = \text{ND}$ ,  $y = \text{RD}$ ,  $z = \text{TD}$ )

smaller particles found within the volume, and generally, the number fraction of dispersoids decreases with increasing particle size. The volume fraction of particles peaks with contributions from dispersoids with equivalent diameters between 180 and 220 nm.

The number and volume fractions of sphericity values for the dispersoids found within the rolled sample are illustrated in figure 4.41. This plot shows the majority of particles within this volume have a high sphericity value (close to spherical), though many of these particles are small. The majority (nearing 30%) of mass of dispersoids is attributed to particles with sphericity values in the range of 0.7 to 0.8, with only  $\approx 10\%$  of the mass owing to particles with a sphericity value of 0.9 to 1.0. Like in the homogenised sample, this deviation from a population of spherical particles is expected, however, the distribution presented here is different from that obtained from the homogenised sample. The two datasets will now be compared to determine whether any effects of hot rolling on the particle distribution found within this alloy

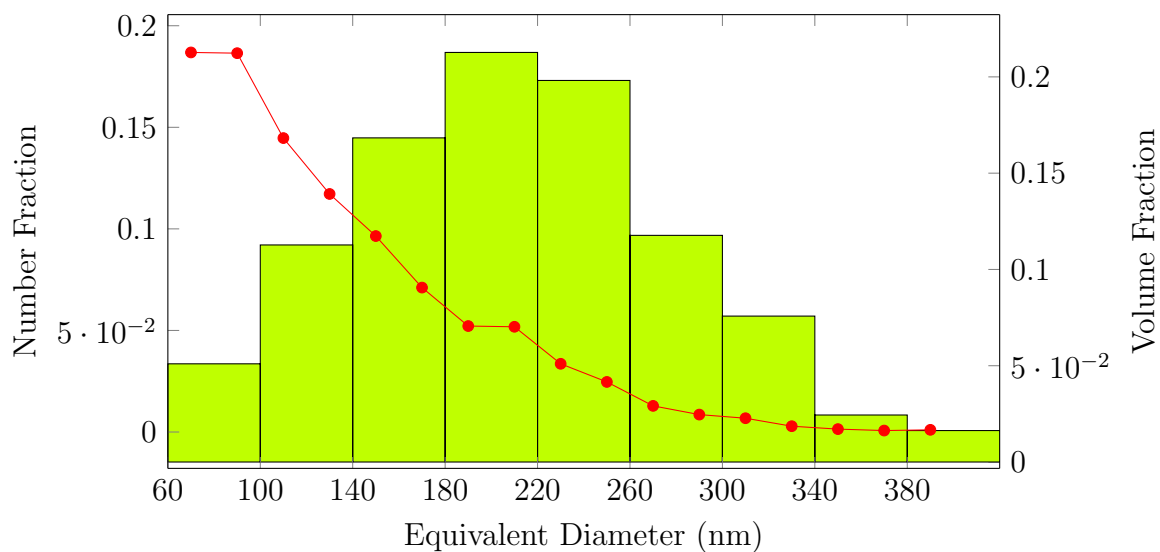


Figure 4.40: Plot showing the number fraction (red) and volume fraction (bar) of dispersoids with a given equivalent diameter in the rolled sample.

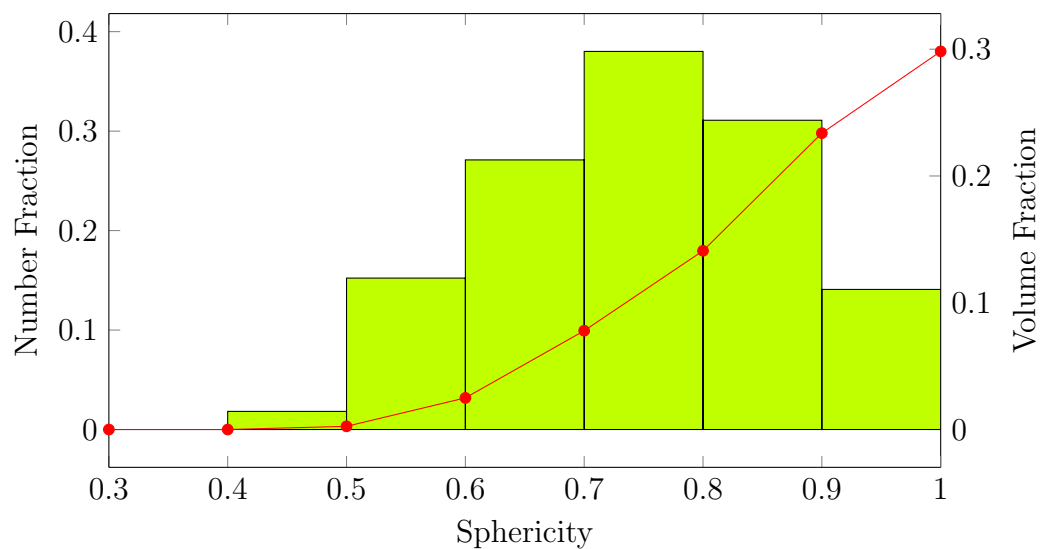


Figure 4.41: Plot showing the number fraction (red) and volume fraction (bar) of sphericity values of dispersoids within the rolled sample.

can be detected.

### Comparing 3D Volumes

The number of particles and resulting volume fraction attributed to dispersoids is shown in table 4.14. From this table, it can be seen that the number of particles identified as dispersoids is almost 68% larger when analysing the rolled material. This coincides with an increase of 0.46% when measuring the total volume fraction of dispersoids.

Table 4.14: Number of Dispersoids above the Threshold Size

Condition	Number of Dispersoids	Volume Fraction
Homogenised	1667	0.00741
Rolled	2799	0.01201

However, care must be taken when comparing these populations as there are many sources of uncertainty regarding the measurements of these particles. One of the biggest causes for concern here is the existence of larger constituent particles within the alloy. Due to the concurrent break up of the constituent network during dispersoid nucleation, uncertainty may arise as to whether a particle is a large dispersoid or a small constituent. In the current dataset, an upper limit of particle size was first established to aid in isolating dispersoids from the primary particle population, though it is possible that very large dispersoid particles have been omitted from population studies as a result of this.

Secondly, the partial break up of larger particles by the cutting process incorporated into the serial sectioning method adds a further obstacle to characterisation. Though these particles have an obvious signature within the captured images, it remains vital that the break off is not included in dispersoid population analysis.

One final consideration here is the effect of the PFZ on any statistical analysis. As the nucleation of dispersoids is known to be affected by proximity to second phase particles and grain boundaries, it could be argued that any dispersoid particle data presented from these volumes is not representative of the bulk, as the PFZs in these volumes may account for an inflated proportion of the volume. For this reason, further volumetric studies could be undertaken in regions away from any grain boundaries or

large particles to determine more accurate representation of the dispersoid population. This is not included as part of this study due to the limited availability of the 3View system. The data presented here could then be expanded upon to determine how important the proximity to a particle or grain boundary is on the resulting population of dispersoids.

The data obtained describing the dispersoids has been compared to provide some insight into the effects that hot rolling to a 52% total reduction can have on the dispersoid particle population.

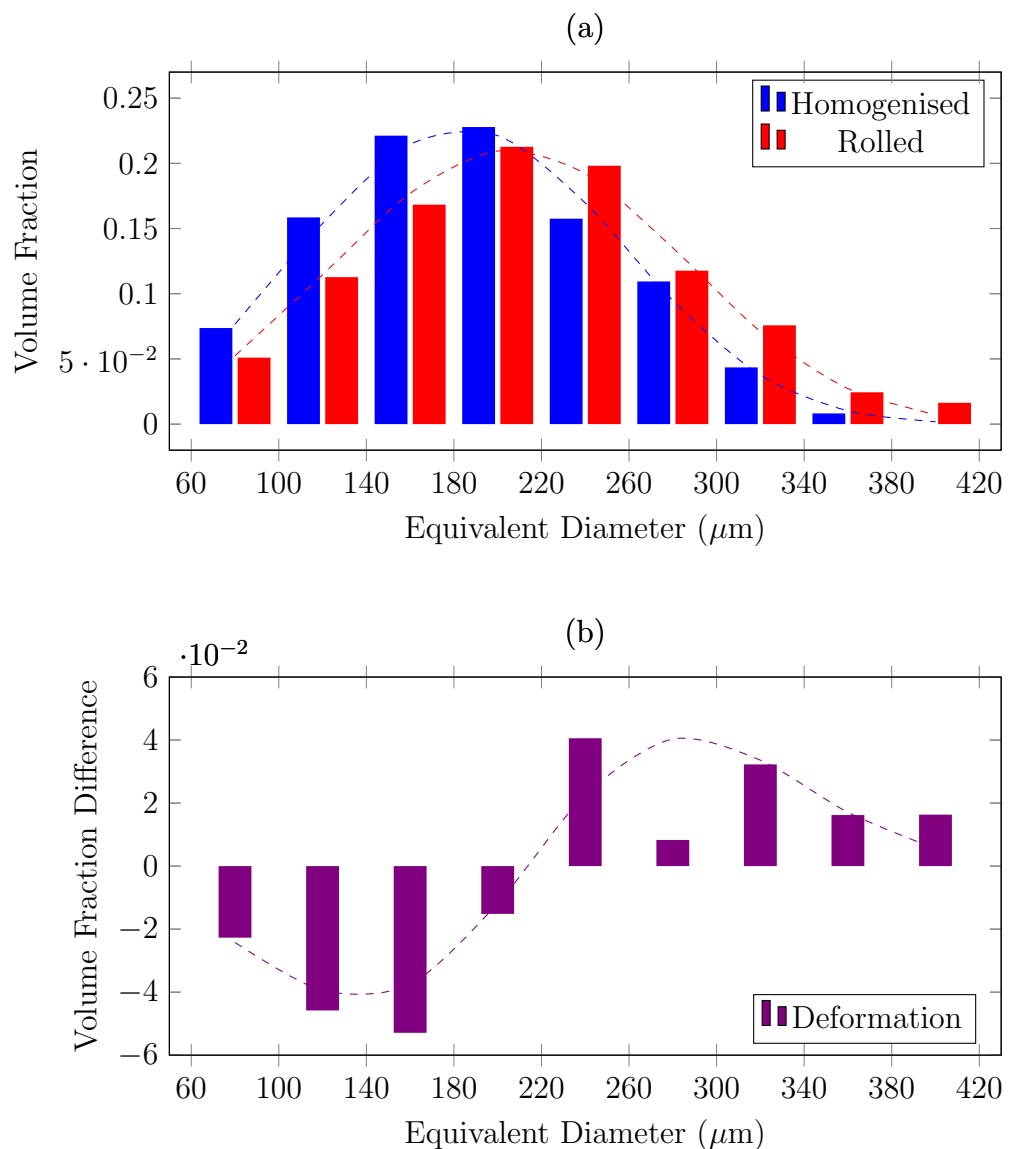


Figure 4.42: Plot showing how the volume fraction contribution of dispersoids changes due to deformation. The dotted lines show the path of the fitted Weibull curves.

Figure 4.42a includes the previously presented volume fraction data for comparative

purposes, which was used to create the plot shown in 4.42b. From first plot, though both distributions seem to follow a normal distribution, it seems that the rolled population is centred around a higher equivalent diameter measurement, therefore indicating that the dispersoids are generally larger within the rolled sample. By measuring the difference between these two populations as shown in 4.42b, this decrease in the contribution of small particles to the overall volume fraction after deformation becomes clear. These populations were again fitted to produce curves using the Weibull equation outlined earlier (equation 4.7), the parameters for which are included in table 4.15.

Table 4.15: Weibull Coeffs and Fit Data for Fitting Curves for Dispersoid Data

Measurement	Sample	Scale Param. ( $\lambda$ )	Shape Param. ( $k$ )	r-squared
Volume Fraction	Homogenised	0.00647	3.039	0.9886
	Rolled	0.00389	3.147	0.9873
Sphericity	Homogenised	$1.567 \times 10^{-6}$	6.604	0.9797
	Rolled	$2.058 \times 10^{-6}$	6.313	0.9889

Similar plots demonstrating the changes to the population of sphericity values for dispersoid particles are shown in figure 4.43. The general trend in this case is an increased contribution to volume fraction attributed to more spherical particles after deformation. This result is in agreement with Hill [Hill, 2014], in which deformation was found to reduce the aspect ratio of dispersoids within the same model alloy. The Weibull coefficients for this dataset are also incorporated into table 4.15.

#### 4.2.4 Combining the 3D Data

By bringing together the data from the high and low resolution scans, a more complete understanding of the intermetallic particle population can be determined. Due to the initial characterisation of 0.2-0.4  $\mu\text{m}$  constituents in the low resolution as-cast scan (which were found as part of constituent clusters), both high and low resolution datasets contain information regarding particles which fall within this size range in the homogenised and rolled condition. The combined volume fraction measurements are shown in table 4.16, while the volume fraction values for each particle size is shown for the combined data in figure 4.44.

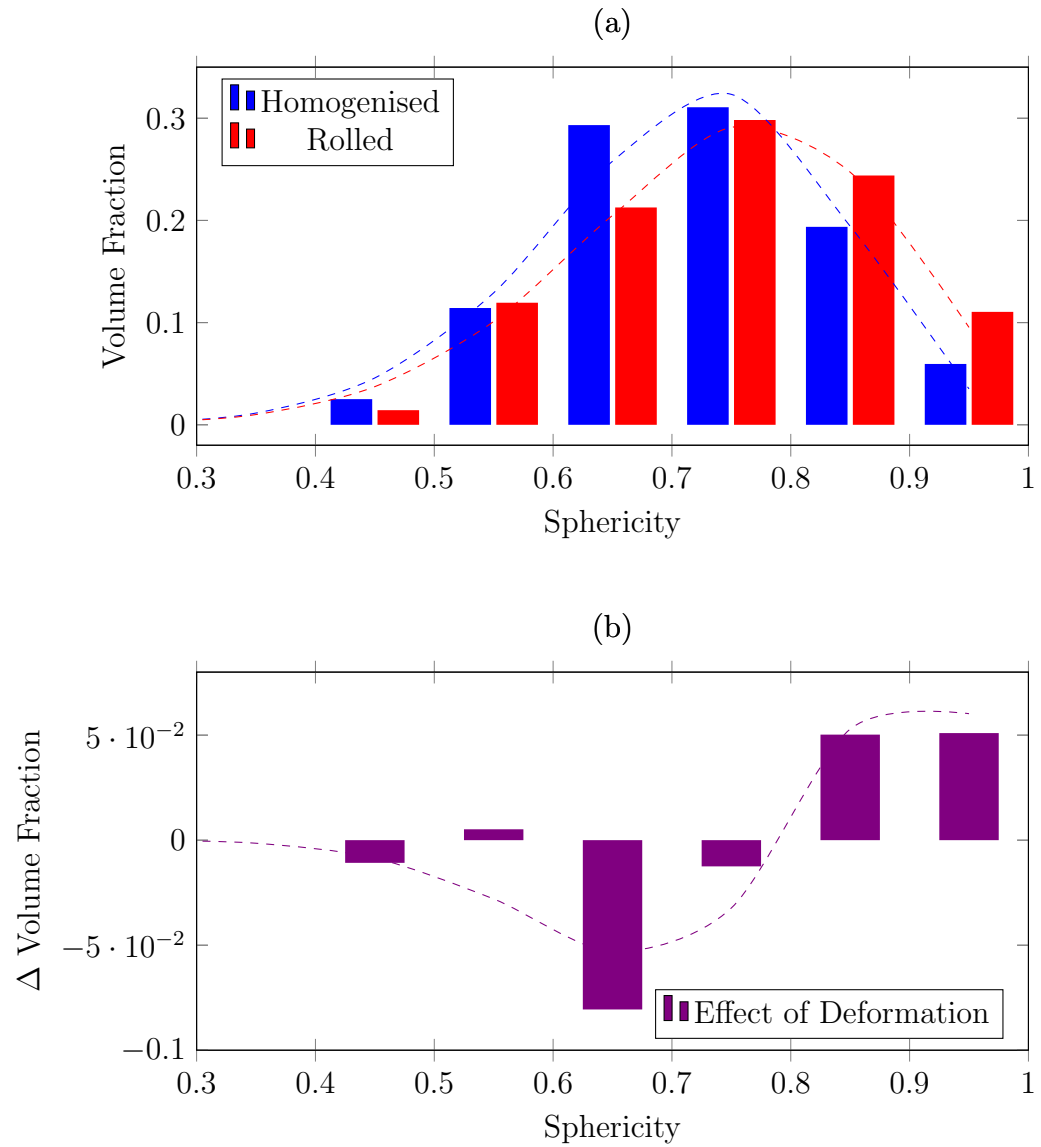


Figure 4.43: Plot showing the change in sphericity of dispersoids size during processing. The dotted lines show the path of the fitted Weibull curves.

Table 4.16: Combined Volume Fractions of Second Phase Particles

Condition	Constituents	Dispersoids	Combined
As Cast	0.02389	–	0.02389
Homogenised	0.01842	0.00741	0.02583
Rolled	0.01157	0.01201	0.02358

From table 4.16, the total measured volume fraction of second phase particles is shown to increase slightly with homogenisation (by 0.19%) with rolling resulting in a similarly scaled reduction (0.23%). Due to the lack of characterisation of particles smaller than  $0.2 \mu\text{m}$  in the as cast condition, and the error introduced into particle

size measurements using the serial sectioning technique (interpolation of data due to incomplete cutting, inherent error in thresholding of particle size due to interaction volume etc) the small differences between the volume fractions obtained for each of the samples are not significant enough to confirm whether any change occurs in the total volume fraction of second phase particles during the homogenisation and rolling processes. However, this data clearly suggests that the volume fraction of constituents decreases during the initial stages of sheet production, while nucleation and coarsening of dispersoids results in an initial population forming during homogenisation and this volume fraction increasing during the rolling stage.

The plots within 4.44 illustrate how the volume fraction distributions of both particle types change during the two implemented stages of processing. In these plots, the volume fraction of constituents with an equivalent diameter of less than  $0.4 \mu\text{m}$  is dwarfed by the measured fractions of dispersoids of the same size. Though not evident from these plots, it should be noted that the dispersoids in the homogenised condition contribute approximately 29% of the total mass of second phase particles if it is assumed that the measured volumes are representative of the entire sample. This increases to 51% of mass of second phase material existing as dispersoids in the rolled condition.

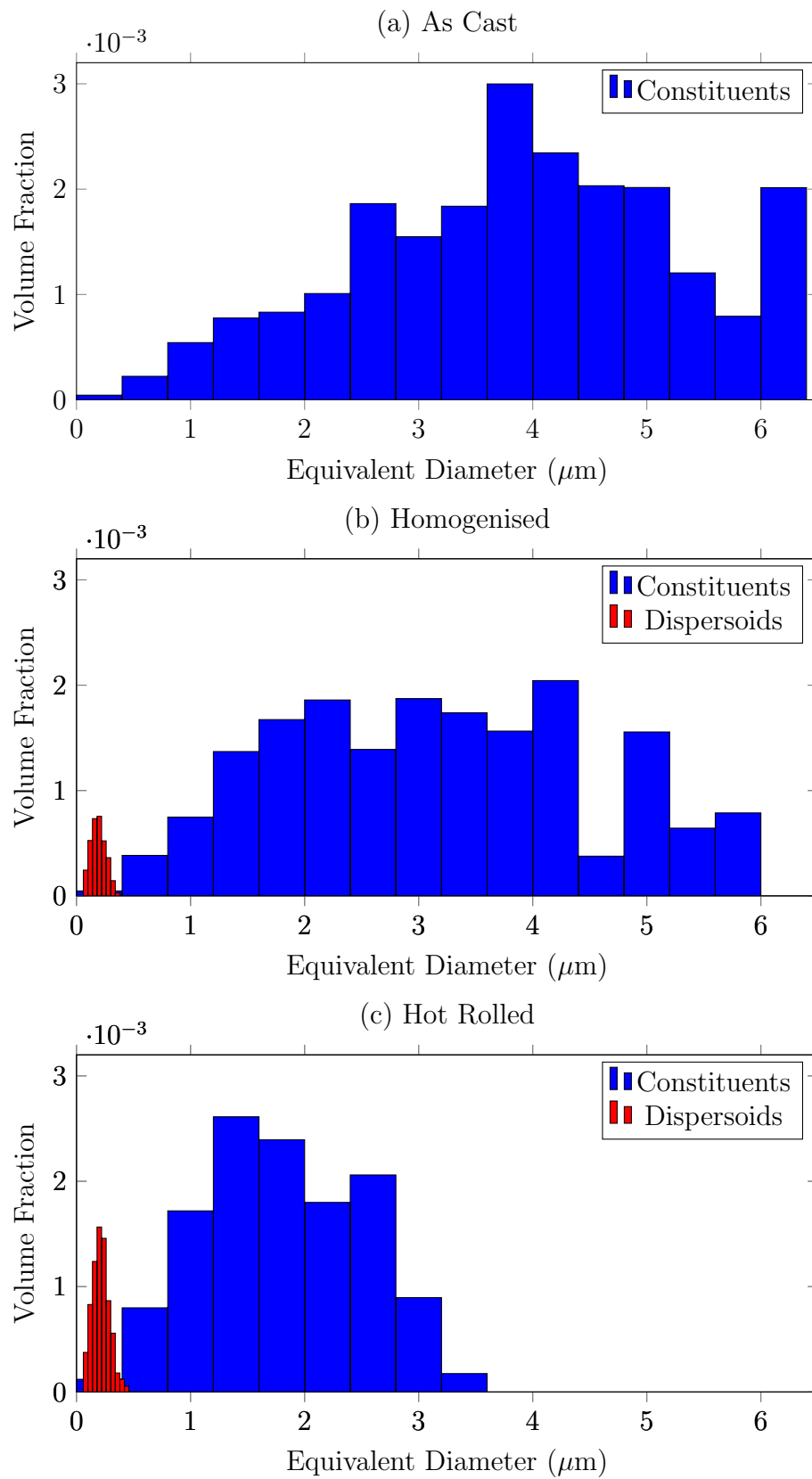


Figure 4.44: Plots showing the volume fraction of dispersoids (red) and constituents (blue) grouped by equivalent diameter.

### 4.3 Deformation Around Particles

It is well documented that the presence of non deformable particles within aluminium affects how the material close to the particle will behave during deformation. The resulting deformation zones of such particles have been studied in depth and equations have been made that describe how the size and rotation of these zones are linked to the particle size and overall applied strain. As the closeness measures calculated earlier help to illustrate, particles are often closely spaced within an alloy, however little published work exists which investigates the effects of multiple closely spaced particles on the resulting deformation zone. Digital image correlation has been used to analyse the deformation of a sample containing second phase particles during plane strain compression, allowing the creation of strain maps which are presented within this section. This section also includes CPFEM simulations which suggest how parameters such as particle orientation and interparticle spacing may affect local rotations and strains within the matrix.

#### 4.3.1 Strain Mapping Around Particles

The evolution of the microstructure of the homogenised alloy during deformation was monitored using digital image correlation. This was performed by comparing micrographs of the nano-patterned surface of the material (which was prepared as described in section 3.3.3) which were obtained at 4% strain intervals. 4% strain intervals were used here as they have been shown in previous works to produce reliable DIC datasets [Ko, 2014]. An example of the gold pattern created for these studies is shown in figure 4.45. The images acquired for the uncompressed and 8% reduced conditions for two regions within the same sample are shown with the resulting strain maps in figures 4.46 and 4.50. Originally, these experiments were planned to proceed at 4% intervals to a total  $\sim 30\%$  reduction, thus mirroring the simulations performed within the CPFEM (see section 4.3.2), however, problems arose with the viability of the gold pattern after successive reductions. At the time of writing, the reason for the failure of the gold pattern is unknown.

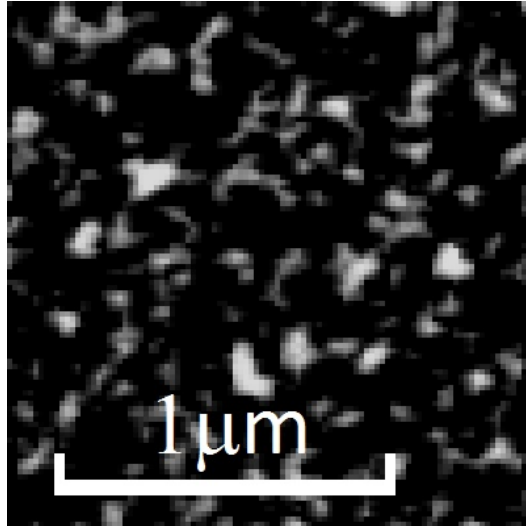


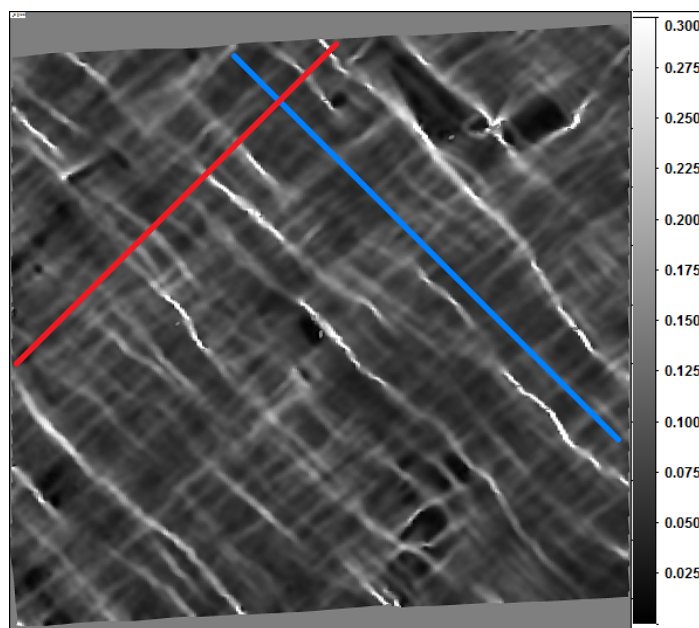
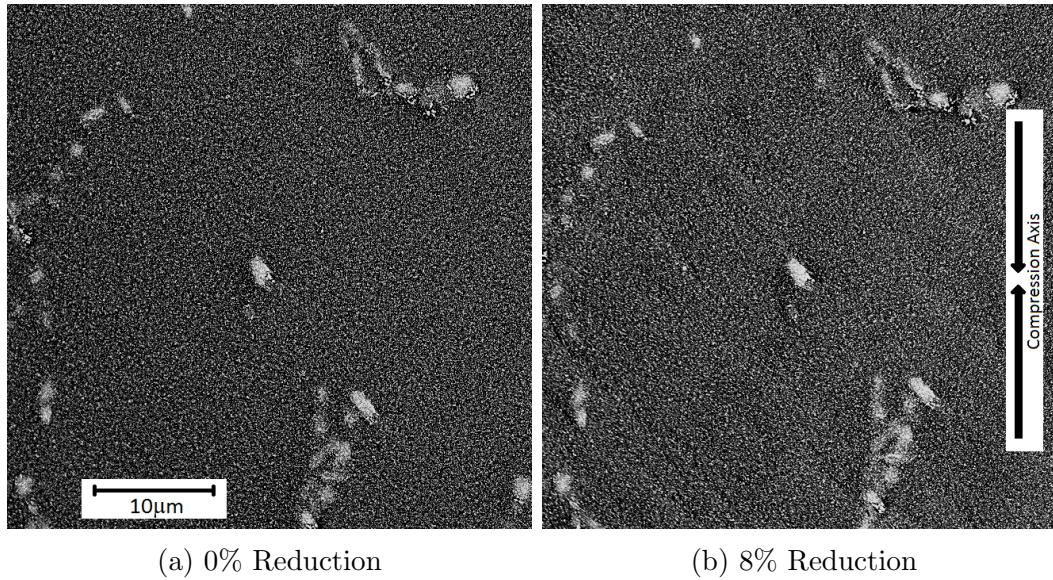
Figure 4.45: Nanopatterned gold on sample surface after remodelling ( $100 \times 100$  pixels in image,  $65 \text{ pixels}/\mu\text{m}$ )

### Single Particle

The region in figure 4.46a centres around a single simple particle (when observed in 2D) within the homogenised sample. The matrix appears to be uniform in this image, and complex particle clusters also visible in the vicinity. The central particle measures approximately  $2.5 \mu\text{m}$  across. After an 8% reduction, as shown in figure 4.46b, variation in the gold pattern now discernible.

The shear strain map produced from these micrographs, shown in figure 4.46c, illustrates that strain is not homogeneous throughout the region, but is concentrated into bands. In this image, bands running parallel to the blue line will be referred to as ‘primary’ bands, while ‘secondary’ will refer to those parallel to the red line. Though the applied strain would equate to  $\approx 0.083$  across the sample assuming homogeneous deformation of all grains, this map shows the localised strain can reach more than three times this amount. Also of note from this image is the numerous areas where strain remains at zero, which when compared to the raw images, corresponds to the particles embedded in the matrix. This confirms the particles are acting as non-deformable regions within the matrix in this alloy system.

The average strain found across the entire region was found to be 0.091, which is slightly higher than the expected value of 0.083 (after a reduction of 8%). Assuming that both the global calculated strain and the average observed strain in this locality are correct, the data suggests that the grain being investigated in this series of images



(c) Shear strain map produced using DIC from images taken at reductions of 0%, 4% and 8%. Red and blue lines indicate source of local strain profiles in figure 4.47

Figure 4.46: Raw images and the resulting strain map produced using step-wise plane strain compression on gold patterned aluminium. X Axis = TD, Y Axis = ND

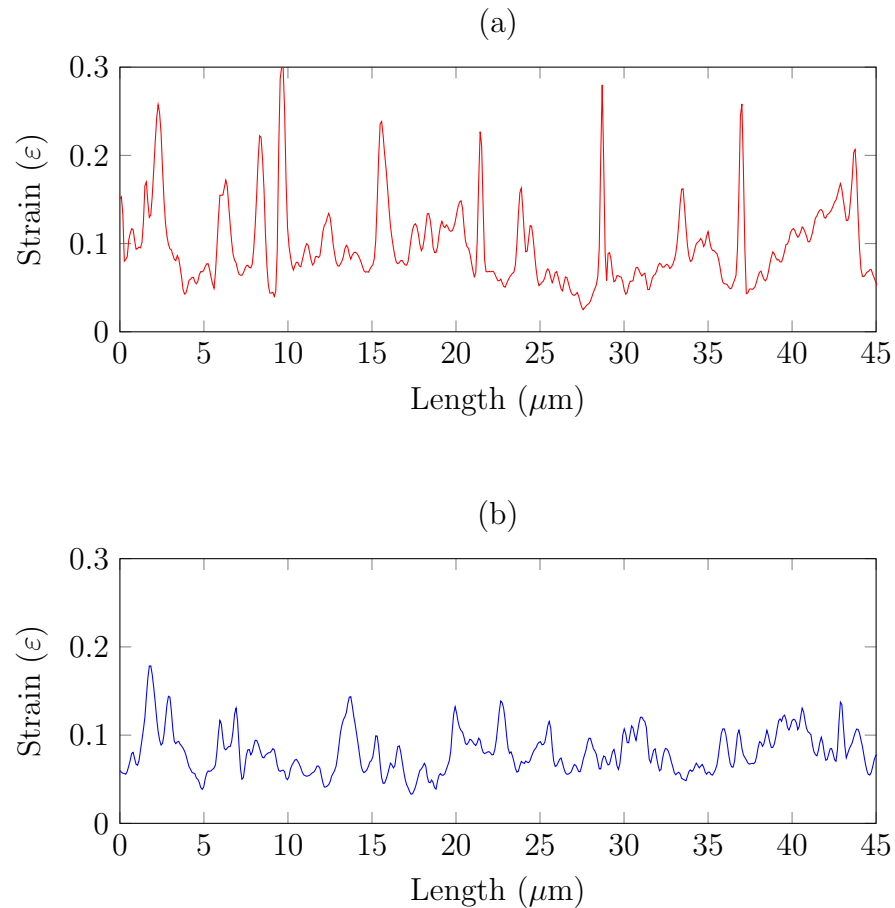


Figure 4.47: Local shear strain profiles taken (a) perpendicular to and (b) parallel to the primary slip bands

is deforming more readily than other nearby grains within the specimen. Though this cannot be confirmed, it helps in illustrating the possible effects of surrounding grains must be considered when studying polycrystalline materials.

Figure 4.47a shows a line plot of the local strain when bisecting the primary slip bands. In this plot, the heterogeneity of deformation is illustrated, with the high observed strain at slip bands peaking at over five times the local strain found in the nearby matrix (on the line plot, this is shown at  $\approx 9 \mu\text{m}$  and  $\approx 28 \mu\text{m}$ ). The minimum distance found between two primary slip bands (i.e. the matrix between the bands has a strain of less than or equal to the expected global strain - in this case 0.083) was found to be  $1.31 \mu\text{m}$ .

The line plot in figure 4.47b shows variation in strain in a region between two primary slip bands. The peaks in this plot illustrate the strain is again concentrated into secondary slip bands, though these slip bands are less prominent from the initial strain

map. Visual inspection of the strain map results in seemingly wider spacing between the primary slip bands than the secondary slip bands, though when comparing the line plots, the spacing of undulations in the strain profile is similar in both directions.

A marching Radon transform<sup>5</sup> was used to determine how the slip bands are aligned within the strain maps produced at 4% and 8% reductions, as shown in figure 4.48. In short, this process characterises the dominant, local line features (slip bands) within the strain map, and determines the orientation of these slip bands. The use of Radon transforms to study alignment of slip bands from DIC data was included in work by Ko [Ko, 2014] and has also been used to study grain boundary alignment [Humphreys and Bate, 2006]. The MATLAB script used to create these plots has been modified from the code included in the work by Ko [Ko, 2014]. The amended script is incorporated into the appendix (section A.3). This script acts to separate the grey scale strain map into subregions ( $\sim 2 \mu\text{m} \times 2 \mu\text{m}$ ) and perform a Radon transform on each subregion. This script also incorporates a noise reduction algorithm which removes outlying data points (greater than twice the standard deviation from the mean). The data from each subregion is then combined, and the resulting data is normalised.

In these Radon transforms, the axes are fixed in the global transverse and normal directions of the sample. This plot indicates that the slip bands are strongly aligned at  $\pm 45^\circ$  to the normal direction after the first compression step (4% reduction), as indicated by the blue dataset. These peaks are narrow as the slip bands themselves are straight and widely spaced throughout the material, thus ensuring that there are few interactions of slip bands which could affect alignment. With increased deformation, the alignment of the slip bands remains centred at  $\pm 45^\circ$ , though these peaks broaden considerably. This broadening is due to the increased number of resolvable slip bands which increases the likelihood of interaction between two perpendicular slip bands, thus leading to a shift in the alignment of each interacting region of the slip bands.

Of note here is that the broadening of the peaks in alignment is not symmetrical around the peaks at  $45^\circ$  and  $-45^\circ$ , but instead the slip bands are found with an increasingly negative rotation after deformation. As this effect is seemingly uniform across the region, the rotation map of the grain was determined using the image correlation

---

<sup>5</sup>A Radon transform is a projection of the image intensity along a radial line oriented at a specific angle [Gindi and Gmitro, 1984].

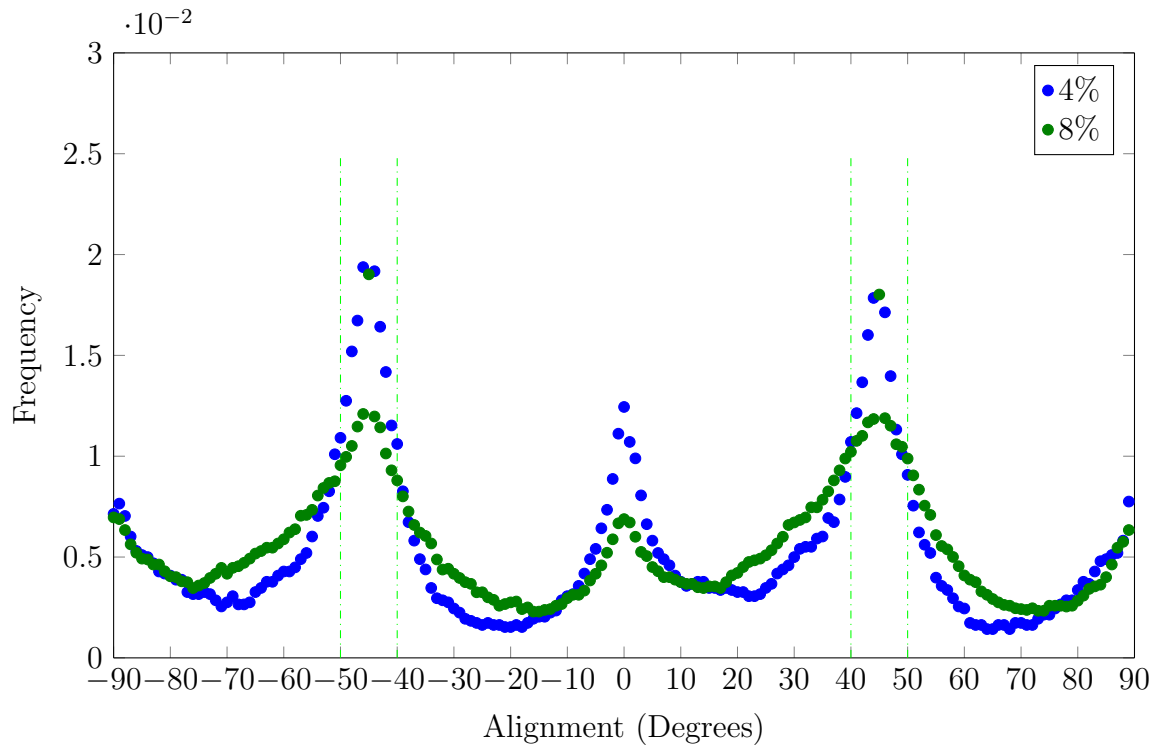


Figure 4.48: Alignment of slip bands at 4% and 8% reductions, produced using a Radon transform from the shear strain data

data as shown in figure 4.49.

The rotation map shows that the grain as a whole is rotated anticlockwise as a result of the 8% compression. The primary slip bands are generally shown to have a near zero rotation from this map, with some isolated positively rotated regions found within these high strain areas.

Also of note from the Radon transform of the DIC data is the peak at  $0^\circ$  which is less prominent after the second compression. After careful study of the original shear strain maps, these peaks have been attributed to artefacts created by the DIC software at low strains. These may be due to drift within the SEM, resulting in very slightly offset regions in the BS-SEM images. When comparing the maps produced at 4% and 8% reductions, the artefacts are no longer visible due to improved contrast of the slip traces within the strain map. The raw strain maps used for the Radon transforms are included in the appendix for comparison (section A.4).

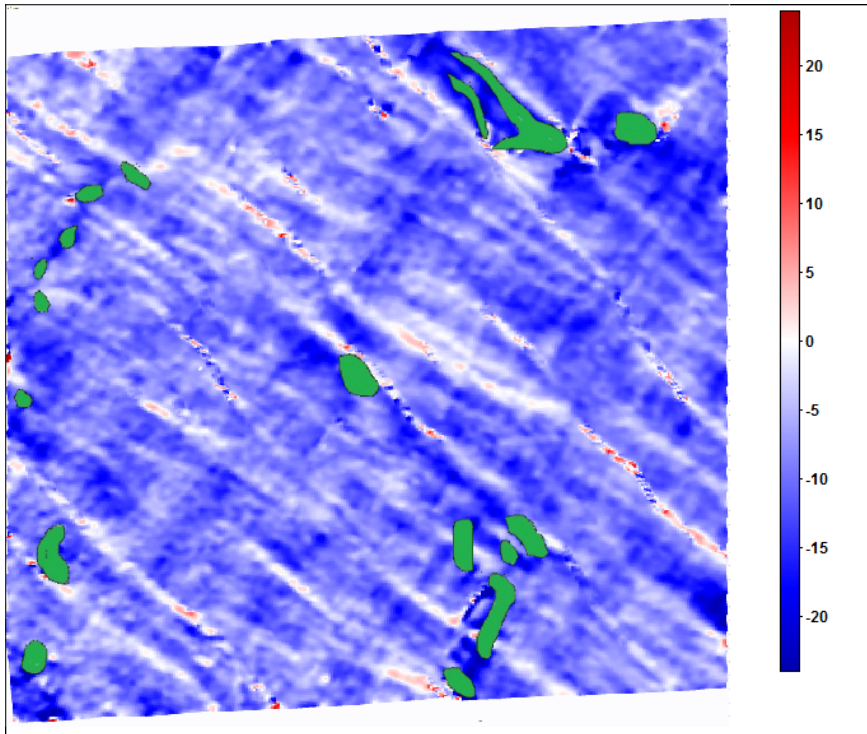
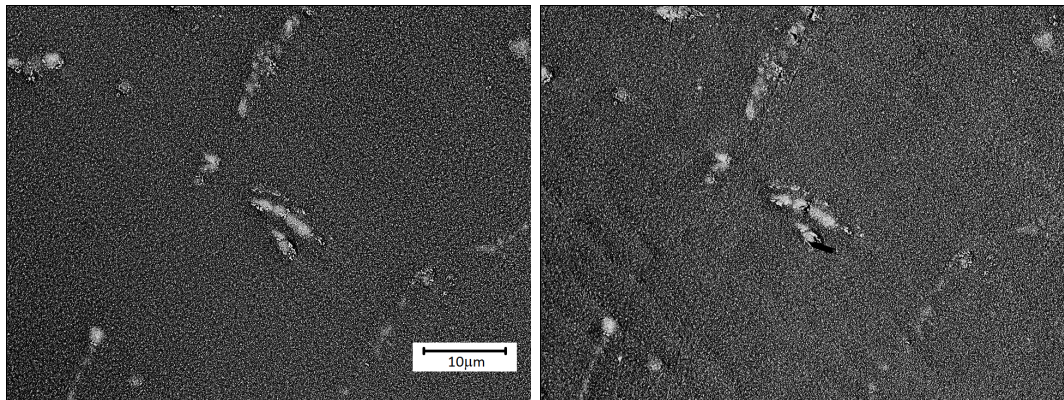


Figure 4.49: Rotation map produced using DIC from images taken at reductions of 0%, 4% and 8%. The particles visible on the surface have been included as a green overlay. All rotations are in degrees.

### Particle Cluster

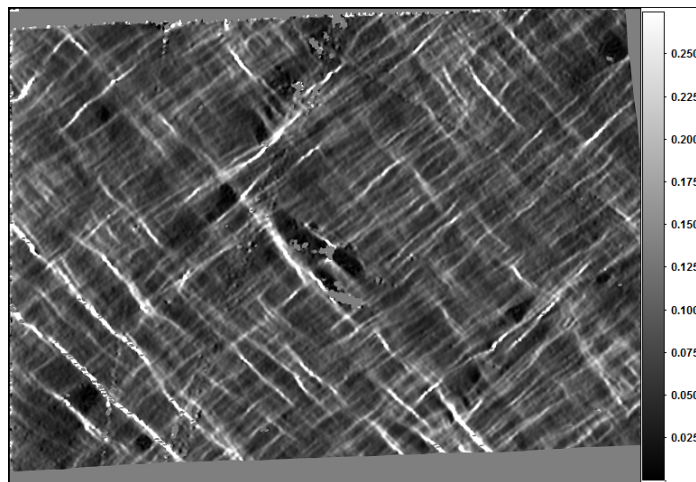
A second dataset was obtained which centres around a small cluster of particles as shown in figure 4.50. The SEM images in this figure indicate that the deformation has resulted in some break up of the central cluster, which translates to a small region which can not be image correlated due to the absence of gold pattern within the void. The strain map obtained for this region contains peaks of the same direction and magnitude to the previous example, while the rotation map indicates similar extremes of local rotation. As these datasets were taken from the same sample of material, it is likely that these regions fell within one large grain. This rotation map again suggests that the formation of highly rotated zones is more apparent in regions close to particles, however, further DIC of material which has undergone larger global strains would be needed to verify this.

The central particle has been magnified in figure 4.51 to allow the local rotations close to the particle cluster to be visualised more clearly. Here the map has been renormalised so that the mean rotation is taken as centre point of the colour map. In this image, the highest rotations and gradients of rotation are found in the matrix in

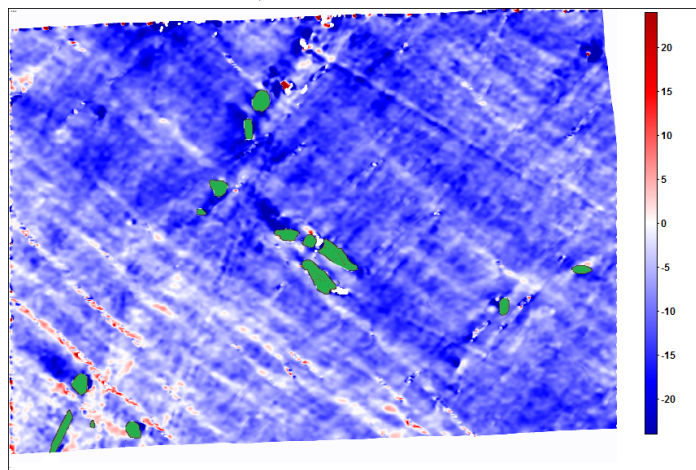


(a) 0% Reduction

(b) 8% Reduction



(c) Strain map produced using DIC from images taken at reductions of 0%, 4% and 8%.



(d) Rotation map produced using DIC from images taken at reductions of 0%, 4% and 8%.

Figure 4.50: Raw images and the resulting strain and rotation maps produced using step-wise plane strain compression on gold patterned aluminium containing a particle cluster. X Axis = TD, Y Axis = ND

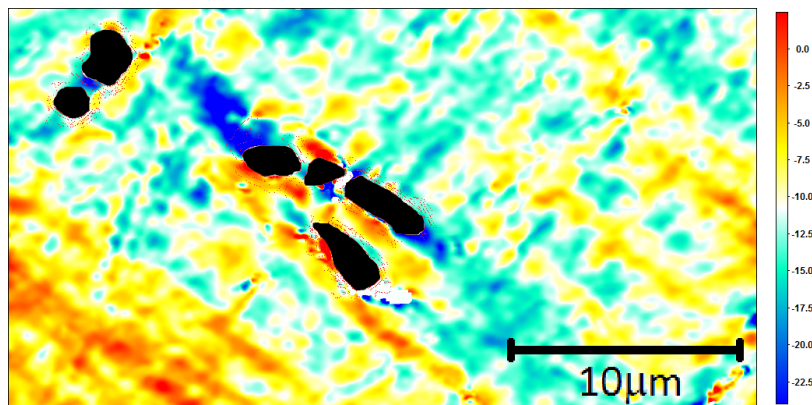


Figure 4.51: Magnified rotation map illustrating the complex rotations near to a particle cluster

regions closest to the second phase particles, and notably, the dark blue plume shown here shows the maximum total rotation found within the rotation map, though the particle that this is attributed to is not the largest particle in the region. Due to the number of non-deforming particles in a small area, the plume configuration does not follow the generally observed ‘4 plume’ structure found in previously reported works [Humphreys et al., 2012, Ko, 2014].

The Radon transform obtained using the strain map for this data (figure 4.50c) is presented in figure 4.52. This shows that the slip band alignment within this dataset behaves in exactly the same manner as the previous data set, thus reinforcing that the two regions are both of the same orientation and are deforming co-operatively.

### 4.3.2 Crystal Plasticity FEM

The crystal plasticity finite element model originally developed by Bate [Bate, 1999] has been used and validated in a number of works [Humphreys et al., 2012, Ko, 2014], acting as a reliable tool to determine the size, shape and rotation of deformation zones. As part of this work, the CPFEM has been altered to allow each element within the model to be assigned material properties individually. This allows particles to be incorporated into the model, thus allowing the model to be expanded for study of the effects of non deformable particles on local deformation within the matrix.

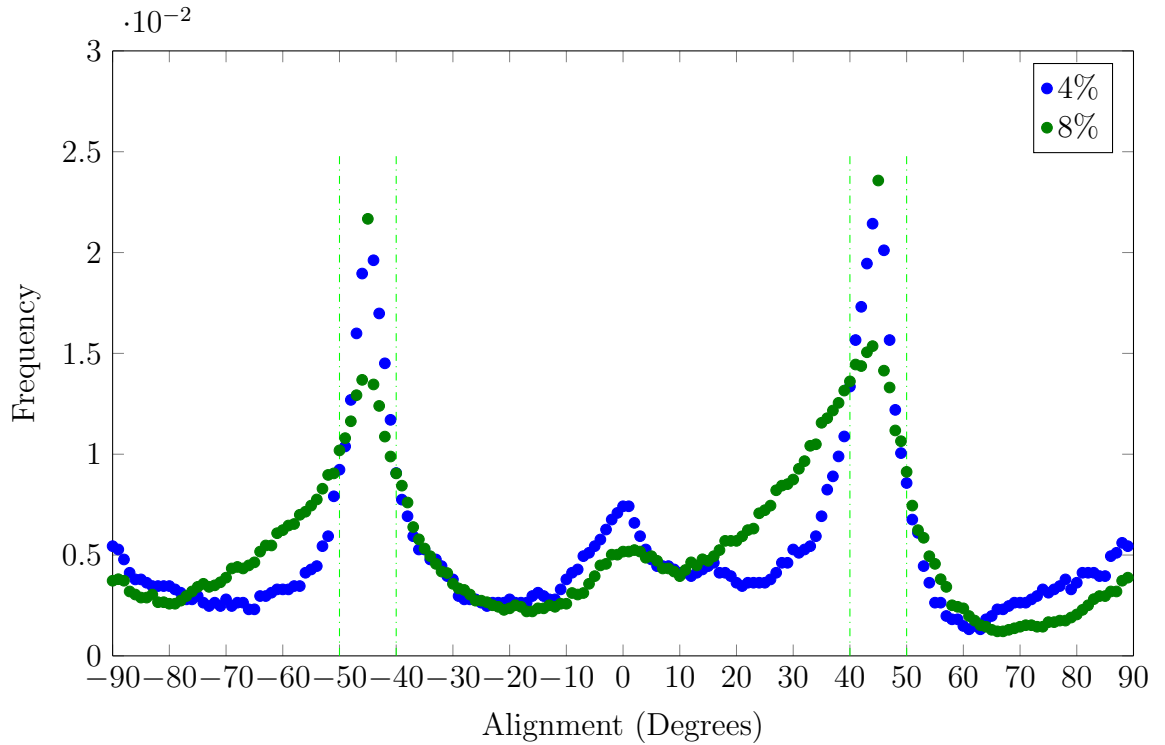


Figure 4.52: Alignment of slip bands at 4% and 8% reductions, produced using a Radon transform from the data in figure 4.50c

### Perturbation Variance

When designating the orientations of elements within the mesh, the model can be designed to act as a single crystal (where all elements have the same starting orientation) and thus model the internal workings of a grain. However, as shown in figure 4.53a, the model proceeds to allow completely homogeneous deformation, resulting in a failure to successfully produce the cellular substructure and strain gradients which are known to be generated within a real grain (as illustrated in the previous section). If this model is designed with a ‘perturbed’ characteristic, each element is programmed to have a very slight variation from the given orientation, which encourages strain gradients to form within the model, as shown in figures 4.53. Using this method, the ‘perturbed’ value indicates the magnitude of variation from the ideal orientation.

From figure 4.53, the strain measured at each point in the mesh after deformation is shown to become increasingly heterogeneous as the starting condition is ‘perturbed’ using larger misorientations. The difference between the maximum and minimum local strain found in each simulation has been determined at a range of deformation steps for a variety of initial misorientations. These strain ranges have been normalised as:

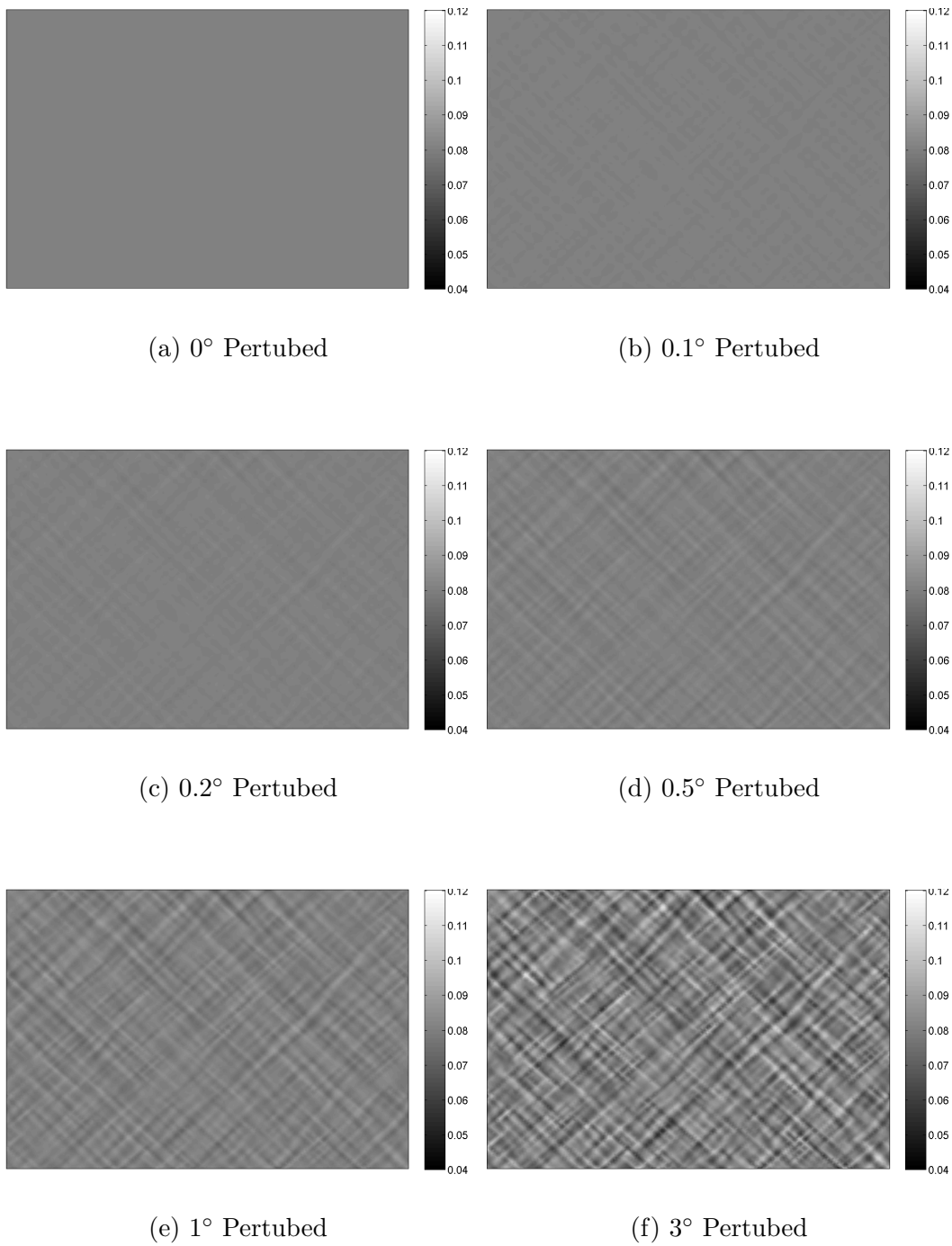


Figure 4.53: Variation in how the orientations are ‘perturbed’ alters local strain, each image shows the result from the 80th iteration of the respective models.

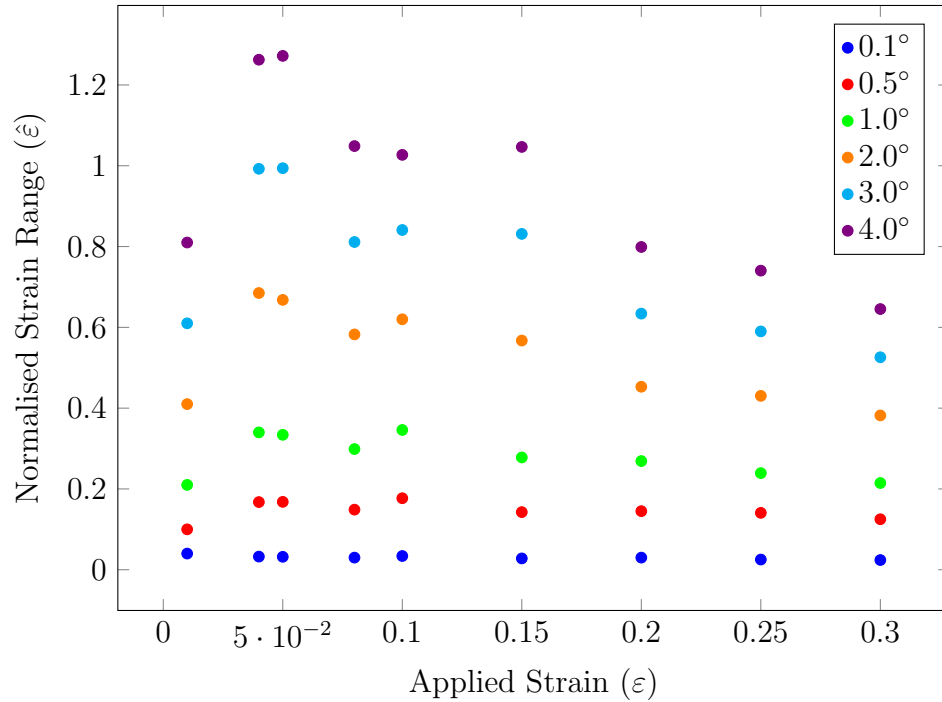


Figure 4.54: The variation in strain in the CPFEM with increasing deformation with varying initial orientation perturbed values

$$\hat{\epsilon} = \frac{\epsilon_{\max} - \epsilon_{\min}}{\epsilon_{\text{mean}}} \quad (4.9)$$

where:

$\hat{\epsilon}$  = Normalised strain range

The evolution of the normalised strain range with varying perturbation within the matrix is shown in figure 4.54.

As shown in figure 4.54, the differences in magnitude of the normalised strain range within the model are found to be a function of both how perturbed the model was programmed to be and the extent of deformation. The plots for each of the perturbed values presented follow similar routes, which have a sharp increase in heterogeneous deformation within the first stages of processing and then peaks at an applied strain of 0.05. The maximum value presented here (for a perturb range of 4°), shows that at an applied strain of 0.05, the range of strain values within the mesh vary by 0.0636 ( $\hat{\epsilon} = 1.27$ ). One explanation for the variations in strain in increasingly perturbed configurations is the effect that altering the orientation of each element has on any mutual deformation between neighbouring elements. In essence, this would allow some

regions of to deform more cooperatively than others. By increasing the extent of the perturbation parameter, it becomes increasingly likely that clusters will become less capable of cooperative deformation, resulting in regions which are progressively more difficult to deform, forcing any aligned cluster of elements to accommodate extra strain to maintain the boundary conditions.

Parallels can be drawn between the strain gradients obtained when changing the perturbed parameter within the CPFEM and the slip bands found when studying deformation using digital image correlation. In all simulations, the spacing found between these regions was independent of the amount of perturbing, with only the intensity of the resulting strain gradient changing as the perturbing parameter was altered. For further simulations, the perturbing parameter was set to 0.5 to ensure that while the presence of strain gradients within the model were ensured, the extent of these gradients would not interfere with the intensity of deformation attributed to a non deformable region, thus allowing the effect of the configuration of non-deformable region to be closely examined.

### 4.3.3 CPFEM - One Particle

Non deformable particles were set by setting the slip resistance of the non-deforming elements to 999,999 MPa. As this slip resistance is much higher than the true value for a constituent particle, it should be noted that any simulation results which demonstrate very high local stresses would not be verifiable in real materials. For these simulations, the terms S1 and S2 will be used to describe the two primary slip systems, the directions of which are demonstrated in the perturbed simulation results (i.e.  $\pm 45^\circ$ ). These labels were chosen in reference to the slip shadowing model mentioned earlier(2.4.3), and the implications of the CPFEM on the slip shadowing model will be discussed in section 5.2.4. All simulation results presented from the 300th iteration of the model ( $\varepsilon = 0.3$ ), and maximum strain values are presented as a multiple of the applied strain.

#### Effect of Particle Size

The images in figure 4.55 illustrate the resulting size and shape of the deformation zones when the size of the non-deformable region was altered. Within these plots, the non deformable region is illustrated in green, with positive and negative rotations of

the matrix indicated by the colours shown in the scale bar. All rotations have been stated in degrees.

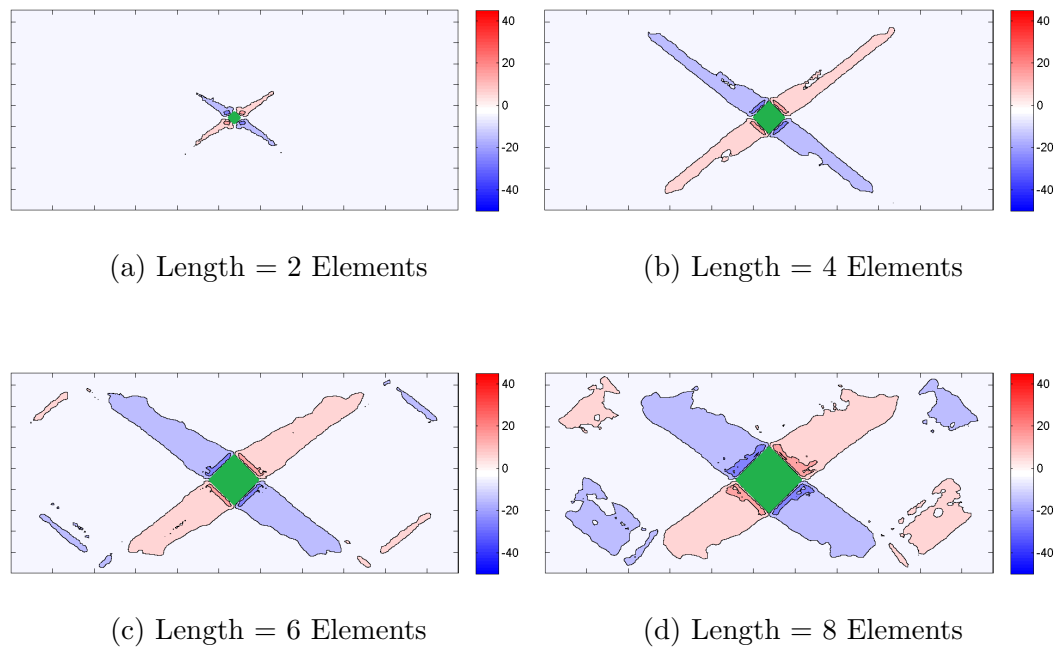


Figure 4.55: Changes in local rotation of the matrix with increasing particle size

In this figure, the rotated zone is shown to extend further from the non-deformable region as the particle size is increased, resulting in interactions with the simulation boundary. This is most clearly shown in figure 4.55d as secondary rotations are generated at the corners of the simulated grain. These simulations were used to determine the size of particles to incorporate into the CPFEM for further simulations, with the particle shown in figure 4.56b used as the standard particle morphology in multiple particle simulations. Figure 4.56a shows how the maximum local strain found within the model increases approximately linearly with respect to the particle size. The highest values of strain are found at the corners of the non deformable region in all cases. Images which demonstrate how the local strain changes as a function of particle size are included in the appendix chapter as figure A.6.

The bar chart in figure 4.56b illustrates how the average area of the highly rotated plumes (regions of rotation larger than  $15^\circ$ ) surrounding the particle changes as larger particles are incorporated into the system. This data fits to an exponential curve.

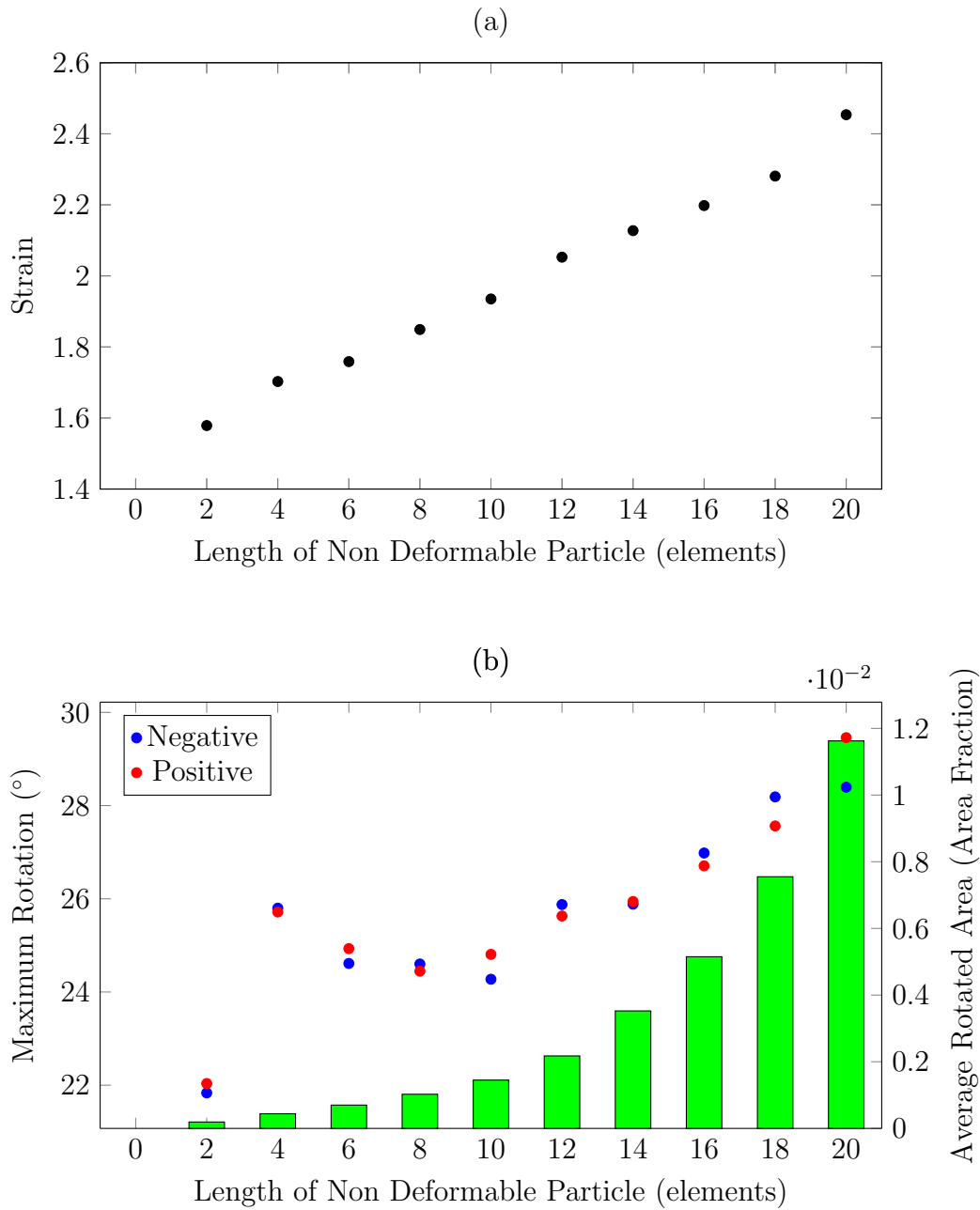


Figure 4.56: (a) Plot showing how the maximum local strain (as a multiple of the global strain) within the CPFEM changes with particle size. (b) Plot showing the largest measured rotations (scatter) and the average area of the highly rotated zones (bar) within the CPFEM with changing particle size

Due to the parameters of the model, it is the length of the particle (or more precisely the length of the boundary between the deformable and non-deformable region) which dictates the behaviour of the non deformable region. The inclusion of hollow particles in this model would yield the same result in terms of large interactions outside the particle, and for this reason, the effect of the area of the particle has not been included when discussing the deformation zone behaviour. In this case, the four plumes of rotation have approximately equal magnitude and volume across all simulations.

The maximum values of rotation found within the simulations are also included in this plot, showing that the maximum rotation is shown to increase in general as a function of the particle size. This increase however is not completely linear with a large initial boost in the outlying rotations as the particle is doubled in length, which then tends towards a linear increase with further boosts to particle size.

### Effect of Aspect Ratio

The effect of altering the aspect ratio of the non-deformable region was also investigated using the CPFEM, resulting in the data presented in figure 4.57. In these simulations, the height of the particle was constant at 7 elements but the length was altered. This allows regions of limited mobility to develop above and below the particle in which, though slip through the particle was blocked, some local rotation occurs. Here the observed maximum strain within the simulation was found to reach a minimum when the aspect ratio was 1 (Note: The aspect ratio of 0.86 refers to a particle 6 elements in length). The maximum observed rotations within the matrix, and the area of the highly rotated zone was found to increase approximately linearly with increasing particle aspect ratio from these simulations.

From the comparison of the aspect ratio and overall size measurements, plotted together in figure 4.58, differences are found between the maximum local strain and maximum rotations near to the non deformable region. The average area of the plumes of rotation are similar for equivalent particle lengths in these simulations.

In the case of the size simulations, the length of the non deformable region which forms a direct boundary with the matrix is:

$$L = \sqrt{2 \times \left(\frac{l}{2}\right)^2} \quad (4.10)$$

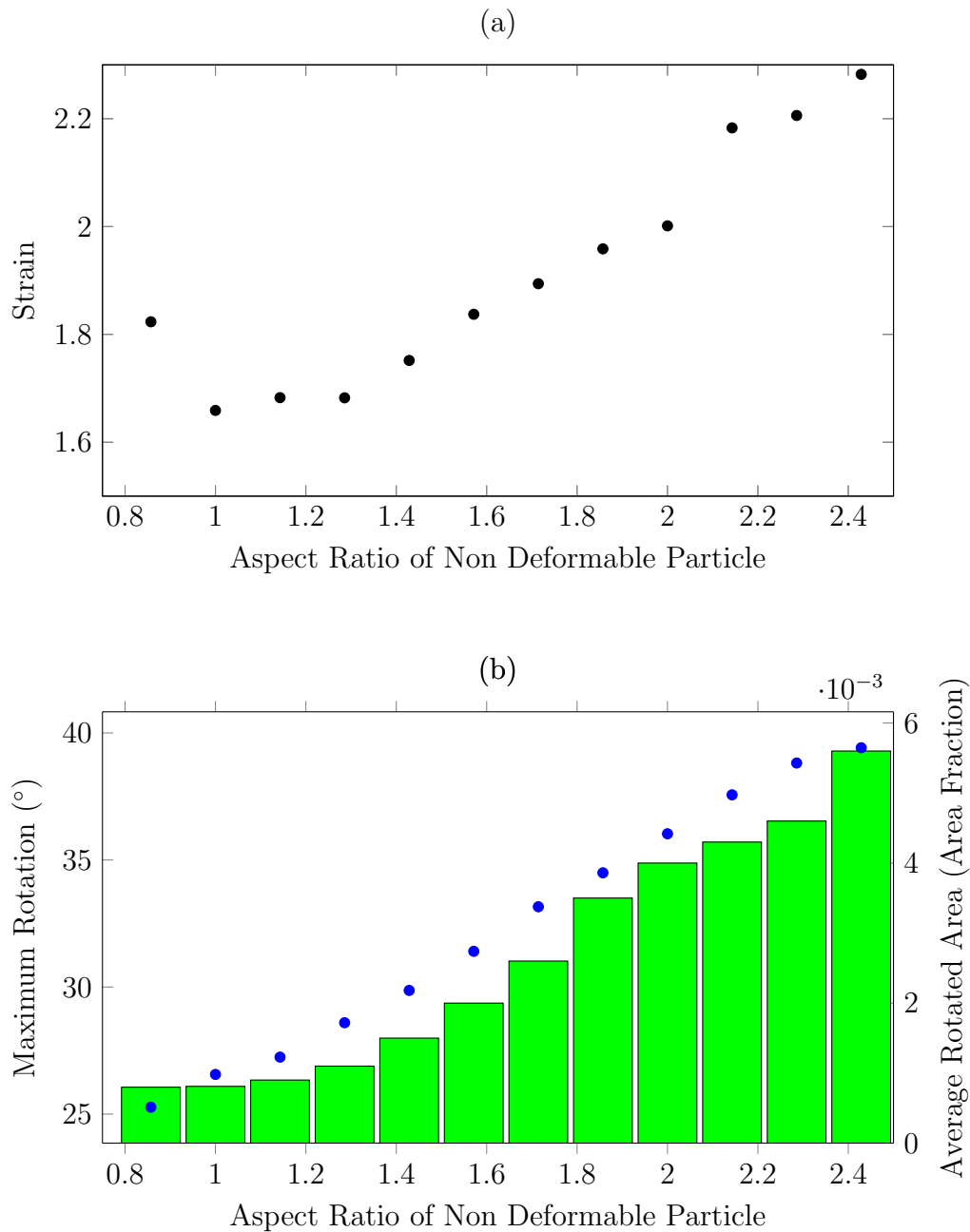


Figure 4.57: (a) Plot illustrating how the maximum local strain within the CPFEM changes with increasing particle aspect ratio. (b) The average size of each heavily rotated plume (bar) and maximum rotation predicted with changing aspect ratio.

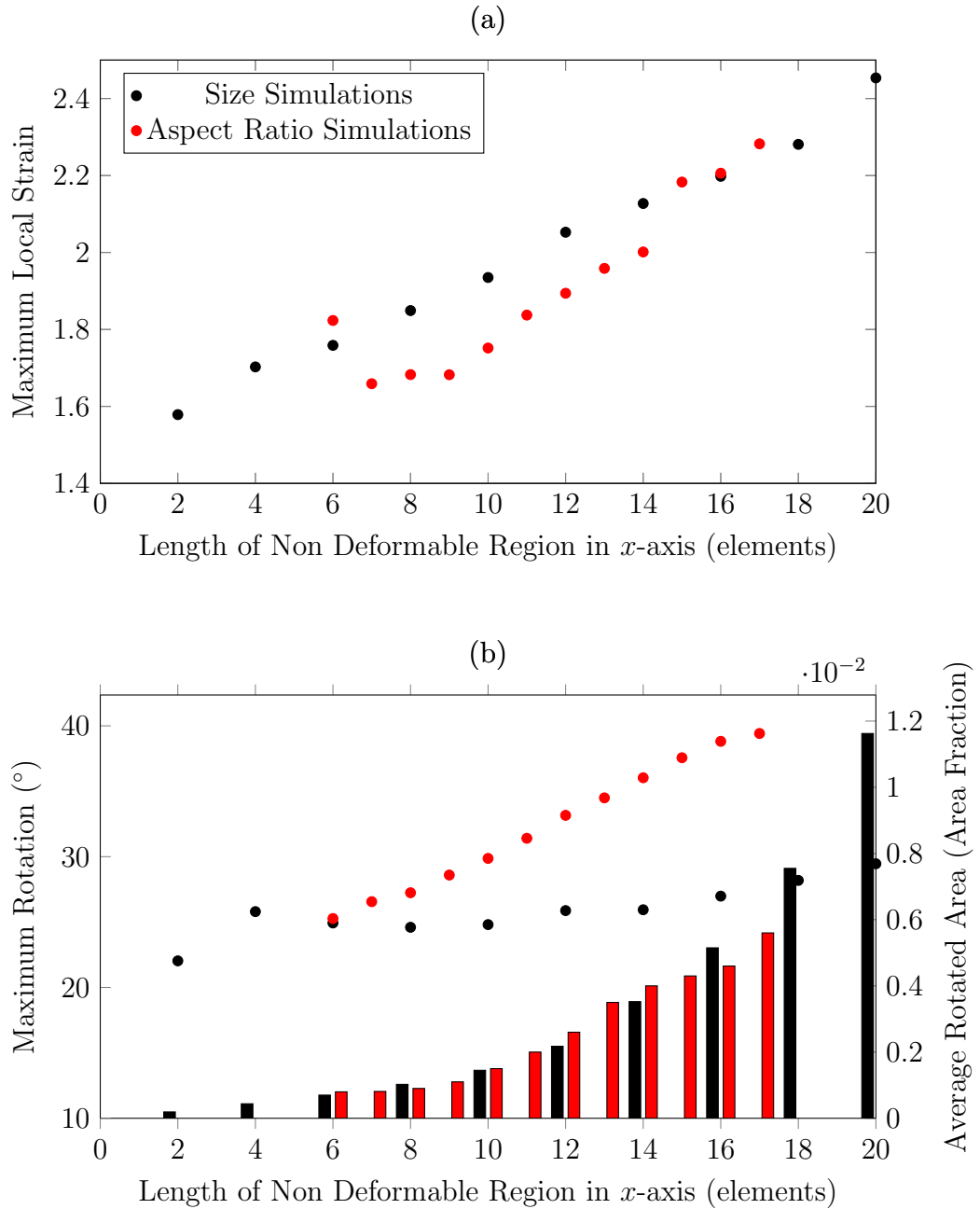


Figure 4.58: Comparison of the particle size and aspect ratio plots for (a) maximum local strain and (b) average size of each heavily rotated zone (bar) and maximum rotation.

where:

$L$  = Interaction length

$l$  = Length of particle in  $x$ -axis

In the aspect ratio measurements however, this direct interaction is  $\approx 5$  elements at each corner. This results in a more localised rotation at the smaller interaction length between the high aspect ratio particle and the matrix, resulting in higher maximum rotations found in simulation of long thin particles. The regions above and below the particle act as possible sites for the strain to dissipate within the aspect ratio simulations, allowing smaller local strain maxima.

### Effect of Orientation

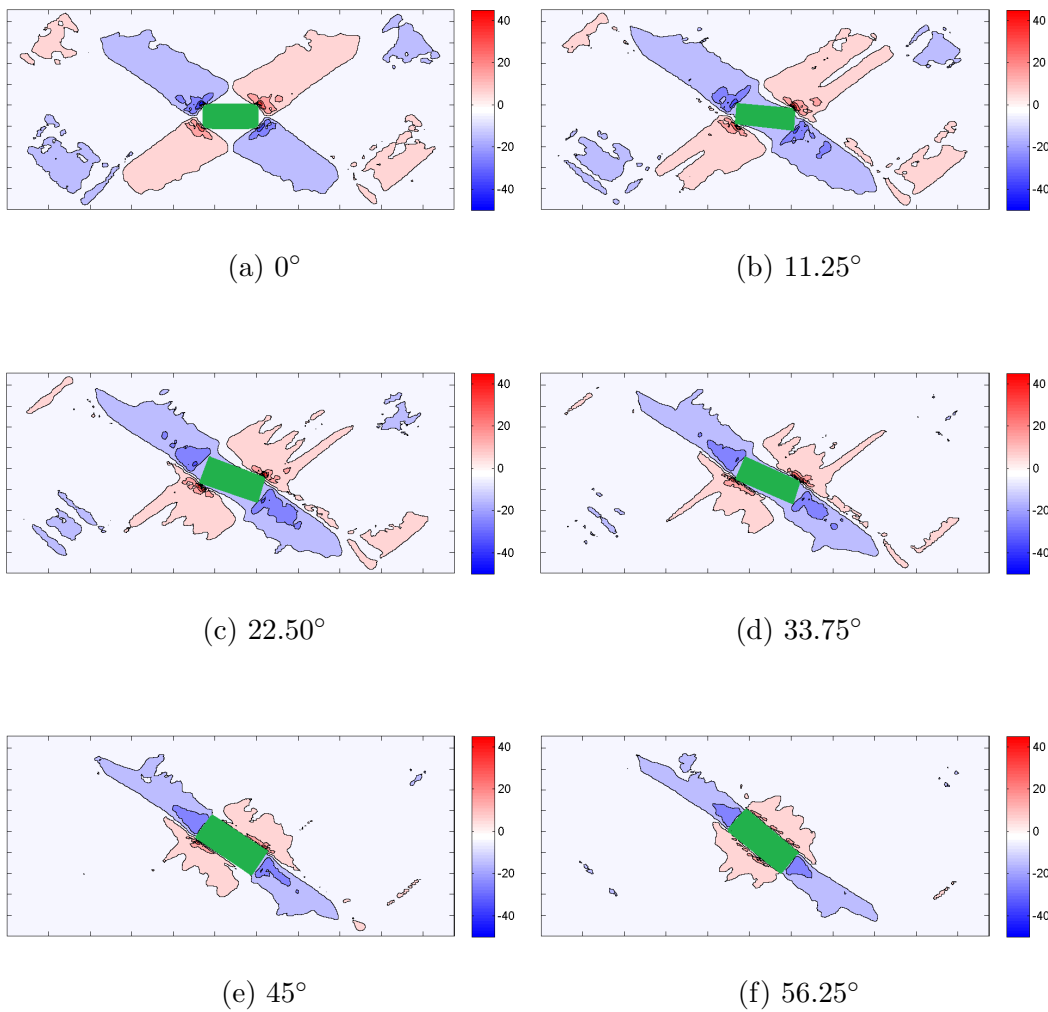


Figure 4.59: Changing the orientation of the non deformable region

The link between deformation zones and the interruption of slip by a non deformable region has been investigated using the CPFEM by altering the orientation of an elongated particle with respect to the main slip systems as shown in figure 4.59.

As the particle is input into the model with an increasing initial rotation with respect to the  $x$  axis, the CPFEM acts to rotate the entire non deformable region, illustrating that the CPFEM can model the alignment of second phase particles towards the rolling direction during deformation processes.

Figure 4.60a shows how the maximum value of strain found within the system changes as the rotation of the input particle is altered. Examples of the strain outputs for these simulations are included the appendix (figure A.7). In this case, the minimum vales are found when the particle is initially aligned parallel, at  $\approx 56^\circ$  to, and perpendicular to the  $x$  axis. Due to the act of the CPFEM rotating the entire non-deformable region during deformation, the particle which is initially included at  $\approx 56^\circ$ , has a final alignment closer to  $\approx 45^\circ$  from the  $x$  axis. This means that any predictions of deformation behaviour in systems in which a particle can rotate should allow for such particle realignments as this would act to change the intensity of the effect of such particles on the local strain and rotation within the matrix.

Due to the different effective lengths of the particles in terms of the number of S1 and S2 traces that are blocked as the particle rotates, the areas corresponding to positive and negative rotations are treated separately for simulations where the particles are not aligned in the  $x$  axis. From figure 4.60b, the largest positive rotations are shown to initially increase as the particle is rotated, with a maximum rotation within the matrix found when the particle is input at  $22.5^\circ$  from the  $x$  axis. This also corresponds to the largest area of the negatively rotated region of all simulations, and the highest local strain. The smallest peak rotations, as well as the smallest rotated zone are found at the  $56.25^\circ$  input, suggesting that this is the optimum initial orientation out of those investigated if the aim is to minimise the effect of particles on the deformation of the matrix. Due to the rotation of the particle during deformation, it is likely that further plane strain compression may act to rotate the particle further, and thus alter the local rotations and strains.

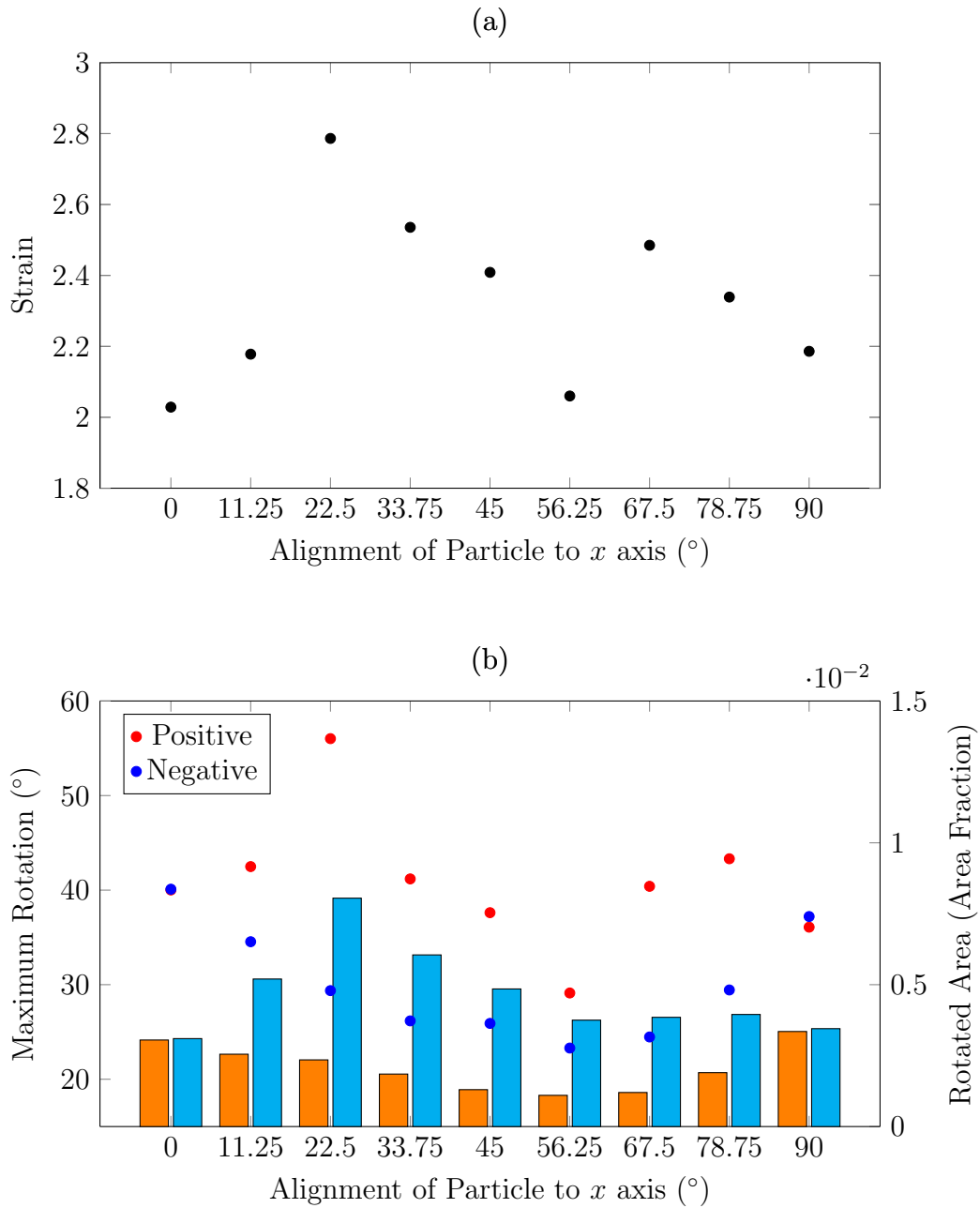


Figure 4.60: (a) Plot showing how the maximum local strain within the CPFEM changes with particle orientation. (b) Plot showing the largest measured rotations (scatter) and the area of the highly rotated zones (bar) within the CPFEM with changing particle orientation with respect to the  $x$  axis

#### 4.3.4 CPFEM - Two Particles

By incorporating two particles of equal size (6 elements) within the CPFEM and altering their relative position, the effects of particle clustering have been investigated.

##### Effect of Distance

Two particles were aligned along one of the major slip systems, and the distance between the particles were altered as shown in figure 4.61. In these simulations, plumes of rotation can interact, and the resulting total areas of the rotated regions are illustrated as part of figure 4.62.

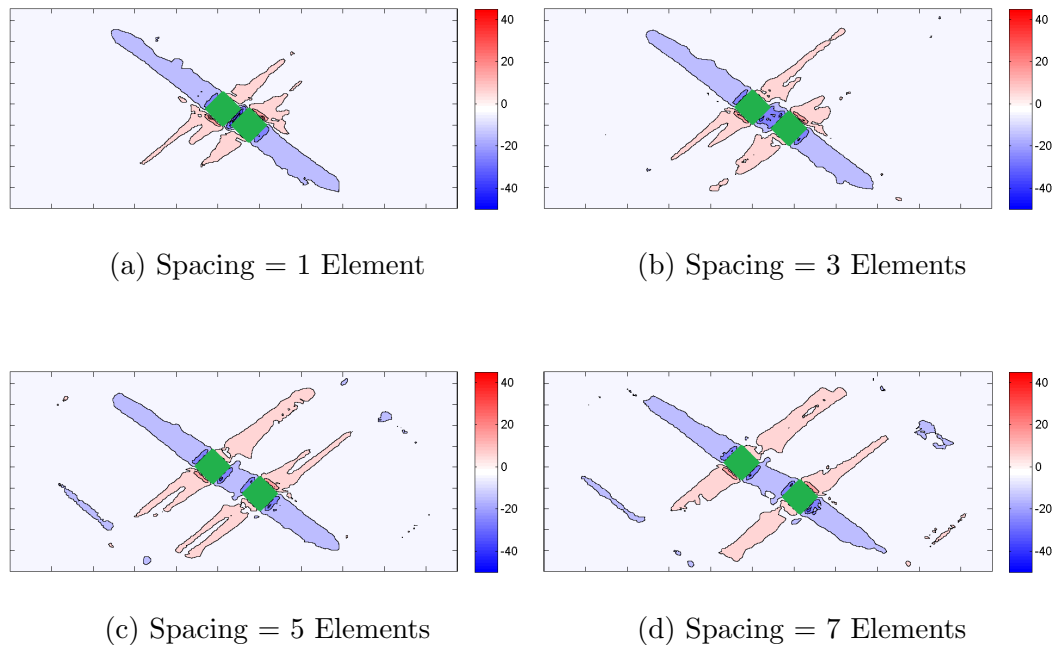


Figure 4.61: Images depicting how changing the distance between two non deformable regions aligned at  $45^\circ$  to the  $x$  axis changes the resulting rotations within the matrix

The maximum local strain found within this range of simulations occurs in matrix between the particles, when the interparticle spacing is at its smallest. In this case, the gap between the particles within the model is one element thick, which allows unencumbered deformation on the second slip axis. As the interparticle spacing increases, the local strain maxima remain adjacent to the non deformable regions, though the intensity of these maxima diminishes initially to minimum with a spacing of 3. This strain value is shown to climb in the remaining simulations. The strain plots are

included as figure A.8.

Figure 4.62b shows that the maximum rotations found within these simulations decrease with increasing interparticle distance. The maximum negative rotation is found to be generally larger than the positive counterpart in all cases, sometimes by a wide margin. These maximum negative rotations are invariably found within the plume generated between the two non deformable regions, suggesting that in some cases the spacing and alignment of particles with respect to the slip plane may result in larger rotations within the matrix than can be generated by a particle in isolation.

The area of the negatively rotated matrix is found to be much larger than the positively rotated areas in all simulations in this sequence. This is firstly attributed to the general trend noted earlier when investigating particle orientation, that when a long particle is placed within the mesh at  $45^\circ$  to the  $x$  axis, the plumes generated after deformation are asymmetrical. However, there is also a notable increase in the area of the negatively rotated region as the two non deformable regions separate. In a similar vein to the case of maximum rotations, this may also be a result of the interaction between the plumes generated between the two particles.

Figure 4.63 illustrates the deformation zones which result from two particles with varying distance which are aligned at  $45^\circ$  from the active slip systems. When the particles are placed with minimal space between them as in figure 4.63a constraints within the model result in the two particles affecting the matrix in the same way as one long particle as shown earlier in figure 4.59a. Though there is space between the non deformable regions in this case, the configuration of particles acts to prevent slip in the space between the two particles. It is this obstruction which forces the model to group the two particles into one larger non deformable region.

As the interparticle spacing increases to the point that slip can occur between the particles, very high rotations are found in plumes which form between the two particles. As spacing increases to a critical point (in this case the spacing is equal to the particle radius) the plumes generated between the two particles reach their highest measured values of rotation. As interparticle spacing increases past this critical point, the four plumes associated with each particle begin to equalise. The strain measured in the model reaches its highest value at the point at which the four internal plumes converge, and the configuration with the highest strain value occurs with the

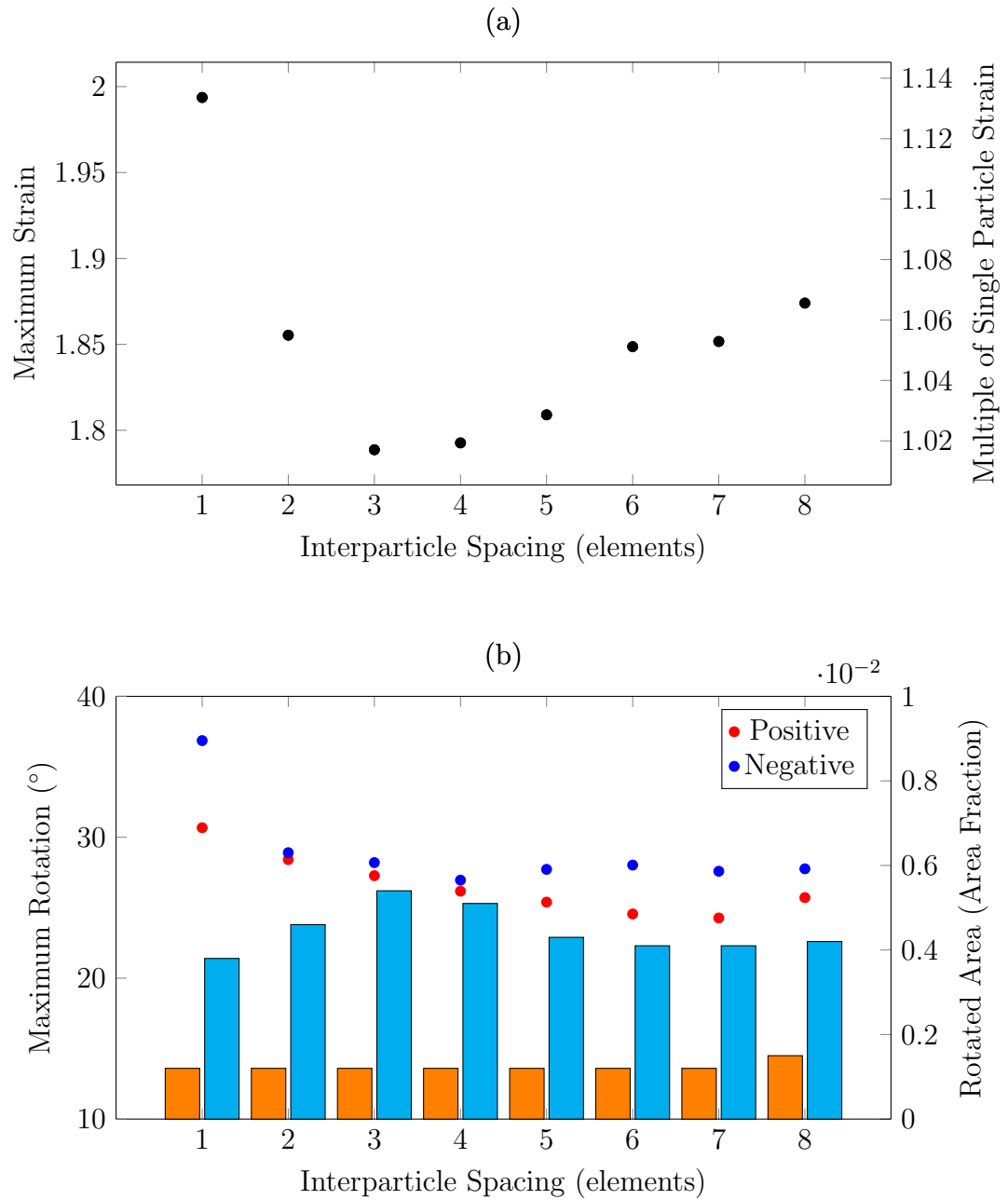


Figure 4.62: (a) Plot showing how the maximum local strain within the CPFEM changes with interparticle spacing. (b) Plot showing the largest measured rotations (scatter) and the area of the highly rotated zones (bar) within the CPFEM with changing interparticle spacing when particles are aligned at  $45^\circ$  to the  $x$  axis

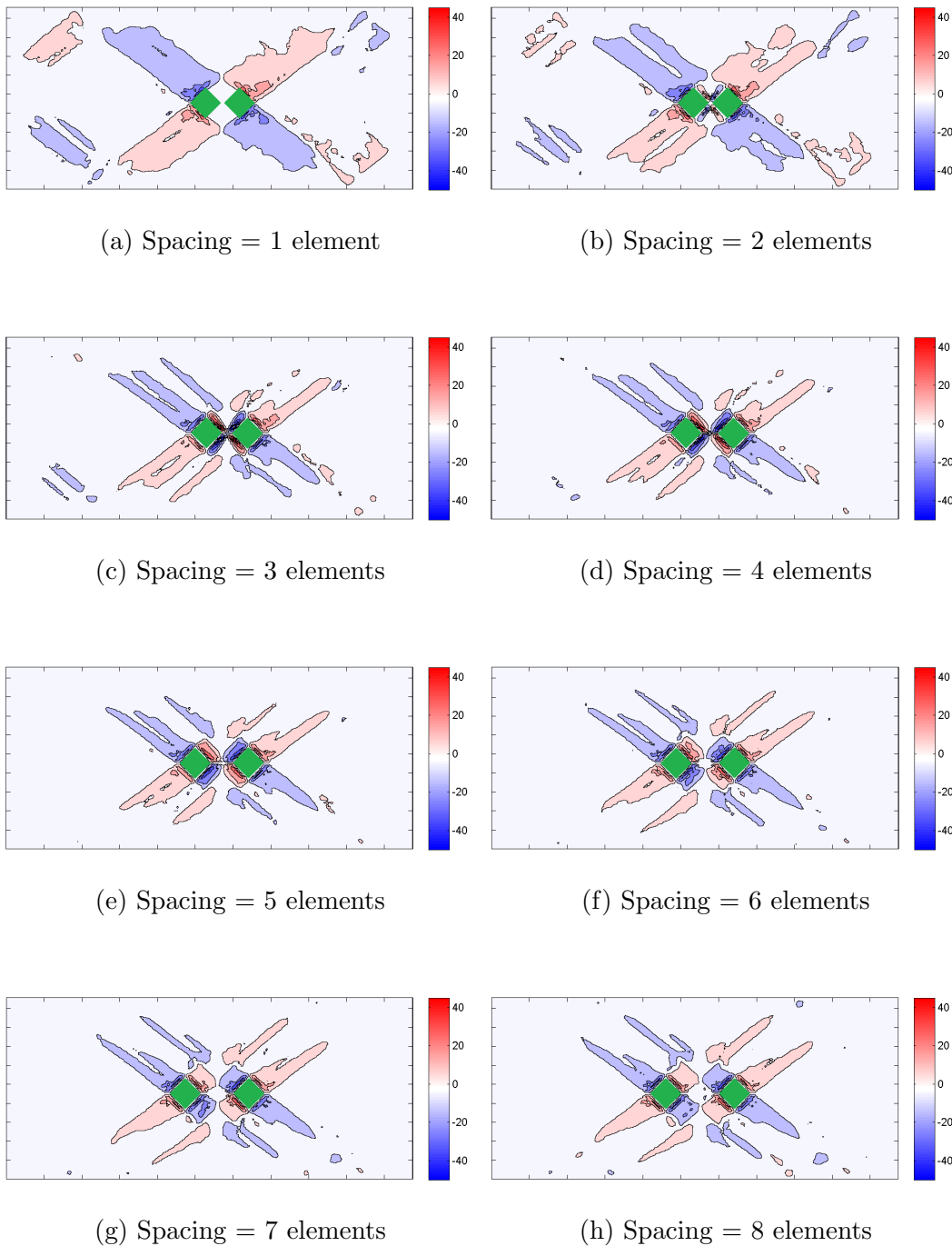


Figure 4.63: Images illustrating how changing the distance between two non deformable regions aligned along the  $x$  axis changes the local rotations within the matrix

spacing of 4 elements. This illustrates the point at which the CPFEM predicts two particles would interact to create the largest overall effect on the local grain in terms of localised strain. The strain found at this point is more than twice the magnitude of the strain determined for a single particle in isolation in the same crystal under

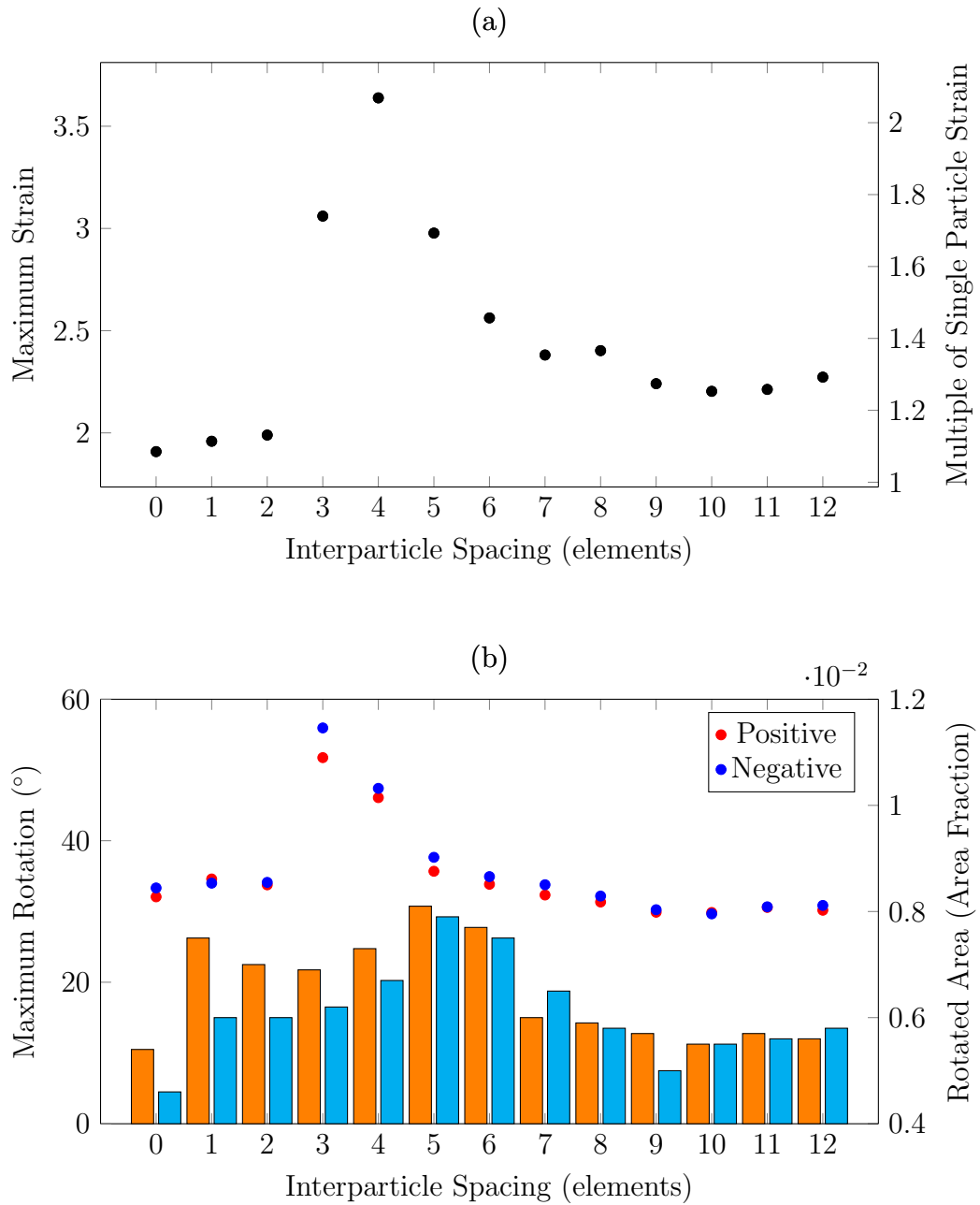


Figure 4.64: (a) Plot showing how the maximum local strain within the CPFEM changes with interparticle spacing. (b) Plot showing the largest measured rotations (scatter) and the area of the highly rotated zones (bar) within the CPFEM with changing interparticle spacing when particles are aligned at  $45^\circ$  to the  $x$  axis

the same deformation conditions. These trends are illustrated in figure 4.64, while the strain plots from which these values have been determined are included in the appendix (figure A.9).

Other important things to note from 4.64b are the differences between the measured areas of the highly rotated regions, focussing on how the areas are not equal when the particles are closely spaced. If deformation of the matrix was set to be homogeneous (i.e. unperturbed), and these particles were placed at the exact centre of the simulated space, these differences would be unexpected. However, as the orientations are perturbed in these models, differences in the balance of positive and negative rotations can be expected.

### Effect of Alignment

The simulations shown in figure 4.65 indicate how changing the alignment of two particles with respect to the primary slip systems can change the size, intensity and interaction of the rotation plumes. The spacing between the two particles before deformation is as close to constant as possible given the limitations of the CPFEM.

From figure 4.65a, the negatively rotated plumes of the particles are shown to interact at an initial alignment of  $51^\circ$  to the  $x$  axis (where after deformation, the particles are close to alignment within a slip system). This interaction is shown to deteriorate in figure 4.65c when the particles are aligned at  $37^\circ$  to the  $x$  axis. At  $27^\circ$ , the interacting plumes have switched, resulting in the positively rotated plume spanning the interparticle space. Regions where both positive and negative plumes are closely spaced within this figure represent regions with very high gradients of rotation. As the particles approach alignment with the  $x$  axis, none of the plumes generated between the two non deformable regions can combine, and instead the centre point between the two particles acts as the convergence point of all plumes. When the particles are aligned in this way, it is the small region between all plumes which corresponds to the highest local strain within the system. However, of all possible alignments of particles, the configuration which generates the highest local strain exists when the particles are aligned at  $\approx 23^\circ$ . This is shown in figure 4.66a. In terms of rotations, this configuration allows the highest gradient of rotation (i.e. highest misorientation) in the interparticle space.

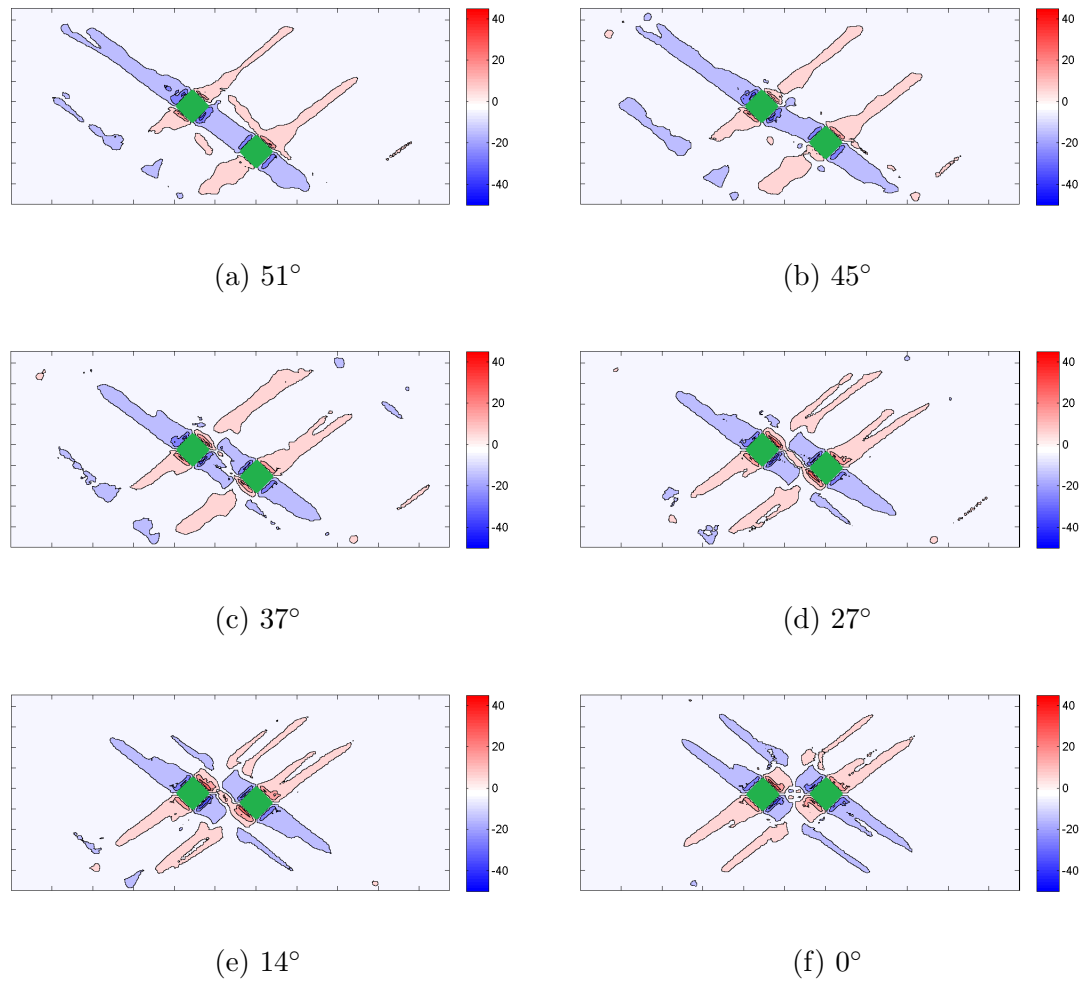


Figure 4.65: Plots illustrating how changing the alignment (angle relative to  $x$  axis) of two non deformable regions whilst maintaining the same interparticle distance affects the rotations of the matrix

This strain plot aids in illustrating that increasing the angle of formed between the particles and the  $x$ -axis past the peak value at  $23^\circ$  towards alignment within a slip band acts to decrease the maximum values of strain found in the simulation.

Figure 4.66b shows how the maximum rotations observed are initially similar when the particles are aligned close to  $0^\circ$ , though these values diverge as the alignment angle increases, with the highest angle of the two corresponding to the direction of the plumes which are interacting in the interparticle space. The rotated areas of matrix also follow diverging paths with larger areas of positive rotations up to an alignment angle of  $\approx 27^\circ$ , and negatively rotated areas then dominant until the particles align within the slip band.

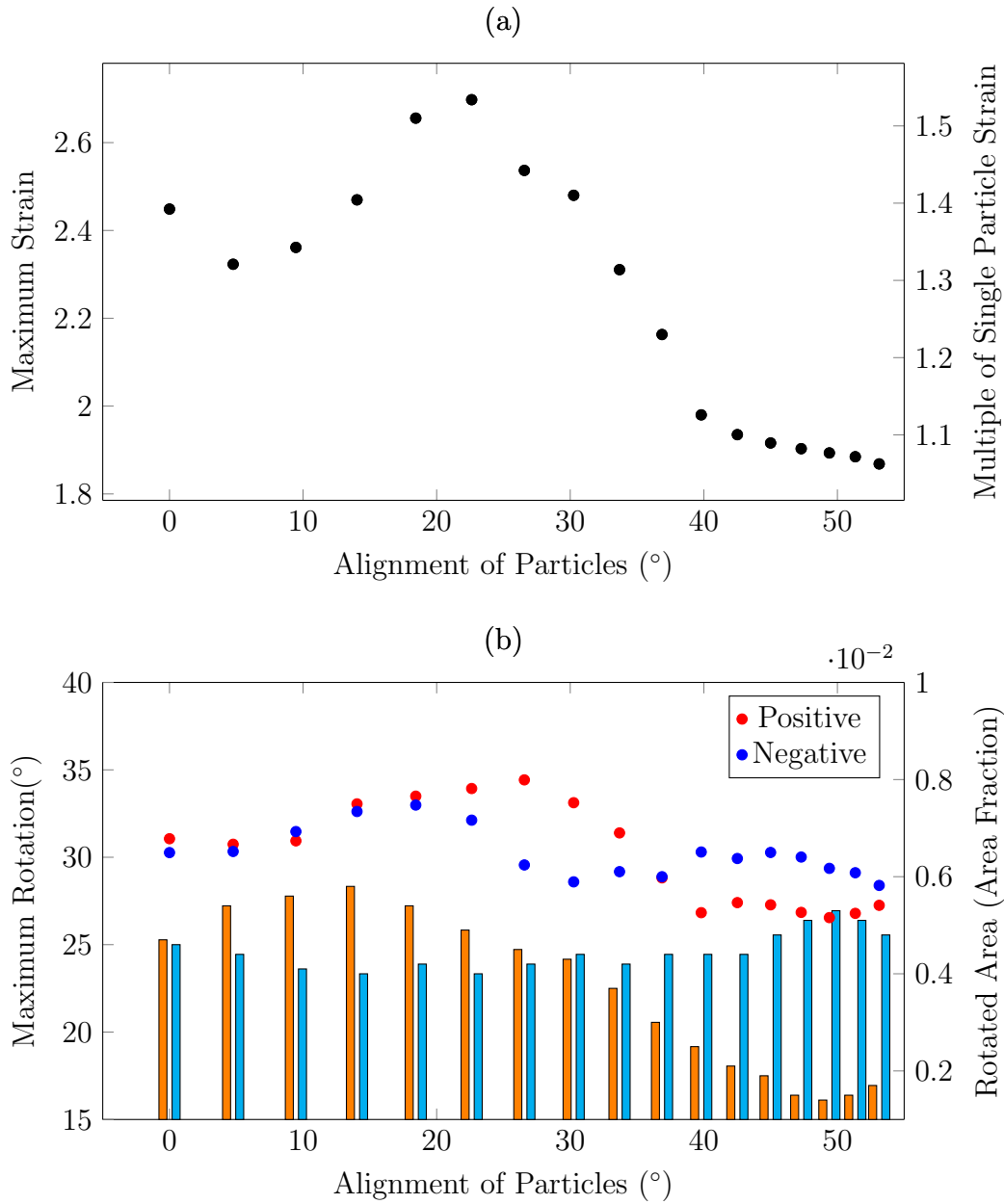


Figure 4.66: (a) Plot showing how the maximum local strain within the CPFEM changes with particle alignment. (b) Plot showing the largest measured rotations (scatter) and the area of the highly rotated zones (bar) within the CPFEM with changing particle alignment

### 4.3.5 Comparing the CPFEM Results

The results presented using the CPFEM have been collated and the implications of the simulations will be presented here.

Table 4.17: Comparison of CPFEM Results

Number of Particles	Variation	Largest Peak Strain (Normalised)	Smallest Peak Strain (Normalised)
None	Perturb Matrix	1.29	1.00
One	Size	2.45 (1.39)	1.58 (0.90)
One	Aspect Ratio	2.28 (1.30)	1.65 (0.94)
One	Orientation	2.79 (1.59)	2.03 (1.15)
Two	Spacing(I)	1.99 (1.13)	1.78 (1.01)
Two	Spacing(II)	3.64 (2.07)	1.91 (1.09)
Two	Alignment	2.69 (1.53)	1.86 (1.06)
Spacing(I) = Particles aligned with the slip plane			
Spacing(II) = Particles aligned with the $x$ axis			

Table 4.17 brings together the maximum values of strain found in each series of CPFEM simulations, presented initially as multiples of the applied strain. The strain obtained when the particle size used for all two-particle simulations (length = 6 elements) was then used to renormalise the maximum strain values for all particle containing simulations. These new normalised results are included in brackets.

The perturbation results are included here to show that in all cases, the incorporation of a non deformable region into the CPFEM acts to create a local maximum strain value, and this exceeds the maximum strain observed by incorporating slight variations in the starting crystallographic orientation.

The incorporation of a single non-deforming region into the CPFEM has been shown to create local strains within the matrix which can reach anywhere between 1.58 and 2.79 times larger than the applied strain. From these results, larger equiaxed particles have a greater influence on local strain than smaller particles, though extending a relatively small particle to increase its aspect ratio can also boost the particle's effect on local strain distribution. For orientation measurements, the aspect ratio was fixed, suggesting that not only does aspect ratio have a role in determining strain distribution, but the orientation of the particle with respect to the active slip systems will also determine how a particle affects local deformation. From these simulations,

it seems that the maximum effect of a single particle on local strain would require a non-deformable region with a high aspect ratio which aligns near to  $22.5^\circ$  from the  $x$  axis, similar to the particle presented in figure 4.59c.

From the two particle simulations, it becomes clear that while spacing is important between the non-deformable regions, it is a combination of how the particles are spaced and their joint alignment with the slip systems that strongly affect local strains and rotations. When comparing these simulations, the normalised strains will be quoted. When comparing how the spacing between two particles affects local strain, two distinct trends are observable. Firstly, if the particles are aligned within the slip system, the largest influence on strain occurs when the particles are at their closest. Overall, though the total region making up the non-deformable structure is twice as large as the single particle used for normalisation, the local strain increases by a maximum of only 13%, and this dissipates further with increasing interparticle distance.

However, when particles are aligned at  $45^\circ$  to the slip systems (aligned to the  $x$  axis), local strain is at a minimum when the regions are together (9% increase compared to single particle induced strain) but reaches a maximum (107% increase) at the point in which there is a 4 element spacing between the two particles. As noted earlier, this coincides with the point at which there is sufficient interparticle spacing to allow interaction between the plumes of deformation which form between the particles. This is most clearly seen on the rotation plots presented in figure 4.63. Increasing this interparticle distance results in the dissipation of the interaction between the plumes, and in turn leads to reductions in the maximum observed strain. In this simulation series, further increases in which the particles were separated by up to twice the diameter of the particles resulted in higher local strain values than when the two particles were close enough to be considered a single particle.

The alignment simulations were performed with an interparticle separation of 6 elements, and while the simulations aligned with the  $x$  axis and active slip systems yielded the expected differences, it was the simulation in which the particles were aligned exactly half way between these orientations which provided the largest effect on local strain. It is this point at which the gradient of rotations (as seen in rotation plots) is at its largest within the interparticle space.

From combining these analyses, it seems that the local inhomogeneities in strain

caused by two non-deformable regions are maximised if these particles are aligned at approximately  $22^\circ$  to an active slip system, and the spacing between the particle approaches the minimum limit at which the four rotational plumes, which are generated between the particles, can strongly interact. From the model, this appears when the spacing between the particles is close to the particle size.

Overall, it has been shown using the CPFEM that both the morphology of the non deformable region, and orientation of this region with respect to the active slip systems will affect the distribution of strain during deformation. Altering the spacing and alignment of two small particles within the CPFEM has also been shown to result in a wide variety of possible strain configurations. This has shown that the spacing can result in two particles acting approximately independently with minimal increases in maximum strain, or particles aligning in such a way that the local maximum strain value is more double that found in a single particle configuration.

## 4.4 Summary of Results

Up to this point, this thesis has presented a unique method to characterise particle distributions from 3D datasets, which has been taken and expanded upon from network theory.

The work has then progressed to illustrate how serial sectioning can be used to obtain datasets describing the morphology and distribution of constituent and dispersoid particles in aluminium alloys. These datasets have indicated constituent particles generally decrease in size during the early stages of thermomechanical processing, whilst also becoming more spherical. The ability to characterise their distribution is however limited as measuring true interparticle distances is difficult for complex particle shapes. Using the same method, the dispersoid population is found to increase in number density during thermomechanical processing.

To investigate how these particles affect local deformation, both digital image correlation and crystal plasticity finite element modelling have been employed. The strain maps produced using DIC have shown that slip traces interact with non-deformable particles, and that particle clusters can act as one large particle. The CPFEM has provided a platform to investigate how small changes in particle configuration would affect the local strain and rotation of the matrix. This has allowed numerous investigations into the effects of particle size, aspect ratio, interparticle distance and alignment with the active slip system to be performed.

The overarching aim of this project has been to make steps in the creation of a through process model for aluminium sheet production. As shown in the DIC and CPFEM simulations, interparticle distance and the overall particle distribution is important in the local deformation behaviour of the aluminium matrix, and therefore some parameter describing the particle distribution must be included in any model. It is the belief of the author that the closeness measures presented here could fill that role.

# Chapter 5

## Discussion

In this section, the results presented in the previous chapter are discussed and, when appropriate, parallels and deviations from current literature are made. This chapter has been split into three sections, with focus shifting from material characterisation, through deformation around particles, to finally combining the different themes of the work to discuss the creation of a through process microstructural model. The emphasis of the final section relates how particle evolution could be incorporated to a through process model and how this would affect deformation zone formation.

### 5.1 Novel 3D Studies using the 3View

Much work has been undertaken to determine the morphology of particles within aluminium alloys, with more emphasis on 3D characterisation techniques appearing in recent years. Though resolution and repeatability has improved from the initial serial sectioning methods employed by Mangan [Mangan et al., 1997], the ability to resolve dispersoids and characterise populations of these particles has not been reported using serial sectioning techniques. Previously reported automated serial sectioning methods offer slice depths of  $\sim 1 \mu\text{m}$  [Alkemper and Voorhees, 2001a], while a slice depth of  $\sim 0.2 \mu\text{m}$  has been reported by Kral using manual techniques [Kral and Spanos, 1999]. The system used throughout this project allows finer slices to be removed, thus creating an image stack with a higher resolution, which can therefore provide greater detail of particle morphology. In this work, the ‘low resolution’ scans are performed with a slice depth of 50 nm, while ‘high resolution’ refers to depths of 15 nm, thus

improving the resolution of the technique to include 20x and 66x more detail than could be extracted using the initial automated method. These resolutions are also much higher than those reported using x-ray tomography, where a typical resolution is a pixel size of  $0.76 \mu\text{m}$  [Singh et al., 2014].

The data presented demonstrates that automated serial sectioning using the 3View system provides useful datasets which, with careful processing, provide 3D resolutions comparable to those created using ion beam milling techniques. However, the action of removing a surface layer of material is much faster using the in-situ ultramicrotome within the 3View system than traditional FIB milling ( $\approx 10$  seconds compared to  $\approx 15$  minutes). At the time of writing, new FIB systems have been reported which provide a cutting time of 2 minutes 12 seconds [Burnett et al., 2016], however this remains much slower than the 3View system. Acquisition time is also improved within the 3View as sample movement is minimal, with only small movements necessary to adjust sample height, whereas the FIB requires rotation of the sample between imaging and milling positions. This further reduces acquisition time per image and helps to avoid possible sources of misalignment between adjacent slices.

Though this technique brings improvements to acquisition time compared to FIB milling, drawbacks remain when using this technique. Firstly, the image stack obtained using this 3View method can contain slices consisting of incomplete cuts, resulting in loss of accuracy. This can be overcome in part by interpolating between two surrounding slices, however particles which would terminate within the mis-cut slice can not be interpolated, resulting in a reduced particle size within the measured volume in such cases. Unlike FIB milling, which can be used to obtain 3D EBSD maps, the action of the ultramicrotome introduces deformation to the surface of the material, meaning that crystallographic orientation measurements can not be obtained. The final drawback of this technique compared to other destructive 3D imaging methods is the break-off and embedding of second phase particles which was outlined earlier. Though displaced particle fragments can be negated with careful data processing, that these regions exist within the reconstructed volume ensures that some of the time saved by using this method rather than FIB milling will be used during the extended processing time required to visualise the data.

Due to the cutting process being instrumental in the creation of the image stack,

the interaction between the ultra-microtome and the material at the nanometre scale is important. The mechanics of the particles themselves during the cut will be vital in determining whether regions will break away from the particle, while knowledge of how the particle and matrix interact could determine whether there are conditions at which the microtome is likely to completely remove the particle from the matrix. The data from these volumes has been presented with the assumption that no particles have been pulled from the matrix on the action of the microtome and this assumption is based on the study of the image stacks themselves (i.e. small voids were not detected when analysing the image stack).

As a novel method for the generation of 3D particle population data, the 3View system has some advantages, however this is not likely to completely replace other destructive techniques such as FIB milling where precision is key. In saying that, this method does allow a viable alternative to FIB milling for 3D structural studies, as shown with the data presented illustrating the evolution of particles within an aluminium alloy. It must be noted here that the viability of the method for 3D structural studies is dependent on the mechanical properties of the material to be studied. 3XXX series aluminium alloys are relatively soft, making them an ideal candidate for the 3View system. For harder materials such as nickel superalloys, a different method would be needed.

Though the benefits of 3D analysis are clear, the small overall volume studied using any of the methods listed so far (FIB milling, 3View, X-ray computed tomography etc) should also be remembered. It is therefore vital that before conclusions are determined from a 3D dataset, it is confirmed that the dataset is a representative example of the overall material. Some thermomechanical processes generate microstructures which are not consistent across the material, and so a series of 2D images may be regarded as a more useful method of analysis. However, it could also be argued that 3D volumes could be generated for multiple regions within the same material to generate a more complete dataset illustrating how the microstructure changes throughout a single sample. In this work, a series of 2D images were taken across multiple samples of the alloy, which supported the notion that the 3D volumes obtained were typical of the bulk of the material.

### 5.1.1 Constituent Population Measurements

Limited quantitative data currently exists within the literature which illustrates the size and distribution of particle populations with 3XXX series aluminium at the early stages of sheet production. Qualitative studies such as those by Alexander and Greer [Alexander and Greer, 2005] suggest that the higher calculated sphericity of constituents in the homogenised sample compared to those in the as cast material are to be expected, assuming that the model alloy used within this study behaves in the same way as the model 3XXX used by Alexander. The spheroidisation mechanism described by Alexander also explains the increased number density of constituents after the homogenisation process. Hamerton et al. [Hamerton et al., 2000] presented how the number density of constituents altered as a result of deformation in a similar model alloy, though this study was limited to particles larger than  $1 \mu\text{m}$  due to characterisation limitations. The results from this study are in agreement with the data presented here, with deformation leading to the presence of more equiaxed particles, and a higher number density of constituents overall. More recent work on the current model alloy by Hill [Hill, 2014] has included similar data confirming reduced constituent particle sizes after homogenisation and deformation measured in 2D. At the time of writing, quantitative data illustrating changes to the population of constituent particles as a result of processing has not been presented using 3D imaging techniques.

The results gained using the 3View have also aided in gaining new insight into the more complex spacial distribution of the particles in the model aluminium alloy, with the newly appropriated closeness measure helping to quantify how the spacing between particles changes during heat treatment and deformation. The visualisations of the particle networks are also useful in understanding the solidification of the material, as measurements such as interdendritic spacing are much easier to determine from a 3D dataset.

The stepwise 2D nature of the full 3D data acquisition has allowed a comparison to be drawn between the measured and expected 3D particle populations using the Schwartz-Saltykov method [DeHoff and Rhines, 1968, Gokhale, 2004]. From the results, it is clear that the Schwartz-Saltykov approximation, when applied to the rolled constituents dataset, is less accurate in its description of the full 3D population than the raw 2D data. As this method relies upon the particles within the volume being

completely spherical for the probability functions to operate correctly, some error was expected in the approximation. However, the extent of the error, which acts to move the distribution further from the true result is surprising. This approximation was performed using the population of constituents with the most spherical particles of the volumes studied, so the Schwartz-Saltykov method should provide the most accurate result for this dataset, yet the approximation still acts to reduce the accuracy in the distribution. This data suggests that Schwartz-Saltykov method in its current iteration, is unsuitable for the approximation of the constituent particle populations within this alloy.

### 5.1.2 Dispersoid Population Measurements

The high resolution capabilities of the 3View system (10 nm pixels) allowed the dispersoids, which were found during the 2D characterisation of the homogenised model alloy, to also be studied as a 3D volume. This type of 3D study of dispersoids has not been reported in the literature at the time of writing. The study of particle morphology for dispersoids within the 3View poses a much more difficult challenge than constituent particles, owing to the small particle size in relation to the resolution of the technique. For this reason, any sphericity values presented here may be larger than those obtained through measurements using TEM, due to the increased ability to resolve particle features using the TEM. The general distributions of particle size however, should be found to agree with other studies. Of note is the inability to include particles smaller than 60 nm in the dispersoid analysis using the 3View, which results in the removal of all very small dispersoids from analysis. The 60 nm threshold is set to ensure that the measured region is indeed a feature within the microstructure and not simply an artefact. This threshold could be improved by improving the resolution of the technique which is currently limited by both the interaction volume of the electrons within the sample, and the minimum cut size.

Due to the initial nucleation process involving dispersoid nuclei which can not be resolved using the 3View, care must be taken when presenting any high resolution work characterising material in which the nucleation processes are still in their infancy. The conditions included in this work involved the use of a isothermal dwell

times during the homogenisation process which is vital in the coarsening of the initially nucleated particles, thus ensuring that the dispersoids were of a suitable size for 3View analysis. The previous works by Hill [Hill, 2014], found that dispersoids nucleated during deformation processes, and while the increase in dispersoid count found between homogenised and rolled material would agree with his findings, the data presented here can not be taken as conclusive proof. This is due to the problem of the unknown population of particles smaller than 60 nm in both populations in the reconstructed volumes. Hill's data shows that these small particles would correspond to a sizeable contribution to the number fraction of dispersoids, and so it could therefore be argued that these unresolvable particles within the homogenised material simply coarsen during deformation.

Hill's dispersoid population data suggests that the number fraction of dispersoids in homogenised material is highest for 40 nm particles and steadily decreases with increasing size. Hill also found that deformation acted to shift this peak, resulting in an overall increase in dispersoid particle size. Though the peak at 40 nm is not present in the 3D datasets due to resolution limits, the overall trends are in agreement with the number fraction data obtained from the 3D datasets presented in figures 4.37 and 4.40 respectively. This is most clearly demonstrated by the decrease in number fraction of 60-80 nm particles from 0.23 to 0.19 after deformation.

## 5.2 Deformation around Particles

The formation of deformation zones in aluminium alloys has been closely linked to the size of constituent particles in previous studies [Humphreys, 1979, Humphreys and Ardakani, 1994, Engler et al., 1997], however a systematic study detailing how other aspects of the particle population affect local deformation have not been presented at the time of writing. The data given by Ko [Ko, 2014] illustrates that the interactions of particles with slip bands is firstly dependent on the particle size as a small enough constituent may fit in the spacing between two slip bands and therefore avoid interaction. It was also suggested that the presence of dispersoids would act to decrease the slip band spacing, thus reducing the minimum particle size for such interactions. The data produced using digital image correlation adds to the current knowledge base regarding slip band spacing in aluminium systems, and aids in showing the effect of second phase particles at the initial stages of compression. The CPFEM has allowed the effects of tailored particle configurations to be simulated, thus providing new insights into how differences in the particle population may affect local deformation.

### 5.2.1 Strain Maps of Model Alloy

As the results from the strain mapping are limited to reductions of 8% and the two areas studied behave identically in terms of slip band intensity and direction, it is clear that any conclusions drawn from the limited data set can not be applied to the bulk material. Further experimentation involving multiple starting orientations would remove this limitation. The first step in accomplishing this would be the creation of a more stable nano-pattern.

The notable difference in the expected value of the average strain and the experimental value obtained for the region investigated using DIC suggests that the measured grain is more deformed than the average grain within the volume. As the Radon transforms for both areas show, the majority of the slip bands are aligned at 45° to the deformation axis (see figures 4.48 and 4.52), the Schmid Factor will be at a maximum, and therefore  $\tau_{CRSS}$  will be hit before other differently oriented grains within the volume. With this insight, it seems likely that the difference between expected and observed strains is in fact due to the orientation of the grain.

The resolved slip bands within the strain map illustrate the heterogeneous nature of deformation on a crystallographic scale and are in agreement with the findings of Ko [Ko, 2014]. These slip bands are essentially regions of concentrated strain, separated by relatively strain free matrix. From the strain maps presented, the presence of non deformable particles is shown to affect the local distribution of slip bands within the grain. Figure 4.50c shows slip bands terminating upon reaching a particle cluster, while figure 4.46c shows slip bands deflecting around a particle. This is again in agreement with work by Ko in which deformation around larger particles (10s of microns in diameter) in a Al-Si binary alloy showed both deflection and termination of slip bands at particles.

From the maps, regions of the highest strain were not exclusively found close to non deformable particles. However, this does not indicate that particles do not affect the distribution of strain, but may suggest that at the low overall strains which have been mapped, the effects of second phase particles may not yet come into play. In a system under higher strain, in which the number of active slip bands was at a maximum, the presence of particles which block slip bands would result in a much greater shift in the local substructure within the grain, and may allow a more detailed investigation into the effects of second phase particles on the formation of deformation zones. In the maps presented here, the particle sizes are close to the expected slip band spacing. To verify the effects of particle morphology on local slip band behaviour, a simpler model alloy may be a more suitable material.

As shown in the rotation map of the particle cluster in figure 4.50c, when groups of these small particles are in close proximity, relatively large interactions can be determined, suggesting that there is an effective distance at which the aluminium matrix would deform around two particles as though it was a single uninterrupted non-deformable region. This helps to illustrate the necessity of knowing not only the size and morphology of particles, but also how they are distributed throughout the alloy.

### 5.2.2 Slip Bands Within CPFEM Simulations

Within the CPFEM, the perturbation variance simulations indicate that the incorporation of a small amount of disorder to the orientations of matrix elements allows the

simulation to mimic the structure of slip bands. The spacing of these slip bands is related to the width of a single element within the CPFEM, and results in giving the CPFEM an illusion of scale. In the work by Ko [Ko, 2014], the capability of the perturbed starting orientation is demonstrated, and the strain concentrations are noted, though this feature is later dismissed. However, this has been evaluated more closely as part of this work.

The normalised strain range ( $\hat{\varepsilon}$ ) obtained for the perturbed data peaks at 1.27 for  $\varepsilon=0.08$  within the CPFEM, however experimental findings using DIC of a mechanically similar alloy (data taken from [Ko, 2014]) illustrate  $\hat{\varepsilon}=19$  for an 11% reduction. This difference can be attributed to the relatively homogeneous strain found within the CPFEM (i.e.  $\varepsilon$  ranges from 0 to 2.4 experimentally in particle free material deformed by 11%, but ranges from 0.05 to 0.15 within the CPFEM for a 10% reduction).

This observed relative homogeneity in the CPFEM is an unavoidable limitation which is due to the continuous nature of the model itself. This ensures that the CPFEM can not accurately portray the extent of slip between two crystals as this would lead to discontinuities in the finite element mesh.

The boundary conditions within the model also act to ensure the external faces of the mesh are conserved. Due to this conservation, strain and rotation are both shown to reflect in the boundaries of the model to create secondary echoes.

It is currently impossible for the CPFEM to model the deformation around a particle smaller than the modelled ‘slip band’ spacing, as each non deformable region must be formed of at least one element. A method of altering the CPFEM may involve changing the approach in which perturbations are incorporated into the simulation. As it stands, this is designed so that each single element is perturbed in relation to its neighbour, however, a small modification of this parameter may allow perturbation to be applied in such a way that small groups of elements (e.g. 2x2 grid), are given the same new orientations. This may allow wider slip band spacings to be produced within the CPFEM which would in turn lead to larger strain gradients.

### 5.2.3 Linking the CPFEM to PSN

The formation of recrystallisation nuclei within the deformation zones of aluminium alloys is a well researched phenomenon with studied by numerous groups [Humphreys,

1997a, Rios and Padilha, 2003]. As it is understood that recrystallisation nuclei form in regions which have high stored energy, in which a high angle grain boundary is able to form (i.e. high gradient of rotation), the results obtained from the CPFEM could be used to aid in a model which predicts which particle parameters are most likely to result in the formation of a recrystallisation nucleus.

From the literature it is known that the efficiency of PSN is not unity (i.e. not all particles generate recrystallisation nuclei), and it has been determined that size of particles play a critical role in whether a nucleus is likely to form, with materials containing larger particles resulting in a higher efficiency overall.

From the CPFEM simulations, it has been shown that increasing parameters such as particle size results in increased local strain around a non deformable region, and also increases the expected maximum rotation. In essence, this therefore suggests that two of the necessary features of a successful recrystallisation nucleus - high stored energy and high angle boundary - are shown to be more easily attainable in a material with a larger non-deforming region when using the CPFEM.

Taking this further, the highest observed rotations within CPFEM simulations with single particles included were obtained when high aspect ratio non deformable regions incorporated at and aligned at  $\approx 23^\circ$  to the primary slip axes (see figure 4.60), whilst this also represented a relatively small rotated area, suggesting a high rotation gradient within the deformation zone. This also corresponded to the highest local strain observed across all single particle simulations, suggesting that if PSN was to be studied at a variety of possible particles the CPFEM predicts that if all other conditions were equal, this would be the most likely candidate for nucleation.

A study of how multiple particles affect the structure of deformation zones has not been presented in the literature at the time of writing, however, the CPFEM has allowed multiple configurations to be investigated and has produced some interesting results overall. The incorporation of two particles within the CPFEM has shown that under some conditions in which there is no direct path for deformation to pass between two particles, they are treated as one large undeformable region. It is only when the spacing between the particles reaches a threshold that strain and rotation build between the particles, resulting in both maximum lattice rotations and local strains which reach double the value obtainable when only one such particle is included. This

alone suggests that the interaction of particle clusters requires further study. The CPFEM simulations so far have indicated that again, such intense strain maxima and rotations are also most likely to occur at a specific alignment away from the both the deformation axis and active slip systems.

If the results of the CPFEM are taken to be accurate in terms of the overall effect that particle alignment, spacing, and size can have on the deformation zones produced around second phase particles, it becomes clear that predicting the efficiency of PSN can not be determined with knowledge of the number fraction of particles alone. As the formation of a recrystallisation nucleus is linked to both local stored energy and the formation of a high angle grain boundary (see 2.5.5), and some configurations of particles, as demonstrated as part of this work, will produce higher degrees of rotation and larger local strains, any model of PSN must incorporate particle population data (such as those obtained from the serial sectioning method) when calculating the expected number of nuclei.

However, before this can be accomplished, further work in which the effect of simple particle shapes and clusters on deformation zone formation must be expanded upon to ensure that the results of the CPFEM can be likened to that of true deformation zones.

#### 5.2.4 Extending the Slip Shadowing Model

The slip shadowing model presented by Humphreys and Ardakani [Humphreys and Ardakani, 1994] (see section 2.4.3) has been shown to match with the CPFEM results for the single particle case [Humphreys et al., 2012, Ko, 2014]. This model can be extended as a way of describing how and why the plumes of rotation in multiple particle systems appear in the configurations shown within the CPFEM.

##### Particle Spacing

Figure 5.1 shows three scenarios in which two particles are placed close to each other, and aligned at  $45^\circ$  to two principal slip systems, named S1 and S2. These scenarios correspond to the simulations shown in figure 4.63. In figure 5.1a, two particles are placed in such a way so that there is no matrix between the two particles, and thus no possible vector for any deformation to take between the particles. In this case, area

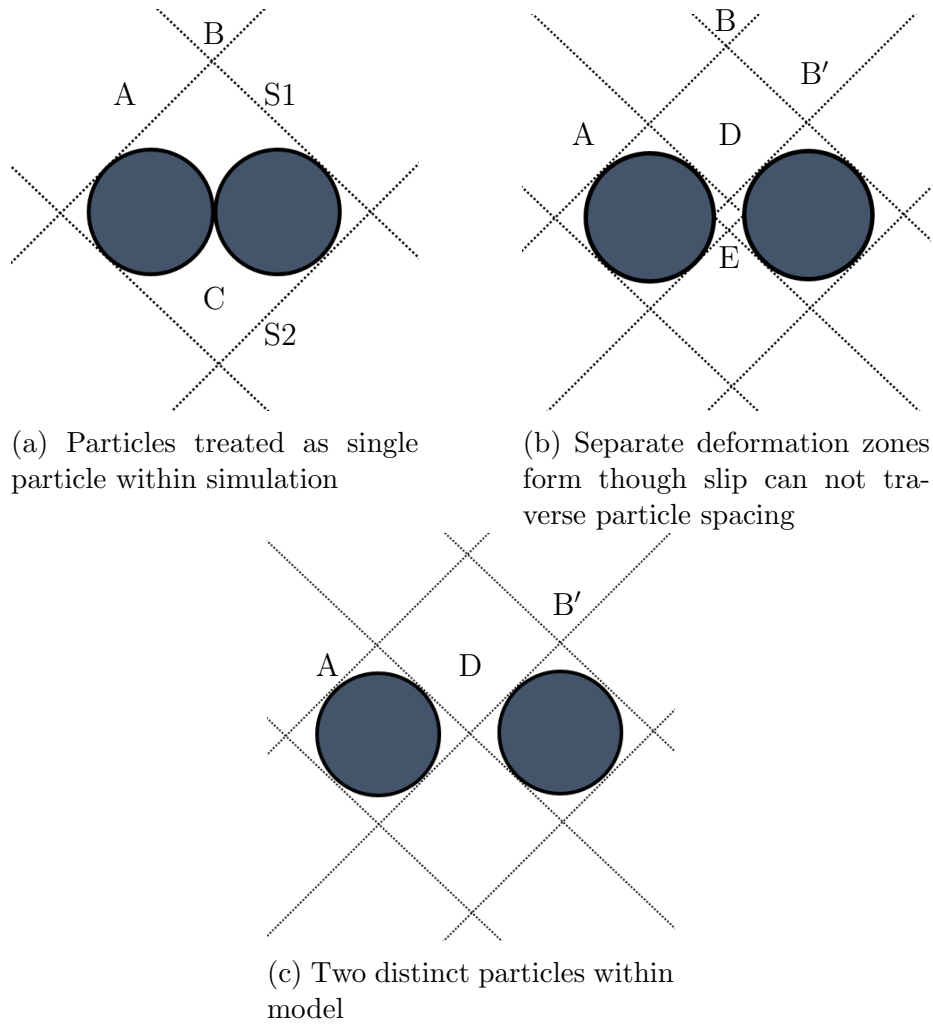


Figure 5.1: Varying separation of particles within the CPFEM results in fundamentally different slip behaviour, as illustrated by extended slip-shadowing diagrams

A illustrates the region in which a single slip system is blocked (in this case the S1 system), area B shows where both slip systems are available, and in this case, both slip systems are blocked in area C. This system behaves in the same way as the single particle case described earlier. Rotation is usually highest in A type regions while high local strain dominates region B. As region C is inactive due to slip shadowing, no noticeable rotations or strains are expected.

Figure 5.1b includes the same two particles with a small interparticle spacing. In this case, A and B remain the same, however now new regions labelled B', D and E are included. B' refers to the regions directly above the particle in which one slip system is mobile, but the other is blocked a short distance away. This leads to slightly different behaviour compared to B with some secondary rotations expected. The region where the rotation plumes between the particles are expected to form has been labelled D.

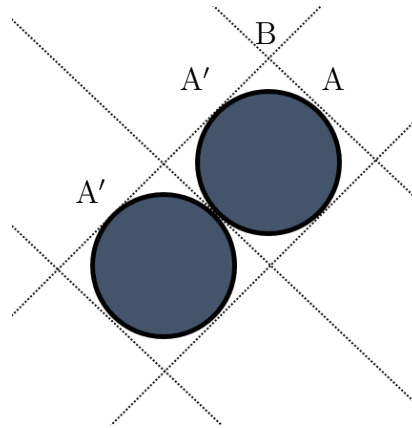


Figure 5.2: Slip shadowing configuration for closely spaced particles aligned with a principle slip system

Here, though slip through the particle is not possible, local rotation is still allowed, resulting in very high rotation gradients. The two plumes generated in this region are of opposite rotations. The small region directly between the particles is labelled E, and this region is bound by the four rotation plumes (two above, two below), resulting in a zero rotation zone with higher strain than that found at B.

With further separation of the particles, region E becomes a single point between the two zone Ds. This is shown to exhibit the highest local strain. Further separations of the particles acts to reduce the interaction of the plumes as the D region is split into two corresponding A regions for each particle.

In the case of particles aligned along a principal slip system as shown in 5.2 (corresponding to the simulations shown in figure 4.61), the intensity of rotation at zones A and A' are very different as the particles are close together (as the rotation at A' occurs over a larger region), however as the spacing between the particles increases, the large A' region will split to form a new A' for each particle. In such aligned configurations, minimal spacing between the particles is sufficient for the (S1) slip system to be activated within the interparticle space, however in real materials, the spacing required to ensure slip activation would be a function of the slip band spacing.

The most complex of these applications of slip shadowing is for particles which are partially aligned within the same slip system, as shown in figure 5.3. The regions labelled A and B' are exposed to the same degree of shadowing as described earlier. Due to the alignment of the particles, plumes of the same direction of rotation can interact in an additive way, marked region F. Conversely, regions G and G'' are regions

of opposite rotation, and as a result of this, the shift in local rotation at the point where regions F, G and G'' meet generates the highest rotation gradient and highest local strain measured within the CPFEM.

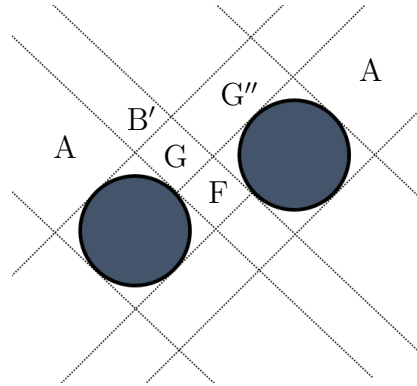


Figure 5.3: Extended slip-shadowing diagram illustrating how partial alignment of particles can lead to partial slip shadowing

The implications of the results of multiple particle simulations from CPFEM fitting closely to this expanded slip shadowing model allows simulations which currently require high performance computing to instead be predicted by hand.

## 5.3 Steps Toward a Through Process Model

The creation of a through-process model of aluminium sheet production requires not only a complete understanding the material properties, but also raw data which can be used to generate equations describing the effects that each stage of processing has on the material.

### 5.3.1 Parameters from the Serial Sectioning Analysis

From the 3D data presented here, the particle size and sphericity measurements for the constituent and dispersoid populations have been used to create simple equations which could be incorporated into a through process model. The generation of these curves is relatively straightforward when population data is present, and as shown in this work, automated serial sectioning can be considered a viable method for obtaining this raw data.

At this time, these equations are only currently viable as a tool for describing material of the same composition which has undergone the same thermomechanical history as the characterised material. For the expansion of the initial equations into a more complete model, populations of particles must be analysed for a wider variety of processing conditions. This would allow the populations of particles, which form as a product of homogenisation and deformation, to be determined if the as cast features of the alloy are known. It is these equations which transform particle population distributions which would be vital in any through process model that aims to determine particle evolution.

The current iteration of the closeness parameter as a scatter plot which represents the particle population as a whole is useful for comparing volumes, but would be difficult to incorporate into a model. However, it may be possible to incorporate the closeness distribution plots in to such a model, which would allow information detailing the spatial configuration of second phase particles to be added to a through process model.

Due to the importance of particle clustering on the local strain, as indicated within the CPFEM, it would be important to ensure some form of parameter which monitors particle spacing is included in any through process model.

### 5.3.2 Parameters from the Deformation Analysis

From the crystal plasticity modelling, it is apparent that the size, shape and proximity to neighbouring particles, as well as the relation of all of these parameters to the active slip systems, play a significant role in determining how the deformation will evolve in multi-phase materials. However, these observations are yet to be experimentally verified in terms of the measurement of strain and rotation around a particle cluster, thus while the CPFEM experiments add new insights into possible effects of particle shape, they must be scaled using data gleaned from further deformation studies.

The formation of a PSN module within a through process model could take some prediction tools from the CPFEM results, using particle size, shape and closeness as inputs and using these values to create probability distributions describing the likelihood that each of the particles would develop a deformation zone with the necessary local stored energy and rotation for a PSN nucleus to form. This would therefore be useful as a way to predict the efficiency of the constituents within an alloy to act as nucleation sites for PSN. Such a model would also be versatile in that any changes to the thermomechanical processing, which would alter the particle population, could then be carried forward into the PSN predictor module

# Chapter 6

## Conclusions

An investigation of the particle populations found within a model aluminium alloy at different stages of thermomechanical processing has been undertaken using a novel three dimensional imaging technique which allows sub micron particles to be resolved. This investigation was expanded to study the effects of the particle morphologies found within the alloy on the local deformation of the matrix. This was undertaken by creating strain maps using digital image correlation and by modifying a crystal plasticity finite element model.

This resulted in the analysis of both constituent and dispersoid particles at varying stages representing steps from aluminium sheet production, as well as providing insight into how the configuration of non-deformable particles within the matrix can alter local strains and rotations. From these results, it can be concluded that:

- Automated serial sectioning is a viable method to examine the structure and distribution of constituent and dispersoid particles in 3XXX aluminium alloys.
- Distributions of particle size and sphericity have been determined at different processing steps in sheet production, allowing equations based on Weibull functions to be generated as a predictor for particle evolution.
- Closeness centrality - a measure used in determining how close a node is to every other node within a complete network - has been successfully applied as novel method of characterising how constituent particles are spatially distributed within an alloy.

- The Schwartz-Saltykov method can act to provide a poorer estimate of 3D particle size than the raw 2D images on which it is based.
- Digital image correlation can be utilised to observe changes in localised strain in a model 3XXX aluminium alloy due to plane strain compression, allowing slip band spacing to be investigated.
- Crystal plasticity finite element modelling (CPFEM) has been used to predict how changing the size and shape of a single particle can affect strain and rotations within the matrix.
- The CPFEM has been expanded to incorporate multiple particles, allowing investigations into the effect of spacing and particle alignment on local deformation.
- The results from the CPFEM have allowed the slip shadowing model for deformation around a single particle to be expanded.

# Chapter 7

## Suggested Future Work

This work has shown that 3D datasets can be obtained with relative ease for 3XXX aluminium alloys, whilst illustrating how a new measure may be useful in aiding the characterisation of particle populations found in such alloys. To continue advancement in this area, it may be interesting to:

- Investigate the effects of crystallographic orientation on the deformation induced by the serial sectioning process, and investigate the effects of slice depth on particle fragmentation.
- Expand the current study to incorporate population data from material which has undergone different homogenisation heat treatments and/or rolling conditions to expand the knowledge base of how the 3D distribution of particles is affected by processing conditions.

Deformation studies within this work have also highlighted new insights into how particle morphologies and configurations of multiple particles may affect the formation of deformation zones within aluminium alloys. To take this further, would could continue in:

- Continuing work on the characterisation of deformation zones with techniques like digital image correlation. This has been proven as a viable technique and it may be possible to use this method to visualise how slip bands interact with particle clusters.

- Make adjustments to the crystal plasticity model, with an investigation into the effect of changing how the perturbation of the matrix is generated.
- As more and more simulations are performed using the CPFEM, a conversion from predicted to real values must be determined. This would allow the presented data to be scaled and incorporated in to a through process model which may help predict the efficiency of PSN.

# Bibliography

- [Alcoa, 2013] Alcoa (2013). Alloy 7075 Plate and Sheet: All Around Consistent Performance.
- [Alexander and Greer, 2002] Alexander, D. and Greer, A. (2002). Solid-state intermetallic phase transformations in 3XXX aluminium alloys. *Acta materialia*, 50(10):2571–2583.
- [Alexander and Greer, 2004a] Alexander, D. and Greer, A. (2004a). Nucleation of the Al<sub>6</sub>(Fe, Mn)-to- $\alpha$ -Al-(Fe, Mn)-Si transformation in 3XXX aluminium alloys. I. Roll-bonded diffusion couples. *Philosophical Magazine*, 84(28):3051–3070.
- [Alexander and Greer, 2004b] Alexander, D. and Greer, A. (2004b). Nucleation of the Al<sub>6</sub>(Fe, Mn)-to- $\alpha$ -Al-(Fe, Mn)-Si transformation in 3XXX aluminium alloys. II. Transformation in cast aluminium alloys. *Philosophical Magazine*, 84(28):3071–3083.
- [Alexander and Greer, 2005] Alexander, D. and Greer, A. (2005). Particle break-up during heat treatment of 3000 series aluminium alloys. *Materials Science and Technology*, 21(8):955–960.
- [Alkemper and Voorhees, 2001a] Alkemper, J. and Voorhees, P. (2001a). Three-dimensional characterization of dendritic microstructures. *Acta Materialia*, 49(5):897–902.
- [Alkemper and Voorhees, 2001b] Alkemper, J. and Voorhees, P. W. (2001b). Quantitative serial sectioning analysis. *Journal of Microscopy*, 201(3):388–394.

- [Anderson and Mehl, 1945] Anderson, W. A. and Mehl, R. F. (1945). Recrystallisation of Aluminum in Terms of the Rate of Nucleation and the Rate of Growth. *Trans. AIME*, 161:140.
- [Anselmino, 2007] Anselmino, E. (2007). *Microstructural effects on grain boundary motion in Al-Mn alloys*. PhD thesis, Delft University of Technology.
- [Ashby, 1970] Ashby, M. (1970). The deformation of plastically non-homogeneous materials. *Philosophical Magazine*, pages 37–41.
- [Ashby et al., 1969] Ashby, M. F., Gelles, S. H., and Tanner, L. E. (1969). The stress at which dislocations are generated at a particle-matrix interface. *Philosophical Magazine*, 19(160):757–771.
- [Bachu and Kalidindi, 1998] Bachu, V. and Kalidindi, S. R. (1998). On the accuracy of the predictions of texture evolution by the finite element technique for fcc polycrystals. *Materials Science and Engineering A*, 257:108–117.
- [Bäckerud et al., 1986] Bäckerud, L., Król, E., and Tamminen, J. (1986). *Solidification Characteristics of Aluminium Alloys. Vol 1*. SkanAluminium/Univesitetforlaget, Oslo.
- [Bate, 1999] Bate, P. (1999). Modelling deformation microstructure with the crystal plasticity finite-element method. *Philosophical Transactions of the Royal Society A: Mathematical, Physical and Engineering Sciences*, 357(1756):1589–1601.
- [Bate and Hutchinson, 1997] Bate, P. and Hutchinson, B. (1997). A re-evaluation of the mechanism of SIBM. *Scripta materialia*, 36(2):195–198.
- [Bay et al., 1989] Bay, B., Hansen, N., and Kuhlmann-Wilsdorf, D. (1989). Deformation structures in lightly rolled pure aluminium. *Materials Science and Engineering: A*, 113:385–397.
- [Blade, 1979] Blade, J. C. (1979). Recrystallization in hot rolling of dilute aluminium alloys. *Metal Science*, 13(3-4):206–210.

- [Bullen and Hutchison, 1962] Bullen, F. P. and Hutchison, M. M. (1962). Dynamic recovery from strain-hardening in polycrystalline copper and aluminium. *Philosophical Magazine*, 7(76):557–572.
- [Burnett et al., 2016] Burnett, T. L., Kelley, R., Winiarski, B., Contreras, L., Daly, M., Gholinia, a., Burke, M. G., and Withers, P. J. (2016). Large volume serial section tomography by Xe Plasma FIB dual beam microscopy. *Ultramicroscopy*, 161:119–129.
- [Cahn, 1950] Cahn, R. W. (1950). A New Theory of Recrystallization Nuclei. *Proceedings of the Physical Society. Section A*, 63(4):323.
- [Çetin and Kalkanli, 2008] Çetin, A. and Kalkanli, A. (2008). Effect of solidification rate on spatial distribution of SiC particles in A356 alloy composites. *Journal of Materials Processing Technology*, 205(1-3):1–8.
- [Chandler, 1996] Chandler, H. (1996). *Heat Treater's Guide: Practices and Procedures for Nonferrous Alloys*. ASM International.
- [Crumbach et al., 2006a] Crumbach, M., Goerdeler, M., and Gottstein, G. (2006a). Modelling of recrystallisation textures in aluminium alloys: I. Model set-up and integration. *Acta Materialia*, 54(12):3275–3289.
- [Crumbach et al., 2006b] Crumbach, M., Goerdeler, M., and Gottstein, G. (2006b). Modelling of recrystallisation textures in aluminium alloys: II. Model performance and experimental validation. *Acta Materialia*, 54(12):3291–3306.
- [Dangalchev, 2006] Dangalchev, C. (2006). Residual closeness in networks. *Physica A: Statistical Mechanics and its Applications*, 365(2):556–564.
- [Das, 2006] Das, S. (2006). Designing aluminum alloys for a recycle-friendly World. *Light Metal Age - Chicago*, 64(3):26.
- [Das and Yin, 2007] Das, S. and Yin, W. (2007). Trends in the global aluminum fabrication industry. *JOM Journal of the Minerals, Metals and Materials Society*, 59(2):83–87.

- [Davies, 1993] Davies, J. R. (1993). *Aluminum and Aluminum Alloys*. ASM International.
- [DeHoff and Rhines, 1968] DeHoff, R. T. and Rhines, F. N. (1968). *Quantitative Microscopy*. McGraw-Hill.
- [Di Gioacchino and Quinta da Fonseca, 2013] Di Gioacchino, F. and Quinta da Fonseca, J. (2013). Plastic Strain Mapping with Sub-micron Resolution Using Digital Image Correlation. *Experimental Mechanics*, 53(5):743–754.
- [Dieter, 2001] Dieter, G. E. (2001). *Mechanical Metallurgy*. McGraw-Hill, third edition.
- [Doherty, 1974] Doherty, R. D. (1974). The Deformed State and Nucleation of Recrystallization. *Metal Science*, 8(1):132–142.
- [Driver et al., 2006] Driver, J. H., Maurice, C., Barou, F., and Lens, A. (2006). Boundary Mobilities in Binary Al-Mn Alloys. *Materials Science Forum*, 519-521:1597–1604.
- [Du et al., 2011] Du, Q., Poole, W., Wells, M., and Parson, N. (2011). Microstructural modeling of the homogenization heat treatment for AA3XXX alloys. *JOM Journal of the Minerals, Metals and Materials Society*, 63(7):35–39.
- [Duchêne and Habraken, 2007] Duchêne, L. and Habraken, A. M. (2007). Multiscale Approaches. In Chinesta, F. and Cueto, E., editors, *Advances in Material Forming: Esaform 10 years on*, pages 125–142. Springer Verlag, Paris.
- [Engler et al., 1997] Engler, O., Kong, X., and Yang, P. (1997). Influence of particle stimulated nucleation on the recrystallization textures in cold deformed Al-alloys Part I Experimental observations. *Scripta Materialia*, 37(11):1665–1674.
- [Eskin, 2008] Eskin, D. E. (2008). *Physical Metallurgy of Direct Chill Casting of Aluminum Alloys*. CRC Press, Boca Raton.
- [Essmann and Mughrabi, 1979] Essmann, U. and Mughrabi, H. (1979). Annihilation of dislocations during tensile and cyclic deformation and limits of dislocation densities. *Philosophical Magazine A*, 40(6):731–756.

- [Exell and Warrington, 1972] Exell, S. F. and Warrington, D. H. (1972). Sub-grain boundary migration in aluminium. *Philosophical Magazine*, 26(5):1121–1136.
- [Gindi and Gmitro, 1984] Gindi, G. R. and Gmitro, A. F. (1984). Optical feature extraction via the Radon transform. *Optical Engineering*, 23(5):235499.
- [Gokhale, 2004] Gokhale, A. M. (2004). Quantitative Characterization and Representation of Global Microstructural Geometry. In *Metallography and Microstructures, Vol 9, ASM Handbook*, pages 428–447. ASM International.
- [Goldstein et al., 2012] Goldstein, J. I., Yakowitz, H., Newbury, D. E., Lifshin, E., Colby, J. W., and Coleman, J. R. (2012). *Practical Scanning Electron Microscopy: Electron and Ion Microprobe Analysis*. Springer Science & Business Media.
- [Green and Skillingberg, 2006] Green, J. and Skillingberg, M. (2006). Recyclable Aluminium Rolled Products. *Light Metal Age - Chicago*, 64(4):33.
- [Hadwiger, 1957] Hadwiger, H. (1957). *Vorlesungen uber Inhalt, Oberflache und isoperimetrie*. Springer Verlag, Berlin.
- [Hamerton et al., 2000] Hamerton, R., Cama, H., and Meredith, M. (2000). Development of the Coarse Intermetallic Particle Population in Wrought Aluminium Alloys During Ingot Casting and Thermo-mechanical Processing. *Materials Science Forum*, 331-337:143–154.
- [Hill, 1965] Hill, R. O. (1965). Continuum micro-mechanics of elastoplastic polycrystals. *Journal of the Mechanics and Physics of Solids*1, 13(2):89–101.
- [Hill, 2014] Hill, T. C. (2014). *Evolution of second phase particles with deformation in aluminium alloys*. PhD thesis, University of Manchester.
- [Hirsch and Lucke, 1988] Hirsch, J. and Lucke, K. (1988). Overview no. 76: Mechanism of deformation and development of rolling textures in polycrystalline f.c.c. metals-II. Simulation and interpretation of experiments on the basis of Taylor-type theories. *Acta Metallurgica*, 36(11):2883–2904.
- [Honniball, 2014] Honniball, P. D. (2014). *The Influence of Temperature upon the Deformation of Alpha Zirconium*. PhD thesis, University of Manchester.

- [Huang and Ou, 2009] Huang, H.-W. and Ou, B.-L. (2009). Evolution of precipitation during different homogenization treatments in a 3003 aluminum alloy. *Materials & Design*, 30(7):2685–2692.
- [Huang and Humphreys, 1999] Huang, Y. and Humphreys, F. (1999). Measurements of grain boundary mobility during recrystallization of a single-phase aluminium alloy. *Acta materialia*, 47(7):2259–2268.
- [Huang and Humphreys, 2000] Huang, Y. and Humphreys, F. (2000). Subgrain growth and low angle boundary mobility in aluminium crystals of orientation  $\{110\}_i001_j$ . *Acta materialia*, 48(8):2017–2030.
- [Humphreys, 1977] Humphreys, F. (1977). The nucleation of recrystallization at second phase particles in deformed aluminium. *Acta metallurgica*, 25(11):1323–1344.
- [Humphreys, 1979] Humphreys, F. (1979). Local lattice rotations at second phase particles in deformed metals. *Acta Metallurgica*, 27(12):1801–1814.
- [Humphreys, 1987] Humphreys, F. (1987). Dislocation-particle interactions during high temperature deformation of two-phase aluminium alloys. *Acta Metallurgica*, 35(12):2815–2829.
- [Humphreys, 1997a] Humphreys, F. (1997a). A unified theory of recovery, recrystallization and grain growth, based on the stability and growth of cellular microstructuresI. The basic model. *Acta Materialia*, 45(10):4231–4240.
- [Humphreys, 1997b] Humphreys, F. (1997b). A unified theory of recovery, recrystallization and grain growth, based on the stability and growth of cellular microstructuresII. The effect of second-phase particles. *Acta materialia*, 45(12):5031–5039.
- [Humphreys, 2000] Humphreys, F. (2000). Particle stimulated nucleation of recrystallization at silica particles in nickel. *Scripta materialia*, 43(7):591–596.
- [Humphreys and Ardakani, 1994] Humphreys, F. and Ardakani, M. (1994). The deformation of particle-containing aluminium single crystals. *Acta metallurgica et materialia*, 42(3):749–761.

- [Humphreys, 1990] Humphreys, F. J. (1990). Particle Stimulated Nucleation of Recrystallisation. *Recrystallisation'90*, pages 113–122.
- [Humphreys and Bate, 2006] Humphreys, F. J. and Bate, P. S. (2006). Measuring the alignment of low-angle boundaries formed during deformation. *Acta Materialia*, 54(3):817–829.
- [Humphreys and Hatherly, 2004] Humphreys, F. J. and Hatherly, M. (2004). *Recrystallisation and Related Annealing Phenomena*. Pergamon, Oxford, 2nd edition.
- [Humphreys and Bate, 2003] Humphreys, J. and Bate, P. (2003). Gradient plasticity and deformation structures around inclusions. *Scripta materialia*, 48:173–178.
- [Humphreys et al., 2012] Humphreys, J. F., Bate, P. S., Gholinia, A., and Brough, I. (2012). Measuring and Modelling the Microstructures of Two-Phase Aluminium Alloys after Deformation. *Materials Science Forum*, 715-716:23–32.
- [Hurley and Humphreys, 2003] Hurley, P. and Humphreys, F. (2003). The application of EBSD to the study of substructural development in a cold rolled single-phase aluminium alloy. *Acta Materialia*, 51(4):1087–1102.
- [International Aluminium Institute, 2015] International Aluminium Institute (2015). World Aluminium.
- [Jena et al., 1981] Jena, A., Lahiri, D., and Ramachandran, T. (1981). Kinetics of precipitation in Al-1 wt% Mn alloy. *Journal of Materials*, 16:2544–2550.
- [Jones and Hansen, 1981] Jones, A. R. and Hansen, N. (1981). The interaction between particles and low angle boundaries during recovery of aluminium-alumina alloys. *Acta Metallurgica*, 29(4):589–599.
- [Kevorkijan, 2010] Kevorkijan, V. (2010). Advances in recycling of wrought aluminium alloys for added value maximisation. *Metallurgija*, 16(2):103–114.
- [Kleemola and Nieminen, 1974] Kleemola, H. J. and Nieminen, M. A. (1974). On the strain-hardening parameters of metals. *Metallurgical Transactions*, 5(8):1863–1866.
- [Ko, 2014] Ko, L. C. L. (2014). *Particle Stimulated Nucleation: Deformation Around Particles*. Phd, University of Manchester.

- [Kral and Spanos, 1999] Kral, M. and Spanos, G. (1999). Three-dimensional analysis of proeutectoid cementite precipitates. *Acta Materialia*, 47(2):711–724.
- [Kramer and Haehner, 1967] Kramer, I. R. and Haehner, C. L. (1967). Low Temperature Recovery of Polycrystalline Aluminum. *Acta Metallurgica*, 15(2):199–202.
- [Kreisler and Doherty, 1978] Kreisler, A. and Doherty, R. D. (1978). Structure of well-defined deformation bands and formation of recrystallization nuclei in aluminium. *Metal Science*, 12(12):551–560.
- [Kuijpers, 2002] Kuijpers, N. (2002). Assessment of different techniques for quantification of  $\alpha$ -Al(FeMn)Si and  $\beta$ -AlFeSi intermetallics in AA 6xxx alloys. *Materials Characterization*, 49(5):409–420.
- [Lagneborg, 1973] Lagneborg, R. (1973). Bypassing of Dislocations Past Particles By A Climb Mechanism. *Scripta Metallurgica*, 7:605–614.
- [Lebensohn and Tome, 1993] Lebensohn, R. A. and Tome, C. N. (1993). A self-consistent anisotropic approach for the simulation of plastic deformation and texture development of polycrystals: application to zirconium alloys. *Acta metallurgica et materialia*, 41(9):2611–2624.
- [Li and Easterling, 1990] Li, W.-B. and Easterling, K. E. (1990). The influence of particle shape on zener drag. *Acta metallurgica et materialia*, 38(6):1045–1052.
- [Li and Arnberg, 2003a] Li, Y. and Arnberg, L. (2003a). Evolution of eutectic intermetallic particles in DC-cast AA3003 alloy during heating and homogenization. *Materials Science and Engineering: A*, 347(1-2):130–135.
- [Li and Arnberg, 2003b] Li, Y. and Arnberg, L. (2003b). Quantitative study on the precipitation behavior of dispersoids in DC-cast AA3003 alloy during heating and homogenization. *Acta Materialia*, 51(12):3415–3428.
- [Li et al., 2012] Li, Y. J., Muggerud, A. M. F., Olsen, A., and Furu, T. (2012). Precipitation of partially coherent  $\alpha$ -Al(Mn,Fe)Si dispersoids and their strengthening effect in AA 3003 alloy. *Acta Materialia*, 60(3):1004–1014.

- [Liu et al., 1998] Liu, Q., Juul Jensen, D., and Hansen, N. (1998). Effect of grain orientation on deformation structure in cold-rolled polycrystalline aluminium. *Acta Materialia*, 46(16):5819–5838.
- [Liu et al., 2009] Liu, Q., Yao, Z., Godfrey, A., and Liu, W. (2009). Effect of particles on microstructural evolution during cold rolling of the aluminum alloy AA3104. *Journal of Alloys and Compounds*, 482(1-2):264–271.
- [Liu and Radhakrishnan, 2010] Liu, W. and Radhakrishnan, B. (2010). Recrystallization behavior of a supersaturated AlMn alloy. *Materials Letters*, 64(16):1829–1832.
- [Lodgaard and Ryum, 2000] Lodgaard, L. and Ryum, N. (2000). Precipitation of dispersoids containing Mn and / or Cr in Al Mg Si alloys. *Materials Science and Engineering: A*, 283:144–152.
- [Lucke and Engler, 1990] Lucke, K. and Engler, O. (1990). Effects of particles on development of microstructure and texture during rolling and recrystallisation in fcc alloys. *Materials Science and Technology*, 6:1113–1130.
- [Lucke and Stuwe, 1971] Lucke, K. and Stuwe, H. P. (1971). On the theory of impurity controlled grain boundary motion. *Acta Metallurgica*, 19:1087–1099.
- [Mackie, 2013] Mackie, D. (2013). *Characterisation of casting defects in DC cast magnesium alloys*. PhD thesis, University of Manchester.
- [Mangan et al., 1997] Mangan, M. A., Lauren, P. D., and Shiflet, G. J. (1997). Three-dimensional reconstruction of Widmanstätten plates in Fe-12.3Mn0.8C. *Journal of Microscopy*, 188(February):36–41.
- [Martin, 1980] Martin, J. W. (1980). *Micromechanisms in Particle Hardened Alloys*. Cambridge University Press.
- [Merchant et al., 1990] Merchant, H., Morris, J., and Hodgson, D. (1990). Characterization of intermetallics in aluminum alloy 3004. *Materials Characterization*, 25(4):339–373.
- [Mott, 1952] Mott, N. F. (1952). CXVII. A theory of work-hardening of metal crystals. *Philosophical Magazine Series 7*, 43(346):1151–1178.

- [Mujahid and Martin, 1994] Mujahid, M. and Martin, J. W. (1994). The effect of oxide particle coherency on Zener pinning in ODS superalloys. *Journal of Materials Science Letters*, 13(3):153–155.
- [Nakajima et al., 2010] Nakajima, K., Takeda, O., Miki, T., Matsubae, K., Nakamura, S., and Nagasaka, T. (2010). Thermodynamic Analysis of Contamination by Alloying Elements in Aluminum Recycling. *Environmental Science & Technology*, 44(14):5594–5600.
- [Nes et al., 1985] Nes, E., Ryum, N., and Hunderi, O. (1985). On the Zener drag. *Acta Metallurgica*, 33(1):11–22.
- [Nishizawa et al., 1997] Nishizawa, T., Ohnuma, I., and Ishida, K. (1997). Examination of the Zener relationship between grain size and particle dispersion.
- [Nix et al., 1985] Nix, W. D., Gibeline, J. C., and Hughes, D. A. (1985). Time-dependent deformation of metals. *Metallurgical Transactions A*, 16(12):2215–2226.
- [Ø rsund and Nes, 1988] Ø rsund, R. and Nes, E. (1988). Effect of particles on recrystallization textures in aluminium-manganese alloys. *Scripta Metallurgica*, 22(5):665–669.
- [Parra-denis, 2007] Parra-denis, E. (2007). *Analyse morphologique 3D de particules de forme complexe : Application aux intermétalliques dans les alliages*. PhD thesis, l'Université de Saint-Étienne.
- [Perryman, 1954] Perryman, E. C. W. (1954). Observations on the Structural Changes Accompanying Recovery in Super-Purity Aluminium. *Acta Metallurgica*, 2(1):26–37.
- [Polmear, 2006] Polmear, I. J. (2006). *Light Alloys*. Elsevier, Oxford, 4th edition.
- [Ponge et al., 1997] Ponge, D., Bredehöft, M., and Gottstein, G. (1997). Dynamic recrystallization in high purity aluminum. *Scripta materialia*, 37(11):1769–1775.
- [Quinta da Fonseca and Bate, 2005] Quinta da Fonseca, J. and Bate, P. S. (2005). Evolution of Internal Stresses during the Plastic Deformation of IF Steel and Their Correlation with Crystal Orientation. *Materials Science Forum*, 495-497:1055–1060.

- [Quinta Da Fonseca et al., 2005] Quinta Da Fonseca, J., Mummary, P., and Withers, P. (2005). Full-field strain mapping by optical correlation of micrographs. *Journal of Microscopy*, 218(April):9–21.
- [Rhines et al., 1976] Rhines, F. N., Craig, K. R., and Rouse, D. a. (1976). Measurement of average grain volume and certain topological parameters by serial section analysis. *Metallurgical Transactions A*, 7(11):1729–1734.
- [Rios and Padilha, 2003] Rios, P. and Padilha, A. (2003). Microstructural path of recrystallization in a commercial Al-Mn-Fe-Si (AA3003) alloy. *Materials Research*, 6(4):605–613.
- [Ryum, 1969] Ryum, N. (1969). Precipitation and recrystallization in an Al-0.5 wt.% Zr-alloy. *Acta Metallurgica*, 17(3):269–278.
- [Sachs, 1928] Sachs, G. (1928). Zur ableitung einer fließbedingung. *Z. Ver. Dtsch. Ing.*, 72:734–736.
- [Samajdar and Doherty, 1994] Samajdar, I. and Doherty, R. D. (1994). Grain boundary misorientation in DC-cast aluminum alloy. *Scripta Metallurgica et Materialia*, 31(5):527–530.
- [Schmitz, 2006] Schmitz, C. (2006). *Handbook of Aluminium Recycling*. Vulkan-Verlag GmbH, Essen, Germany.
- [Scientific Forming Technologies Corporation, 2016] Scientific Forming Technologies Corporation (2016). DEFORM - Design Environment for Forming.
- [Singh et al., 2014] Singh, S. S., Schwartzstein, C., Williams, J. J., Xiao, X., De Carlo, F., and Chawla, N. (2014). 3D microstructural characterization and mechanical properties of constituent particles in Al 7075 alloys using X-ray synchrotron tomography and nanoindentation. *Journal of Alloys and Compounds*, 602:163–174.
- [Smith, 1948] Smith, C. S. (1948). Grains, phases and interfaces: an interpretation of microstructure. *Transactions of the Metallurgical Society of AIME*, 175:15–51.

- [Somerdar and Humphreys, 2003] Somerdar, M. and Humphreys, F. J. (2003). Recrystallisation behaviour of supersaturated Al-Mn alloys Part 1 - Al-1.3 wt-%Mn. *Materials Science and Technology*, 19:20–29.
- [Taylor, 1938] Taylor, G. I. (1938). Plastic Strain in Metals. *Journal of the Institute of Metals*, 62:307–324.
- [The Aluminum Association, 2011] The Aluminum Association (2011). Aluminum: The element of sustainability. Technical Report September, The Aluminum Association.
- [Thompson et al., 2013] Thompson, G. E., Hashimoto, T., Zhong, X. L., Curioni, M., Zhou, X., Skeldon, P., Withers, P. J., Carr, J. A., and Monteith, A. G. (2013). Revealing the three dimensional internal structure of aluminium alloys. *Surface and Interface Analysis*, 45(10):1536–1542.
- [Utigard et al., 1998] Utigard, T. A., Friesen, K., Roy, R. R., Lim, J., Silny, A., and Dupuis, C. (1998). The Properties and Uses of Fluxes in Molten Aluminum Processing. *JOM; Aluminum Overview*, pages 38–42.
- [Van Houtte et al., 1999] Van Houtte, P., Delannay, L., and Samajdar, I. (1999). Quantitative Prediction of Cold Rolling Textures in Low-Carbon Steel by Means of the Lamel Model. *Textures and Microstructures*, 31(3):109–149.
- [Van Houtte et al., 2005] Van Houtte, P., Li, S., Seefeldt, M., and Delannay, L. (2005). Deformation texture prediction: From the Taylor model to the advanced Lamel model. *International Journal of Plasticity*, 21(3):589–624.
- [Velichko et al., 2007] Velichko, A., Holzapfel, C., and Mücklich, F. (2007). 3D characterization of graphite morphologies in cast iron. *Advanced Engineering Materials*, 9(1-2):39–45.
- [Waddel, 1935] Waddel, H. (1935). Volume, shape, and roundness of rock particles. *Journal of Geology*, 43(3):250–280.
- [World Aluminium, 2015] World Aluminium (2015). World Aluminium Primary Aluminium Production.

- [Xue et al., 2000] Xue, X. J., Kozaczek, K. J., Kurtz, S. K., and Kurtz, D. S. (2000). Modeling of X-Ray Diffraction Stress Analysis in Polycrystalline Interconnects With Sharp Fiber Textures. *Advances in X-ray Analysis*, 42:634–645.
- [Zaefferer et al., 2008] Zaefferer, S., Wright, S. I., and Raabe, D. (2008). Three-dimensional orientation microscopy in a focused ion beam-scanning electron microscope: A new dimension of microstructure characterization. *Metallurgical and Materials Transactions A: Physical Metallurgy and Materials Science*, 39(2):374–389.
- [Zankel et al., 2009] Zankel, A., Kraus, B., Poelt, P., Schaffer, M., and Ingolic, E. (2009). Ultramicrotomy in the ESEM, a versatile method for materials and life sciences. *Journal of Microscopy*, 233(1):140–148.
- [Zhang et al., 2012] Zhang, L., Gao, J., Damoah, L. N. W., and Robertson, D. G. (2012). Removal of Iron From Aluminum: A Review. *Mineral Processing and Extractive Metallurgy Review*, 33(2):99–157.



# Appendix A

## Appendix

### A.1 Modified Preprogram Subroutine

```
!*****!  
!  
!      SUBROUTINE SETSTATE                                !  
!          Sets the internal element state                !  
!  
!*****!  
SUBROUTINE SETSTATE( nein , location )  
  
      USE FAS.COM  
!  
      USE DFLIB  
  
      IMPLICIT NONE  
      LOGICAL(4)                l_file  
      INTEGER(4)    nein , iselect , i , j , k , location , ilocal , set_type , nclusters  
          , iclus  
      REAL(4)    ph1 , phi , ph2 , ch1 , chi , ch2 , r1 , r2 , r3 , dummy , ax , by , cz ,  
          ld1 , ld2 , alpha , lh , lv  
      DIMENSION    nein(1:3) , location(1:3 , 1:*) , ilocal(1:3)  
  
      REAL(4)    sumf , r  
      REAL(4) , DIMENSION(1:12) ::          frac  
  
      INTEGER(4) , ALLOCATABLE :: cluster ( : )  
      REAL(4) ,          ALLOCATABLE :: ass_ang ( : , : )  
  
      ALLOCATE ( cluster (1:nlmnt) , ass_ang (1:3 , 1:nlmnt) )  
  
!-----get number of slip systems  
      WRITE(* , '(//,2X, ''Enter max. no. of slip systems involved: '' , \) ')
```

```

READ(*,*) nsv
nsv= nsv + 3

```

```

!-----get type of operation
WRITE(*,'(//, '' Select bicrystal      (1) ',/, &
& ''      perturbed-ideal      (2) ',/, &
& ''      included grain      (3) ',/, &
& ''      file orientations    (4) ',/, &
& ''      cubic particle      (5) ',/, &
& ''      diagonal particles   (6) ',/, &
& ''      linear particles     (7) ',/, &
& ''      specific particle    (8) ',/, &
& ''              -or random   (9): ',\)' )
READ(*,*) iselect

SELECT CASE( iselect )

CASE(1)
WRITE(*,'(10X, ''Enter Euler angles for bottom half: ',\)' )
READ(*,*) ph1, phi, ph2
ph1= ph1/ 57.295779513
phi= phi/ 57.295779513
ph2= ph2/ 57.295779513

WRITE(*,'(10X, ''Enter Euler angles for top half: ',\)' )
READ(*,*) ch1, chi, ch2
ch1= ch1/ 57.295779513
chi= chi/ 57.295779513
ch2= ch2/ 57.295779513

CASE(2)
WRITE(*,'(10X, ''Enter Euler angles and chi spread: ',\)' )
READ(*,*) ph1, phi, ph2, chi
ph1= ph1/ 57.295779513
phi= phi/ 57.295779513
ph2= ph2/ 57.295779513
chi= chi/ 57.295779513

CASE(3)
WRITE(*,'(10X, ''Enter Euler angles for central region: ',\)' )
)
READ(*,*) ph1, phi, ph2
ph1= ph1/ 57.295779513
phi= phi/ 57.295779513
ph2= ph2/ 57.295779513

CASE(4)
WRITE(*,'(10X, ''Enter number of orientation sets: ',\)' )
READ(*,*) nmat1

```

CASE(5)

```
WRITE(*,'(10X, 'Enter Euler angles and chi spread: ',\)' )
READ(*,*) ph1, phi, ph2, chi
ph1= ph1/ 57.295779513
phi= phi/ 57.295779513
ph2= ph2/ 57.295779513
chi= chi/ 57.295779513

WRITE(*,'(10X, 'Enter size of particle (ax, by, cz): ',\)' )
READ(*,*) ax,by,cz
```

CASE(6)

```
WRITE(*,'(10X, 'Enter Euler angles and chi spread: ',\)' )
READ(*,*) ph1, phi, ph2, chi
ph1= ph1/ 57.295779513
phi= phi/ 57.295779513
ph2= ph2/ 57.295779513
chi= chi/ 57.295779513

WRITE(*,'(10X, 'Enter size of particle (ax, by, cz): ',\)' )
READ(*,*) ax,by,cz

WRITE(*,'(10X, 'Enter particle parameters (ld1, ld2): ',\)' )
READ(*,*) ld1,ld2
```

CASE(7)

```
WRITE(*,'(10X, 'Enter Euler angles and chi spread: ',\)' )
READ(*,*) ph1, phi, ph2, chi
ph1= ph1/ 57.295779513
phi= phi/ 57.295779513
ph2= ph2/ 57.295779513
chi= chi/ 57.295779513

WRITE(*,'(10X, 'Enter size of particle (ax, by, cz): ',\)' )
READ(*,*) ax,by,cz

WRITE(*,'(10X, 'Enter particle parameters (lh, lv): ',\)' )
READ(*,*) lh,lv
```

CASE(8)

```
! Read file here.-----

OPEN(76,FILE='particleshape.txt',STATUS='OLD', ACTION='READ')

DO i= 1, nlmnt
READ(76,*) lfromfile(i)
END DO
```

```

CLOSE(76)

WRITE(*, '(10X, ''Enter Euler angles and chi spread: '',\)' )
READ(*,*) ph1, phi, ph2, chi
ph1= ph1/ 57.295779513
phi= phi/ 57.295779513
ph2= ph2/ 57.295779513
chi= chi/ 57.295779513

CASE DEFAULT
    ! no i/o required

END SELECT

! CALL SEED( RND$TIMESEED )
! initialise random sequence !DIGITAL Fortran only?

!-----get list of different location orientations ( for options 2, 4 and default)

! IF ( iselect.NE. 1 .AND. iselect.NE. 3 .AND. iselect.NE. 4 ) THEN
! IF ( iselect.NE. 1 .AND. iselect.NE. 3 .AND. iselect.NE. 5 .AND. iselect.NE.
6 .AND. iselect.NE. 7 .AND. iselect.NE. 8 ) THEN

    ass_ang(1,1:nlmnt)= -999.      ! flag for not set
    set_type= -1                  ! modular number for element
    code

    DO i= 1, nlmnt

        IF ( ass_ang(1,i) .EQ. -999.) THEN                ! new 'grain'

            set_type= set_type + 1                ! increment type
            number

!-----get next orientation depending on option

SELECT CASE( iselect)

CASE(2)                ! perturbed ideal
    orientations

    CALL PERTID( ph1, phi, ph2, chi, r1, r2, r3 )

CASE DEFAULT           ! random orientations
    CALL RANDOMNUMBER(r1)
    CALL RANDOMNUMBER(r2)
    CALL RANDOMNUMBER(r3)

```

```

                r1= 6.2832*r1
                r2= ACOS(2.*r2-1.)
                r3= 6.2832*r3
            END SELECT

!-----check here and upstream for same location , set angles and code
            ilocal(1:3)=location(1:3,i)

            DO j= i, nlmnt
                IF ( ( ilocal(1) .EQ. location(1,j)) .AND.      &
                    & ( ilocal(2) .EQ. location(2,j)) .AND. &
                    & ( ilocal(3) .EQ. location(3,j)) ) THEN
                    ass_ang(1,j)= r1
                    ass_ang(2,j)= r2
                    ass_ang(3,j)= r3

                    le(j)= 1 + set_type
                END IF
            END DO

            END IF

        END DO

    END IF

!-----Loop on elements setting orientation
    IF ( iselect .EQ. 4 ) THEN                ! file orientations

        WRITE(*,'(/,15X, '' Assigning orientation sets: enter fraction for: ''
            ')
        DO i= 1, nmatl
            WRITE(*,'(18X, '' set '' ,I3, '' : '' ,\ ) ' ) i
            READ(*,*) frac(i)
        END DO

!-----normalise and make cumulative
        sumf= SUM(frac(1:nmatl)) ; frac(1:nmatl)= frac(1:nmatl)/sumf
        IF ( nmatl.GT.1 ) THEN
            DO i=2, nmatl
                frac(i)= frac(i)+frac(i-1)
            END DO
        END IF

!-----assign set to clusters (random)
        cluster= le                ! assign element cluster number

        nclusters=0

```

```

DO i= 1, nlmnt
    IF ( cluster(i) .GT. nclusters) nclusters= cluster(i)
END DO

DO i= 1, nclusters
    CALL RANDOMNUMBER(r)
    k=0
    DO j= 1, nmatl
        IF ( r .GT. frac(j) ) k=j
    END DO

    DO j= 1, nlmnt
        IF ( cluster(j) .EQ. i ) le(j)= k+1
    END DO
END DO

! DO i= 1, nlmnt
!     CALL RANDOMNUMBER(r)
!     k=0
!     DO j= 1, nmatl
!         IF ( r .GT. frac(j) ) k=j
!     END DO
!     le(i)= k+1
! END DO

DO j= 1, nmatl

    WRITE(*,'(25X,''<enter> to input orientation for set'',I3,\)
        ' ) j
    READ(*,*)
    CALL ORIFILE(51,l_file)

    DO i=1, nlmnt
        IF ( le(i) .EQ. j ) THEN
            IF ( cluster(i) .GT. 0 ) THEN

                READ(51,*) dummy, r1, r2, r3

                iclus= cluster(i)

                DO k= i, nlmnt
                    IF ( cluster(k) .EQ.
                        iclus ) THEN
                        ass_ang(1,k)=
                            r1
                        ass_ang(2,k)=
                            r2

```

```

                                                                    ass_ang(3,k)=
                                                                    r3
                                                                    cluster(k)= -
                                                                    cluster(k)
                                                                    )
                                                                    END IF
                                                                    END DO

                                                                    END IF
                                                                    END IF
                                                                    END DO

!      DO i=1, nlmnt
!          IF ( le(i) .EQ. j ) THEN
!              READ(51,*) dummy, r1, r2, r3
!              ass_ang(1,i)= r1
!              ass_ang(2,i)= r2
!              ass_ang(3,i)= r3
!          END IF
!      END DO

CLOSE(51)
END DO

ELSE

DO i=1, nlmnt

SELECT CASE( iselect)

CASE(1)      !      allocate bottom and top halves, set
types
              IF ( location(3,i) .LE. nein(3)/2 ) THEN
                  r1=ph1
                  r2=phi
                  r3=ph2
                  le(i)= 1

                  ELSE
                  r1=ch1
                  r2=chi
                  r3=ch2
                  le(i)= 2

                  END IF

                  ass_ang(1,i)= r1
                  ass_ang(2,i)= r2
                  ass_ang(3,i)= r3

```

```

CASE(3)          ! 'included' grains
IF ( ( ABS( 2*location(3,i) -nein(3) -1 ).LT. nein
      (3)/2 ) .AND.      &
&      ( ABS( 2*location(2,i) -nein(2) -1 ).LT. nein
      (2)/2 ) .AND.      &
&      ( ABS( 2*location(1,i) -nein(1) -1 ).LT. nein
      (1)/2 ) ) THEN
      r1=ph1
      r2=phi
      r3=ph2
      le(i)= 1

ELSE

      CALL RANDOMNUMBER(r1)
      CALL RANDOMNUMBER(r2)
      CALL RANDOMNUMBER(r3)
      r1=6.2832*r1
      r2=acos(2.*r2-1.)
      r3=6.2832*r3
      le(i)= 2

END IF

      ass_ang(1,i)= r1
      ass_ang(2,i)= r2
      ass_ang(3,i)= r3

CASE(5)          ! 'included grains' rectangle
IF ( ( ABS( 2*location(3,i) -nein(3) -1 ).LT. cz )
      .AND.      &
&      ( ABS( 2*location(1,i) -nein(1) -1 ).LT. ax )
      .AND.      &
&      ( ABS( 2*location(2,i) -nein(2) -1 ).LT. by )
      ) THEN
      r1=0
      r2=0
      r3=0
      le(i)= 1

ELSE

      CALL PERTID( ph1, phi, ph2, chi, r1, r2, r3 )
      le(i)= 2

END IF

      ass_ang(1,i)= r1
      ass_ang(2,i)= r2
      ass_ang(3,i)= r3

```

```

CASE(6)          ! 'included particles' Diag
IF              ( ( ABS ( 20- ABS ( 2*location(3,i) -
nein(3) -1 -ld1)).LT. cz ) .AND.      &
&              ( ABS ( 20- ABS ( 2*location(1,i) -nein(1) -1
-ld1)).LT. ax ) .AND.      &
&              ( ABS ( 2*location(2,i) -nein(2) -1 ) .LT. by
) ) THEN
                r1=0
                r2=0
                r3=0
                le(i)= 1

ELSE IF ( ( ABS (20-ABS( 2*location(3,i) -nein
(3) -1 -ld2)).LT. cz ) .AND.      &
&        ( ABS (20-ABS( 2*location(1,i) -nein
(1) -1 -ld2)).LT. ax ) .AND.      &
&        ( ABS ( 2*location(2,i) -nein(2) -1 )
.LT. by ) ) THEN
                r1=0
                r2=0
                r3=0
                le(i)= 1

ELSE
                CALL PERTID( ph1, phi, ph2, chi, r1, r2, r3 )
                le(i)= 2

END IF

                ass_ang(1,i)= r1
                ass_ang(2,i)= r2
                ass_ang(3,i)= r3

CASE(7)          ! 'included particles' Linear
IF              ( ( ABS ( lh - ABS ( 2*location(3,i) -
nein(3) -1)).LT. cz ) .AND. &
&              ( ABS ( lv - ABS ( 2*location(1,i) -
nein(1) -1)).LT. ax ) .AND. &
&              ( ABS ( 2*location(2,i) -nein(2) -1 )
.LT. by ) ) THEN
                r1=0
                r2=0
                r3=0
                le(i)= 1

ELSE
                CALL PERTID( ph1, phi, ph2, chi, r1, r2, r3 )
                le(i)= 2

```

```

                                END IF

                                ass_ang(1,i)= r1
                                ass_ang(2,i)= r2
                                ass_ang(3,i)= r3

                                CASE(8)      ! 'Included Particle - Specific Input'
                                CALL PERTID( ph1, phi, ph2, chi, r1, r2, r3 )
                                le(i)= lefromfile(i)

                                ass_ang(1,i)= r1
                                ass_ang(2,i)= r2
                                ass_ang(3,i)= r3

                                END SELECT

                                END DO

                                END IF

!-----assign orientation state variable values
DO i= 1, nlmnt
    DO j=1,np(i)
        k= np(i)*(i-1) + j
        sv(1,k)=ass_ang(1,i)
        sv(2,k)=ass_ang(2,i)
        sv(3,k)=ass_ang(3,i)
    END DO

END DO

!-----null for all other states
DO i=1,ngps
    eps(i)=0.
    dep(i)=0.
    st(1:6,i)=0.
    ep(1:6,i)=0.
    ds(1:6,i)=0.
    de(1:6,i)=0.
    rt(1:3,i)=0.
    dr(1:3,i)=0.
END DO

DEALLOCATE ( ass_ang, cluster)

END SUBROUTINE

```

## A.2 Saltykov Method: Supplementary Plots

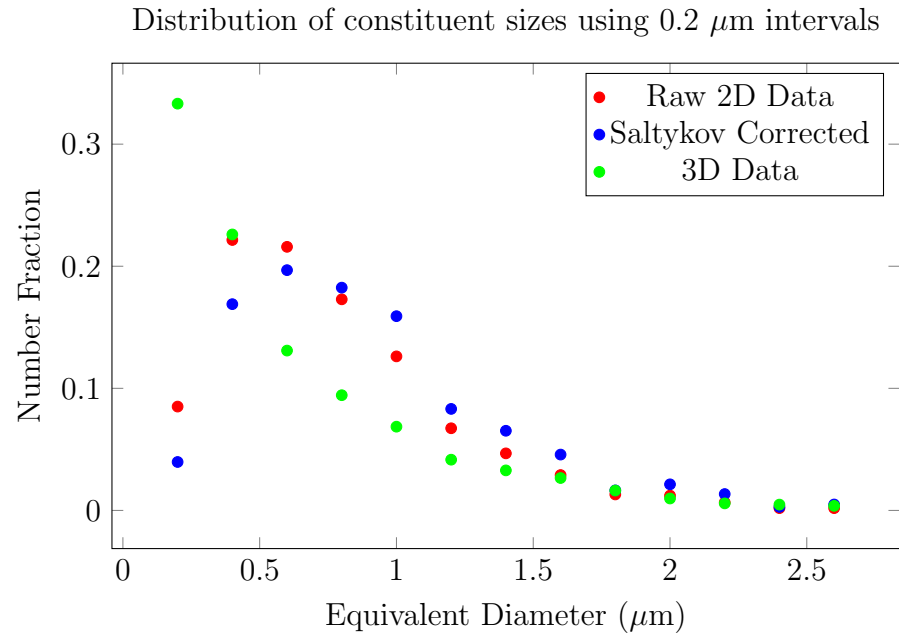


Figure A.1: Raw 2D and Saltykov corrected equivalent diameters of rolled aluminium grouped using  $0.2 \mu\text{m}$  intervals

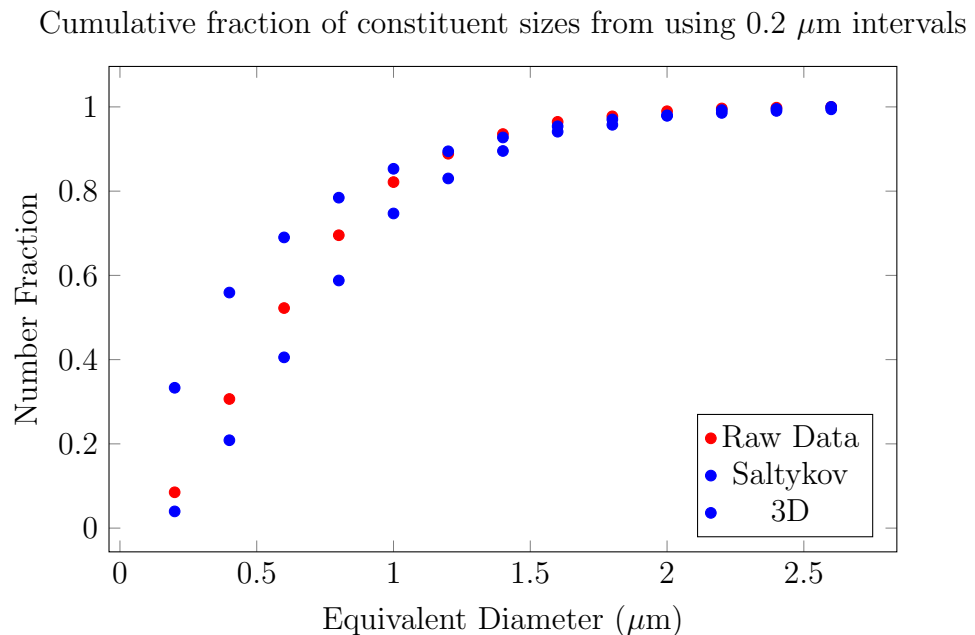


Figure A.2: Raw 2D and Saltykov corrected cumulative equivalent diameters of rolled aluminium grouped using  $0.2 \mu\text{m}$  intervals

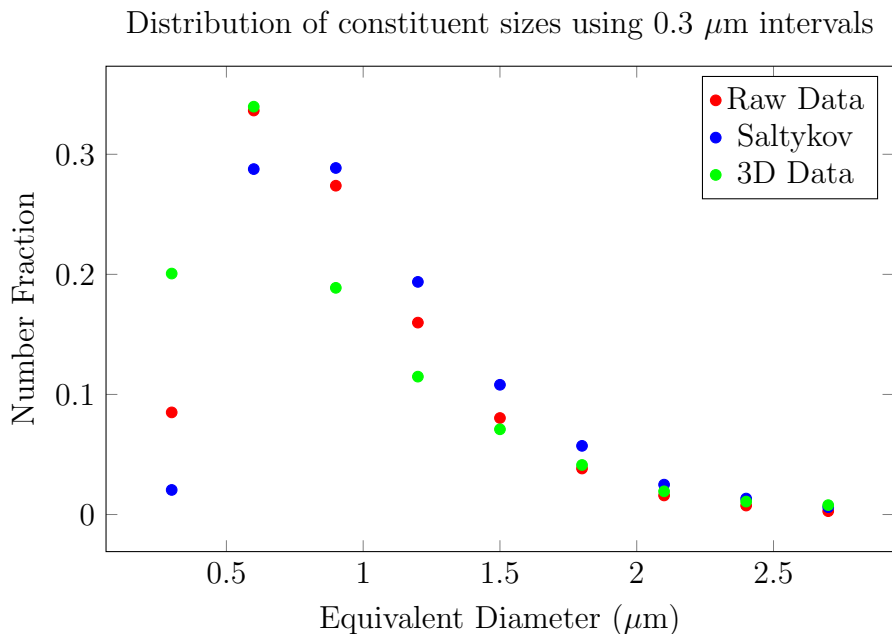


Figure A.3: Raw 2D and Saltykov corrected equivalent diameters of rolled aluminium grouped using 0.3  $\mu\text{m}$  intervals

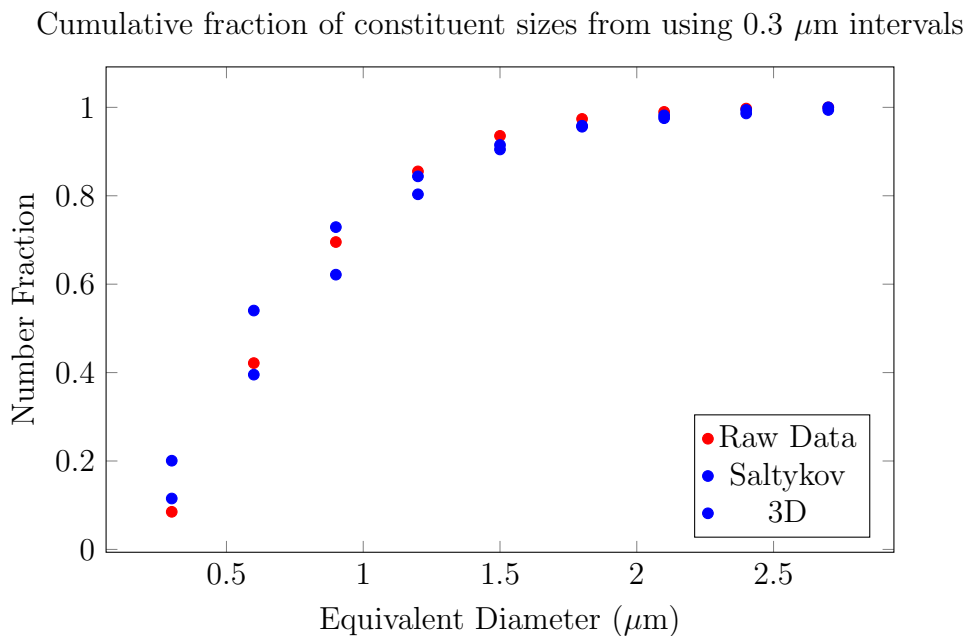


Figure A.4: Raw 2D and Saltykov corrected cumulative equivalent diameters of rolled aluminium grouped using 0.3  $\mu\text{m}$  intervals

## A.3 Radon Transform MATLAB Code

```

clear, clc

% input image (Max. shear strain)
file = 'StrainMap.jpg';
I = imread(file);
imagesc(I), colormap(gray); grid on, grid minor,

prompt = ...
    {'Start of X:', 'End of X:', 'Start of Y:', 'End of Y:', 'Window Size:'};
dlg_title = 'Input for Radon Transform';
num_lines = 1;
def = {'0', '2500', '0', '2500', '100'};
input = (inputdlg(prompt, dlg_title, num_lines, def));

% apply window
W1 = str2double(input{5});
a1 = floor( (str2double(input{2}) - str2double(input{1}) ) / W1);
b1 = floor( (str2double(input{4}) - str2double(input{3}) ) / W1);
AA1 = str2double(input{3}) +1 :str2double(input{3}) + b1*W1;
AA2 = str2double(input{1}) +1 :str2double(input{1}) + a1*W1;
A=I(AA1,AA2);
imagesc(I), colormap(gray); figure, imagesc(A), colormap(gray);

clear I
[m n] = size(A);
C1 = mat2cell( A , W1*ones(1,b1) , W1*ones(1,a1) );

% apply Radon transform
theta = 0:179;
R1 = cell(size(C1)); xp1 = cell(size(C1));
parfor ci = 1:numel(C1)
[R1{ci} xp1{ci}] = radon(C1{ci},theta);
end

% remove data (noise) which is more than
%2 times of the standard deviation above or below the mean
mul = cell(size(R1)); sd1 = cell(size(R1)); ...
    L1_sd2 = cell(size(R1)); Rc1_sd2 = cell(size(R1));
parfor ci = 1:numel(R1)
mul{ci} = mean2(R1{ci});
sd1{ci} = std2(R1{ci});
L1_sd2{ci} = abs(R1{ci}-mul{ci}) > 2*sd1{ci};
Rc1_sd2{ci} = R1{ci}.*L1_sd2{ci};
end

for i = 1:a1

```

```

for j = 1:b1
for k = 1:180;
p1_sd2{j,i}(:,k) = length(findpeaks(Rc1_sd2{j,i}(:,k)));
end
end
end

% save result
for i = 1:a1
for j = 1:b1
dlmwrite ...
('RadonOutput.txt', [i j p1_sd2{j,i}], 'delimiter', '\t', '-append')
end
end

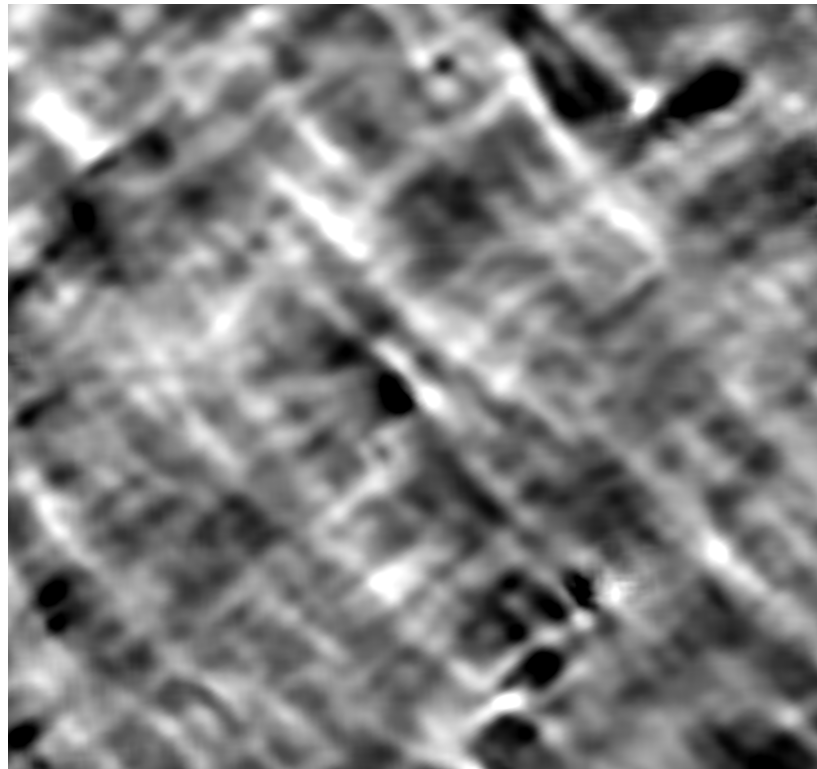
% load results
clear,clc

temp = load('RadonOutput.txt');
StrainRadon = temp(:,3:182);
clear temp
StrainRadonPlot = sum(StrainRadon) / sum(sum(StrainRadon));

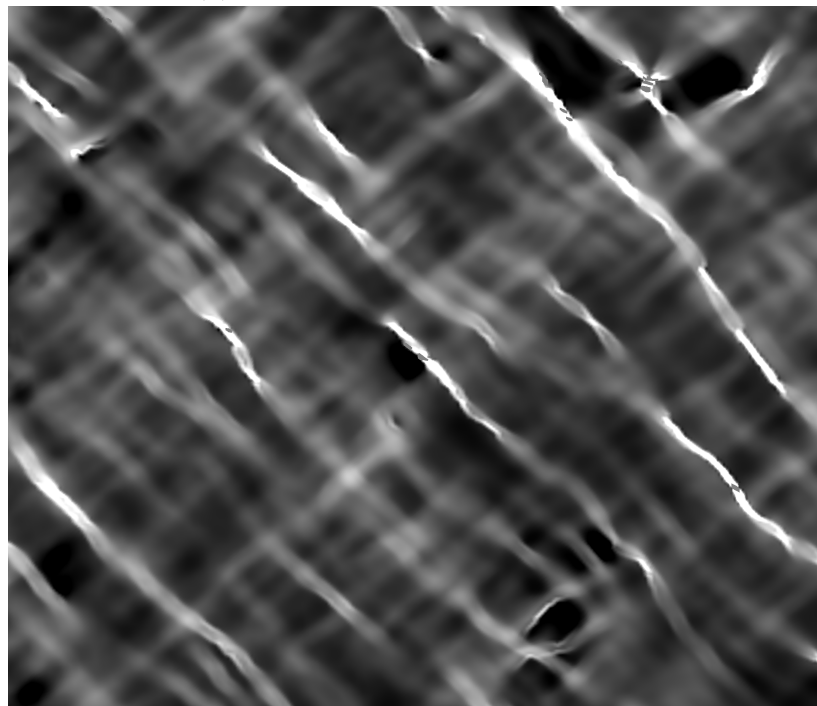
%plot
THETA = [-90:89];
plot(THETA, StrainRadonPlot, '+')
set(gca, 'XLim', [-90 90], 'XTick', [-90:10:90])
xlabel('theta (deg.)', 'FontSize', 14)
ylabel('Frequency', 'FontSize', 14)
line([-40 -40], [0 0.03], 'Color', 'g', 'LineStyle', '-.'), ...
line([-50 -50], [0 0.03], 'Color', 'g', 'LineStyle', '-.'), ...
line([40 40], [0 0.03], 'Color', 'g', 'LineStyle', '-.'), ...
line([50 50], [0 0.03], 'Color', 'g', 'LineStyle', '-.')

```

## A.4 Radon Transforms - Input Strain Maps



(a) Single particle at 4% reduction



(b) Single particle at 8% reduction

Figure A.5: DIC Strain maps for the single particle case illustrating the presence of artefacts which diminish upon subsequent compression.

## A.5 CPFEM: Supplementary Strain Plots

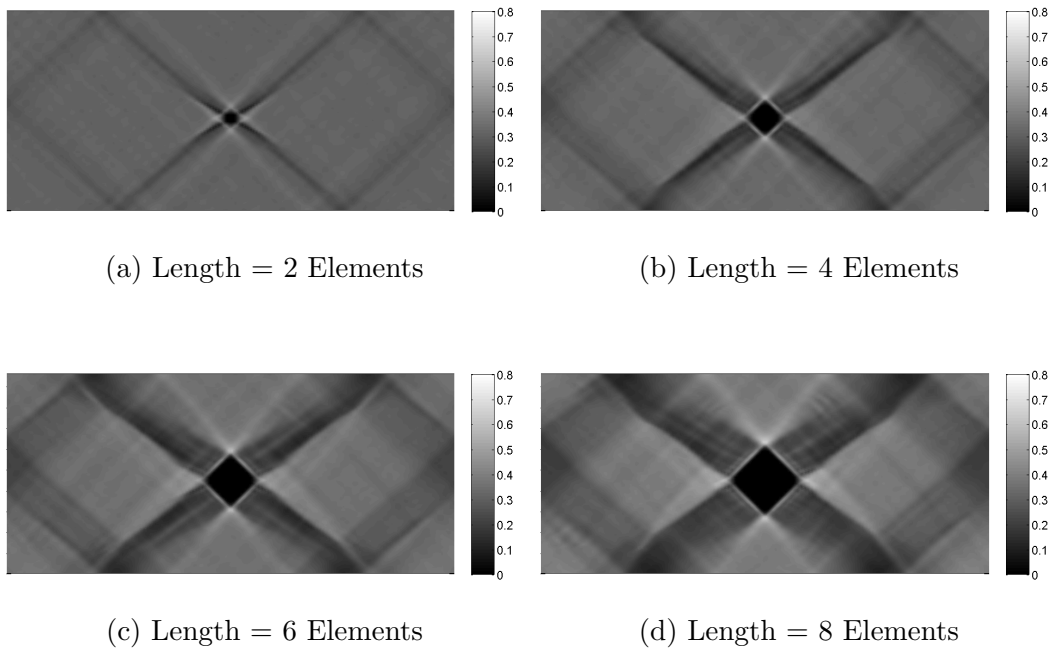


Figure A.6: Changing the particle size effects the local strain found within the matrix

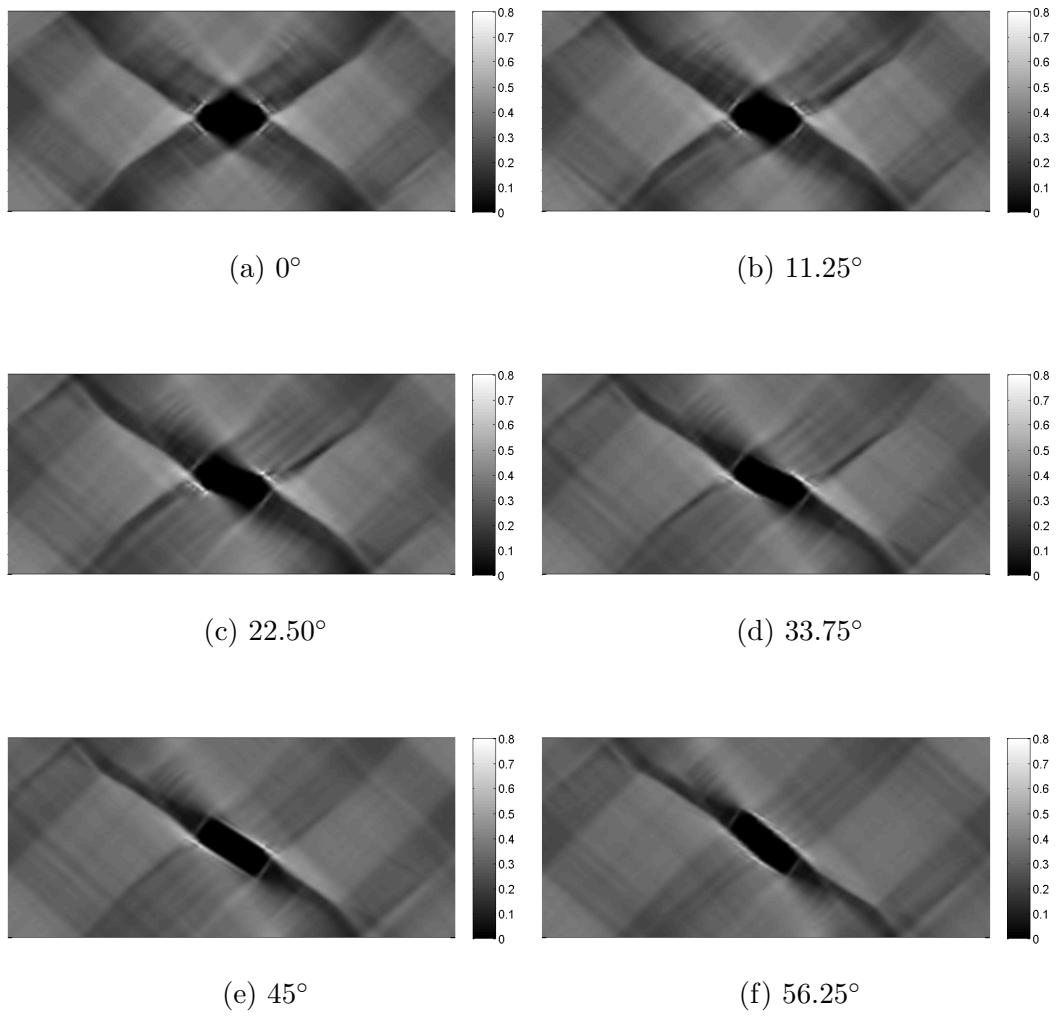


Figure A.7: Changing the orientation of the non deformable region alters the resulting local strains

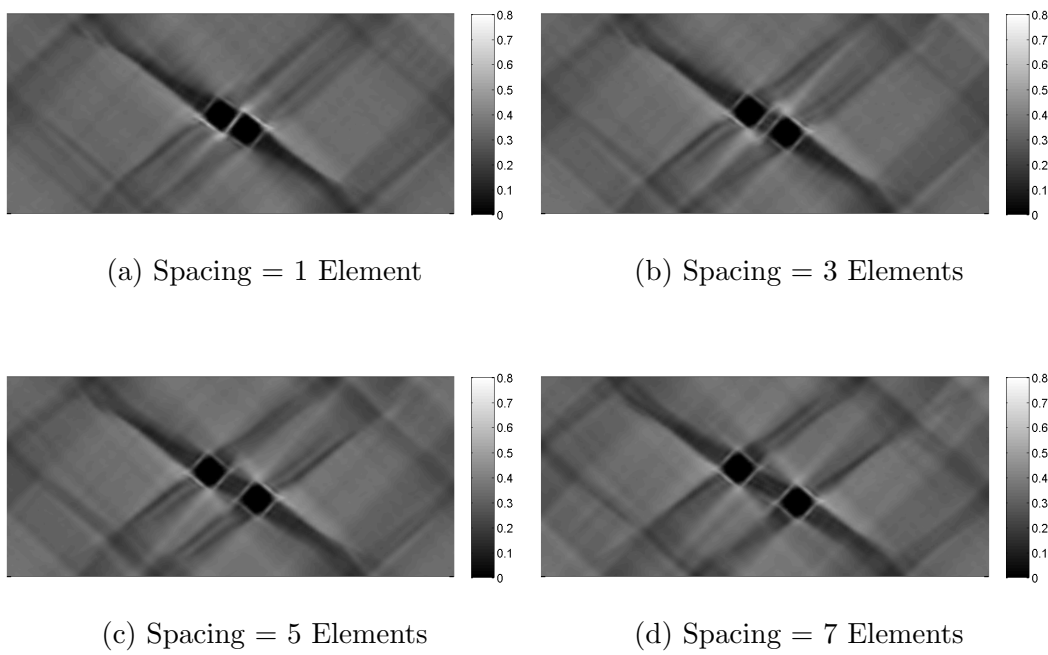


Figure A.8: Images depicting how changing the distance between two non deformable regions aligned at  $45^\circ$  to the  $x$  axis changes the resulting local strain within the matrix

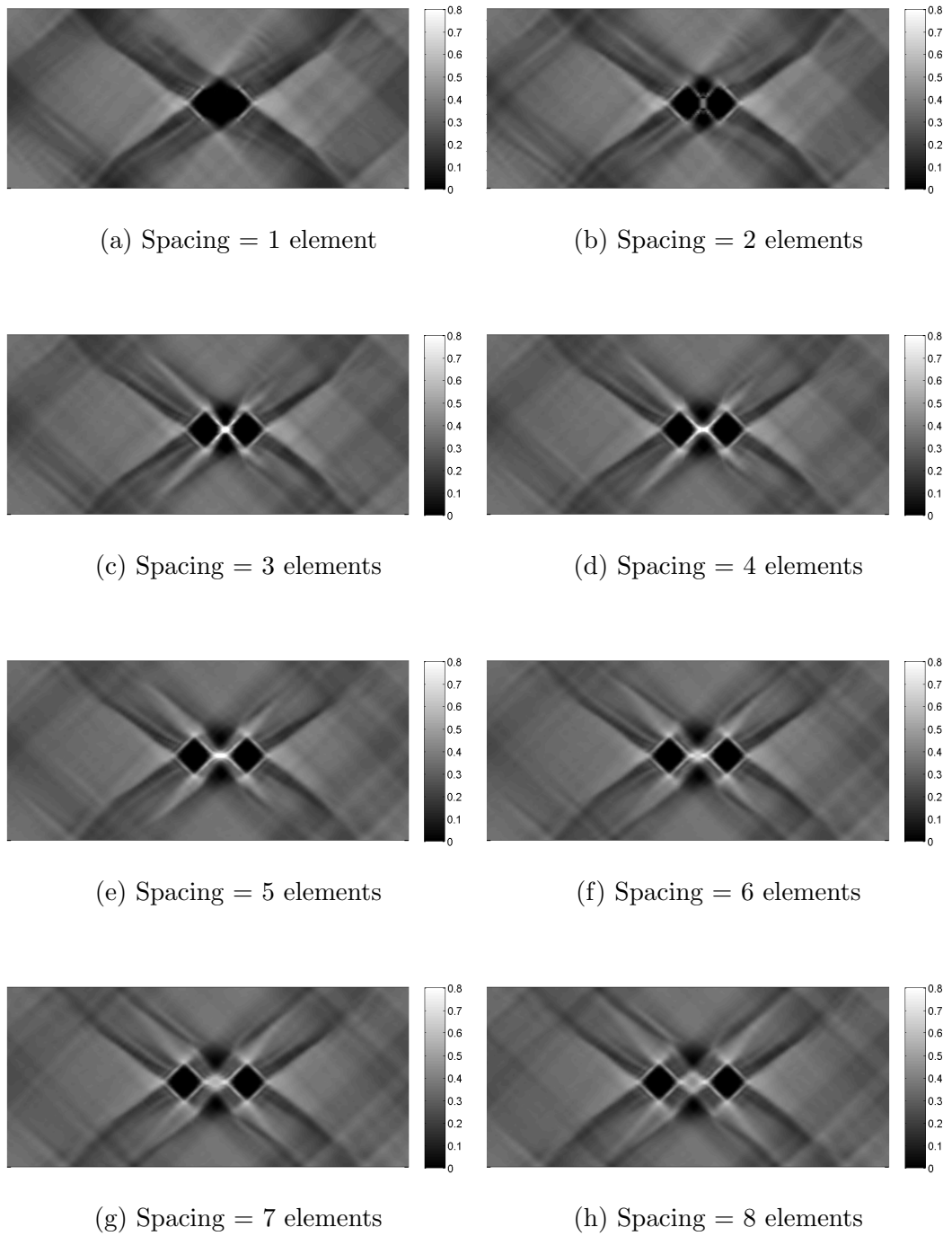


Figure A.9: Images illustrating how changing the distance between two non deformable regions aligned along the  $x$  axis changes the local strain within the matrix

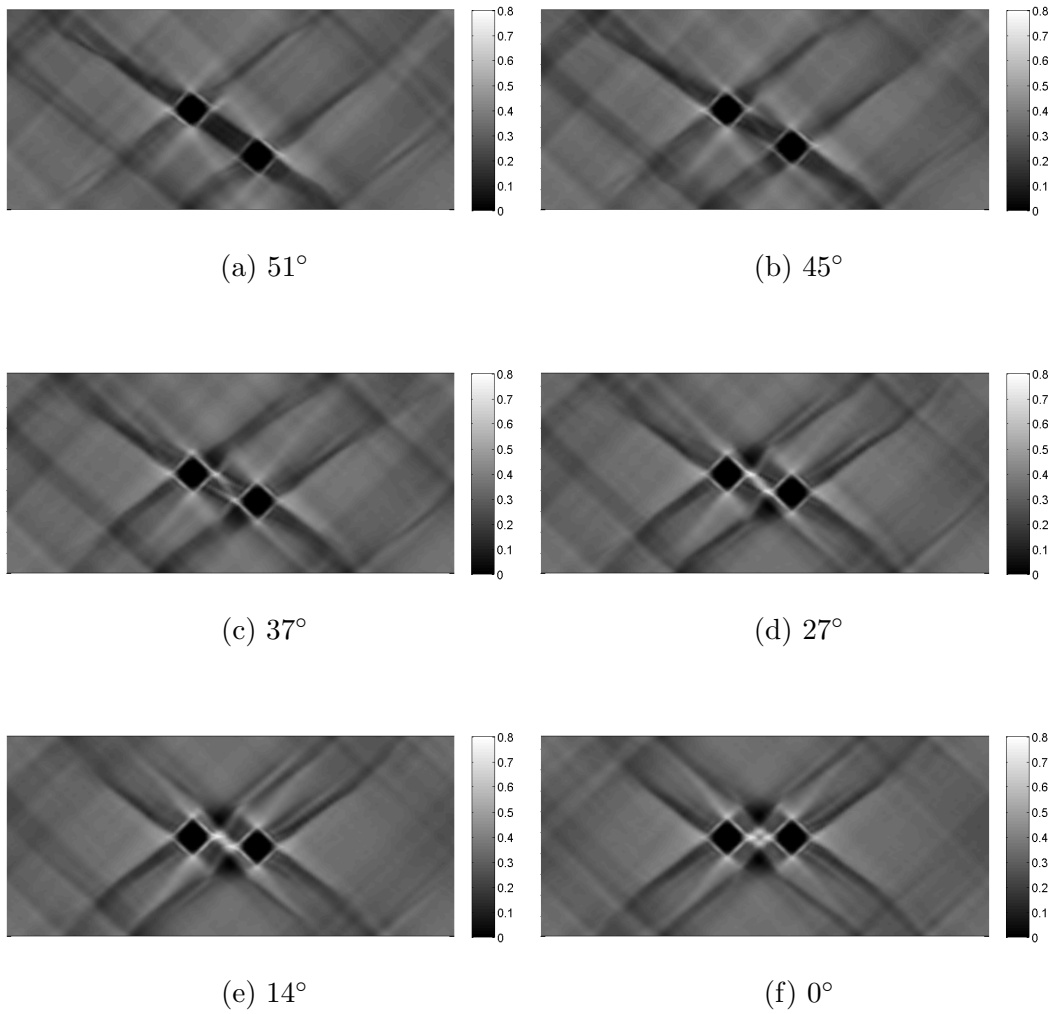


Figure A.10: Plots illustrating how changing the alignment (angle relative to  $x$  axis) of two non deformable regions whilst maintaining the same interparticle distance affects the local strain within the matrix